UNIVERSITY OF SEVILLE

DOCTORAL THESIS

Towards PET range verification in proton therapy: new cross sections for improved accuracy

Author: M. Teresa RODRÍGUEZ GONZÁLEZ

Supervisors: Prof. Dr. Carlos GUERRERO SÁNCHEZ
Prof. Dr. Jose Manuel QUESADA MOLINA

A thesis submitted in fulfillment of the requirements
for the degree of Doctor of Philosophy

in the

Physical Sciences and Technologies Doctoral Programme

Departament of Atomic, Molecular and Nuclear Physics. Faculty of Physics
Centro Nacional de Aceleradores

March 10, 2023

Acknowledgements

I would like to express my most sincere gratitude to my supervisors Dr. Jose Manuel Quesada and Dr. Carlos Guerrero, for giving me the opportunity and continuous help on the realization of this thesis. Thank you for all the good advice, support and guidance I received in all stages of this work; for your mentoring and insightful discussions in the daily work and for your detailed supervision in the writing of this manuscript; thank you for your closeness and empathy any time I needed it. I am grateful for everything I have learnt and experienced throughout these years, especially for bringing me the opportunity to perform experiments in research and clinical facilities across Europe, there I could enjoy the most exciting part of this work. I could always count on your motivating attitude during the tough times, and your enthusiasm and mentorship inspired me to love this work.

Carlos, Jose Manuel, siempre os estaré agradecida por la confianza que depositasteis en mí y todo lo que me habéis transmitido. Todo ello me ha permitido y me ha ayudado muchísimo a crecer como investigadora, y, más importante, como persona.

I would like to acknowledge all the people who have contributed in some extent to this work. I sincerely thank all the people of the West German Proton Therapy Center (WPE): Dr. Christian Baümer, for his valuable help and for allowing me to perform the experiments of long-lived isotopes at WPE; Walter Jentzen, for facilitating the use of the PET scanner from the Nuclear Medicine department and for always creating such a cheerful atmosphere; Dr. Maximiliam Bäcker, for his willingness, for helping with the beam delivering system, and, above all, for his friendship and sticking with me during the long night shifts at WPE.

I would also like to thank all the people who contributed to the experimental campaign at KVI - Center for Advanced Radiation Technology, in Groningen: Dr. Peter Dendooven, for his essential help, experience and productive discussions on the measurement of short-lived isotopes; Dr. Ikechi Ozoemelam, for his help and the opportunity to learn about his thesis; and Dr. Luis Mario Fraile, Dr. Samuel España and Víctor Valladolid, for providing the detectors and their great support with the experimental work. The setbacks and complications I had to face at KVI-CART made me familiar with the difficulties of working in experimental physics. Now, I am grateful for all I learnt from this experience, not only about the work, but also about the attitude and disposition to cope with the challenges.

I want to express my most sincere gratitude to all people who helped me during my research stay at HIT: Dr. Stephan Bröns, for his kind support during my entire time at HIT and his remarkable willingness to provide anything I needed to perform the experiments; Dr. Christian Schömers, for his help, specially for assisting and adjusting the beam pulse structure to measure the production of the short-lived isotopes; and Dr. Julia Bauer, for her mentoring, her kind support and always good disposition. Thank you for hosting me during those three months, which turned out to be the most productive of my thesis. Julia, thank for your warm and caring hospitality, which made me to feel at home!

I sincerely thank all the members from the IFIC team: Dr. César Domingo, for letting me have the opportunity to be collaborate with his team, for his input and experience on the subject; Ion Ladarescu, for his valuable help operating the iTEDs and his interesting conversations during the breaks; Dr. Javier Balibrea for his kind and remarkable support, enthusiasm and be always there to help, he truly became a friend; and Dr. Jorge Lerendegui, these words are not sufficient to express my thanks and gratitude for all he has helped and taught me throughout these years. From when I was an undergraduate coursing "Técnicas Experimentales de Física Nuclear" and forward, I really appreciate his experience, teaching abilities and continuous help in this work.

I would like to express my grateful to the Spanish FPI Research Fellowship, associated to the project with grant number FPA2016-77689-C2-1-R *from the Spanish "Ministerio de Ciencia e Innovación", former "Ministerio de Economía y Competitividad", which allowed me to realize this work. I would also thank projects* RTI2018-098117-B-C21 *also from the "Ministerio de Ciencia e Innovación",* P18-RT-1900 *from the "Consejeruía de Economía y Conocimiento de la Junta de Andalucía", and the European Union's Horizon 2020* H2020-847552 *(SANDA) and 101008548 (HITRIplus) projects. I would like to express my grateful to Dr. Joaquín Gómez Camacho, co-PI of the research project associated to my fellowship, for his trust, his support and help to obtain funding.*

Me gustaría extender mi agradecimiento a todos los miembros del Departamento de Física Atómica, Molecular y Nuclear y del Centro Nacional de Aceleradores, por la acogida y motivación que me han transmitido a lo largo de estos años. En especial, quiero dar las gracias al Prof. Dr. Jose Miguel Arias Carrasco, por su buen consejo; a la Dra. M^a Isabel Gallardo, por ser una gran inspiración desde el día que la conocí, al Dr. Jose M. Espino, por abrirme la puerta; al Dr. Miguel Cortés, por su siempre buena disposición y apoyo; y a la Dra. M. del Carmen Jiménez, por su ayuda y colaboración en las medidas experimentales.

Durante este período, he tenido también la oportunidad y la suerte de poder colaborar en las tareas docentes de este departamento. Quiero mostrar mi gratitud y reconocimiento a todos los profesores con los que he podido compartir esta experiencia, por todo lo que me han transmitido y enseñado, y ser una inspiración en esta vocación docente.

Además, me gustaría reconocer el trabajo de Nadia, Ento, Patricia y resto de administrativos, por su inagotable paciencia y ayuda. Gracias a Ángel Romero, Miguel Ángel Seller, Ángel Parrado, David Pascual, y resto de personal técnico, por su trabajo, y por proporcionarme todo lo que he necesitado.

Durante mi trayectoria académica he tenido la inmensa suerte de encontrarme con profesores que, con verdadera vocación, me han ayudado a crecer y sacar la mejor versión de mí misma. No puedo nombrarlos a todos, pero permitidme recordar en estas líneas a mis maestros del colegio: Doña Pepa, que hizo de la docencia una inspiración, y Don Emilio, que despertó en mí esta vocación científica y me enseñó a amar la ciencia y las matemáticas desde que tenía 11 años.

A lo largo de estos años he coincidido y conocido personas maravillosas, tanto profesional como personalmente, que desde el primer momento me hicieron sentir acogida y querida. Gracias a todos aquellos que me han acompañado en este camino. En especial, gracias Anna, gracias Damián, por vuestra amistad, por estar desde el principio, por celebrar juntos nuestros logros y llorar juntos nuestras penas.

Llevo conmigo a todas las personas de mi día a día. Echaré mucho de menos el "¿café?" a las diez y media, esos ratitos de despeje y conversación, que siempre alegraban la mañana. Me gustaría agradecer a Javier Ferrer, proveedor exclusivo de nuestros más exquisitos desayunos, su amistad y buenos consejos. Gracias a Begoña, mi compañera de despacho, y amiga, por todas las conversaciones que hemos compartido, por permitirme desahogarme cuando lo he necesitado, y darme los mejores consejos que me ha podido dar. No sé que hubiera hecho este último año sin ella. Por último, quiero dar las gracias a Llanlle, mi compañera y amiga desde que comenzamos juntas este camino. He tenido la inmensa suerte de tenerla a mi lado estos años. Ella sabe todo por lo que estoy agradecida.

Por último, me gustaría dar las gracias a mi familia... A mi abuelo Curro, cuyo ejemplo de buen hacer y ser me ha acompañado a lo largo de mi vida. A mi abuela Antonia, quien siempre estaba orgullosa de todo lo que iba consiguiendo, por velar por mí, aquí o en cada viaje al extranjero. A mi abuelo Juan, por su ternura, cariño y bondad; guardo en mi corazón todas las historias que me ha contado mientras me sostenía la mano. A mi abuela Teresa, por cuidarme desde que era pequeña, por ser y enseñarme a ser fuerte, y siempre hacerlo con una sonrisa.

Quiero dar las gracias a mi tía Estrella, por apoyarme y preocuparse por mí, por estar siempre pendiente de todos nosotros. A mi tía Mari Carmen, a quien estoy inmensamente agradecida. Gracias tita, por ser mi hogar a lo largo de todos estos años, por quererme y cuidarme por encima de todo. A mi hermana Irene, por su apoyo incondicional, no sólo durante la tesis, si no durante toda mi vida. Gracias, Javi, por ser mi presente y mi futuro, la mano que me sostiene siempre, porque mi vida contigo es simplemente mejor.

Y, finalmente, quiero dar las gracias a mis padres. Es imposible poner en palabras la gratitud que siento hacia ellos. Papá, mamá, gracias por vuestro sacrificio, esfuerzo y por todas las oportunidades que me habéis dado. Gracias por vuestro continuo apoyo, y por educarme para hacer las cosas lo mejor posible.

- Teresa
March 10, 2023

Abstract

PROTON THERAPY is a form of radiotherapy that allows maximizing the deposited dose inside the tumour while reducing the dose in the healthy tissues, thanks to its superior depth-dose distribution when compared against conventional photon therapy. Uncertainties in the beam range, however, require considering additional safety margins to ensure the tumour coverage and the non-irradiation of surrounding tissues. In this context, a method to validate the range of the beam *in-vivo* should lead to better treatment designs, minimizing normal tissue complications and hence improving tumour control. Among the different options proposed for this, PET range verification has received a very significant attention in the last 15 years and has even been clinically tested. Correspondingly, there is a worldwide effort to make it feasible and reliable aiming at its eventual clinical implementation.

PET range verification requires a comparison of the measured (with a PET scanner) and expected (from Monte Carlo simulations) β^+ activity distributions produced by the proton field in the patient's body, which can be, depending on the half-life of the isotope involved, online (ms to seconds) or offline (minutes). The accuracy of the mentioned expected activity distribution is based, among others factors, on the accuracy of production cross sections resulting in β^+ emitters used as input in the Monte Carlo simulations, which are ^{11}C with $t_{1/2}$=20.36 min, ^{13}N with $t_{1/2}$=9.97 min, and ^{15}O with $t_{1/2}$=122 s, produced in C, N y O, ^{12}N with $t_{1/2}$=11.0 ms, produced in C, ^{38m}K with $t_{1/2}$=926 ms, produced in Ca and ^{29}P with $t_{1/2}$=4.14 s, produced in P. Unfortunately, the situation is such that experimental data are completely missing for some reactions of interest and there are sizable discrepancies between the data sets available in EXFOR. Therefore, both the IAEA nuclear data evaluators and the medical physics community have call for a significant improvement of these nuclear data in order to reduce the uncertainties in the estimation of the activity distributions to a level that allows detecting beam range variations within 1 mm.

In this context, the work developed in this thesis consists on the determination of the cross sections up to 200 MeV of the reactions involved in PET range verification to improve the simulations of the expected activity distributions in the patient. The reactions of interest are 11 in total, producing either the long-lived isotopes via ^{12}C(p,x)^{11}C, ^{12}C(p,x)^{13}N, ^{14}N(p,x)^{11}C, ^{14}N(p,x)^{13}N, ^{14}N(p,x)^{15}O, ^{16}O(p,x)^{11}C, ^{16}O(p,x)^{13}N and ^{16}O(p,x)^{15}O, or the short-lived isotopes via ^{12}C(p,x)^{12}N, ^{40}Ca(p,x)^{38m}K and ^{31}P(p,x)^{29}P.

In this manuscript, a description of the experiments, analyses and results is presented. The experiments have been performed at the National Center of Accelerators (CNA, Spain), the West German Proton Therapy Center (WPE, Germany) and the Heidelberg Ion-Beam Therapy Center (HIT, Germany), using three different detection systems (PET scanners, NaI and $LaBr_3$ detectors). The data presented herein have been obtained either by the multi-foil activation technique combined with the measurement with a PET scanner or by single foil activation and conventional detectors. A wide variety of strategies have been implemented to validate and ensure the accuracy of the results.

In order to assess the impact for PET range verification of these new cross sections, in some cases measured for the first time, they have been used to simulate the β^+ production and activity profiles (as a function of time) of each isotope in tissue-equivalent phantoms and compared with the ones calculated with the current evaluations. The results illustrate the importance of new data and the need of revised evaluations for a reliable implementation of PET range verification. This is specially relevant for some of the reactions producing long-lived isotopes, but it is of upmost importance for reactions producing the short-lived isotopes needed for online verification, as these are the first cross section data ever. Overall, the new cross sections data base is expected to have an impact on the eventual implementation of both offline and online PET range verification aiming at adaptive proton therapy treatments.

Resumen

LA PROTONTERAPIA es un tipo de radioterapia externa que se emplea para irradiar zonas tumorales, especialmente para tumores cercanos a órganos de riesgo y cánceres pediátricos. Dicha técnica presenta, como ventaja fundamental frente a la radioterapia convencional, una deposición de dosis más baja en los tejidos sanos adyacentes al tumor y una alta deposición de dosis justo al final del recorrido del haz, en el denominado pico de Bragg, permitiendo una excelente conformación de la dosis en el tumor y una reducción de la dosis en los tejidos sanos. A pesar de que esta técnica ya se aplica en decenas de clínicas en todo el mundo, uno de los puntos clave de la protonterapia reside en el control del rango del haz de protones y por tanto de la posición del pico de Bragg, para reducir los amplios márgenes de seguridad aplicados actualmente. Para ello, es necesaria la verificación del rango "in vivo" del haz de protones, que se puede realizar por ejemplo mediante la detección de radiación secundaria emitida desde el interior del cuerpo.

En concreto, esta tesis doctoral está enfocada en la verificación de rango usando tomografía por emisión de positrones (PET). En esta técnica, la exactitud del tratamiento (en particular, la posición del pico de Bragg) es verificada mediante la medida con un escáner PET de la actividad β^+ inducida por la interacción del haz con el cuerpo del paciente. Dicha medida se puede realizar durante el tratamiento (verificación *online*), observando isótopos de vida media muy corta (~ms-s), o justo después del tratamiento (verificación *offline*), observando isótopos de vida media larga (~min). En ambos casos es necesario comparar la distribución de actividad medida con el escáner PET con una curva esperada, calculada mediante simulaciones Monte Carlo y cuya precisión depende de la exactitud de las secciones eficaces de producción de estos isótopos. En cuanto a estas, varios estudios han puesto de manifiesto su precisión más que limitada y han destacado la necesidad de nuevas medidas de las reacciones nucleares de interés, varias de ellas nunca antes estudiadas, en todo el rango de energía (hasta ~200 MeV).

Es por ello que este trabajo tiene como objetivo fundamental medir las secciones eficaces de las distintas reacciones nucleares que tienen lugar en el cuerpo humano durante un tratamiento de protonterapia y que dan lugar a los emisores de positrones de interés. Estos son tanto de vida media larga (^{11}C con $t_{1/2}$=20.36 min, ^{13}N con $t_{1/2}$=9.97 min, y ^{15}O con $t_{1/2}$=122 s, producidos en C, N y O) como de vida media corta (^{12}N con $t_{1/2}$=11.0 ms, producido en C, ^{38m}K con $t_{1/2}$=926 ms, producido en Ca y ^{29}P con $t_{1/2}$=4.14 s, producido en P). Las medidas se han realizado en el Centro Nacional de Aceleradores (CNA), en Sevilla (España), en el West German Proton Therapy Center (WPE), en Essen (Alemania), y en el Heidelberg Ion-Beam Therapy Center (HIT), Heidelberg (Alemania). Esta memoria describe el procedimiento experimental seguido en cada caso, el análisis de los datos y las estrategias empleadas para validar los resultados.

El fruto de esta tesis doctoral es un conjunto de secciones eficaces referentes a once reacciones nucleares: ^{12}C(p,x)^{11}C, ^{12}C(p,x)^{13}N, ^{14}N(p,x)^{11}C, ^{14}N(p,x)^{13}N, ^{14}N(p,x)^{15}O, ^{16}O(p,x)^{11}C, ^{16}O(p,x)^{13}N, ^{16}O(p,x)^{15}O, ^{12}C(p,x)^{12}N, ^{40}Ca(p,x)^{38m}K y ^{31}P(p,x)^{29}P, en todo el rango de energía de interés en protonterapia. Se ha estudiado además el impacto de estos nuevos datos en cálculos de verificación de rango mediante la comparación de curvas de actividad inducidas en materiales equivalentes al cuerpo humano, utilizando los datos de esta tesis y las evaluaciones actuales. Los resultados ilustran la importancia de los nuevos datos y la necesidad de actualizar las evaluaciones para una correcta y precisa implementación de la técnica de verificación del rango, especialmente para las reacciones más relevantes en carbono y oxígeno. Además, los datos de producción de isótopos de vida media corta, medidos por primera vez en este trabajo, son fundamentalespara comenzar a trabajar en la verificación *online*, que permita un tratamiento de protonterapia adaptativo en tiempo real.

Contents

List of Figures

List of Tables

"Es puerta de la luz
un libro abierto.
Entra por ella, niña,
y de seguro,
que para ti será el futuro..."

- En recuerdo de mi bisabuelo, Ildefonso

Chapter 1

Context and motivation

In this chapter, an overview of the incidence of cancer and current treatments are presented, with a specific emphasis on the rationale for particle therapy. The current status of this technique and issue of range uncertainty are discussed. In this context, the motivation, scope and outline of this thesis are presented.

RADIATION THERAPY is one of the main procedures to treat malignant tumours. This technique consists in the irradiation of the tumour with ionizing radiation to induce irreversible damage to the DNA. Along with other techniques, such as surgery or chemotherapy, radiation therapy can be applied for multiple purposes: to treat, minimize side effects or control the tumour. In radiation therapy, it is fundamental to control the deposited dose in the patient and verify the actual dose delivered to the tumour. For that reason, research worldwide is devoted to conform and monitor the radiation dose in the patient.

1.1 Incidence of cancer and current treatments

In accordance with the definition of the World Health Organization (WHO), cancer, neoplasm or malignant tumours are generic terms for a large group of diseases that can affect any part of the body. It is defined as the rapid creation of abnormal cells that grow beyond their usual boundaries and invade surrounding parts of the body, the so-called metastasis process [1].

Cancer is one of the two leading causes of death in most countries with a high Human Development Index (HDI), accounting for nearly 10 million deaths in 2020, or nearly one in six deaths. Due to the increased life expectancy, its incidence is expected to increase by about 70% over the next two decades. The most common cancers vary between countries, with breast (2.26 million cases), lung (2.21 million cases) and colon and rectum (1.93 million cases) being the most common in terms of new cases of cancer during the year 2020. During that year, the most deadly cancer was lung (1.80 million deaths), followed by colon and rectum (916.000 deaths) and liver (830.000 deaths). Cervical cancer was the most common in 23 countries. Each year, approximately 400.000 children develop cancer. However, thanks to a continuous worldwide effort in science and technology, nowadays many cancers can be cured when detected early and treated effectively [1].

Depending on the type of malignancy, location, stage of the disease and patient's health, there are different procedures and drugs available. Treatment usually includes one or several of the following: surgery, radiation therapy, and/or systemic therapy (such as chemotherapy, hormonal treatments or targeted biological therapies). A correct cancer diagnosis is essential for an appropriate and effective treatment because every cancer type requires a specific treatment regimen.

Local treatments, like surgery or radiation therapy, are used to treat a specific tumour or area of the body. When the tumour is operable, surgery is the most preferable option because it directly removes all the cancerous tissues. Systemic treatments or pharmaceutical drug treatments, on the other hand, affect the entire body, being the most commonly-used chemotherapy, which targets the rapidly-growing cells, such as cancer ones, in the whole body. For this reason, chemotherapy is, although effective, an aggressive treatment for patients, as it also affects normal cells causing considerable side effects [1]. Radiation therapy, a localised treatment that uses ionising radiation to kill cancer cells or to slow their growth by damaging their deoxyribonucleic acid (DNA), is also a very frequently used treatment. It can be performed as an independent procedure, or in combination of other therapy modalities, such as surgery, chemotherapy, and immunotherapy. Radiation therapy may be given before, during, or after other treatments to improve its effectiveness. The timing and type of radiation therapy depends on the type of cancer and whether the therapy aims at treating the cancer or easing its symptoms. Overall, about 70% of all patients diagnosed with cancer receives curative or palliative radiation treatments [2].

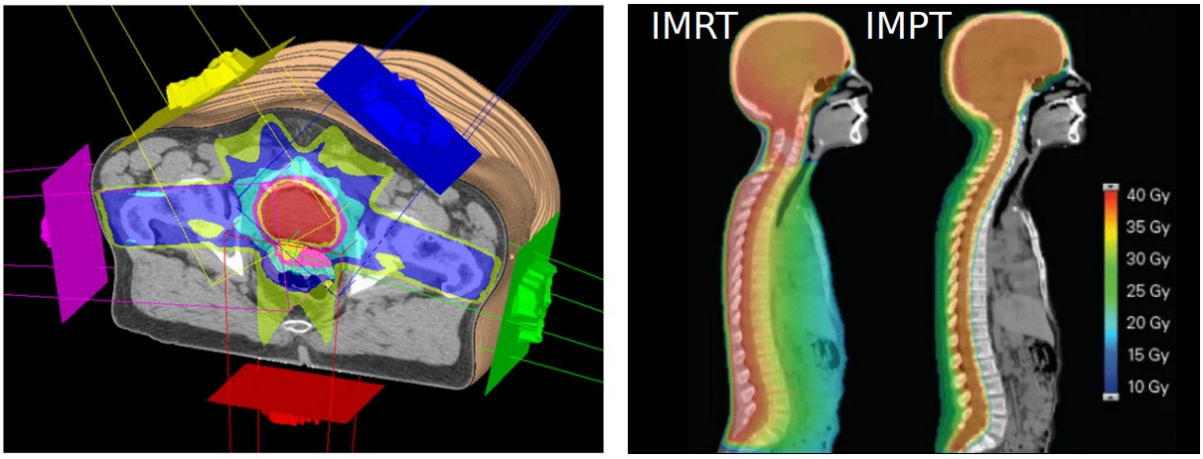

FIGURE 1.1: (Left) An example IMRT treatment plan [6]. (Right) Dosimetric comparison of photon and proton treatment plans for a child treated of craniospinal tumour [7].

1.2 Rationale for particle therapy

When applied properly, radiation therapy destroys cancer cells or reduces their growth by irreversible damaging their DNA so they stop dividing. Once the cells die, they are decomposed and removed by the body. There are two main types of radiation therapy, external beam and internal therapy, the use of which depends on many factors, including the type, size and location of cancer, general health of the patient and proximity of the tumour to other organs at risk (OAR) [2].

Internal radiation therapy consists on introducing radiation sources inside the body. In brachytherapy treatments, radiation sources as part of seeds, ribbons or capsules are placed inside the body, embedded or in the vicinity of the tumour, thus considered to be a localised procedure. However, in other internal radiation therapies (so-called systemic therapies), the radiation emitting isotopes travel in the blood, seeking out and adhering to cancer tissues [2].

External radiation therapy consist in the irradiation of the body using an external beam. There are many types of external beam therapy, all of which share the objective of delivering the highest prescribed dose of radiation to the tumor while sparing the normal tissue around it. The choice of one or another type relies on the diagnostic images and calculations techniques that allow predicting the most precise dose and treatment path possible. The 3D Conformal Radiation Therapy (CRT) is the most commonly used procedure, which uses body images to design radiation beams that conform to the shape of the tumor. As exemplified in Figure 1.1 (left), the Intensity Modulated Radiation Therapy (IMRT), a type of 3DRT, uses many, but smaller, beams, and the intensity of the beams in some areas can be modulated to give higher doses to certain parts of the tumour. At present, the IMRT is one of the cutting edge technologies. Typically, multiple fields coming from different directions are combined to deliver a patient specific radiation dose, aiming at maximising the dose in the tumour while minimising it in the adjacent normal tissues [2–4]. The number of patients effectively treated with radiation therapy due to the improvement of this treatment modality has increased during the last decades, thus having a significant effect on the global outcome of cancer treatment [5].

Nowadays, radiation therapy is most commonly delivered with external beams of X-rays or electrons, generated by linear accelerators. However, the use of protons or light ions (commonly known as *particle therapy*) is of growing interest for its multiples advantages [8]. In some situations, conventional radiation therapy is not sufficient to conform the dose in the tumour and it results in the delivery of a radiation dose in healthy tissues adjacent to the tumour, as shown in Figure 1.1 (right),

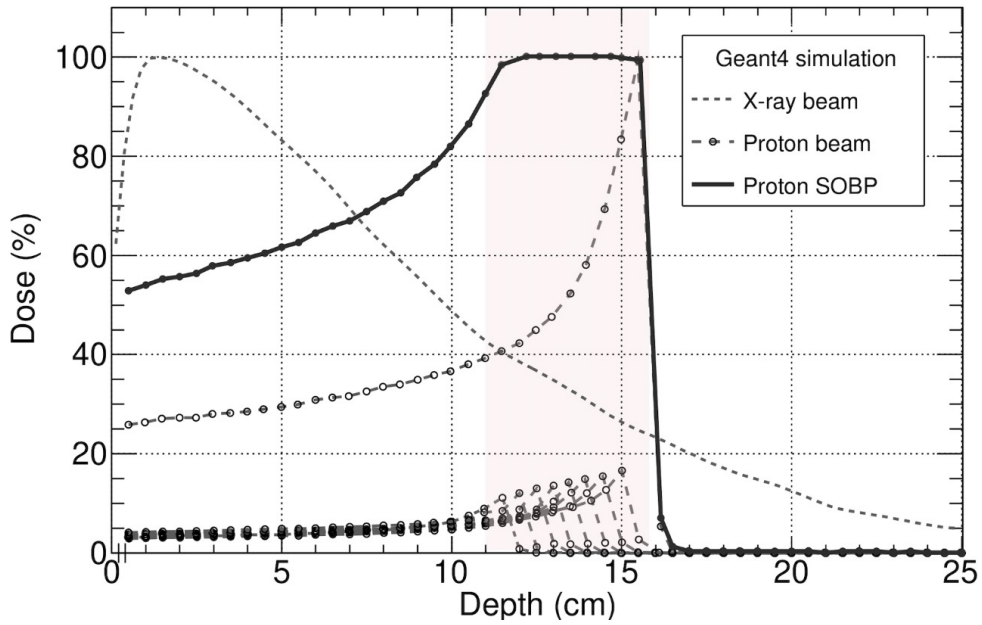

FIGURE 1.2: Comparison of the depth-dose distribution of an 100 keV monoenergetic X-ray beam and proton beams in water, calculated with Geant4. Red shadow indicates the targeted volume (tumour). Several beams are simulated to target a tumour at a depth of 11 cm to 16 cm (SOBP).

having considerable side effects in the patient when the tumour is located close to OARs and the received radiation dose is above their tolerance. The necessity of a clinical solution to treat these cases has stimulated the technological development for the use of particle beams.

The key advantage of particle therapy over conventional radiation therapy is its superior depth-dose distribution in the patient. During the interaction of X-rays with the patient's body, the photons energy is transferred to secondary electrons, mainly by Compton Scattering, which deposit the radiation dose by ionization processes, damaging the DNA of the cells. The characteristic spatial dose distribution of the photons is displayed in Figure 1.2. The X-ray beam deposits its energy slowly and mainly exponentially as it penetrates tissue, due to attenuation effects.

However, particle therapy allows the delivery of the same dose to target while delivering less than half of the integral dose of the X-ray beam, as illustrated in Figure 1.2. This is explained by the characteristic of the interaction of the charged particles with matter. Their depth-dose distribution features a well-defined and finite penetration depth in the body and a high dose deposition close to the end of the trajectory, the so-called Bragg peak, which exhibits a rapid fall-off [9]. In order to target a well-defined region at a certain depth in the body, beams of different energies are used. The resulting superposition is called the spread-out Bragg peak (SOBP) [8]. Figure 1.2 shows nine proton beams traversing 25 cm of water-equivalent tissue, where the tumour volume is located at a depth between 11 cm and 16 cm. The conformal dose at the tumour forms the SOBP.

In addition to the energy loss mechanism of charged particles and its benefits over conventional radiation therapy, the use of particles in radiation therapy is advantageous due to its important biological effects, since their higher number of ionisation processes during their path induce more severe damage to the cells. This superior biological effects and the different cellular responses are quantified by the Relative Biological Effectiveness (RBE), defined by the ratio between a reference radiation dose (generally 250 keV photons) and the dose of a considered radiation type producing the same biological effect [10].

Considering the previous paragraphs, tumours indicated for particle therapy are generally those

close to OARs, specially to the brain, head and neck, and spinal regions, being chordomas and chondrosarcomas of the base of the skull and eye tumours some common cases. In accordance with the NIH, long- and short-term side effects are reduced for those who received particle therapy in comparison to those who received traditional radiation. Thus, this technique is very well suited for children and young patients, as they are expected to have a long life expectancy and can therefore be affected by long-term side effects such as secondary radiation-induced tumours. This technique is also appropriate for patients with genetic radiosensitive syndromes [11]. In fact, the high-precision and non-invasiveness of the technique would be advantageous for most cancer cases.

1.3 Brief history and state of the art of particle therapy

In 1946, Robert Wilson established the therapeutic interest of protons and proposed the use accelerator-produced beams of protons to treat tumours in humans [9]. Less than ten years later, in 1954, the first patient was treated of a pituitary-gland tumour with the 340 MeV proton beam of the Lawrence Berkeley Laboratory (Berkeley, CA, USA) [12]. In 1962, specialized radiosurgical proton treatments started at the Harvard Cyclotron Laboratory [13, 14], followed in the mid 1970s by treatments for ocular cancers [15] and larger tumours [16]. During the last two decades, translation of proton, and in general particle, therapy technology from nuclear research laboratories to hospitals made it a more commonly available treatment option.

Today, particle therapy has grown into an advanced clinical modality, counting more than 325.000 patients treated worldwide with particles per end of 2021, close to 280.000 with protons, about 42.000 with carbon ions and about 3.500 with helium and other ions [17]. Even so, the widespread of particle therapy has been slow compared to the development of other techniques, as for instance the development of intensity modulated photon therapy. The main reason for this is the expensive cost, both in terms of initial investment and expenses per treatment. Although commercial proton delivery systems appeared in 2001, the cost of particle therapy equipment remains significantly higher than that of comparable photon therapy gear, then requiring to weigh the cost-benefit ratio, which in some cases is controversial [18].

However, investment in technology development and research helps reducing prices while clinical evidence of the advantages of particle therapy is being demonstrated. Hence, today there are 112 particle therapy centres in operation worldwide, with another 36 under construction [17].

Technological developments to customize the lateral and longitudinal distribution of the beam, often with a specific time structure, have significantly increased in the last years, resulting in new and more convenient beam delivery modalities. In addition, further advances in accelerators and beam extraction systems to reduce the cost of clinical implementation would enable the spread of particle therapy.

1.4 Range verification in particle therapy: uncertainties and needs

Figure 1.2 illustrates how the depth-dose distribution in the patient using particle beam allows a higher dose deposition in the tumour whereas it reduces the radiation dose in the healthy tissues surrounding the tumour. However, this distribution does not take into account the uncertainty in the position of the Bragg peak when the beam is delivered to the patient.

Therefore, one of the most critical challenges of particle therapy lies on the accuracy on treatment delivery. There are different sources of uncertainty that can vary the beam range, and thus, the position of the Bragg peak, just where the beam features its sharpest dose gradient. Some of these

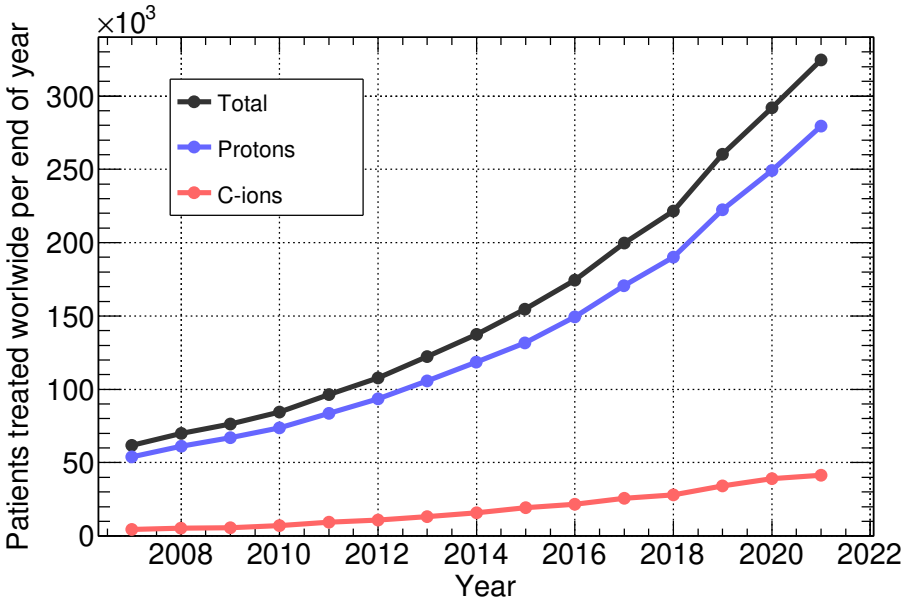

FIGURE 1.3: Statistics of patients per end of year treated with protons, C-ions and in total, from all facilities worldwide (in and out of operation). Data extracted from the Particle Therapy Cooperative Group (PTCOG) annual reports [17].

sources of uncertainty are related to patient positioning, anatomical changes or uncertainties in the estimation of stopping power from the X-ray computed tomography imaging used later in treatment plannings (see Section 2.3.1 for more details) [19].

Considering all of this, variations in the beam range could lead to the distal edge of the tumour not receiving the proper dose and/or substantial increment of the dose delivered in the healthy tissues close to the tumour. For that reason, range uncertainties are incorporated as part of treatment plannings adding a safety margin to the distal surface of the target. This comes with the cost of additional dose being delivered to ensure that the tumour is receiving the proper dose. Other compromises might be required when the target is located near an OAR [19].

A reduction of the uncertainty in the beam range is highly desired in order to reduce the above-mentioned limitations of particle therapy. There are several areas of current research to reduce the range uncertainty. Among others, positron emission tomography (PET) monitoring of the dose delivered is considered to be a promising technique, which could reduce the sizeable safety margins applied nowadays in the clinic [20]. This verification technique consists on the comparison of the measured β^+ activity distribution induced in the patient's body by the proton beam with that expected from the treatment plan. A detailed overview of the technique, advantages, limitations and objectives of this work are given in the following chapter.

1.5 Structure of this thesis

This thesis is focused on the experimental determination of the reaction cross sections of the β^+ emitters of interest in PET range verification. These new nuclear data have been obtained in the full energy range of interest in proton therapy, from the reaction thresholds up to 200 MeV, in three different facilities. This thesis is structured as follows:

Chapter 2 discusses the physical and biological characteristics of proton therapy in comparison to conventional radiation therapy. The different techniques of implementation of proton therapy, including novel types of acceleration technologies, beam delivery modes and procedures of dose verification are presented. Finally, a detailed description of PET range verification, current status and needs of nuclear data are also included, followed by the objectives of this thesis.

Chapter 3 presents the methodology to measure the production cross sections. The different facilities in which this work has been performed (CNA, WPE and HIT), detection systems, methods and validation strategies are presented.

Chapter 4 summarizes the analysis of the measurements carried out at the CNA, WPE and HIT facilities. It includes detailed discussions about the corrections, decay curve fitting and validations strategies. Last, the determination of the cross section values from the observables is explained and the summary of uncertainties assessed.

In chapter 5, the results of the reaction cross section are presented, discussed and compared to the previous evaluations and data in the literature. Along the cross sections comparisons, the last section contains realistic calculations of activation of phantoms to illustrate the impact of the new cross section data in PET range verification.

Finally, Chapter 6 summarizes the main conclusions of this thesis and provide recommendations for future work and strategic new lines of research.

Chapter 2

Fundamentals of particle therapy

This chapter summarizes the theoretical background of particle therapy and range verification. A brief introduction to the physical and radiobiological mechanisms of the interaction of protons with matter, the implementation of particle therapy in the clinic and sources of range uncertainties are presented. This chapter introduces the state-of-the-art range verification methods. In this respect, a detailed overview of PET range monitoring and current requirements are discussed.

PARTICLE THERAPY allows to maximize deposited dose inside the tumour while reducing the dose in the healthy tissues, thanks to its superior depth-dose distribution when compared against conventional photon therapy. Range uncertainties in the particle beam, however, require the use of additional margins to ensure the tumour coverage and the non-irradiation of surrounding OARs. Due to these limitations, a method to validate the beam range *in-vivo* should lead to better treatment designs, minimizing normal tissue complications and improving tumour control. In this context, PET range monitoring is one of the main verification techniques. Research projects worldwide are focused on the improvement and clinical implementation of this technique. In particular, this thesis is focused on the characterization of the nuclear interactions relevant for PET range verification.

2.1 Interaction of charged particles with matter

This section describes the physics governing the interaction of protons and light ions (hereinafter referred as charged particles) with atoms and nuclei, which determines the dose deposition by the beam in the patient. The corresponding damage caused by the radiation in the human tissues and its relevant biological parameters are also addressed.

2.1.1 Physical processes

2.1.1.1 Electronic energy loss

When charged particles, in particular protons or light ions such as helium or carbon ions, penetrate through matter, they interact primarily through Coulomb forces between their positive charge and the negative charge of the electrons of the absorbing medium. Depending on the energy transferred to the electrons, the atoms can be either excited or ionized; in which case the freed electrons can cause further ionisations [21].

Macroscopically, the energy transferred from the charged particle to the electrons is quantified by the *linear stopping power*, defined as the differential energy loss (dE) of that particle in the corresponding differential path length (dx).

The linear stopping power for protons and light ions can be approximated by the relativistic version of the Bethe-Bloch formula, considering the shell and density corrections [22–24]:

$$-\frac{dE}{dx} = 4\pi\left(\frac{e^2}{4\pi\varepsilon_0}\right)^2 \frac{N_A Z\rho}{AM_u}\frac{z^2}{m_0c^2\beta^2}\left[\ln\left(\frac{2m_0c^2\gamma^2\beta^2}{I}\right) - \beta^2 - \frac{C}{Z} - \frac{\delta}{2}\right], \tag{2.1}$$

where m_0 is the electron rest mass, c is the speed of light, e is the electron charge and z is atomic number of the incident ion, N_A is the Avogrado's number, and ρ is the mass density, Z the atomic number and M_A the molar mass of the medium. The parameter I represents the average excitation and ionization potential of the medium and is normally treated as an experimentally-determined parameter for each element. Equation 2.1 is generally valid for different types of charged particles provided their velocity is large with respect to the velocities of the orbital electrons in the absorbing atoms. Equation 2.1 is written as a function of the relativistic parameters $\beta = v/c$ and $\gamma = (1-\beta^2)^{-1/2}$. The shell and density correction factors, C and δ respectively, are derived from relativistic theory and quantum mechanics. The shell correction C is important when the projectile velocity approaches to the velocity of atomic electrons (below few MeV for protons [25]). The Equation 2.1 is built on the assumption that the electrons are stationary with respect to the incoming particle, but this assumption is not true for low velocities, and therefore the shell correction C is needed, which is generally small. The density

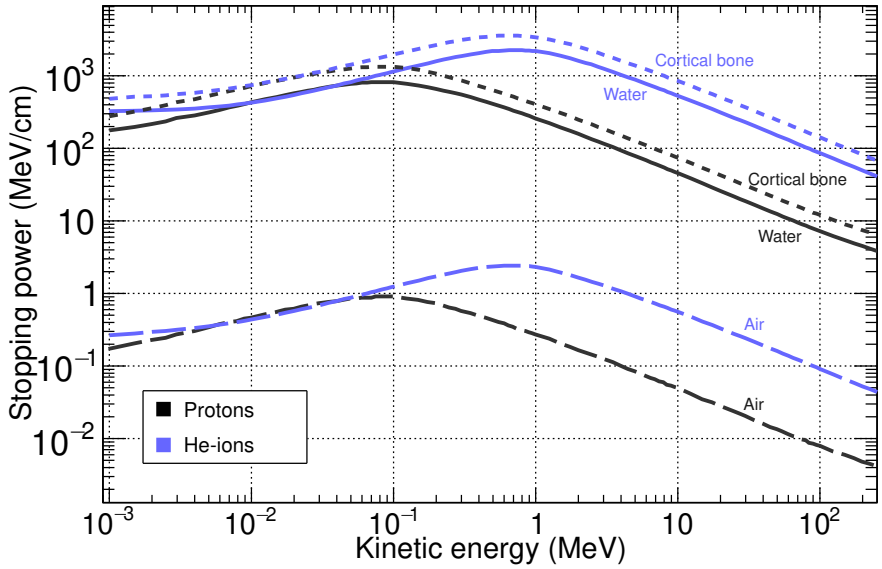

FIGURE 2.1: Comparison of the electronic stopping powers of protons and He ions in water (ρ = 1.00 g/cm^3), cortical bone (ρ = 1.85 g/cm^3) and air (ρ = 1.20E-03 g/cm^3), expressed in MeV/cm, over the energy range used in particle therapy. Data extracted from the PSTAR and ASTAR Databases for Protons and Helium Ions [27].

effect δ, instead, arises as the energy and thus the velocity of the incoming particle is high (close to 1 GeV for protons in biological materials [26]). This effect is originated from the fact that the electric field of the projectiles will flatten and extend. This electric field tends to polarise atoms of the medium along its path. Due to this polarization, electrons far from the incoming particle will be shielded from the full electric field. Collisions with these shielded electrons will contribute less to the total energy loss than predicted by the original Bethe-Bloch formula and thus this effect increases with the particle energy.

Figure 2.1 shows the energy loss of two incident particle with different charge and mass, protons and He ions, in three different materials, as a function of energies of relevance for clinical practices (up to 230 MeV). Equation 2.1 is highly dependent on the target material, as it can be shown in Figure 2.1. This dependency comes from the I value and the material density. Although the I value varies from about 19 eV for hydrogen to about 820 eV for lead, being 78 eV the one used in water [28], this term scales with $\ln(1/I)$. This effect is, although small, non-negligible. On the other hand, the material density has a strong influence on the stopping power. For instance, figure 2.1 shows how the energy loss can vary between the air in the lung to the cortical bone by about three orders of magnitude.

Due to the $1/\beta^2$ dependence of the stopping power in Equation 2.1, the energy loss increases as the particle slows down. This determines a larger amount of energy deposited by the end of its path rather than at its beginning, which is extremely beneficial for clinical applications. As shown in Figure 2.1, the stopping power tends to vary by a factor of ~50 for energies of proton in water between 1 and 230 MeV. The depth-energy deposition curve by a particle is known as *Bragg curve*, and its maximum is usually indicated as *Bragg peak*. Figure 1.2 shows the deposited dose in a water phantom for several incident proton beam energies. In this figure, one can conclude that the clear advantage of particle therapy over conventional radiation therapy stems from the characteristic Bragg peaks, where the energy deposited in the surrounding tissues is reduced.

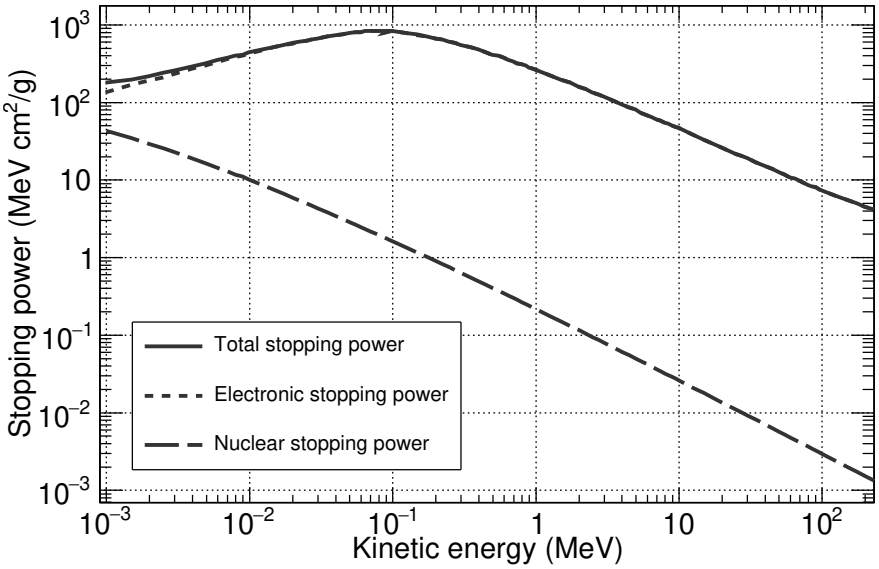

FIGURE 2.2: Stopping power of protons in water. Figure representing the contribution of the electronic and nuclear energy loss to the total one. Data extracted from the PSTAR Databases for Protons [27].

2.1.1.2 Elastic scattering

While the interaction of incident particles with the atomic electrons of the absorbing material hardly contributes to changing the direction of the incident particles, due to the significant mass difference between them, the repulsive Coulomb field of the atomic nuclei allows the deflection of the incident particles from its original straight-line trajectory, then leading to a lateral broadened beam width and energy loss. The single scattering, described by the usual Rutherford formula, gives a very small average deviation angle. Plural scattering, when the number of Coulomb scattering events increases but remains under few tens of interactions, occurs in thin targets and is the hardest case to model. For thicker targets, lateral spread is dominated by multiple Coulomb scattering (MCS), which are well described by the Molière's theory [29, 30].

The nuclear stopping power refers to the energy loss due to these elastic collisions between the projectiles and atomic nuclei. Figure 2.2 shows an example of its contribution to the total stopping power for a proton beam in water. This contribution is minor ($\sim 10^{-4}$ in the energy range of interest) due to the lower number of particles featuring elastic collisions with atomic nuclei when compared against the interaction with the bound electrons in the medium.

In particle therapy, the MCS is responsible for the lateral penumbra sharpness of the beam: a punctual proton beam of 230 MeV traversing 30 cm of water has a radial straggling of ~5 mm. Due to their comparably higher mass, this beam broadening is significantly lower for carbon ions: ~1 mm after travelling also 30 cm of water. During a particle therapy treatment, not only the beam spreading due to scattering in the patient tissues needs to be considered, but also that due to scattering in the exit window, beam monitor ionization chambers and multi-wire chambers upstream of the patient. These components, which form the so-called beam nozzle, typically have a total water-equivalent thickness of 2 mm. That is significant when considering that the distance from nozzle to patient of typically 1 m and a small angular spread translates into a significant enlargement of the beam spot. This scatter component is particularly important for pencil beams and low beam energies.

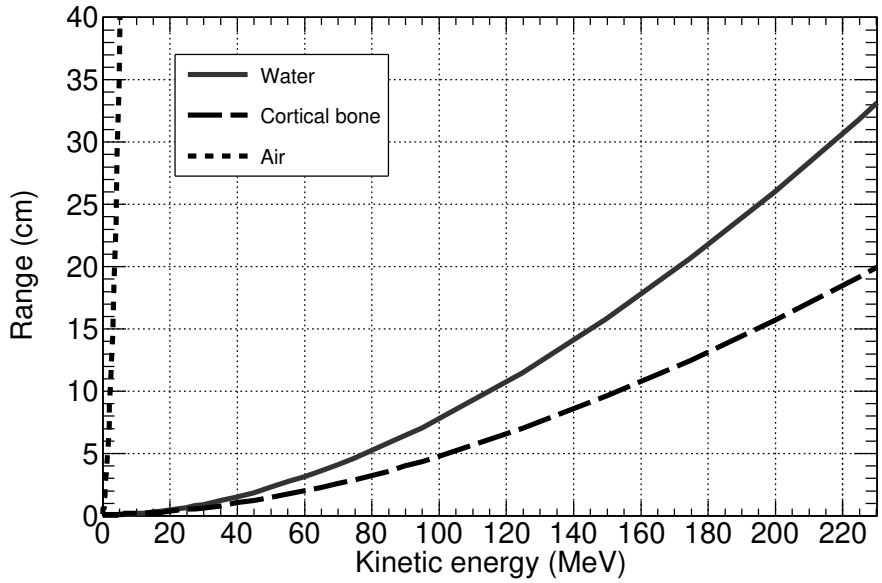

FIGURE 2.3: Mean range in water, cortical bone and air as a function of the proton energy in the clinical energy range. Data extracted from the PSTAR Databases for Protons [27].

2.1.1.3 Nuclear reactions

The incident ions can undergo inelastic nuclear reactions during the collisions with the target nuclei in their way through matter, provided their energy exceeds the corresponding Coulomb barrier. Nuclear reactions can produce excitation of the target nuclei, formation of compound nuclei, or interaction of the incident particle with individual components of the nuclei. These processes are followed by a significant reduction of primary incident particles and deviation, entailing a shorter range than that of the corresponding primary particles.

Considering these nuclear reactions is required for an adequate implementation of particle therapy: the ejected particles of such reactions must be considered during calculations of the prescribed dose delivered to the patient and in radiation protection and shielding issues. For instance, the resulting neutrons of nuclear interactions in the beam nozzle or patient's body have very long penetration lengths. This causes undesirable dose in healthy tissues far away from the tumour region. Therefore, nuclear interactions have a strong influence on the actual delivered dose profile [11, 31, 32], therefore accurate characterization of these nuclear reactions is essential for the radiation transport codes used in dose calculation.

Furthermore, these nuclear reactions also produce radioactive residual nuclei of interest for particle therapy applications. For instance, the production of unstable nuclei is one of the most relevant elements in dose monitoring techniques, and a comprehensive study of these reactions is required for their development and clinical implementation.

2.1.1.4 Bragg peak, energy straggling and beam range

During their path inside the matter, the incident particles are slowing down as previously described in Section 2.1.1.1 by Equation 2.1. The distinctive energy loss of the incident particles as a function of their path is known as the Bragg curve. This curve is characterised by a sharp peak called *Bragg peak*, which represents the greater amount of energy deposited close to the end of the trajectory. As seen in

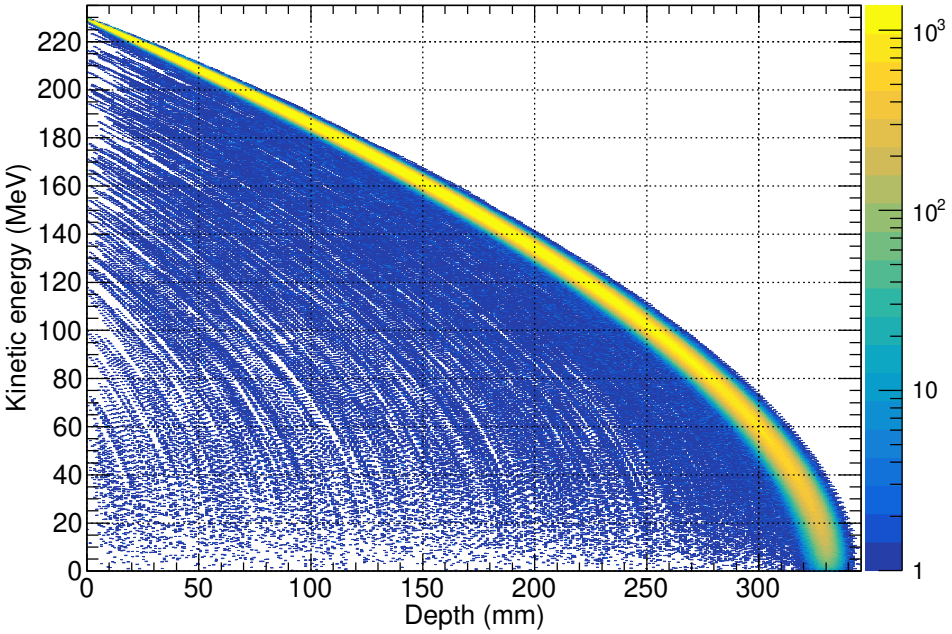

FIGURE 2.4: 2D plot of the depth-kinetic energy distribution of protons, calculated with a Geant4 simulation of a 230 MeV mono-energetic beam impinging on a water phantom. Note that the 2D plot is in log-scale and the secondary protons at lower energies (blue points below yellow trace) are minimal.

Equation 2.1, particles energy loss increases while slowing down due to the $1/v^2$ dependence. Figure 1.2 shows different Bragg curves of different proton energies in a water phantom.

The range of a particle is defined as the distance traversed until it loses its energy. After the particle stops, no radiation dose is deposited further along the beam path. From an analytical point of view and under the hypothesis of Continuous Slowing Down Approximation (CSDA), the range R of an incident particle with initial energy E_p is calculated by integrating the inverse stopping power (Equation 2.1) as follows [33]:

$$R = \int_{E_p}^{0} \frac{1}{S(E)}\, dE \tag{2.2}$$

Figure 2.3 shows the relation between the proton energy and the range in water, cortical bone and air. In particular, a 230 MeV proton has a range of 33 cm in water and 23 cm in cortical bone, compared to more than 300 m in air. This energy is hence sufficient to reach tumours throughout the human body, being this the typical maximum energy used in proton therapy.

However, due to the fact that the details of microscopic interactions undergone by the charged particles and their respective energy loss are statistical processes, a spread in energy always results after a beam of mono-energetic particles traverses a medium. The width of this energy distribution is called *energy straggling*. It affects the depth reached and is described by the asymmetric Vavilov distribution [34]. Figure 2.4 represents the 2D energy distribution of a initial mono-energetic proton beam as it traverses a water phantom calculated with the Geant4 Monte Carlo simulation toolkit [35]. The figure illustrates how the beam spreads in energy and space along its path, leading to the so-called range straggling related to variations in the range of individual particles. The range of a beam therefore is different from that defined above: given the stochastic nature of the processes involved, the mean range is defined as the depth at which 50% of the beam particles have stopped (see Figure 2.5).

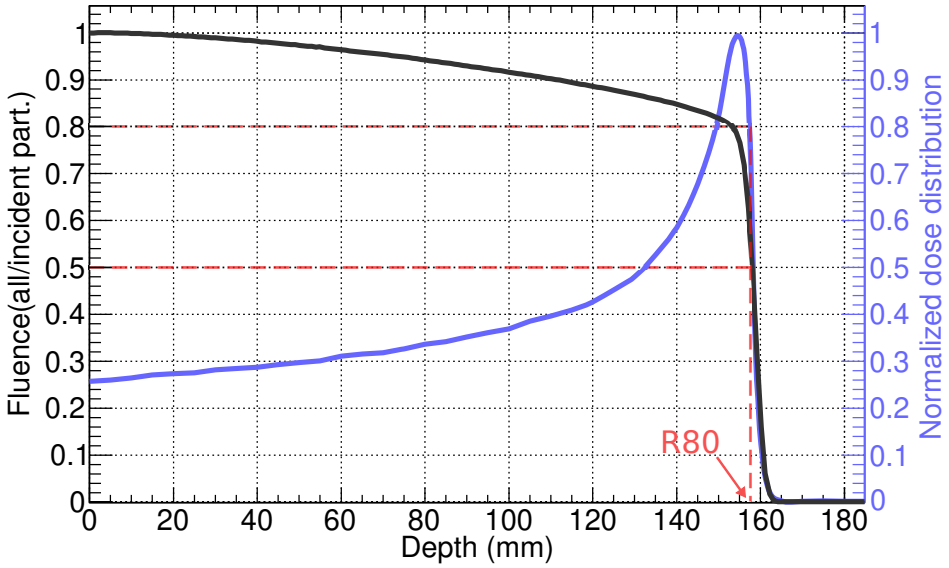

FIGURE 2.5: Ratio of the fluence of primary and secondary protons to the total incident protons (black line) and deposited dose (blue line) as a function of the depth, calculated with a Geant4 simulation of a 150 MeV mono-energetic beam impinging on a water phantom. The dotted red line corresponds to the beam range at the 50% and 80% drop-off of the fluence curve and dose curve, respectively.

In this figure, the gradual depletion of protons from entrance to near the end of range is caused by removal of protons undergoing nuclear reactions. Furthermore, in the fluence calculations it should be considered both primary incident protons and secondary protons produced in such nuclear reactions. In clinical practise, the range of a beam is normally defined relative to a certain point in the dose distribution, usually at the distal 80% of the maximum dose (so-called R80). The 80% dose fall-off coincides approximately with the mean range. For the sake of simplicity, in the following, we will refer to the mean range as *range*.

2.1.2 Radiobiological aspects

2.1.2.1 Radiation damage in DNA structures

Ionizing radiation is able to damage the cancer cells by destroying their DNA molecules. This process takes place directly via the breakage of the DNA structures by ionization processes or indirectly via the interaction with water molecules surrounding the DNA molecule. The indirect interaction produces highly reactive molecules known as free radicals which can then react with the DNA. The induced biological damage in the tissues is a consequence of the lesions in the DNA that can not be repaired, eventually leading to the death of the cells. This ionizing radiation, such as photons, protons or heavy ions, produces two main types of DNA damage: Single-Strand Breaks (SSB) and Double-Strand Breaks (DSB). SSB, or injuries affecting only one strand of the double helix, can be potentially repaired by using the specular information of the DNA molecule. On the other hand, DSB is not as easily repair, leading to the induction of lethal lesions in the cells.

In this context, the main advantage of particle therapy over conventional photon therapy resides in the different microscopic and nanoscopic ionization patterns. The ionization density is much more localised in the case of charged particles when compared against photons, implying a higher probability for DSBs, and thus a more severe damage and death of the cells [36].

2.1.2.2 Definitions of absorbed dose and linear energy transfer

The *absorbed dose* D is defined as the mean energy per unit mass deposited by ionizing radiation in a mass element:

$$D = \frac{dE}{dm}. \tag{2.3}$$

This physical quantity serves to characterise the damage induced in the tissues of the patient during a radiation therapy treatment. The International System (SI) unit for the absorbed dose is the Gray (Gy), where 1 Gy = 1 J kg^{-1}. The *Linear Energy Transfer* (LET) is also a physical quantity used to describe the radiobiological damage, and it is defined as the mean energy lost in the medium by a slowing-down particle in a track segment of length. It is usually measured in keV μm^{-1}:

$$LET = \frac{dE}{dl}. \tag{2.4}$$

From the physical point of view, it is equal to the electronic stopping power, but addressing the energy locally transferred to the medium rather than the energy lost by the incident particle. As previously mentioned, densely ionizing radiation (high-LET radiation), like ions, is more effective than sparsely ionizing radiation (low-LET radiation), like photons, because a dense ionization pattern produces more lesions to the DNA helix, such as DSBs [10, 37, 38].

2.1.2.3 Relative biological effectiveness (RBE)

The induced damage in cells is often studied with isolated cells (in-vitro), monitoring what fraction of the cell population survives for a specific absorbed dose. A cell-survival curve represents the fraction of survival cells as a function of absorbed dose and is modelled by a linear-quadratic function as follows:

$$\frac{S}{S_0} = e^{-(\alpha D+\beta D^2)}. \tag{2.5}$$

Where the α-term represents the lethal DNA damages induced by a single incident particle and the β-term represents the lethal DNA damages resulting from the interaction of different radiation tracks.

Figure 2.6 displays the survival curves for two types of incident radiation: photons and carbon ions. The dose to produce the same biological effect, i.e., fraction of survival cells, varies for different incident radiation. As the radiobiological effect of photons is well-known, the absorbed dose in a particle therapy treatment is weighted by the *relative biological effectiveness* (RBE), so that treatment plans for different radiation therapy techniques become comparable in form of biologically equivalent doses and damage. Therefore, the RBE is defined as the ratio of the doses of the low-LET reference radiation (photons) and the light ion of interest (such as protons, He ions or C ions), that produce the same biological effect:

$$RBE = \left.\frac{D_{ref}}{D_{test}}\right|_{iso}. \tag{2.6}$$

Where D_{ref} and D_{test} are the respective doses of the low-LET reference radiation and high-LET charged particle.

As previously mentioned, protons and light ions with high LET show an increased RBE in comparison to photons due to the concentrated energy deposition along their tracks, irreparably damaging the DNA more effectively than low-LET radiation. In particular, in previous studies using proton irradiations, it was obtained, on average, a 10% larger damage compared to conventional photon irradiation with the same absorbed dose [41, 42]. However, this effect is still under investigation, and, the RBE value for protons oscillates between 0.9 and 2.1 on different studies. Typically, that parameter is simply estimated as RBE = 1.1 [41–43]. This is a rather strong simplification and the actual RBE depends

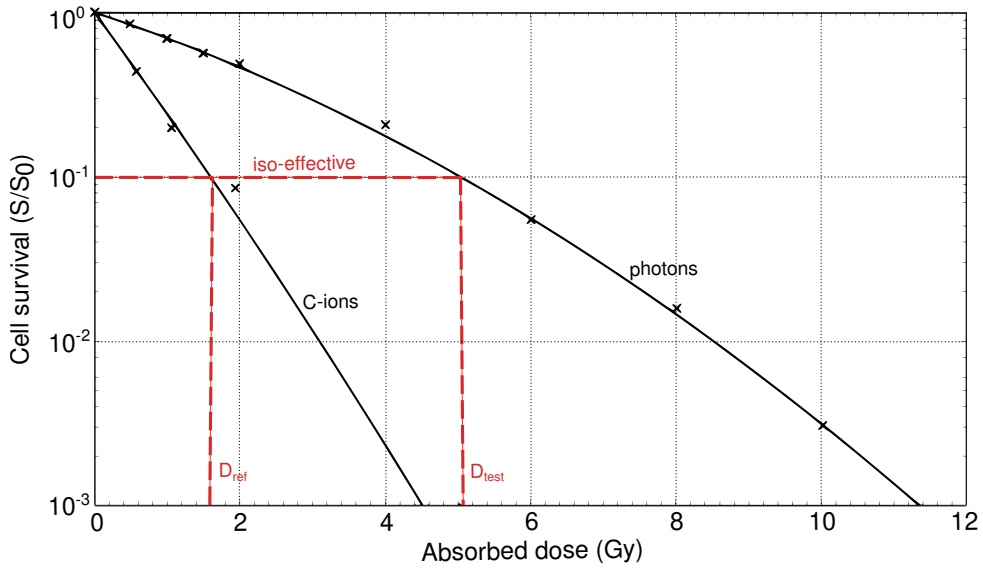

FIGURE 2.6: Survival curve for photons and carbon ions, including the determination of their respective doses at an iso-effective survival level. The plotted data is extracted from [39]. That study considers A549 human lung adenocarcinoma cells. Extrapolation curves obtained from [40].

strongly on the dose. Therefore, a biophysical model that can predict accurately and fast the values of RBE is still required for the biological treatment plan optimization in particle therapy.

2.2 Implementation of particle therapy

2.2.1 Particle accelerators

During the first decades of particle therapy, treatments were performed in nuclear physics laboratories equipped with particle accelerators, normally isochronous cyclotrons or synchrocyclotrons. Most of the particle therapy research and treatments were performed at the facilities of Berkeley (California, USA), Cambridge (Massachusetts, USA), PSI (Switzerland) and Uppsala (Sweden), until the first hospital-based facility was built in Loma Linda in 1992 (California, USA) [44]. Since then, commercial companies have developed clinical accelerators and now offer complete treatment facilities, combining accelerator and gantries. The treatment rooms of these facilities can be designed with fixed beams, usually horizontal, and are used for specific treatments. They can also include a rotating gantry, to easily treat the patient with beams from multiple angles.

In this section, a general overview of the currently-used particles accelerators is presented. The experimental work of this thesis has been carried out at three facilities: the National Center of Accelerators (CNA, Spain), the West German Proton Therapy Center (WPE, Germany) and the Heidelberg Ion-Beam Therapy Center (HIT, Germany), the first two based on a isochronous cyclotron and the latter on a synchrotron accelerator.

2.2.1.1 Cyclotron

The modern isochronous cyclotrons specifically designed for proton therapy are more compact than the classical cyclotrons in nuclear laboratories, with a magnet height of approximately 1.5 m. The diameter oscillates between 3.5 m (100 tons) and 5 m (200 tons) depending on the use or not of superconducting coils. Despite the additional space required to host the ion source and support devices,

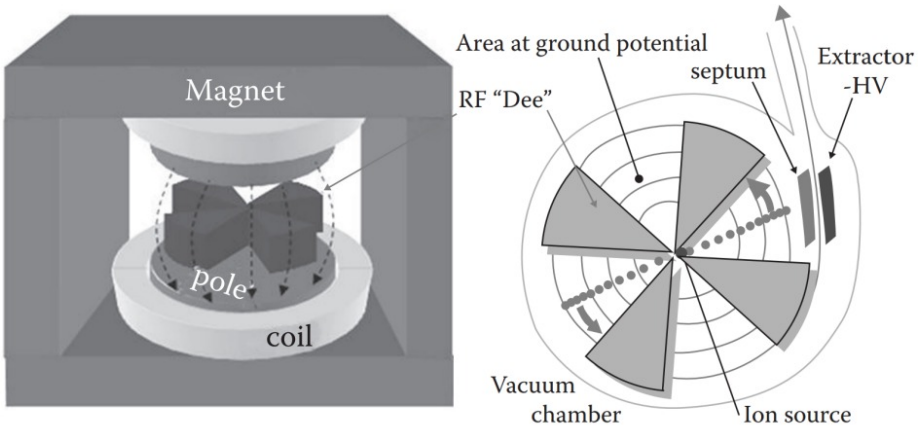

FIGURE 2.7: Schematic of the major components of a cyclotron, including the ion source, magnet, "Dees", and extraction elements. The accelerated protons are depicted on their spiral-like trajectories. Figures extracted from [44]

cyclotrons are well suited to a hospital environment due to their relatively compact size and simplicity [44].

Therapeutic cyclotrons can accelerate protons to a fixed energy of about ~230 MeV. H^- ions are injected in the center of the cyclotron and, a radio frequency (RF) system providing strong and alternating electric fields between two or four electrodes (so-called "Dee"), accelerate the particles as they cross the gap between consecutive Dees. The strong and fixed magnetic field created by the magnets is perpendicular to the direction of particle motion, so the Lorentz force forces the particle into an arc-shaped orbit inside the Dee. In two-Dees cyclotrons, H^- ions turn 180° along their trajectory. The repeatedly acceleration is caused by the RF system: the alternating electric field between Dees allows to accelerate the particle from one Dee to the following, and it has a fixed frequency of several 10 MHz up to 100 MHz, which depends on the treatment machine, and a power of several 10 kW. After multiple rounds in the cyclotron defined by the energy and charge exchange by using a stripping foil, the beam is extracted from the cyclotron with an additional electromagnetic field [44]. Figure 2.7 shows a general view of the cyclotron components previously mentioned together with the acceleration and extraction systems.

The main advantages of a cyclotron are the continuity of the beam and the fact that its intensity can be easily adjusted. Although the cyclotron has a fixed energy, the beam energy at the patient can be accurately tuned using a degrader together with an appropriate beam line design, so reducing the energy from ~230 to ~60 MeV.

2.2.1.2 Synchrotron

The main advantage of a synchrotron over a isochronous cyclotron is that the particles are accelerated at a specific energy of choice. This means that almost no radioactivity nor secondary particles (as neutrons) are generated by beam interaction with the degrader. Also, low-energy beams have the same intensity as high-energy ones because there is no transmission loss in the degrader. Moreover, while both cyclotrons and synchrotrons are used for proton therapy, synchrotrons are the only devices currently in operation for heavy-ion (e.g. He or C) therapy, improving the treatment options. On the other hand, the space required by a synchrotron is larger than the required by a cyclotron. A proton synchrotron has usually a diameter of 6–8 m, compared to the 3-5 m of a cyclotron [44].

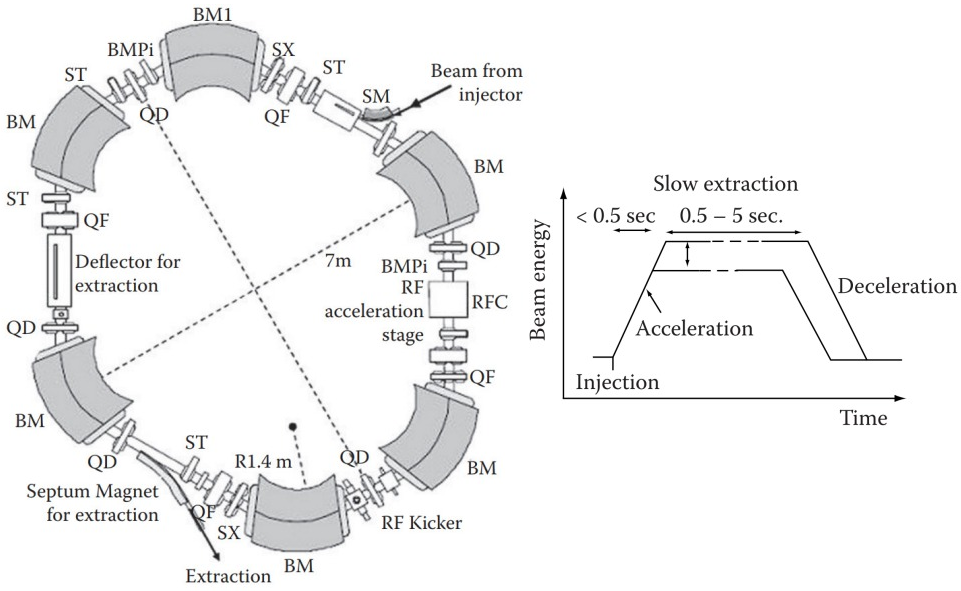

FIGURE 2.8: (Left) Schematic view of the major components of a Hitachi synchrotron, including a RF device, magnets and extraction elements (ion injector not depicted). (Right) A typical spill from a synchrotron. Figures taken from [44]

Therapeutic synchrotrons accelerates protons between, ~60 and 250 MeV. In this case, the injection system consists on an ion source, one or two linear accelerators in series and a beam transport system, about 6–10 m long. After this pre-acceleration process (up to 2-7 MeV, depending on the linear accelerator), a bunch of ~10^{10} particles is transferred into the circular beam line of the synchrotron, equipped with quadrupole magnets to focus the beam, sextupole magnets to increase the acceptance of beam energy spread, and a radio-frequency (RF) unit to accelerate the particles. In this type of accelerators, the particles are confined to a single path, thus the strength of the magnetic fields must be increased during the acceleration process to maintain the trajectory and focus of the beam. Given the path length, the time period for a particle to make one revolution of the accelerator depends on the particle velocity during the acceleration cycle. Therefore, the frequency of the RF system must maintain synchronicity between the arrival of the particle bunch at a cavity and the phase of the RF.

Once the particles are accelerated up to the desired energy, they are extracted, and the unused remaining ions are decelerated and dumped. This sequenced process in a synchrotron takes place over cycles (so-called spills, see Figure 2.8, right). It is necessary to start with a new process when the energy needs to be changed [44]. Figure 2.8 shows a general view of the mentioned synchrotron components.

2.2.1.3 Novel accelerator technologies

The main objective in particle accelerator research is to scale down the size and price of treatment facilities, so the cost of a particle therapy treatment can be eventually comparable to a photon therapy treatment. In this spirit, facilities with multiple rooms reduce the cost per treatment because all rooms share a single common accelerator. Indeed, R&D activities during the last decade made particle therapy as accessible as photon therapy, both in the field of the currently-used accelerators (cyclotron and synchrotron) and in the development of new and novel acceleration techniques, such as the ones described below:

Fixed-field alternating gradient (FFAG) accelerators

In recent years, fixed field alternating gradient (FFAG) accelerators for particle therapy have been the subject of several studies [45–47]. These studies claim that this type of acceleration technique offers the benefits of both synchrotrons and cyclotrons, while enabling a rapid dose delivery thanks to their variable energy extraction and high repetition rate.

As with a synchrotrons, FFAGs have a ring type design. However, like a cyclotron, the magnetic fields remain constant during the acceleration process. It is able to confine the particles into a ring because the strong radial gradient of the magnetic field, therefore a particle follows paths in the region of stronger magnetic fields as its velocity increases. However, although FFAGs have the advantage of using less expensive fixed magnets than a synchrotron, the large gradient changes require a complex design process and operation [48].

Linac-based accelerators

The most widely used accelerators in radiation therapy are linear accelerators (linac), which can accelerate electrons to typically 6-25 MeV. These electrons can be directly used in electron therapy, or, create an electromagnetic radiation during their deceleration into a target (*Bremsstrahlung*) and be used in photon therapy.

However, it is harder to accelerate protons or heavy ions [44] to the desired energy for particle therapy. Therefore, low-energy linear accelerators are used only as injectors for other kind of accelerators, such as the previously described synchrotron.

Several projects aim to develop a suitable linear-based accelerators for proton therapy. One of them is LIGHT (Linac for Image Guided Hadron Therapy) [49, 50], an innovative linear accelerator using a Radio Frequency Quadrupole and more than ten RF systems, which will provide a better quality beam. The current design allows LIGHT to generate an extremely focused beam of 70 to 230 MeV and to target tumours in three dimensions, by varying the depth at which the radiation dose is delivered much faster than existing circular accelerators can. Other projects, such as the "cyclinac" option, combines a cyclotron (used as injector) with a high frequency linac [51, 52]. This would reduce the number of acceleration cavities, and thus, the length of the accelerator. Once a sufficient repetition rate and accuracy of the dose delivery per pulse is achieved, a linac might be suitable for rapid spot scanning in proton therapy.

Laser-driven accelerators

Generating energetic proton beams might be interesting using a laser, since the laser and light transmission components are as large as a typical room and do not require to be surrounded by heavy shielding [53].

At the moment, most research has been done with the target normal sheet acceleration (TNSA) method. It consists on the irradiation by a high-intensity laser of the front side of a hydrogen-enriched solid target. At the front surface, a plasma is created due to the energy absorption by the foil. The electrons in this plasma are heated to high energies, and penetrate through the target and emerge from the opposite surface. This induces strong electrostatic fields, which pull and accelerate ions and the protons out of the rear side of the target [54].

Besides the quest to obtain high proton energies, the obtained energy spectrum is concerning. The observed energy spectra show a broad continuum not suitable for proton therapy. Although some filter and energy compression techniques have been studied, it must be considered that this can produce secondary neutrons, very important if produced close to the patient [55, 56].

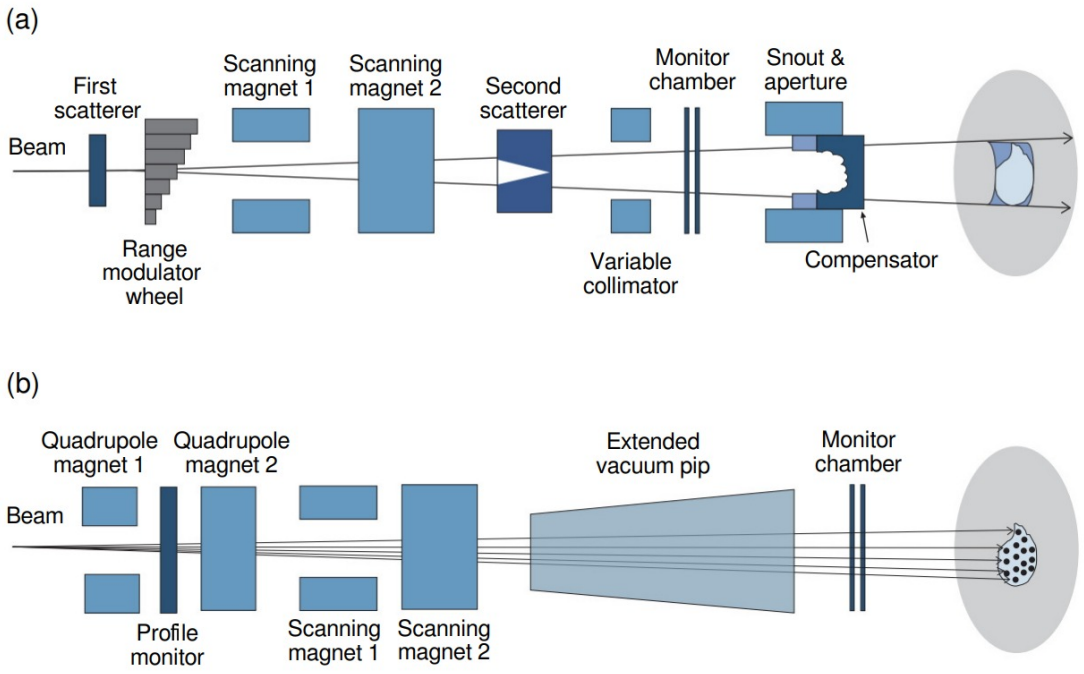

FIGURE 2.9: Schematic examples of (a) double scattering technique with block and compensator and (b) pencil scanning technique. Figures modified from [59].

2.2.2 Beam delivery modalities

Different treatment modes are used in clinical practice to deliver particle fields. In the following, a general overview of the different delivery modes is presented. During the experimental work of this thesis, a pencil beam has been used at both particle therapy facilities: WPE and HIT.

2.2.2.1 Passive Beam Scanning

As shown in Figure 2.9 (a), this technique consists on the scattering of a small beam coming to the nozzle. The scatterers are specially designed so that the beam has a uniform penetration and uniform intensity across the tumour, collimating the beam to match the tumour shape with the so-called compensators. At the same time, the energy of the beam is modulated (typically using a Lucite or PMMA blocks with varying thicknesses) to spread out the location of the Bragg peaks over the target volume in depth. The system is usually configured to produce a homogeneous dose distribution and to produce the same beam penetration [57].

This is the conventional method to create a particle field over the tumour. A disadvantage of this method consists on the sizeable production of secondary neutrons and other particles, by interactions of the beam with the scattering and collimating devices. This results in a undesired dose distribution in the patient [58].

2.2.2.2 Pencil Beam Scanning

Pencil-beam scanning is a more recent method, where the pencil-beam is directly sent into the patient without interacting with any scattering or energy-modulation devices. The dose distribution in the tumour is created by steering the beam with magnetic dipoles to reach the full lateral extent of the tumour. The beam energy is modified to irradiate at multiple depths. Compared to passively scattered delivery, pencil-beam scanning has more degrees of freedom, enabling the dose distribution of

each beam to conform with the proximal and distal surfaces of the tumour. Another advantage is the avoidance of the production of secondary neutrons in scattering devices [60]. The beam delivery is monitored by several ionization chambers to measure the delivered dose and the lateral position of the delivered treatment fields.

If using intensity-modulated particle therapy (IMPT), the homogeneous dose distribution over the target volume is constructed by the combination of two or more treatment fields. The beam intensity of each field is also customized. The beam fields can be delivered with fixed beam lines, mostly implemented as horizontal beam lines, or a beam line can be mounted on a gantry system, which can be rotated 360° around the patient, nearly every geometry for the irradiation is possible. The gantry weights about 100 tons because the beam line needs several magnets for beam alignment and focusing [44].

2.2.2.3 Recent developments in beam delivery

Mini-beams therapy

Proton minibeam radiation therapy (pMBRT) is a novel dose delivery method consisting in the irradiation of the tumour with submillimetric beams, roughly one order of magnitude smaller than state-of-the-art pencil beams. pMBRT has proven to be promising in terms of reduced side effects, due to the spatial dose fraction, and its apparent superior tumour control, which encourage the possible application to patient treatments [61]. Recent investigations aim at an optimized implementation of pMBRT in a clinical pencil beam scanning system [61–63].

Arc therapy

In arc proton therapy, the proton beams are delivered continuously as the gantry rotates around the patient. During this rotation, the beam energy and intensity are adjusted to match the desired dose distribution in the target volume. Although arc proton therapy is a beam delivery method technically challenging, it offers improved target dose conformity and better sparing of nearby vital organs when compared against IMPT, being a technique more robust to changes in patient set-up and anatomy [64, 65]. Novel investigations have been doing since it was first proposed in 1997, extending the technique to spot-scanning hadron arc therapy using He and C ions [66].

FLASH therapy

FLASH therapy is the delivery of ultra-high dose rate radiation several orders of magnitude higher than what is currently used in conventional clinical therapy. In such irradiation, a phenomenon known as FLASH effect takes place. It consists on the ultra-high dose rate reducing toxicities in healthy tissues while maintaining local tumor control. This effect has been confirmed in several studies in recent years for electron beams, but studies with proton beams, although increasing over the last years, are yet scarce. The underlying mechanisms responsible for this effect are yet to be fully understood. This technique seems to be a very promising technique, but further investigations are still required [67].

2.3 Beam range verification

A particle therapy treatment is based on a carefully personalized plan, elaborated using a computed tomography (CT) of the patient in the same position as used during treatment. The treatment planning system consist on the design of the dose delivered to the patient, as described in Section 2.2.2.

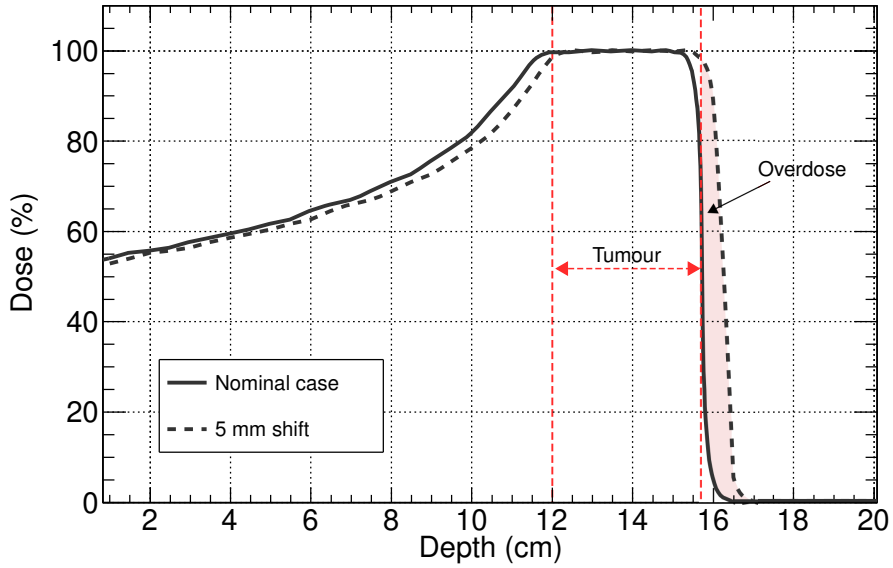

FIGURE 2.10: The effect on the depth-dose distribution of a shift of 5 mm in the range of a proton beam in water using Geant4.

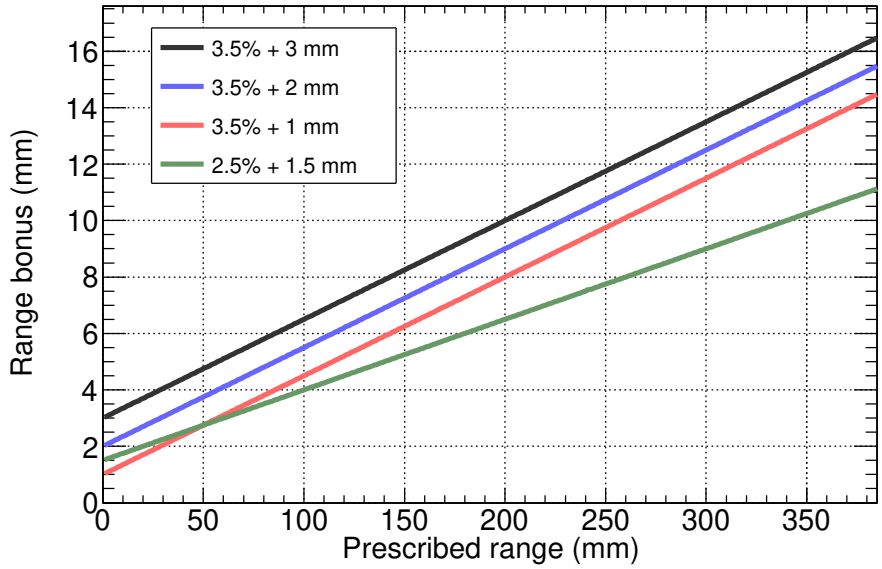

FIGURE 2.11: Safety margins applied at different clinical proton therapy facilities.

This process is optimized with complex computer algorithms to create a high and uniform dose in the tumour and avoid OAR and healthy tissues.

However, there could be problems related to the calculation of the beam range or to the actual implementation of the irradiation that could potentially cause the treatment beam to miss the distal part of the tumour or irradiate more healthy tissue behind the tumour, as represented in Figure 2.10. In the following, the main sources of range uncertainty and verification techniques are discussed.

2.3.1 Sources of range uncertainty and safety margins

There are multiple sources of uncertainties in the beam range that can limit the advantages of particle therapy over conventional radiation therapy, which were collected and evaluated, for instance, by H. Paganetti in [20] and [44].

One of the main sources of uncertainty stems from the determination of the stopping powers in the body of the patients using the CT images. It consists on a conversion from the CT numbers (the so-called CT Hounsfield units, HU) to tissue densities and thus stopping powers [68]. Its calibration is not exact, requiring certain assumptions on the composition and ionization potential of the tissues [69]. For instance, the uncertainty in the I-values results in a difference in the range of about 1.5–2.0%. Furthermore, the HU calibration can be affected by the fact that the same X-ray attenuation (i.e. the same HU) might correspond to different stopping powers, image noises [70] and/or spatial resolution [71]. These uncertainties generally are systematic for most of the tissue traversed by a typical beam. Therefore, the magnitude of the total uncertainty is proportional to the range of the beam. In [20], the estimation due to this source is approximately ±2.5% of the beam range in water for most tumour sites, with larger values in specific cases, such as when there are metal implants. Furthermore, the algorithm used in treatment planning systems to calculate the range of the particle beams can be a source of uncertainty due to its complexity, especially when particles traverse tissues with different densities and the analytical algorithms are not able to correctly predict the effect of range degradation caused by multiple Coulomb scattering, where an additional ±2.5% uncertainty can be introduced. Monte Carlo dose calculations may be needed to ensure more accurate dose computations to improve target coverage and sparing of OARs in proton therapy.

Moreover, changes in the patient anatomy or position from the initial plans are also sources of uncertainty [72]. The patient conformation may change from day to day (e.g. change in metabolism) or even during the beam delivery (e.g. breathing motion). In this regard, due to its motion during the treatment, tumours in the lung or abdomen are particularly susceptible.

Besides that, there are uncertainties that are independent of dose calculation, for instance, the reproducibility of the beam delivery, the degraders design to ensure lateral and distal target conformation, or the commissioning measurements in water. In this regard, and together with the patient setup and modifications, a random uncertainty of about ±1 mm is additionally considered [20].

Clinically, the aforementioned uncertainties are taken into account by adding a safety margin to the prescribed range to ensure the coverage of the tumour. Some of these safety margins assumed in the treatment planning are described in [20]. Figure 2.11 illustrates the range bonus applied to the prescribed range at different facilities. For instance, the safety margins at the Massachusetts General Hospital (MGH) is assumed as 3.5% of the range plus an additional 1 mm, while the MD Anderson Proton Therapy Center in Houston, the Loma Linda University Medical Center and the Roberts Proton Therapy Center at the University of Pennsylvania apply 3.5% + 3 mm. On the other hand, the University of Florida Proton Therapy Institute uses 2.5% + 1.5 mm.

Overall, the safety margins applied to make sure that the full tumour volume is correctly irradiated results in a overdose of nearby healthy tissue or, worse, OAR. For instance, the 3.5% + 1 mm margin at the MGH results in an actual delivered range of 15.625 cm for a prescribed range of 15 cm, i.e. an overdose for more than 6 mm.

2.3.2 Techniques of range verification

Considering all the above-mentioned, it is highly desirable to reduce the safety margins related to the beam range uncertainty to profit from the superior depth-distribution of particle therapy. In response

to this need, there are various methods for range verification under development. The main strategies under study are:

PET imaging

Positron Emission Tomography (PET) range verification is based on the detection of β^+ emitters produced in the body of the patient by nuclear reactions induced by the protons in the beam. As with γ-ray imaging, this technique requires the comparison of the measured activity distribution with a simulated one. The PET imaging can be applied online or offline depending on the half-lives of the β^+ emitters that one looks at, which can vary from milliseconds to minutes.

PET range verification is the main motivation behind this thesis, which aims at improving the accuracy of the corresponding simulations by providing a complete set of production cross sections for the production of the β^+ emitters of interest.

Prompt γ-ray imaging

On its way through matter, the incident beam undergoes inelastic nuclear reactions, which result in the excitation of target nuclei followed by a nearly instantaneous emission of γ-ray photons with energies of up to tens of MeV. As the emission of these γ-rays is directly correlated with the beam trajectory, it can be employed for range verification by means of the comparison with simulations of the expected activity distributions [73].

The main advantage of γ-ray imaging is the potential for real-time verification, as the half-lives of the most relevant nuclear excited states are in the order of femtoseconds to picoseconds. The implementation of this technique is challenging, and has not yet been performed clinically, but plenty of ongoing research focuses on Monte Carlo simulations and improving the detector systems, such as Compton cameras with a high detection efficiency [74, 75].

Neutron emission

As a result of the nuclear interactions of the particle beam with the body, secondary neutrons are produced and can be thus used as verification system of the range [76]. Implementing this technique requires not only detecting the secondary neutrons but also determining their origin in space. Very recent studies have proposed detector concepts based on a hydrogen-rich converter material followed by two charged particle tracking detectors. Neutrons incident on the converter material are converted into protons through elastic and inelastic (n,p) interactions. The protons are subsequently detected in the tracking detectors. The information about the direction and position of these protons is then employed by a reconstruction algorithm to estimate the depth distribution of neutron production by the incident beam, that correlates with the beam trajectory and hence its range.

Acoustics

The acoustic signature of the pulsed proton beam could also be used for range verification. This technique was first proposed in the late 1970s [77], and received more attention in the last few years [78].

The main advantage of this method is the direct relation between the dose and the signal. If the proton beam is pulsed with a sufficient number of protons per pulse, sound waves due to the thermal effects of the radiation beam can be detected with ultrasound equipment. However, the considerable difficulties to model the propagation of the wave to the surface of the patient and the required pulse

delivery not being compatible with current acceleration systems, make the implementation of this technique very challenging.

Direct dose measurement

Direct dose measurement using implantable dosimeters could also be an option for some treatments, such as prostate tumours. Whereas this technique is limited to specific tumours, it has the advantage of directly measuring the dose, in contrast to other methods based on secondary radiation, and it could be a complimentary technique for other *in vivo* range verification methods [79].

Magnetic Resonance Imaging

Another methodology proposed for range verification consists on the conventional magnetic resonance imaging (MRI) [80]. This technique is based on the interpretation of standard T1-signal intensity, as in the conventional use of MRI scans, but the signal is induced by the radiation. This signal can be detected as early as 10 days after radiation therapy and it is observed to persist up to 21 months after the treatment. Although the verification technique can not provide real-time verification for a specific patient, such post-treatment verification could provide essential clinical information for improvement of population-based treatment margins in specific indications.

2.3.3 Positron Emission Tomography (PET) range verification

This section focuses on the basis of PET range verification, data acquisition strategies, state-of-the-art and requirements for clinical implementation.

2.3.3.1 β decay

A small fraction of the incident beam particles, usually 0.5-1%, undergoes nuclear reactions which sometimes results in radioactive nuclei as illustrated in Figure 2.12 (a). These unstable isotopes can decay via β emission or electron capture. Proton-rich nuclei decay either by electron capture or β^+ emission, while neutron-rich nuclei decay by β^- emission. Electron capture is the radioactive decay process by which an atom's inner orbital electron is absorbed by the nucleus, within which a proton is converted into a neutron emitting an electron neutrino. In β^- decay, a neutron of the atomic nucleus is transformed into a proton while releasing an electron and an electron antineutrino. On the other hand, in β^+ decay, a proton of the atomic nucleus is transformed into a neutron while releasing a positron and an electron neutrino. In all cases there is nuclear transmutation: an atom of one chemical element is changed into another with an atomic number that is different by one unit.

In the case of β^+ decay:

$$ {}^{A}_{Z}X \rightarrow {}^{A}_{Z-1}X + e^{+} + \nu_e. \tag{2.7} $$

Isotopes which undergo β^+ decay and thereby emit positrons are called β^+ emitters (see Figure 2.12 (b)).

The total energy available following a β^+ decay is the difference between the initial and final states:

$$ Q_{\beta^+} = \left[m_N({}^{A}_{Z}X) - m_N({}^{A}_{Z-1}X) - m_e \right] c^2, \tag{2.8} $$

where m_N are the nuclear mass of the parent and daughter atom and m_e is the electron mass. This energy has to be shared between the three bodies involved (the daughter nucleus, the positron, and

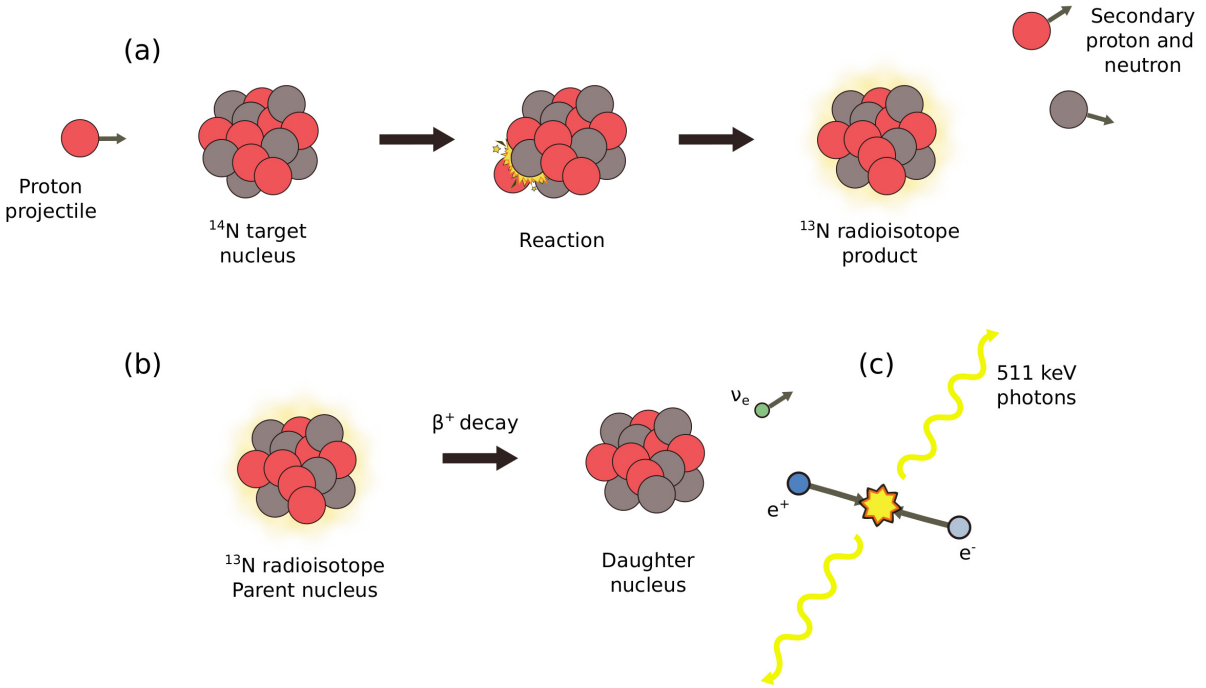

FIGURE 2.12: Illustration of (a) a (p,pn) nuclear reaction by incident proton colliding with ^{14}N target nucleus and producing ^{13}N product nucleus, secondary proton and neutron. (b) The ^{13}N unstable radionuclide decays via β^+ emitting a positron and a neutrino. (c) The positron is subsequently annihilated with an electron of the medium emitting two 511 keV photons in opposite directions.

the neutrino). Therefore, the emitted β^+ particles feature a continuous distribution of energies, from zero up to Q_{β^+}.

Taking into consideration that the atom's neutral mass can be expressed as

$$m(^A_Z X)c^2 = m_N(^A_Z X)c^2 + Zm_e c^2 - \sum_{i=1}^{Z} B_i, \tag{2.9}$$

where B is the binding energy of each i-electron, theQ_{β^+} value can be calculated as:

$$Q_{\beta^+} = \left[m(^A_Z X) - m(^A_{Z-1} X) - 2m_e\right]c^2. \tag{2.10}$$

From Equation 3.4, one can conclude that the β^+ decay is energetically possible as far as the mass of the parent atom exceeds by at least two electron masses the daughter atom (1.022 MeV) [81].

Fermi's theory applied to β^+ decay

In 1934, Fermi developed a theory for β decay based on Pauli's neutrino existence hypothesis [82]. In general terms, Fermi assumed that the β decay is a transition that depends on the strength of coupling between the initial and final states and the number of ways the transition can happen (i.e. the density of the final states). Fermi developed an expression which is now referred to as Fermi's Golden Rule:

$$\lambda_{i-f} = \frac{2\pi}{\hbar}|M_{i-f}|^2 \rho_f, \tag{2.11}$$

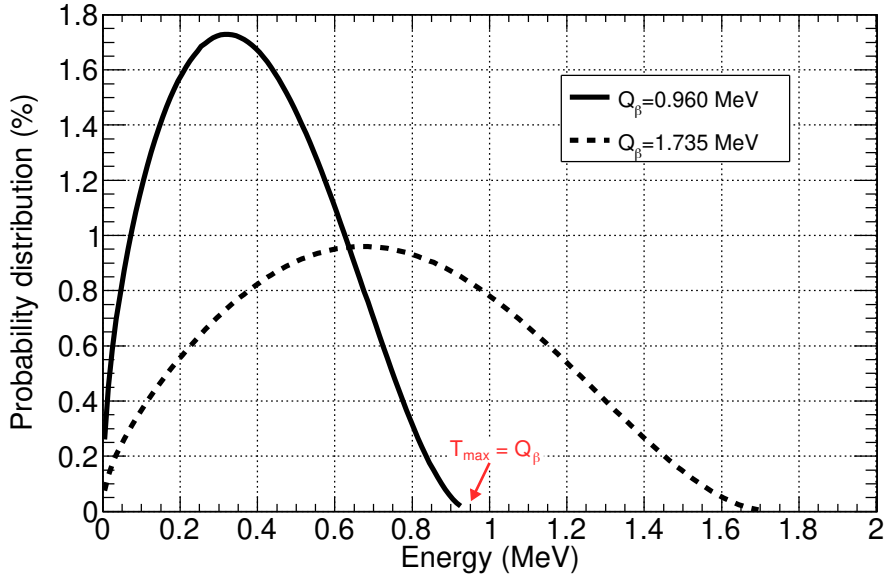

FIGURE 2.13: Expected positron energy distribution from Equation 2.13. These distributions are drawn for Q=0.960 MeV and Q=1.735 MeV, corresponding to the Q-values of the decay of ^{11}C and ^{15}O isotopes, respectively.

where λ_{i-f} is the transition probability between the initial and final state, $\hbar$ the reduced Planck constant, M_{i-f} the matrix element for the interaction and ρ_f the density of final states. The transition probability λ is also called the decay probability (also refereed as decay constant), and it is related to the mean lifetime τ of the state by $\lambda = 1/\tau$. The matrix element describes the coupling between the initial and final states. In this case, a transition will proceed more rapidly if the coupling between the initial and final states is stronger. The matrix element can be placed in the form of an integral where the interaction causing the transition is expressed as a potential V that operates on the initial state wave function:

$$M_{i-f} = \int \Psi_f^* V \Psi_i \, dv, \tag{2.12}$$

where Ψ is the wave function for the initial and final state and V represent the operator for the physical interaction that couples the initial and final states of the system. The transition probability is proportional to the square of the integral of this interaction over the spatial domain. The transition probability is also proportional to the density of final states ρ_f. It is reasonably common that the final state is composed of several states with the same energy. These states are called "degenerate" states. This degeneracy is sometimes expressed as a "statistical weight" that appears as a factor in the transition probability. In many cases, there is a continuum of final states, so this density of final states is expressed as a function of energy.

Considering the above-mentioned factors for the case of β decay, the resulting continuous energy distribution of the emitted β particles is:

$$N(T_\beta) = k\sqrt{T_\beta^2 + 2T_\beta m_e c^2}(Q - T_\beta)^2(T_\beta + m_e c^2), \tag{2.13}$$

where T_β is the kinetic energy of the resulting positrons and k is a constant [81]. An example of the energy probability distribution is shown in Figure 2.13. The consequence of featuring a continuous energy distribution up to a sizeable energy is that the positrons emitted and of interest for PET range verification will travel a variable distance from their origin before they are annihilated with electrons of

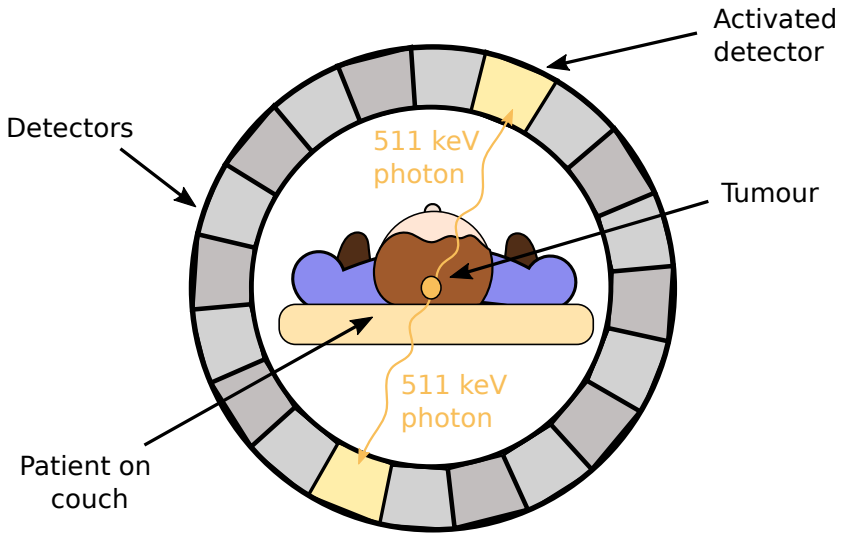

FIGURE 2.14: Positron emission tomography (PET) scanner.

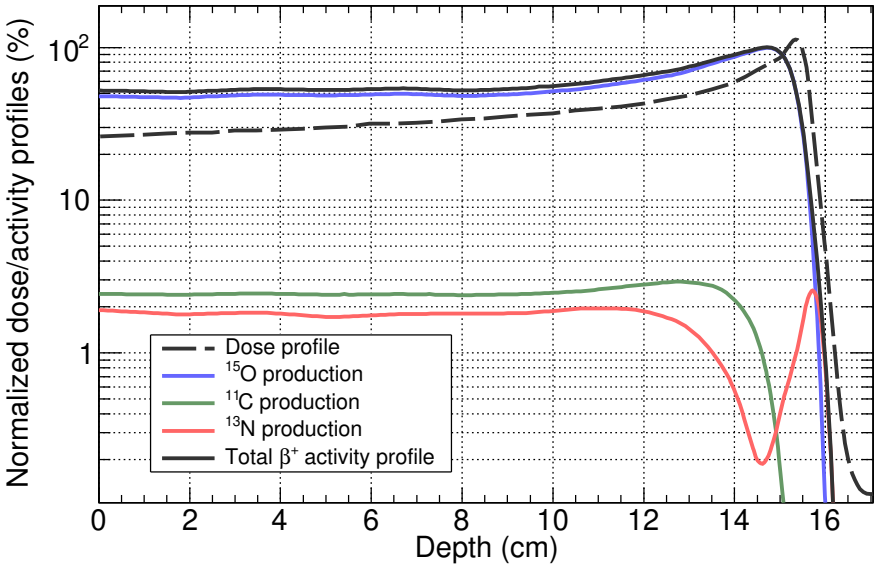

FIGURE 2.15: ^{11}C, ^{13}N, ^{15}O and total activity profiles in a water phantom, induced by a 150 MeV proton beam, and compared to the depth-dose profile. The profiles were calculated by folding the proton flux calculated with Geant4 with the ICRU63 cross sections library [83].

the medium, which has to be considered for the corresponding clinical implementation of this range verification method. The result of this annihilation is the emission of two 511 keV-photons in opposite directions as follows:

$$e^+ + e^- \rightarrow \gamma + \gamma. \tag{2.14}$$

This process must satisfy conservation laws, i.e. conservation of electric charge, linear momentum, total energy, angular momemtum and net mass or lepton number (which is the number of leptons, such as the electron, minus the number of antileptons, such as the positron) [81]. Figure 2.12 (c) illustrates the annihilation of the emitted positron.

2.3.3.2 Basis and requirements of PET range verification

The basic goal of PET range verification is to determine the β^+ activity distribution of the irradiated patient and compare it with the expectation from simulations, so that potential differences in dose deposition with respect to the treatment planning can be identified, and then the planning re-adapted. The β^+ activity distribution is measured with a PET scanner, conformed by multiple scintillators detectors forming a ring (see Figure 2.14). When two photons are detected within a coincidence time window, it is assumed that the the annihilation has taken place along the line, so-called line of response (LOR), that connects those two detectors. The scintillators convert the photons in a light signal, which is subsequently converted into a charge signal by the SiPM and processed by read-out electronics. The tomographic reconstruction of the signals from multiple, intersecting LORs, provides a 3D distribution of the positron annihilation. This emission is correlated to the delivered dose in the patient. Further improvements have been implemented to improve spatial resolution, e.g. time of flight (ToF-PET), a method consisting in reconstruction algorithms based on the timing information from the two photons reaching the detectors. Although conventional PET scanners were initially designed for diagnostic applications, they offer considerable advantages for the clinical implementation of PET range verification [84–89].

However, there is not a straightforward correlation between the β^+ activity distribution from the PET image and the delivered dose, since β^+ emitters are produced by nuclear interactions and the delivered those by electromagnetic processes. The activity distribution drops prior to the dose distribution due to the threshold energies for the production of β^+ isotopes [85, 86], thus the fall-off positions of the activity and dose distribution are shifted with respect each other, as illustrated in Figure 2.15. Furthermore, the activity distribution changes depending on the time span between the irradiation of the patient and the PET image, due to the different half-lives of the variety β^+ isotopes produced [86]. Another effect of this time span is the blurring of the PET image as the activity signal washes-out over time due to the diffusion of the β^+ emitters produced in the body [89].

All these factors prevent a direct range verification by simply comparing dose and activity profiles. In consequence, the β^+ activity distribution must be predicted using Monte Carlo simulations to compare against the measured activity patterns. Only from this comparison it is possible to evaluate the correctness of the dose profile delivered and, if necessary, update the treatment planning to compensate the dose profile accordingly; delivering thus the desired dose distribution by the end of the overall treatment.

The Monte Carlo tools available nowadays are capable of simulating very well the transport of the light ions of interest through the patient's body. However, in order to make estimations of the corresponding β^+ activity profile, they need as input detailed information of the associated reactions. The problem, pointed out for instance in Ref. [71, 90–93], is that these nuclear data, the cross section of the reactions producing the β^+ emitters of interest, are not as well-known as it would be desirable. The current data bases and evaluations available do not allow to predict activity curves with a submillimetric accuracy [20], and it is precisely the aim of this work to develop the technique and perform experiments and analysis necessary to produce a new data base that solves this issue.

2.3.3.3 Types of PET range verification, current status and clinical implementation

In-vivo PET range verification can be performed either in-beam [88], in-room [94] or off-line [89], depending on when and where the imaging acquisition is performed, as illustrated in Figure 2.16.

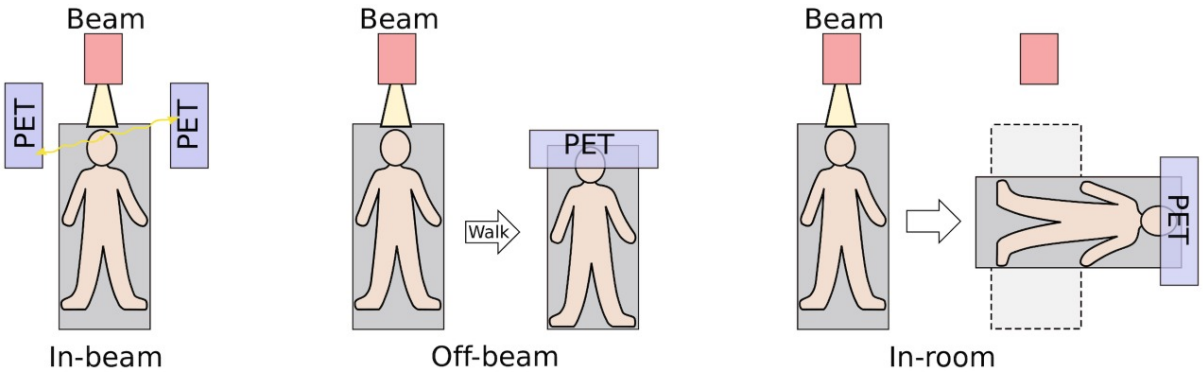

FIGURE 2.16: Three operational modalities for PET verification of proton therapy: in-beam PET, which uses PET detection panels integrated with the beam delivery system; off-line PET, the patients walk to a nearby PET facility for the verification scan; in-room PET, which uses a stand-alone, full-ring PET scanner positioned in the treatment room to scan the patient (still in the treatment bed) soon after treatment.

Off-line images are recorded using a conventional PET scanner located outside the treatment room. These images show activity from radioisotopes whose half-life is equal or longer than the time required for transportation and positioning of the patient, i.e. basically ^{11}C ($t_{1/2}$ = 20.36 min) and ^{13}N ($t_{1/2}$ = 9.97 min). This method has been successfully tested in some specific treatment centers, such as the Hyogo Ion Beam Medical Center of Hyogo, Japan [95], at the Massachusetts General Hospital (MGH), USA [89, 96] and at the Proton Therapy Institute, University of Florida, USA [97]. In this approach, commercial, full-ring PET scanners have been used and, when combined with a CT scanner (PET/CT), have enabled an accurate correlation between the treatment and imaging position, which helps compensating for the unavoidable patient movement caused by transportation and/or repositioning. This constitutes a promising technique because it employs conventional scanners, without requiring the acquisition of new specific devices.

The main disadvantage of off-line PET range verification is the influence of disturbing biological wash-out processes which blur the images [89] due to the diffusion of the produced radioisotopes by the fluids of the body before they decay. Furthermore, one does not have real-time feedback control of the dose delivered to the patient, and the signal represents an accumulation of the different treatment beams (with different directions and energies) that have been delivered.

The online in-beam PET acquisition is an alternative to the off-line method. It reduces the influence of disturbing biological wash-out effects, repositioning of the patient is not required and, in principle, online corrections of the treatment would be possible if differences between measured and predicted activation distribution are observed. In online PET verification, all PET nuclides, independent of their half-life, contribute to the image, with the shortest-lived ones, defined as isotopes with a half-life shorter than that of ^{10}C ($t_{1/2}$ = 19.29 s), contributing more (relative to their production rate). The most abundant short-lived isotopes produced in the human body have been studied and discussed in [98]. This study concluded that the β^+ emitters of interest for online PET imaging are ^{12}N ($t_{1/2}$ = 11 ms), ^{38m}K ($t_{1/2}$ = 925 ms) and ^{29}P ($t_{1/2}$ = 4.14 s) produced in carbon, calcium and phosphorus, respectively.

Online acquisition requires PET devices coupled to the beam nozzle and a specific beam duty cycle, so PET acquisition can be performed between consecutive spills. The integration of a PET scanner with the nozzle is geometrically challenging and typically results in a dual-head configuration, with the corresponding reduction of efficiency. Furthermore, this technique has to deal with the production of background radiation during beam extraction and the synchronization of the PET data acquisition with the beam control system. This challenging method is currently being investigated at, for

TABLE 2.1: β^+ emitters, half-lifes and reaction channels of interest for PET range verification in proton therapy.

Isotope	Half-life	Q_{β^+} (MeV)	Reaction channel	Threshold (MeV)
^{11}C	20.36 min	0.960	^{12}C(p,x)^{11}C	17.9
			^{14}N(p,x)^{11}C	3.13
			^{16}O(p,x)^{11}C	23.6
^{13}N	9.97 min	1.198	^{12}C(p,x)^{13}N	-
			^{14}N(p,x)^{13}N	8.93
			^{16}O(p,x)^{13}N	5.55
^{15}O	122 s	1.735	^{14}N(p,x)^{15}O	-
			^{16}O(p,x)^{15}O	14.3
^{12}N	11 ms	16.316	^{12}C(p,x)^{12}N	19.6
^{38m}K	0.925	5.022	^{40}Ca(p,x)^{38m}K	14.0
^{29}P	4.14 s	3.921	^{31}P(p,x)^{29}P	15.6

instance, the Italian National Center of Oncologic Hadrontherapy (CNAO) [99], the Gesellschaft fuer Schwerionenforschung (GSI), Germany [100], the Heavy Ion Medical Accelerator in Chiba, Japan [101] and the Kashiwa Center, Japan [102].

A compromise solution between offline and online PET measurements is to use an in-room, stand-alone PET system [94]. In this case, the imaging is performed directly after the treatment, using the same patient immobilization and treatment couch. The in-room PET approach is a good compromise to solve the problems of online and off-line verification, because it reduces relatively the wash-out effects while enabling a feasible clinical implementation using conventional PET scanners. Although all PET nuclides contribute to the image, shorter-lived isotopes than in off-line monitoring but longer than in online monitoring are envisaged, being ^{15}O ($t_{1/2}$ = 122 s) the best candidate.

The β^+ emitters produced in the main elements of the human body (carbon, nitrogen, oxygen, calcium and phosphorus) of interest for offline, in-beam and in-room PET range verification, their half-lives, endpoint energy, production reaction channel and energy threshold are listed in Table 2.1.

2.3.3.4 The role of nuclear data: available cross sections and requirements

As already mentioned, PET range verification relies on the comparison of the measured activity distribution with an expected curve by a Monte Carlo simulation of the treatment plan, such as the one represented in Figure 2.15. In this figure, the induced activity distributions of the radioisotopes produced in water by a mono-energetic proton beam is calculated with the Geant4 simulation toolkit [35]. The long-lived β^+ emitters produced in water are ^{11}C, ^{13}N and ^{15}O, hence one of the inputs of the Monte Carlo simulation is the probability with which the incident beam produces these β^+ emitters in the elements of the human body. These nuclear reaction probabilities are usually expressed in the form of *cross sections*, which represent the area that the target nucleus presents to the projectile for the particular interaction process of interest. For instance, to obtain the Figure 2.15, the ICRU63 cross sections library [83] has been used as input to the Geant4 simulation.

The cross section databases available in the literature contain experimental and evaluated data.

The EXFOR library [103] contains an extensive compilation of experimental nuclear reaction data. The web database provides data search, output to various formats, plotting and comparison to a evaluated library, re-normalization old data to new standards, calculating data for inverse reactions and kinematics, constructing correlation matrices from partial uncertainties, etc, containing data from more than 24.400 experiments.

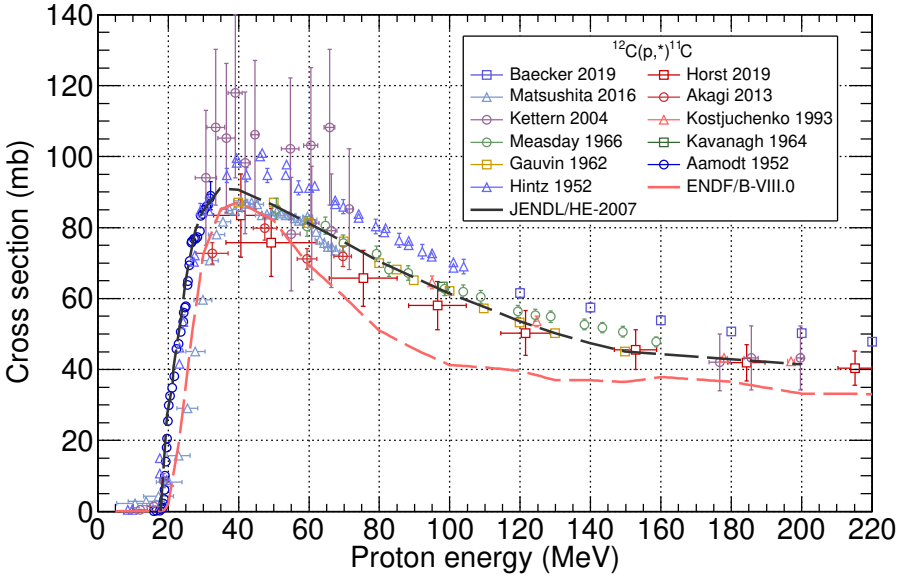

FIGURE 2.17: Available evaluated and experimental cross section data of ^{11}C(p,x)^{11}C.

The number of experimental data regarding the production of the β^+ emitters listed in Table 2.1 varies depending on the nuclear reaction. In general, there are several experiments addressing the longer-lived β^+ emitters in proton-induced reaction on ^{12}C, ^{14}N and ^{16}O. Most of them, however, were performed below 30 MeV, which is the energy range of interest for the production of medical isotopes for diagnostics. If one considers up to ~200 MeV, which is the range of interest in proton therapy, the most studied reaction channel is ^{12}C(p,x)^{11}C, as it is β^+ isotope most-copiously produced in the human body at these energies. As shown in Figure 2.17, there are quite some data sets in the literature, some of them very recent [104, 105], but none of them covers the full energy range of interest and there are deviations from 15 up to 25% between different measurements. It is important to note that this is the best scenario: other reactions producing the mentioned long-lived isotopes have been less investigated and the data are very scarce, with significant deviations with respect to the evaluations. As an example, the reaction cross section to produce ^{11}C in oxygen (the most abundant element in the human body) and the reaction cross section to produce ^{13}N in nitrogen are also displayed in Figures 2.18 and 2.19, respectively. As illustrated in these figures, the data are scarce and differ significantly between them. For instance, in ^{16}O(p,x)^{11}C reaction there are differences of ~40% at low energy (~50 MeV) and even larger discrepancies above the reaction threshold. The situation presented herein reflects the necessity for new data with enhanced accuracy covering the full range of interest in proton therapy.

Regarding the short-lived isotopes listed in Table 2.1, there are no previous data regarding the excitation functions of these isotopes up to clinical energies in proton radiotherapy, besides the integral production yield below 55 MeV studied by [98]. The different evaluated databases do not agree between them, which makes sense because there are no previous experimental data and they depends only on theoretical calculations. A complete comparison between the data available in the literature for all the reactions of interest listed in Table 2.1, including our measurements, is presented in Chapter 5.

Due to the differences between the different data sets, some of them incomplete, the available experimental cross section data have been combined and analyzed by experienced nuclear physicists to produce "evaluated" libraries over the years. This is done in the context of national or regional nuclear

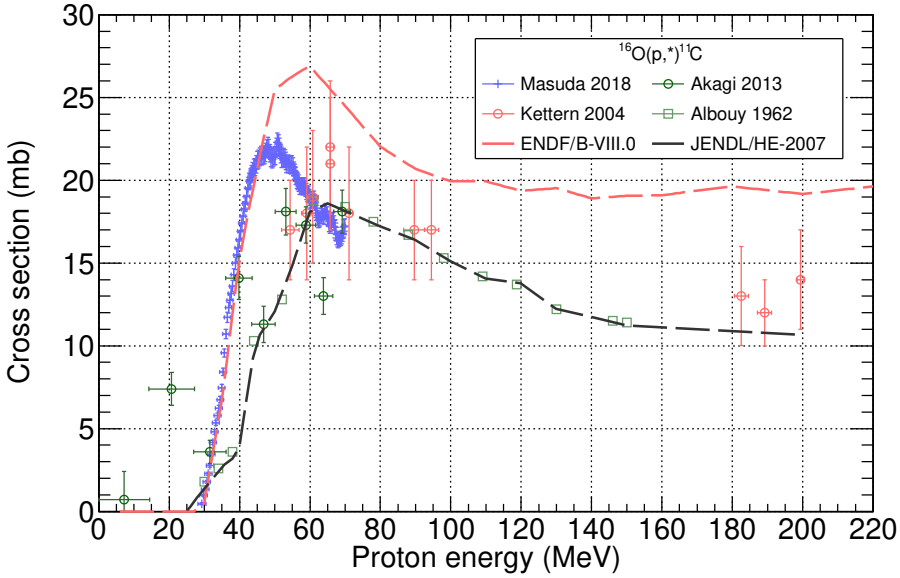

FIGURE 2.18: Available evaluated and experimental cross section data of ^{16}O(p,x)^{11}C.

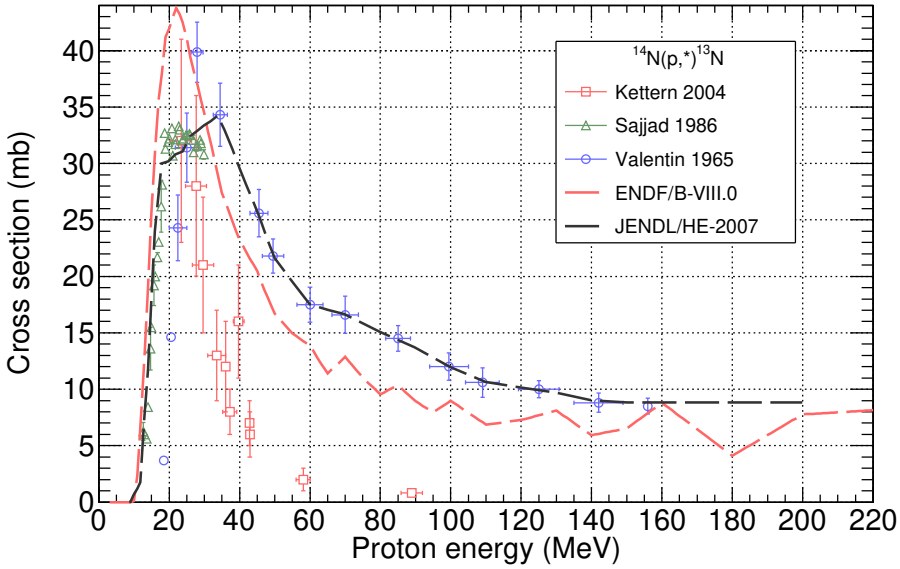

FIGURE 2.19: Available evaluated and experimental cross section data of ^{14}N(p,x)^{13}N.

data projects from USA, Europe, Japan and China that have developed their own databases which contain recommended evaluated cross sections, angular distributions, fission product yields and other nuclear data of interest. These are usually generated using nuclear reaction models benchmarked to the available experimental data, and, in some cases, these libraries introduce *ad hoc* corrections to ensure the compatibility of different experimental data. The major evaluated data libraries are:

- ENDF/B (US Evaluated Nuclear Data File)
- JEFF (Joint Evaluated Fission and Fusion Library)
- JENDL (Japanese Evaluated Nuclear Data Library)
- CENDL (Chinese Evaluated Nuclear Data Library)

- BROND (Russian Recommended Evaluated Neutron Data Library)
- RUSFOND (Russian file of evaluated neutron data)
- TENDL (TALYS-based Evaluated Nuclear Data Library)

Although these major libraries are specifically dedicated to neutrons, some of them contain also evaluated cross section data for proton-induced reactions. This is the case of the JENDL, with data up to 3 GeV, and ENDF/B and TENDL libraries, with data up to 150 MeV and 200 MeV, respectively. The data from the ENDF/B library [106], being the ENDF/B-VIII.0 the latest version, were provided by the evaluation performed in the 1990s at Los Alamos National Laboratory (USA) up to 150 MeV, referred also as LA-150 [107]. In 2001, the International Commission on Radiation Units and Measurements (ICRU) reported a comprehensive tabulation of nuclear data especially relevant for medical, industrial, research, and protection applications. This ICRU63 library [83] is the extension to 250 MeV of ENDF/B-VI.0 library for several isotopes of particular interest in proton therapy (as the ones studied in this work).

Additionally, there are theoretical calculation codes for modeling of nuclear reactions, such as EMPIRE or TALYS. In particular, the above mentioned TENDL nuclear data library is based mainly on TALYS calculations, although from version TENDL-2019, it includes ENDF/B data whenever they are available. As both ICRU and TENDL-2019 are based on the ENDF/B library (with no detected changes between versions VI and VIII) in the following we refer to all of the data libraries as the ENDF/B-VIII.0 library.

Due to the significant differences between the experimental data sets available in the literature, the evaluations do not reproduce all of them, as expected. Furthermore, the ENDF/B-VIII.0 and JENDL/HE-2007 differ significantly with each other, as they are based on different models and experimental data sets. In the best case scenario (the ^{12}C(p,x)^{11}C reaction), all measurements indicate an underestimation of the corresponding ENDF/B-VIII.0 evaluation, whiles the JENDL/HE-2007 evaluation reproduces the data from [105, 108, 109] as illustrated in Figure 2.17. On the other hand, as shown in Figures 2.18 and 2.19, the ENDF/B-VIII.0 evaluation is over- and underestimated in comparison with the experimental data, while the JENDL/HE-2007 evaluation has been performed to reproduce the data from [110] and [111], respectively.

The International Atomic Energy Agency (IAEA) has performed two evaluations for the reactions ^{14}N(p,x)^{11}C and ^{16}O(p,x)^{13}N [112] below 30 MeV, since these are the typical reactions for PET diagnostic imaging and, therefore, there was a general interest concerning this radioisotope production for medical purposes. However, at higher energies and for the rest of nuclear reactions involved in PET range verification, there is not any IAEA evaluation yet, as the data set corresponding to these reactions are quite limited, especially for energies above 20 MeV, and show sizable discrepancies. The need of new measurements and subsequent data evaluations of these reactions at higher energies has been highlighted at the IAEA Technical Meeting held in Vienna on December 2018 [113] and also by [92, 93].

Moreover, the need of an accurate characterization of the production cross sections in order to reduce uncertainties in the estimation of the activity depth profiles, enabling the aimed millimetric beam range verification, has been also addressed by the medical physics community [20, 114]. As an illustrative example of the effect of cross sections in the calculation of β^+ activity profiles, the activity distribution of the β^+ isotope ^{11}C produced by a 150 MeV proton beam in carbon has been calculated with Geant4 using:

- A data set combining the experimental data from Hintz et al. (1952) [115], Aamodt et al. (1952) [108] and Bäcker et al. (2019) [104], because all of them follow the same tendency and, combined, allow covering the full energy range.

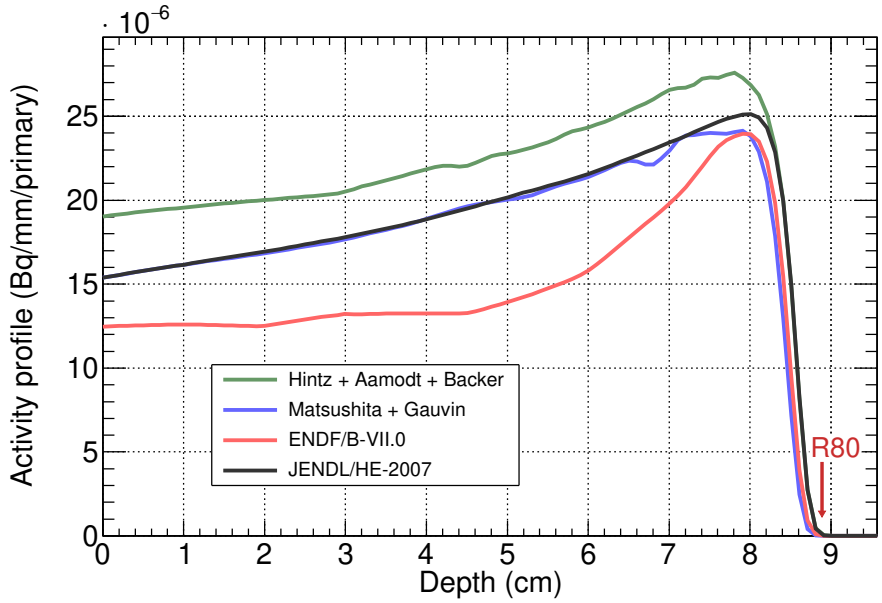

FIGURE 2.20: Comparison of the activity distribution of ^{11}C produced by a 150 MeV proton beam in carbon, calculated with different cross sections data sets.

- A data set combining the experimental data from Matsushita et al. (2016) [116] and Gauvin et al. (1962) [109], for the same reason.
- The ENDF/B-VIII.0 library.
- The JENDL/HE-2007 library.

The results are displayed in Figure 2.20. It is evident that the activity curves differ significantly, about 60% in the intermediate depth region. More surprisingly, the results differ (by 2 mm) in the position of the activity curve fall-off near the end of the range, which is the key feature to relate the activity and dose delivered profiles.

2.4 Objective of this thesis

In summary, the very limited reliability of the cross section data used in the activity calculations for PET range verification is related to the fact that:

- The available experimental data sets for all the reactions of interest do not always cover the full energy range up to 200 MeV.
- When available, their accuracy is very limited, resulting in sizable discrepancies between different data sets.
- The evaluations available, relying on models and the mentioned limited data base, are hence not accurate enough neither consistent with each other.

In this context, the work developed in this thesis combines basic and experimental nuclear physics investigations to improve PET range verification. The main goal is to measure the nuclear reactions involved in this verification technique in order to improve the calculations of the expected induced activity distribution in the patient. Thus, this thesis contains a compendium of new nuclear cross

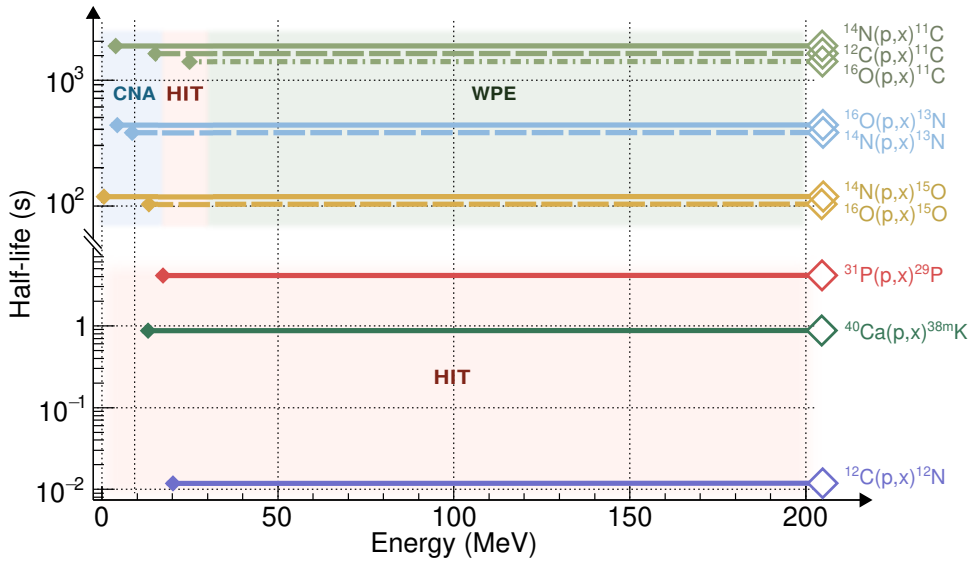

FIGURE 2.21: Schematic representation of the objectives of this thesis: Measuring the production cross sections of the long-lived β^+ emitters (~min) ^{11}C, ^{13}N, ^{15}O in C, N and O, and the short-lived β^+ emitters (~ms-s) ^{12}N in C, ^{38m}K in Ca, ^{29}P in P, in the full energy range of interest in proton therapy (from threshold, indicated as ◆, up to 200 MeV). The background colours indicate the accelerator-based facility in which energy range of each reaction is measured.

section values of interest in PET range verification from threshold up to 200 MeV, and a preliminary study of their impact in the accuracy of the corresponding Monte Carlo simulations. As illustrated in Figure 2.21, a total of 11 reaction cross sections have been measured: the proton-induced reactions for the long-lived isotopes ^{12}C(p,x)^{11}C, ^{12}C(p,x)^{13}N, ^{14}N(p,x)^{11}C, ^{14}N(p,x)^{13}N, ^{14}N(p,x)^{15}O, ^{16}O(p,x)^{11}C, ^{16}O(p,x)^{13}N and ^{16}O(p,x)^{15}O, and the proton-induced reactions for the short-lived isotopes ^{12}C(p,x)^{12}N, ^{40}Ca(p,x)^{38m}K and ^{31}P(p,x)^{29}P.

In this manuscript, a description of the experiments, analyses and results is presented. The experimental measurements have been performed at the National Center of Accelerators (CNA, Spain), the West German Proton Therapy Center (WPE, Germany) and the Heidelberg Ion-Beam Therapy Center (HIT, Germany), using three different detection systems (PET scanners, NaI and $LaBr_3$ detectors). Furthermore, the point-wise cross sections have been used to define an analytical curve that reproduces them accurately and can be used for PET range verification calculations and serve as starting point in forthcoming evaluations. In order to assess the impact of these new cross sections, in some cases measured for the first time, they have been used to study the production profiles of each isotope in tissue-equivalent phantoms and compared with the ones calculated with the previous cross section data and evaluations.

Chapter 3

Cross sections measurements: principles, tools and strategies

This chapter introduces the concept of cross section and presents the activation method to measure the proton-induced reaction cross sections of β^+ emitters. It introduces the different proton facilities where experiments have been performed, detection systems and applied techniques, with special emphasis on the validation strategies used in this work.

NUCLEAR REACTION [117] refers to the change in the identity or characteristics of an atomic nucleus, induced by bombarding it with an energetic particle, which, if positively charged, must have enough energy to approach the positively charged nucleus to within range of the strong nuclear force.

3.1 Introduction to cross section measurements

This section introduces the basic concepts of nuclear reactions and defines the relevant terms related to the cross sections and integral yields measurements. The nuclear activation technique is also described.

3.1.1 Nuclear reactions

A typical nuclear reaction is denoted as:

$$a + A \rightarrow b + B, \tag{3.1}$$

where a is the accelerated projectile, A is the target, and B and b are the reaction products. Usually, B is a heavy product, while a and b are nucleons or light nuclei. An alternative and compact way of expressing the reaction is:

$$A(a,b)B, \tag{3.2}$$

which is convenient since it provides a natural way to refer to a general class of reactions with common properties, for instance, (p,n) or (n,γ) reactions.

In this work, different approaches are applied to experimentally determine the proton-induced reactions of interest in PET range verification, where A stands for the target nucleus in the initial state (carbon, nitrogen, oxygen, phosphorus, calcium), a stands for protons, and b and B stand for the ejectiles and target residual in the final state, respectively. In this work, the target residual would be the radioisotope decaying by β^+ emission.

For instance, as shown in Figure 3.1, the proton-induced reaction on a ^{12}C target nucleus produces the β^+ emitter ^{11}C, together with either a secondary proton and neutron or a deuteron. If the projectile, target and products are all well-known, the cross section for this specific channel is called *exclusive* cross section. In this example, they will be denoted as ^{12}C(p,pn)^{11}C or ^{12}C(p,d)^{11}C, respectively. Typically, only a part of the final state is measured in experiments because this considerably reduces the complexity of the experimental setup. Therefore, if one is looking just at the ^{11}C product, the corresponding reaction would be called ^{12}C(p,x)^{11}C, where the unidentified parts are denoted with x. The cross sections obtained in such experiments are called *inclusive* cross sections or *production* cross sections.

The conservation law of the total relativistic energy in a nuclear reaction leads to:

$$m_a c^2 + T_a + m_A c^2 + T_A = m_b c^2 + T_b + m_B c^2 + T_B, \tag{3.3}$$

where T stands for the kinetic energy and m stands for the mass at rest. The *reaction Q-value* is defined as the difference between the initial and final mass energies:

$$Q = (m_{initial} - m_{final})c^2 = (m_a + m_A - m_b - m_B)c^2, \tag{3.4}$$

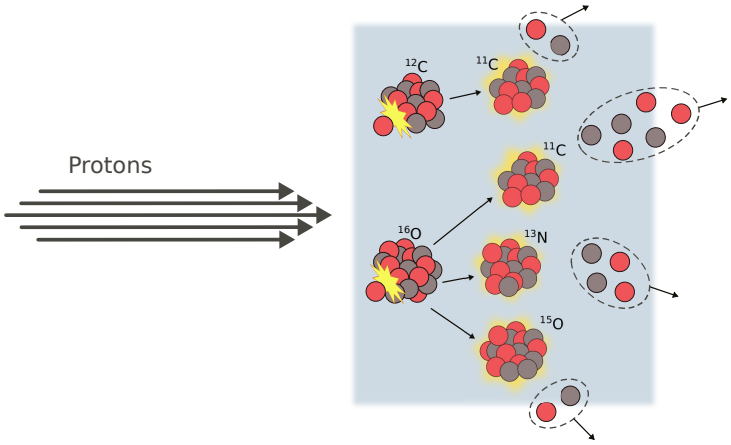

FIGURE 3.1: Schematic illustration of a proton beam impinging in a foil containing C and O atoms. The reaction products of the nuclear reactions are β^+ emitters (^{11}C, ^{13}N or ^{15}O), and nucleons, which can be emitted individually and/or forming light nuclei, such as α particles or deuterons.

The kinetic energy of the final products ($T_b + T_B$) depends on the the initial kinetic energies ($T_a + T_A$) and this Q-value, as:

$$T_b + T_B = T_a + T_A + Q. \tag{3.5}$$

The Q-value may be positive, negative, or zero. If $Q > 0$, the reaction is called exothermic. In that case, nuclear mass or binding energy is released as kinetic energy of the final products. When $Q < 0$, the reaction is endothermic, and the initial kinetic energy is converted into nuclear mass or binding energy. In this case, the *threshold energy* is defined as the absolute minimum energy value of T_a, and below this value the reaction is not possible. From Equations 3.4 and 3.5, the threshold can be calculated as:

$$T_{th} = -Q\frac{m_b + m_B}{m_b + m_B - m_a}. \tag{3.6}$$

3.1.2 Measuring reaction cross sections

The *cross section* (σ) is a physical quantity that describes the interaction probability for a given process of a particle with a specific nucleus, and represents the area that the target nucleus presents to the projectile in order to produce such process. Cross sections in nuclear and particle physics are typically given in units of *barn* (1 b = 10^{-28} m^2), which corresponds to the approximate order of magnitude of the cross-sectional area of the atomic nucleus.

Figure 3.2 illustrates the different interaction mechanisms (a, b, c) of a proton beam impinging on a thin foil, which are described in Section 2.1.1. Focusing on the interaction with atomic nuclei, two processes can occur: elastic scattering and nuclear reactions.

The total cross section σ_T encompasses the different specific processes that may occur when a particle interacts with a given nucleus and is defined as:

$$\sigma_T = \sigma_{el} + \sigma_R, \tag{3.7}$$

where the partial cross sections σ_{el} is the elastic cross section for the elastic scattering of the projectile with the target nucleus (interaction (b) in Figure 3.2) and σ_R is the reaction cross section for inelastic nuclear reactions (interaction (c) in Figure 3.2). The partial cross section for the different reaction channels changes drastically for different reaction channels and depends strongly on the proton kinetic energy, due to the sensitivity to the structure of the involved nuclei. The reaction cross sections

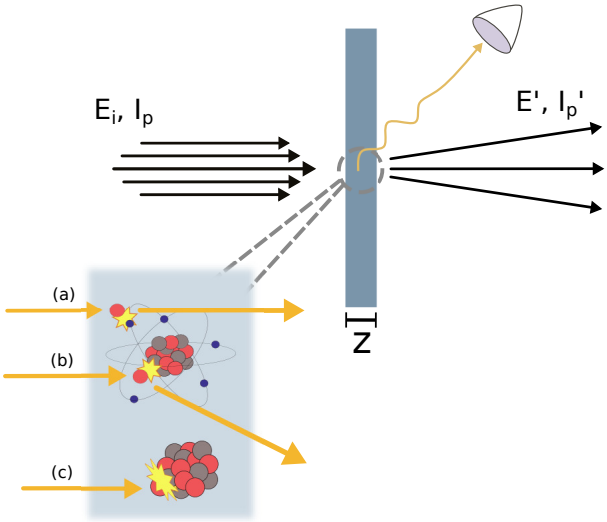

FIGURE 3.2: Schematic illustration of a proton beam impinging in a thin foil and interaction mechanisms: energy loss ($E_i - E^{'}$) via inelastic Coulombic interactions (a), deflection of protons trajectory by the screened Coulomb and nuclear elastic scattering with nuclei (b), removal of primary protons and creation of secondary particles via non-elastic nuclear interaction (c).

as a function of the projectile energy, also known as *excitation functions*, are of great interest for multiple applications such as fission, fusion, radiation therapy, medical diagnostic, waste management, radiation safety, etc.

Besides that, another quantity of interest in such applications is the *integral cross section* or *thick target yield*, which is obtained as:

$$Y = \int I(x) \cdot \rho \cdot \sigma dx = \int_0^L I(x) \cdot \sigma \left[\frac{1}{\rho} \frac{dE}{dx} \right]^{-1} dE. \tag{3.8}$$

Considering a constant flux in function of the depth, the thick target yield can be calculated by integration of the cross section divided by the stopping power from zero up to the corresponding energy:

$$Y = I_0 \int_{E_0}^{0} \frac{\sigma(E)}{S(E)} dE. \tag{3.9}$$

The nuclear cross sections can be predicted with models or measured in laboratories. The cross section evaluations, already introduced in Section 2.3.3.4, are the result of the combined analysis of theoretical predictions, models and the (necessarily) limited set of available experimental data in an attempt to produce point-wise nuclear data as accurate as possible covering the full energy range of interest and including all the partial cross sections.

Indeed, most of the current theoretical models divide the reaction process depending on the time scale of the interaction within the nucleus and incident particle [118–120]. We concentrate in the reaction mechanisms of interest in the energy range of proton therapy (up to about 250 MeV).

- At the highest energies (approximately above 150 MeV), when the wavelength is comparable to intra-nucleon distances, the projectile "sees" the target nucleons individually and the reaction is modeled by the cascade models, describing it as a series of binary collisions of the projectile with target nucleons which lead to a sequence of particle emissions.

- At lower energies of the projectile (or when the excitation energy of the nuclear system falls below a certain threshold if it comes from the cascade stage), the pre-equilibrium mechanism takes

over. Pre-equilibrium reactions are the doorway to the equilibrium stage (compound nucleus) where the energy imparted by the projectile is partially shared by the target nucleons. During this phase the nuclear system evolves towards equilibrium (namely: the excitation energy is increasingly shared by the nuclear degrees of freedom) through a series of internal transitions which compete with nucleon or light cluster emissions, which in turn may take place when they gather enough energy.

- At the lowest energies of the projectile (or when the excited nuclear system reaches the thermal equilibrium if it comes from the pre-equilibrium stage) the compound nucleus mechanism is the responsible of the final deexcitation of the nuclear system via particle emissions (nucleons, light clusters and even intermediate mass fragments), photon evaporation, statistical fragmentation, break-up and, eventually, fission.

The previous reaction mechanisms are the ones included in the software tools for Monte Carlo simulations of radiation transport. They are the main contributors to the nuclear interactions between the beam and the nuclei of the target materials and, moreover, provide probability distributions suitable for their implementation in the codes. On the other hand, the direct reactions (transfer of nucleons and surface excitations) take place in approximately the same range of incident energies as the pre-equilibrium reactions, but play minor role in the global description since only a small number of target nucleons intervene (hence they also called "grazing" collisions). Moreover, while the pre-equilibrium and equilibrium mechanisms can be described by relatively simple statistical models, the direct reactions ask for a strict quantum mechanical treatment by solving the Shroedinger equation with nuclear structure information via the interaction potential and form factors. Accordingly, although the direct reaction mechanisms are fundamental for studies of nuclear physics, they are omitted for simulations of radiation transport.

The timescales of the various reaction mechanisms are very different. Whereas the tipical times of direct reactions, due to their "grazing" nature, are of the order of the passage through the nuclear region (10^{-21} s), pre-equilibrium and, mainly, equilibrium stages take longer, since the imply thermalization among the nuclear degrees of freedom (10^{-18}-10^{-15} s typically).

In experimental nuclear physics, the cross sections of reactions that, as in our case, result in radioactive nuclei, are often measured using the activation technique of very thin foils, which are referred to as a target where the energy loss is negligible with respect to the projectile energy itself and the reduction in the number of incident particles as they pass through the foil is negligible.

As schematized in Figure 3.1 and 3.2, this method considers the projectiles as point particles with incident beam intensity I_p (particles per unit of time), impinging on a very thin target of a given isotope with areal density of target nuclei n_s (nuclei per unit area). In this situation, one can detect the radiation emitted as a consequence of the decay of the radioactive nuclei to determine the nuclear reaction rate R (reactions per unit time) for a specific k-process. It must be proportional to the above-mentioned magnitudes, being the proportionality constant the reaction cross section:

$$R_k = \sigma_k \cdot I_p \cdot n_s, \tag{3.10}$$

where σ_k is the cross section for k-process, featuring units of *area*. Indeed, considering the classical point of view (the incident particles are point particles and the target nuclei are solid spheres), σ can be understood as the characteristic cross-sectional area, where a larger area means a larger probability of interaction.

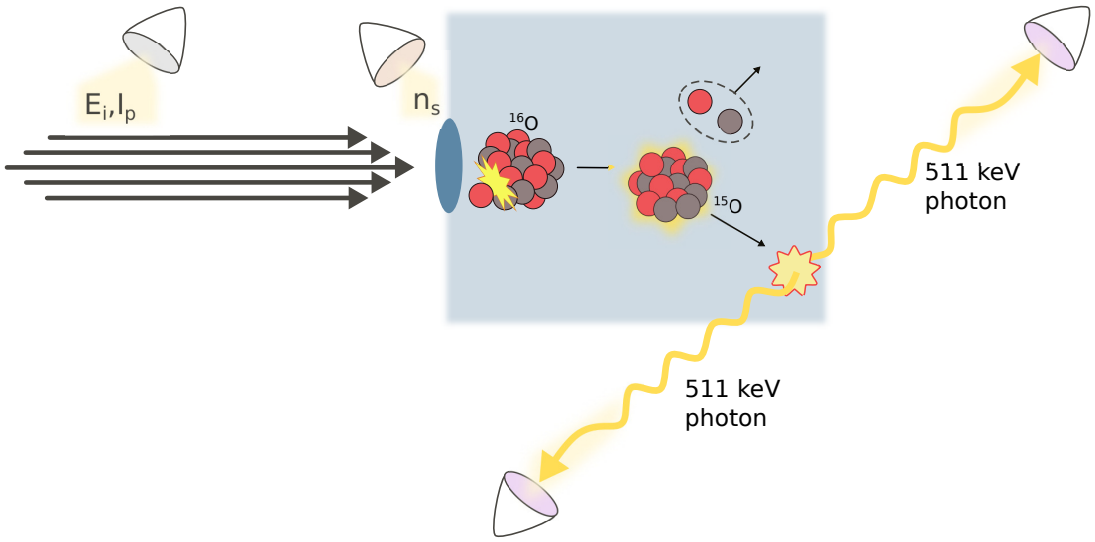

FIGURE 3.3: Schematic illustration of a proton beam impinging in a foil containing O atoms and producing ^{15}O. The magnitudes to determine the reaction cross sections are marked as "illuminated" by each schematic measuring device.

Therefore, experimentally the cross section can be determined as:

$$\sigma_k = \frac{R_k}{I_p \cdot n_s}, \tag{3.11}$$

which means that one needs to measure the reaction rate and the intensity of incident particles, and to ascertain the target composition and geometry. Considering that the cross section depends on the incident particle energy, the quantity of interest of PET range verification is the energy differential cross section, which means than both the reaction rate and the particle flux will have to be determined as function of the beam energy.

3.1.3 Observables in the reaction cross section measurements of β^+ emitters

As illustrated in Figure 3.3, the activation methodology to determine the excitation functions or energy differential cross section requires a mono-energetic proton beam, a thin sample as isotopically pure as possible, and an activity detection system. As explained in the previous section in Equation 3.11, the cross section are calculated by determining the following physical quantities:

- The number of nuclei per area (n_s) that the beam finds in its path through the thin foil, which is calculated as:

  $$n_s = \rho \cdot z \cdot N_A \frac{n_x}{M_m}, \tag{3.12}$$

  where ρ is the mass density of the foil, z is the foil's thickness, N_A is the Avogrado's number ($6.02214 \cdot 10^{23}$ molecules/mol), n_x is the number of target nuclei x in each molecule and M_m is the molecular mass.

- The flux of incident particles. The different techniques to measure the beam current during each irradiation are described in Section 3.2.

- The reaction rate, i.e., number of produced radioisotopes per second. The observable quantity in these measurements is the counting rate C_k, which, in this case, is the number of detected 511 keV photons using scintillator detectors.

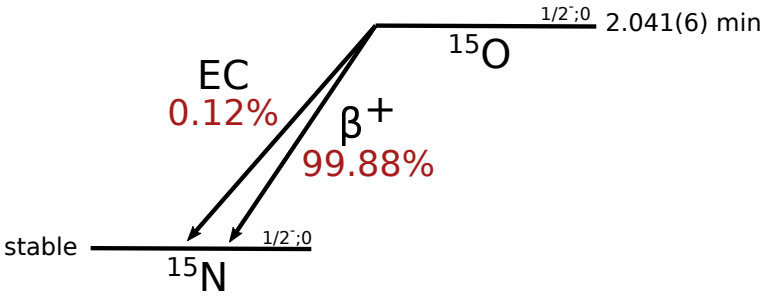

FIGURE 3.4: Simplified decay scheme of ^{15}O.

Taking into account the fundamental law of radioactivity, the activity A (in units of Bq = 1 disintegration per second) is expressed as the decay rate of a particular radionuclide with decay constant λ and the number of atoms N:

$$-\frac{dN}{dt} = \lambda \cdot N = A. \tag{3.13}$$

The decay constant, λ, is the reciprocal of the mean lifetime (τ), which is the average lifetime of a radioactive particle before decay. The half-life, $t_{1/2}$, is defined as the time taken for a given amount of a radioactive substance to decay to half of its initial value as $t_{1/2} = {}^{\ln 2}/_{\lambda}$.

Experimentally, the number of produced radioisotopes (N_k) can be calculated as ${}^{A_k}/_{\lambda}$. The induced activity is determined by measuring the counting rate (counts per unit of time, C_k) of 511 keV photons after the irradiation, but considering the detection efficiency of each specific detection system (ε_{det}) (see Section 3.3) and the probability intensity associated to each specific decay (I_l) (for instance, Figure 3.4 represents the decay diagram of ^{15}O, which can decay either by electron capture (0.12%) or β^+ emission (99.88%)).

Considering the number of produced radioisotopes as a function of the induced activity and integrating the number of incident particles during the entire length of the irradiation (C_{total}), the cross section at a specific beam energy can be expressed from Equation 3.11 as a function of the induced activity at the end of the irradiation:

$$\sigma_k(E_i) = \frac{N_k}{C_{total} \cdot n_s} = \frac{C_k}{\lambda \cdot \varepsilon_{det} \cdot I_l \cdot C_{total} \cdot n_s} = \frac{A_k}{\lambda \cdot C_{total} \cdot n_s}, \tag{3.14}$$

where the term:

$$y_k(E_i) = \frac{A_k}{\lambda \cdot C_{total}}, \tag{3.15}$$

is defined as thin-target yield at E_i. Fundamentally, the experiments performed in this thesis consisted on the irradiation of very thin samples with a well-known proton flux and the subsequent activity measurements to determine the reaction cross sections. In the following, the experimental setup in each irradiation facility and detection systems will be described.

3.2 Irradiation facilities

This section describes the irradiation facilities where the experiments have been carried out. Three accelerator-based facilities are presented: the National Centre of Accelerators in Seville (Spain), the West German Proton Therapy Centre in Essen (Germany) and the Heidelberg Ion-Beam Therapy Centre in Heidelberg (Germany). In the following, a brief description of the characteristic elements in each facility, irradiation lines and beam current measurements are presented.

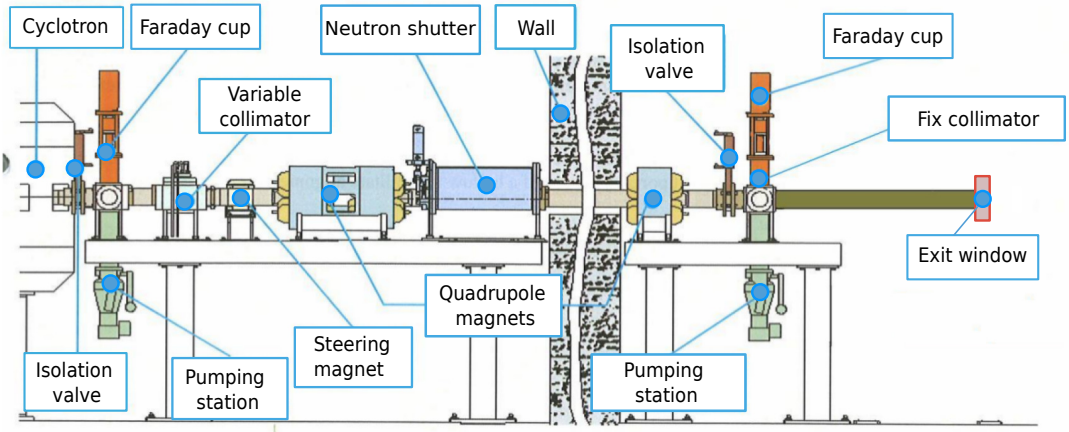

FIGURE 3.5: Schematic representation of the experimental beam line at CNA (not to scale).

3.2.1 National Centre of Accelerators

The National Centre of Accelerators ("Centro Nacional de Aceleradores", CNA) [121, 122] is a joint scientific research centre of the University of Seville, Regional Administration ("Junta de Andalucía") and National Council of Scientific Research ("Consejo Superior de Investigaciones Científicas", CSIC). It is denominated as a Spanish Unique Scientific-Technical Facility (ICTS), dedicated to interdisciplinary research and open to external users. It has six different installations: a Van de Graaff 3 MV tandem accelerator, a 18/9 MeV cyclotron accelerator, a 1 MV Cockcroft-Walton tandem accelerator used for mass spectrometry, a PET/CT scanner, a radiocarbon dating system, and a ^{60}Co irradiator.

The cyclotron *Cyclone 18/9* from the IBA company (Ion Beam Applications, Louvain La-Neuve, Belgium) accelerates protons and deuterons up to 18 and 9 MeV, respectively, with maximum beam intensities in the internal target ports of 80 μA for protons and 35 μA for deuterons. Seven out of the eight target ports are devoted to the production of PET radioisotopes used in diagnostic imaging, and the remaining port is employed for the transport of the beam to an external beam line for interdisciplinary research.

The external beam line of the cyclotron at CNA is sketched in Figure 3.5. The first part is inside the cyclotron vault and it includes a series of remote control permanent elements to monitor and to define the beam current and size. It has a retractable graphite Faraday cup (FC) to stop the beam and measure the beam current, a variable graphite slit with a maximum aperture of 15 x 15 mm, a XY set of magnetic steerers and a doublet quadrupole. Moreover, there is a neutron shutter to protect the downstream section of the unused beam line from radiations originated in the cyclotron vault. The second part is outside, separated from the other by a two-meters thick wall, and it is equipped with a single quadrupole, a 15 mm diameter collimator, a pumping station and another FC with a phosphor scintillator (ZnS:Ag) in order to see the size and shape of the beam by means of a video camera. Several nozzles with different sizes are available, where diverse materials windows can be adapted, and is possible to accommodate graphite collimators with various diameters.

As depicted in Figure 3.5, the 18 MeV proton beam produced by the cyclotron, proceeds horizontally to the experimental room. The end of the beam line was closed by a 125 μm thick Mylar window and the irradiations were performed in air. A target holder placed just after the exit window was specifically installed to place the thin foils in a motorized table, hence allowing the remote control and minimizing the time between consecutive irradiations. The beam current during the irradiation is monitored using a Brookhaven 1000c Current Integrator. An electrically isolated 2 mm thick graphite

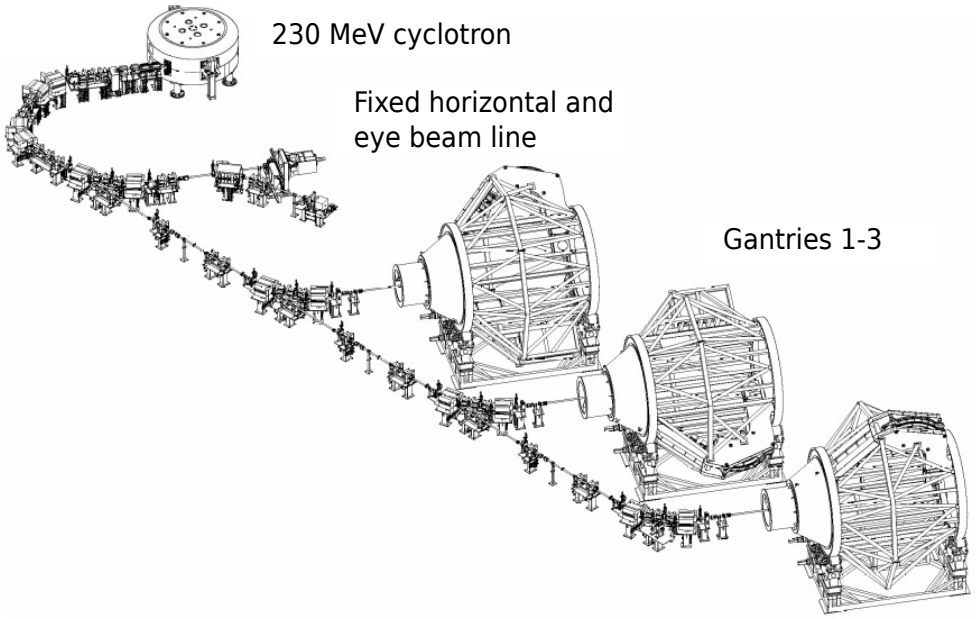

FIGURE 3.6: Schematic representation of the WPE facility.

foil, which was placed after the target foils during the experiments, was used as beam dump and connected to the current integrator. The total charge is calculated considering the secondary electron losses (of about 10%) in graphite characterized in a previous work by biasing a graphite target into a vacuum chamber. The model 1000c Current Integrator accepts pulsed or continuous currents ranging from a small fraction of a nanoampere to 20 milliamperes. It provides a series of digital output pulses proportional to the accumulated quantity of charge. A digitizing rate of 1000 pulses per second is achieved at full-scale input current and an external connector makes the digital pulses available for external counting by a computer [123]. In the experiments carried out in this work, the beam current was calibrated using a standard reaction from the International Atomic Energy Agency (IAEA), as described later in Section 3.4.3.2.

3.2.2 West German Proton Therapy Centre

The West German Proton Therapy Centre ("Westdeutsches Protonentherapiezentrum Essen", WPE) [124] is one of the leading institutions for proton radiotherapy in Germany, which is specialised in sensitive or deeply-located tumours and, specifically, in paediatric tumours. The WPE is an affiliate centre of the University Hospital Essen and works closely with neighboring hospitals and institutes, being part of one of the largest oncological centres in Germany (Westdeutsche Tumorzentrum, WTZ).

The cyclotron at the WPE is a 230 MeV isochronous cyclotron from IBA, implemented in a Proteus Plus system with four treatment rooms and five clinical beam lines. Three treatment rooms are equipped with a gantry which can be rotated 360° around the patient. The fixed-beam treatment room features a conventional beam line, comparable to the beam lines in the gantry treatment rooms but fixed to a horizontal beam direction, and a dedicated beam line for eye treatment which features a special treatment mode with high dose rates and low ranges. A sketch of the facility is shown in Figure 3.6.

The degrader system mounted at the cyclotron exit delivers proton energies between 100 MeV and 226.7 MeV, which correspond to R80 (see Section 2.1.1.4 for definition) of 7.7 cm and 32 cm in water, respectively. This system consists on a wheel-mounted wedge followed by analyzing magnets and energy slits. Lower residual range for patient treatment can be achieved with PMMA range shifter (RS)

mounted on the nozzle exit [125]. For the different treatment rooms, two or three RS with defined water-equivalent thicknesses can be used for treatment with PBS delivery mode.

The experiments were performed in the horizontal fixed beam line, which can operate in PBS mode. As previously mentioned in Section 2.2.2.2, the PBS has the advantage of less production of secondary particles, like neutrons, which results in more accurate results for the measurement of activation cross sections due to the delivery of quasi mono-energetic proton beams. Furthermore, PBS treatment fields can be implemented more easily in Monte Carlo simulations when compared to passively scattered treatment fields. An additional advantage is that the beam can be deflected by dipole magnets in order to select the desired lateral position on a time scale in the order of milliseconds.

The beam line is also equipped with an ionization chamber placed at the nozzle entrance to check the centering of the beam, and two monitor chambers placed close to the nozzle exit to check the spot position and width. The number of protons per dose were determined prior to the presented studies in Ref. [126] modifying a Faraday cup (FC) from Ref. [127] and considering the impact of nonelastic hadronic interactions in the FC on the fluence of charged particles by means of Monte Carlo simulations. Since then, the stability and consistency of the dose measurement was verified in the frame of periodical quality assurance (QA) for clinical operation. The number of protons for each field was determined with an accuracy of about 1%, and it is internally measured in so-called monitor units (MU).

3.2.3 Heidelberg Ion-Beam Therapy Centre

The Heidelberg Ion-Beam Therapy Centre ("Heidelberger Ionenstrahl-Therapiezentrum", HIT) [128] was the first European hospital-based facility for proton and heavy ion radiotherapy, which started its operation in 2009 and utilizes scanned ion beams for the irradiation of tumours. HIT is linked to the National Center for Tumor Diseases (NCT), which is a joint institution of the German Cancer Research Center (DKFZ), the Heidelberg University Hospital (UKHD) and the German Cancer Aid (DKH). In addition, it is the first facility to use cooperating robots for automated imaging and ultrahigh-precision patient positioning and the first heavy ion therapy facility with a 360° rotating beam delivery system. Therefore, the state-of-the-art and most innovative treatment methods are available at HIT for most cancer types, being a leading oncological center in the world [129].

HIT is a synchrotron-based particle therapy center with two horizontal fixed-beam rooms, a gantry that can rotate 360° around the patient and an experimental fixed-beam room for technical and scientific research. A sketch of the facility is shown in Figure 3.7. Three ion sources provide several ion types in parallel, which are first pre-accelerated by a two-stage linac up to ~7 MeV/u, and then injected into the synchrotron, where six 60° magnets bend the particles into a circular path and the RF system accelerates them to the desired energy. At HIT, both carbon ions and protons are currently used for therapy, while helium and oxygen ions are used for experiments. The beam spot size is adjusted by quadrupole magnets close to the patient, with typical FWHM at the isocentre of 4 to 30 mm. In order to reach penetration depths of 2 to 30 cm in human tissue, the particles can be accelerated in the synchrotron to 255 different energy levels from 48 up to 221 MeV/u for protons and from 88 up to 430 MeV/u for carbon ions. The beam delivery system at HIT allows to irradiate tumours using IMPT. Typical intensities at HIT are $2 \cdot 10^6$ to $1 \cdot 10^8$ and $8 \cdot 10^7$ to $4 \cdot 10^9$ particles per second (pps) for carbon and protons, respectively. Including the different gantry-angles, more than 10^5 combinations of beam parameters are available [130].

After the extraction, the beam is sent to one of the rooms and then passed through a monitoring system (so-called BAMS), which consists of three ionization chambers (ICs) and two multi-wire proportional chambers (MWPCs) in the beam line before the exit window with the goal of monitoring

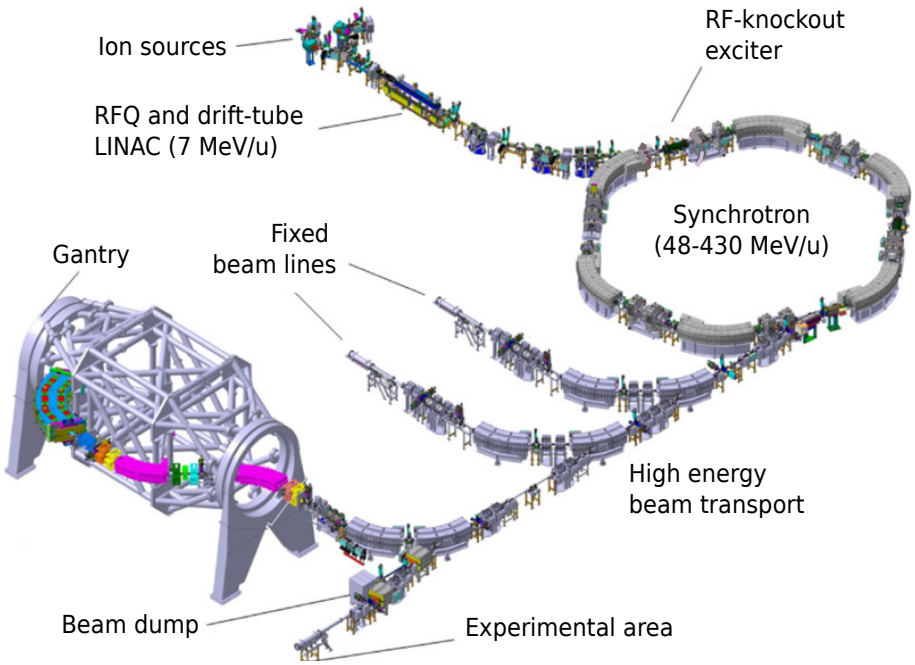

FIGURE 3.7: Schematic representation of the HIT facility.

the beam position, width and intensity [130–132]. The experiments described in this thesis were performed in the experimental room, which is also equipped with the BAMS system. The beam current is measured with an IC placed at the nozzle before the exit window. The number of protons I_{beam} is determined from the secondary current I_{sec} measured with the IC as [133]:

$$I_{beam} = \left(\frac{dE}{dx}\right)^{-1} \cdot \frac{W_{Ar}}{L_{chamber}} \cdot I_{sec}, \tag{3.16}$$

where the active length of the BAMS-IC ($L_{chamber}$) is 2 cm, the W-value of Argon is 26 eV and $\frac{dE}{dx}$ is the energy loss according to the Bethe-Bloch-formula (Equation 2.1) in the target material of the IC (mainly Ar).

3.3 Detection and acquisition systems

This section describes the systems employed for measuring the 511 keV photons following the decay of the β^+ emitters: a commercial PET/CT scanner typically used for clinical diagnostic, and scintillator detectors commonly used in nuclear physics experiments.

Both detection systems consist of scintillation detectors. The γ-rays can interact with the detector material by means of photoelectric effect, Compton scattering or pair production. In the photoelectric process, the γ-ray interacts with an electron of an atom, vanishing and giving all its energy to the electron, which escapes. In Compton interactions, the incoming γ-ray is undergoes elastic scattering with an electron from the outer shells of an atom. In the process, the γ-ray can be scattered to any angle and the fraction of its energy transferred to the electron will depend on that specific angle, following the laws of conservation of energy and momentum. Finally, the process of pair production is energetically possible when the γ-ray energy exceeds twice the rest-mass energy of an electron (1.022 MeV). In this interaction, which takes place in the Coulomb field of a nucleus in order to conserve the linear momentum, the photon disappears and is replaced by an electron-positron pair.

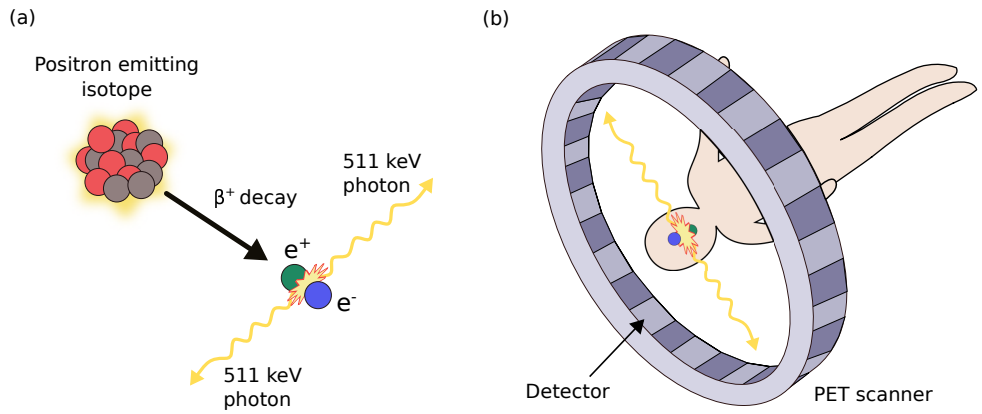

FIGURE 3.8: Schematic representation of (a) the emission of 511 keV photons in the annihilation of a positron produced in the β^+ decay of a radionuclide, and (b) PET scanner (multiples scintillator detectors forming a ring) detecting pairs of 511 keV photons emitted in coincidence.

Photoelectric absorption predominates for low-energy γ-rays (up to a few hundred keV), pair production predominates for high energy photons (above 5-10 MeV), and Compton scattering is the most probable process over the intermediate range of energies. In each case, the resulting electron, so-called fast electron, interacts with the atoms of the scintillator, producing multiple excitations and consecutive de-excitations, emitting photons in the visible (or near-visible) light range. The number of photons produced is proportional to the energy deposited by the initial photon, i.e. carried by the fast electron. The light pulses are collected by a photocathode. Electrons, emitted from the photocathode by photoelectric absorption, are accelerated by the applied high voltage and amplified at the dynodes of the attached photomultiplier tube (PMT), resulting in an electric pulse proportional to the absorbed energy.

3.3.1 PET/CT scanners

3.3.1.1 Principles of PET/CT scanners

Positron Emission Tomography – Computed Tomography (PET/CT) is a nuclear medicine technique that combines, in a single equipment, a positron emission tomography scanner and an X-ray computed tomography (CT) scanner. It acquires sequential images from both devices in the same session, and combines them into a single superposed image. Thus, functional imaging obtained by PET, which depicts the spatial distribution of metabolic or biochemical activity in the body, can be more precisely aligned with the anatomic image obtained by CT scanning.

The PET system (see Figure 3.8) consists on multiples scintillator detectors forming a ring in order to detect pairs of 511 keV photons emitted in coincidence, following the annihilation of a positron produced in the β^+ decay of a radionuclide. These detectors are made of inorganic scintillation materials with a very high effective atomic number and a high density, thus making them detectors with a high detection efficiency. For instance, the ones used in this work are made of Lutetium Oxyorthosilicate (LSO).

The fact that, depending on their spatial origin, the γ-rays have to traverse different amounts of material before reaching the detectors is accounted for by an "attenuation" correction that the systems applies to the acquired image considering the information from the CT scanner. As a result, the tomographic reconstruction of the detected photons in coincidence provides a 3D activity map. This

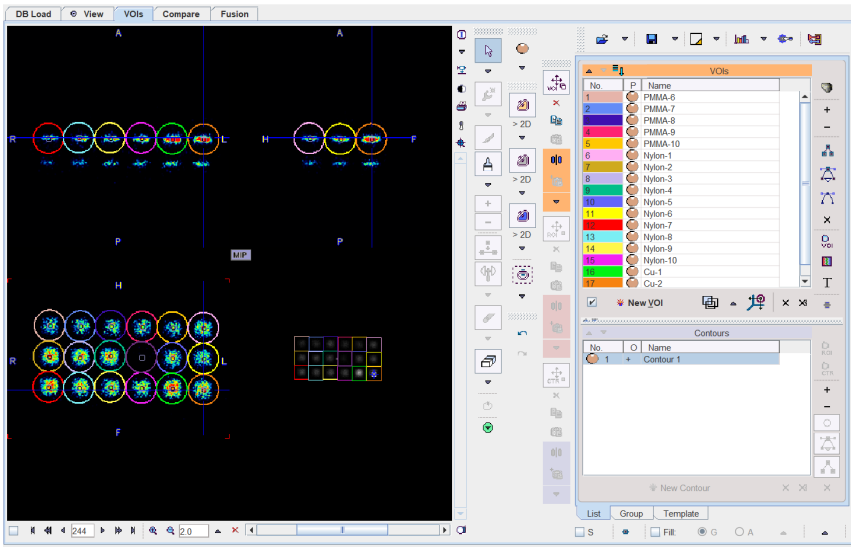

FIGURE 3.9: View of PMOD interface for imaging processing.

can be achieved using a numerical reconstruction algorithm, such as True X [134] or iterative [135] protocol, with or without the time of flight (ToF) algorithm.

PET/CT scanners have been conventionally used and manufactured for diagnostic applications. In these kind of applications, the radionuclide, known as tracer, is introduced into the body on a biologically active molecule, such as fludeoxyglucose (FDG), and the imaged concentration of the tracer indicates where the glucose has been uptaken by the tumor cells. However, as referred in Section 2.3.3, these clinical devices can be also employed to monitor the dose delivered to the patient in a proton therapy treatment. Nevertheless, in this work, PET/CT scanners are devoted to measure the activity induced by nuclear activation, serving as an innovative detection system, not-previously used in common nuclear physics experiments. While in conventional applications the PET scanner is operated in a static mode (accumulating signals during a specific time), in this novel application the PET scanner is operated in dynamic mode, recording 60 s-interval acquisitions during several hours in order to follow the decay in time of the different β^+ emitters produced by the beam in the human body, which feature different half-lives.

Imaging analysis

PMOD (v.4.203, 2020) [136] is a software environment developed exclusively for imaging research. It provides the required infrastructure to import DICOM (Digital Imaging and Communications in Medicine) images [137] from the PET scanner, which have been previously corrected by the PET/CT Siemens software using the gamma attenuation information from the CT images. The Image Processing and VOI Analysis Tool (PBAS) allows the viewing, processing and quantitative analysis of the reconstructed images. The volumes of interest (VOI) functionality enables the creation of specific volumes of different shapes and size to extract quantitative information from the image inside each VOI.

Figure 3.9 shows the software interface, with the corresponding PET image and defined VOIs. Defining the corresponding VOI for each foil, it is possible to quantify the induced activity by the activation of each foil (explained later in Section 3.4.1). The output of the PMOD software is the number of counts per second ("propcps") as a function of time (thanks to the dynamic PET acquisition mode), which was converted into activity by measuring a calibrated β^+ ^{22}Na source together with the activated foils.

TABLE 3.1: Technical specifications of Biograph Vision and Biograph mCT. Data taken from [139].

	Vision	mCT
Crystals	LSO, 3.2×3.2×20 mm	LSO, 4.0×4.0×20 mm
Detector elements	Silicon photomultipliers	Photomultiplier tubes
Axial FoV	26.1 cm	22.1 cm
ToF timing resolution	210–215 ps	540 ps
Transverse spatial resolution (measured at 1 cm vertically from the centre of the FoV with ^{18}F)	3.7 mm (FWHM)	4.4 mm (FWHM)
Sensitivity (according to NEMA NU-2 2012)	16.4 kcps/MBq	10.0 kcps/MBq
Time coincidence window	4.7 ns	4.1 ns
Energy window	435–585 keV	435–650 keV
Bed overlap	49%	43%

3.3.1.2 PET/CT scanners at CNA and WPE

Both PET scanners are provided by Siemens Healthineers. The technical specifications of both PET scanners are listed in Table 3.1. The system at CNA is a Siemens Biograph mCT PET scanner with a 221 mm axial field of view, coupled to a CT scanner, that allows to obtain 64-slices images. The PET scanner is made of 144 LSO scintillator with 4 photomultiplier tubes each and looks for γ-rays depositing energy between 435 and 650 keV within a time window of 4.1 ns [121].

The system at WPE is a Siemens Healthineers - Biograph Vision PET/CT scanner from the Nuclear Medicine department of the University Hospital Essen, but located at the same building than the WPE. This scanner is made of 3.2x3.2x20 mm^3 LSO crystals and silicon photomultiplier (SiPMs) providing a time resolution of just 214 ps and a higher spatial resolution than the previous one [138].

Since the radioactive isotope ^{176}Lu, with $t_{1/2}$=3.78·10^{10} years, amounts to a 2.6% of the natural lutetium present in LSO detectors, there is an intrinsic background in PET images due to the decay by β^- emission and the three γ-rays of 88, 202 and 307 keV. As both scanners at CNA and WPE are made of the same scintillator material and provided by Siemens, they have similar characteristics in terms of the intrinsic radioactivity, reconstruction protocols and FoV.

3.3.1.3 Efficiency calibration of the PET scanners

PET scanners for medical imaging do not require a very accurate efficiency calibration, neither in absolute value nor in its dependency with the position. Therefore, an spatial efficiency calibration of these devices is required for an absolute measurement of the induced activity and subsequent calculation of the reaction cross sections.

The strategies followed in each experimental facility to determine the scanner efficiency calibrations are limited by the available operating time and the resources to perform the experiments. In the following, the employed methodology, experiments and results for each facility are described.

PET/CT scanner at CNA

The characterization of the spatial efficiency and statistic uncertainty of the PET scanner was carried out using a calibrated ^{22}Na source. The calibration from "propcps" to activity units was achieved by measuring a 120.8(24) kBq ^{22}Na source, and comparing it against the obtained number of "propcps" within the corresponding VOI. The activity of this source was corrected by a 1.04 factor and its uncertainty reduced from 6% to 2%, as explained in Section 3.3.2.2.

The spatial efficiency map of the scanner was made by placing the source in different positions and recording static 1 min images. The source was placed at a total of 72 positions in a polyethylene (PE)

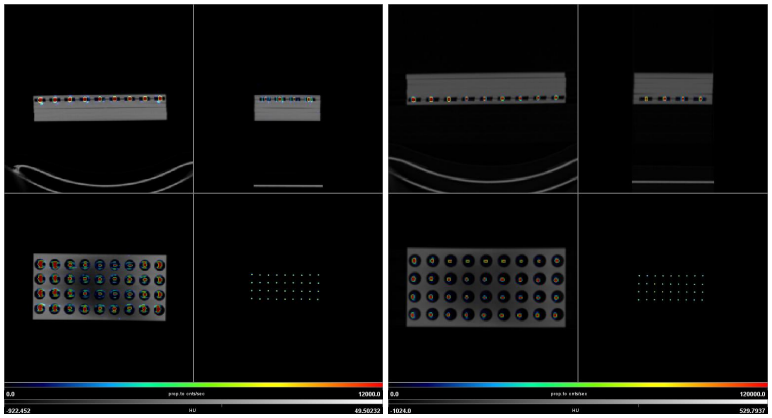

FIGURE 3.10: Axial, sagittal and coronal PET/CT image of the two planes of the polyethylene matrix with the ^{22}Na source in their corresponding positions.

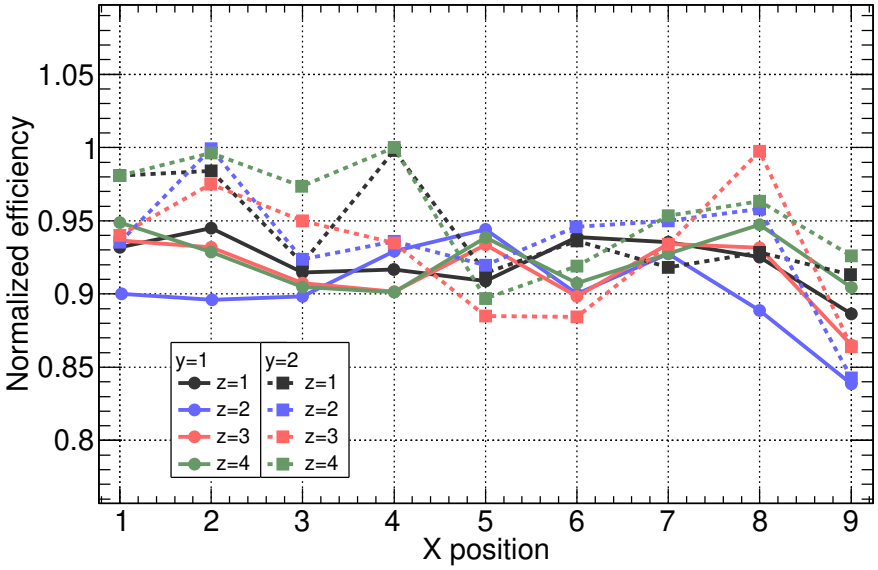

FIGURE 3.11: Spatial calibration efficiency of PET/CT scanner at CNA.

matrix (9x4 holes inside the PE matrix, in two different planes), serving as converter of the emitted positron, in order to cover the full field of view (FoV). This PE matrix is also used during the measurement of the irradiated foils because the range of the positrons of interest in this work, emitted by ^{11}C, ^{13}N and ^{15}O, is of 5, 6 and 9 mm in PE, respectively, compared to more than 8 m in air for the lowest end-point energy isotope (0.960 MeV, in the case of ^{11}C). Figure 3.10 shows the superimposed PET/CT images of the calibrated source inside the holes in the PE matrix. The results, depicted in Figure 3.11, show variations in the order of 5-10%, being fairly constant at the center of the scanner FoV.

Besides that, the possible statistical variations were assessed by measuring two different ^{22}Na sources of ~120 and ~800 kBq during 2 and 10 minutes, then covering the range of activity reached during the experiments of the production cross sections. The results of the static PET images show that 2 minutes acquisitions provide a 1% statistical variation, while 10 minutes acquisitions reduce the variation to 0.5%, for both ^{22}Na sources. In this regard, a 4% statistical variations in the determination of the number of counts is considered for the dynamic 1 minute measurements to determine the production cross sections.

In conclusion, the detection efficiency and uncertainty during the experiments at CNA were considered as follows:

- The number of "propcps" are converted to activity units by measuring a calibrated ^{22}Na source, embedded in the PE matrix together with the rest of the irradiated foils.
- The measured activity in each foil is divided by the detection efficiency at that (x,y,z) position (as displayed in Figure 3.11) to take into account the significant variations in the 3D spatial efficiency map of the PET scanner.
- The resulting uncertainty in the PET scanner efficiency is affected by the uncertainty in the calibration source (2%) and the statistical uncertainty (estimated as 4%), giving a 4.5% overall uncertainty.

PET/CT scanner at WPE

The available time at WPE was more limited than that at CNA, so it was not possible to measure a β^+ source in each position. However, fortunately, it was possible to produce an extensive β^+ source. Therefore, the spatial calibration efficiency map was assessed by measuring this extensive source, instead of measuring the point-like source in each position. The spatial efficiency of the scanner is assessed as follows.

First, a calibrated 1.70(3) kBq ^{22}Na source was placed at 5 different positions and static PET images were taken in intervals of 1 and 15 minutes, to check the reproducibility of the measurements. The shorter exposure of 1 minute resulted in values in agreement within 3.3%, a reproducibility that improved down to 0.7% for the 15 minutes exposures.

Then, two 150x30x1 mm^3 graphite sheets were activated with a 150 MeV proton beam to produce a homogeneous ^{11}C source via (p,x) reactions, as shown in Figure 3.12 (left). The broad beam, obtained by scattering in a degrader, covered the large area of the sheets with an accuracy of 1.5% in the number of delivered protons [140]. Following the irradiation, these two graphite sheets were placed into two different planes of the PET scanner (see 3.12, right) inside a PE matrix, where the conversion of the positrons into two 511 keV photons emitted in opposite directions takes place. Then, dynamic PET images of 1 minute interval during 30 minutes and static images of 3 minutes were taken. The 3 minutes images were reconstructed using two different protocols: iterative and True X, both with ToF algorithms. The analysis was performed selecting as VOIs the same used later for the experiment (described later in Section 4.1) and avoiding the edges of the PE matrix to prevent border effects. The outcome from the 3 minutes images evidences that both reconstruction protocols provide the same result within 1%, thus in the following only True X with ToF is considered. The number of counts per second from the selected VOIs in the dynamic 30 minutes images were extracted as a function of the time and fitted to the decay of ^{11}C, with a half-life of 20.36 min. Using the known ^{22}Na source to calibrate from number of counts to activity, the estimated activity at the end of bombardment of the selected VOIs is, on average, 3.04 kBq, with a standard deviation of 4.4%.

Overall, the PET spatial efficiency is considered as constant and, since the activities produced in the irradiations to determine the cross sections are in the order of tens of kBq, with some of them of just a few kBq, a conservative value of 4% is chosen as spatial efficiency uncertainty.

In conclusion, the detection efficiency and uncertainty during the experiments at WPE were considered as follows:

- The results from the ^{22}Na source show that, in this case, the PET spatial efficiency can be considered practically constant, where the observed deviations are merely statistical, due to the limited

FIGURE 3.12: (Left) Irradiation of two graphite sheets. (Right) PET/CT measurement of the activated sheets inside the PE converter.

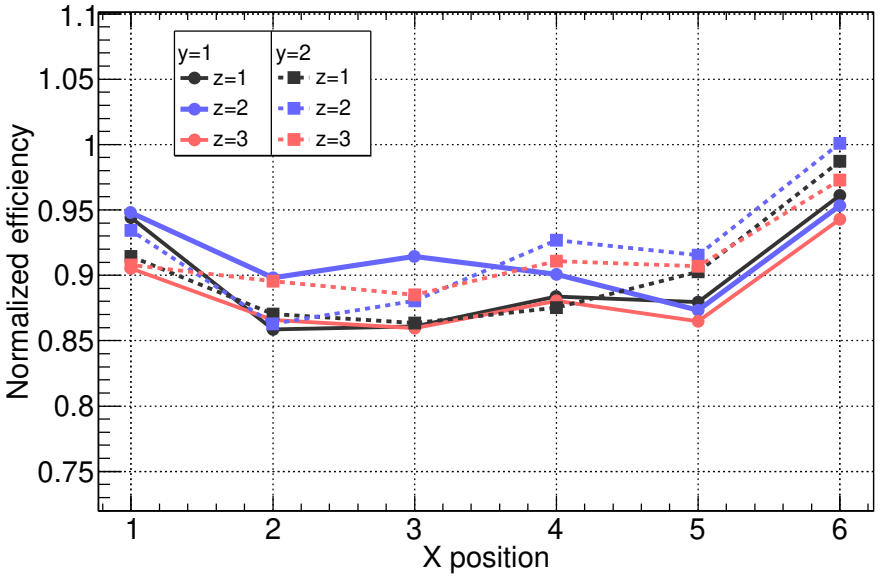

FIGURE 3.13: Relative induced activity at the end of bombardment for each specific VOI of the graphite sheets at WPE.

acquisition times and/or low activities. Furthermore, the outcome from the analysis of the activated graphite sheets confirms the mentioned homogeneity of the PET spacial efficiency, within the mentioned 4.4%. Therefore, the PET spatial efficiency map will be considered as constant.

- The absolute calibration from number of counts to activity is performed using a a calibrated ^{22}Na source, embedded in the PE matrix together with the rest of the irradiated foils.
- The mentioned 4.4% variation is consistent with the contributions from the statistic variations of 1 minute acquisitions (estimated as ~3% for a few kBq) and the 1.5% inhomogeneities of the irradiation field used to activate the graphite sheet. Therefore, since the activities produced in the irradiations to determine the cross sections are in the order of tens of kBq, with some of then of just a few kBq, a conservative value of 4% uncertainty is chosen in regard of the statistical variations.
- The resulting uncertainty in the PET scanner efficiency is affected by the uncertainty in the calibration source (1.7%) and the statistical uncertainty (estimated as 4%), giving a 4.4% overall

uncertainty.

3.3.2 $LaBr_3$(Ce) and NaI(Tl) detectors

During the experiments described in this work, two types of inorganic detectors have been used [141]:

- A 2" × 2" cylindrical sodium iodide crystals (NaI(Tl)) optically coupled to the photomultiplier tube (PMT). It was manufactured by Bicron Corp./Saint Gobain (model 2M2/2-X).
- A 1.5" × 1.5" lanthanum bromide crystals ($LaBr_3$(Ce)), coupled to the PMT. It was manufactured by Saint Gobain (model 38S38/1.5).

Both NaI and $LaBr_3$ crystals and PMTs are directly coupled to a Canberra 2007 or 2007P bases respectively, which contains a high-voltage divider network to supply the bias voltages for the PMTs. The Model 2007P includes a preamplifier, but it was not used in the experiments performed in this work. Our group owns two $LaBr_3$(Ce) detector and four NaI(Tl), so one type of detector or another is used as required by the experimental setup.

Since the radioactive isotope ^{138}La, with $t_{1/2}$=1.03·10^{11} years, amounts up to a 0.09% of the natural lanthanum present in $LaBr_3$ detectors, there is an intrinsic radioactivity due to its decay: a 788 keV γ-ray from β^- decay to stable ^{138}Ce, and 1435 keV γ-ray from β^+ and EC decay to stable ^{138}Ba. Furthermore, the radioisotope ^{227}Ac, with $t_{1/2}$=21.8 years, can be found in these detectors as a trace. This isotope, which occurs naturally as part of the ^{235}U decay series, is chemically very similar to lanthanum and is directly below it on the periodic table, which is why this contaminant is found in the scintillator. The ^{227}Ac's radioactivity is due to its decay chain to stable ^{207}Pb, which includes five α decays.

3.3.2.1 Data acquisition systems

The data acquisition systems (DAQ) employed during the experiments are CAEN Digitizers [142]. These systems are platform-independent instruments housing high speed multichannel Analog-to-Digital Converters (ADC) with local memory and Field-Programmable Gate Arrays (FPGA) for real-time data processing. This digital systems allow to acquire and process detector signals without additional electronic modules. Two types of CAEN Digitizers are used:

1. Model DT5730: It is a portable (15x16x5 cm) desktop digitizer that can be directly connected via USB to a PC. It has 8 channels, and features a 14 bits Flash ADC module sampling at 500 MS/s, which is well suited for mid-fast signals.
2. Model V1751: It consists on a VME 64X compliant connected to a PC via optical link. It has 8 channels and features a 10 bits Flash ADC sampling at 1 GS/s, which is well suited for fast signals.

Both models are compatible with the CAEN Multi-PArameter Spectroscopy Software (CoMPASS). CoMPASS software is a user-friendly interface to manage the acquisition. It allows an easy setting of the acquisition parameters and to display different plots and histograms at the same time. CoMPASS incorporates the ROOT Analysis Framework [143] and provides the possibility of saving the output files (lists waveforms and spectra) in the ROOT TTree for an easy post processing [144]. The detectors are connected directly to the inputs of the digitizer and the software returns the integral, time and Pulse Shape Discrimination (no needed to this experiment) of each signal, providing as well visualization of a selection of histogram during the data taking.

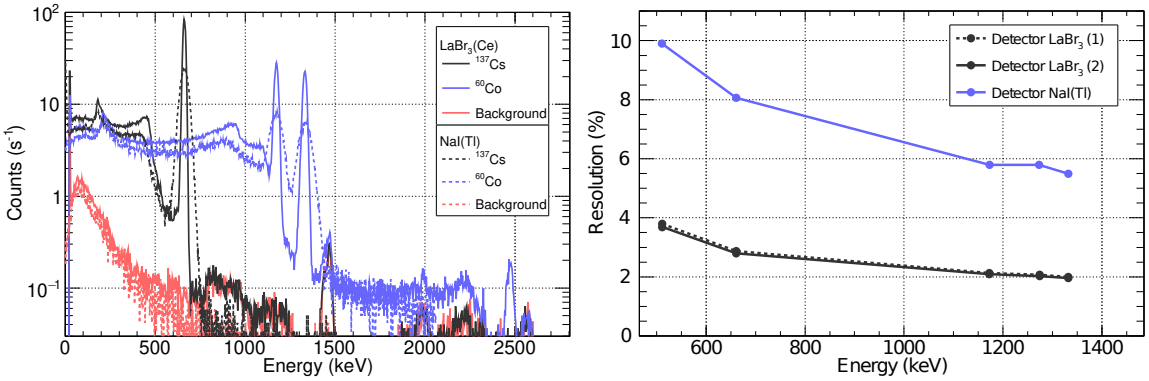

FIGURE 3.14: (Left) Energy spectrum taken with two types of scintillation crystals. (Right) Energy resolution for two $LaBr_3$ and a NaI crystals.

3.3.2.2 Energy resolution

The energy resolution of each detector is determined as [21]:

$$R = \frac{FWHM}{H_0}, \tag{3.17}$$

where *FWHM* is the FWHM of the photopeak and H_0 is the centroid of the photopeak due to photoelectric absorption. In order to characterize the energy resolution of the different detectors, γ-rays sources of ^{22}Na, ^{60}Co and ^{137}Cs have been measured. The corresponding photopeaks which can be observed in Figure 3.14 (left), have been fitted to a Gaussian distribution and the resolution has been calculated from the corresponding centroids and standard deviations, taking into consideration that:

$$FWHM = 2\sqrt{2\ln 2}\sigma. \tag{3.18}$$

The resolution of each detector as a function of the energy is displayed in Figure 3.14 (right), noticing the better energy resolution of the $LaBr_3$ crystal compared to the NaI.

3.3.2.3 Detection efficiency

As previously mentioned, the calculation of the production cross sections depends on the absolute value of the induced activity produced by the proton beam within the foils. Therefore, the detection efficiency of the $LaBr_3$ and NaI detectors must be determined. The detection efficiency relates the number of particles detected in the photopeak to the total of particles emitted from the source, which depends, for a given scintillator material and source material, on the energy deposited in the detector, spatial distribution of the emitting source, distance from the source to the detector and size of the detector.

In order to determine the detection efficiencies for each experimental setup, it is required an accurate Monte Carlo calculation in which all the mentioned factors are taking into account. In order to validate the developed Geant4 simulation and to characterize the detector geometries, a comparison with experimental detection efficiencies using calibrated γ-rays sources was performed. The general idea is to reproduce the 511 keV photons-emitting source at its corresponding distance from the front face of the detector, counting the number of 511 keV photons depositing all its energy in the sensitive volume of the detector.

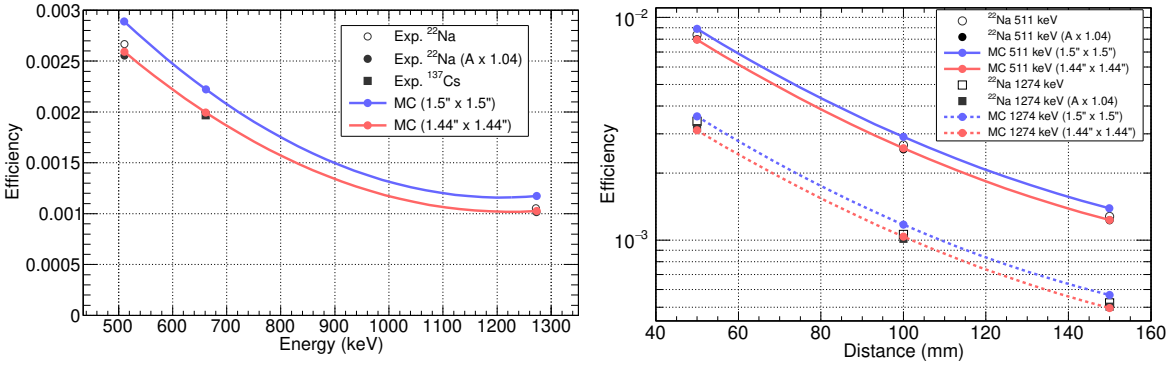

FIGURE 3.15: (Left) Detection efficiency of the $LaBr_3$ detector as a function of the energy. (Right) Detection efficiency of the $LaBr_3$ detector as a function of the distance between source and detector. The simulation considers the nominal (blue) and a reduced (red) detector volume.

The detection efficiency curve for both $LaBr_3$ and NaI detectors as a function of the energy at a distance of 100 mm were determined from a ^{137}Cs and a ^{22}Na γ-ray sources from CNA. The experimental efficiency is calculated as:

$$\epsilon = \frac{n - f}{A \cdot I}, \tag{3.19}$$

where n and f are the total counting rate of the photopeak of interest and the background, respectively, A is the activity of the source, and I is the intensity of the decay.

The Geant4 simulations were performed considering a point source, encapsulated in a 20 mm diameter and 6 mm thick plastic disk and placed at 100 mm from the detector. It emits isotropically 661.7 (^{137}Cs source), 511 or 1274 keV (^{22}Na source) photons. The efficiency was calculated by counting the number of photons depositing all its energy in the detector.

Since the activity of the ^{137}Cs source was known with an accuracy of 1% (632(7) Bq), there is a high confidence in the experimental value of the detection efficiency obtained for this source. The comparison between this experimental value and the Geant4 simulation indicates that the $LaBr_3$ crystal size should be actually 1.44" × 1.44" to reproduce this experimental data. It is illustrated in Figure 3.15 (left), where the experimental and simulated efficiencies as a function of the energy is displayed, for the nominal (1.5" × 1.5") and updated (1.44" × 1.44") size of the detector.

Besides that, the comparison between the experimental efficiency of the ^{22}Na source, whose activity (106(6) kBq) is known within 6%, with the simulated efficiencies using a 1.44" × 1.44" detector, indicates that it is required to scale the ^{22}Na activity by a 1.04 factor in order to reproduce the experimental values with a single simulated efficiency curve within a 1%, as illustrated in Figure 3.15 (left).

Furthermore, Geant4 simulations to obtain the efficiencies at 50, 100 and 150 mm were also performed and compared to experimental measurements. The results are shown in Figure 3.15 (right). This figure displays the experimental detection efficiency for the 511 keV and 1274 keV γ-rays at 50, 100 and 150 mm, calculated using the uncorrected and corrected (by 1.04) values of the source's activity. Also, this figure shows the MC simulations of these 511 keV and 1274 keV γ-rays, considering the nominal and updated size of the dectector. As previously mentioned, the comparison between the experimental (considering the corrected activity of the ^{22}Na source) and simulated efficiencies confirms the actual size of 1.44" × 1.44" of the detector, instead of the nominal value, in order to reproduced the experimental data with a single efficiency curve.

In conclusion, these experiences evidences that:

- The activity in the ^{22}Na source at CNA used on the determination of the efficiency of the PET/CT scanner needs to be scaled by a 1.04 factor.
- The size of the detectors used in the Geant4 simulations to reproduced the experimental data needs to be lower than the nominal one.

Taking the above-mentioned geometry construction aspects into consideration, the absolute detection efficiencies to obtain the production cross sections were calculated for each specific target foil, distance from the detector, beam spot size in the target and actual β^+ activity distribution. The MC simulations must consider also the effect of the escaping positrons from the target and the photon attenuation in the target itself and in the air. The results of the Geant4 absolute efficiencies to obtain the production cross sections are detailed in Section 4.1.

3.4 The strategy to measure the reaction cross sections up to 200 MeV

This section describes the two experimental methods developed in this work to measure the reaction cross sections in the full energy range of interest, both of them based on the activation technique. In addition, a description of each of the set-ups and the employed validation strategies are described as well.

In both methods, thin foils are irradiated with a proton beam that features a given energy distribution and losses energy as it traverses it. In order to determine the actual proton energy distribution inside each foil, the same procedure has been followed in all cases. First, the proton energy distribution at the entrance and exit of each foil has been calculated with Geant4 and each one of these energy distributions has been fitted to a Gaussian distribution. The parameters of the fits (mean values and standard deviations) have been used for the calculation of the energy distribution inside each foil. Therefore, considering an initial and final proton energy distributions:

$$P_{i,f}(E) = G(E, \mu_{i,f}, \sigma_{i,f}), \tag{3.20}$$

where G is a Gaussian function and μ (mean) and σ (standard deviation) its parameters, we can extend the proton energy distribution as a function of the depth z as:

$$P_z(E) = G(E, \mu_z, \sigma_z). \tag{3.21}$$

Considering a linear dependence of the parameters of the distribution on z:

$$\mu_z(E) = a_\mu + b_\mu \cdot z, \tag{3.22}$$

$$\sigma_z(E) = a_\sigma + b_\sigma \cdot z, \tag{3.23}$$

The parameters a_μ, b_μ, a_σ and b_σ are calculated from the values at the entrance and at the exit distributions as:

$$a_\mu = \mu_{z_i} - a_\mu \cdot z_i, \tag{3.24}$$

$$b_\mu = \frac{\mu_{z_i} - \mu_{z_f}}{z_i - z_f}, \tag{3.25}$$

$$a_\sigma = \sigma z_i - a_\sigma \cdot z_i, \tag{3.26}$$

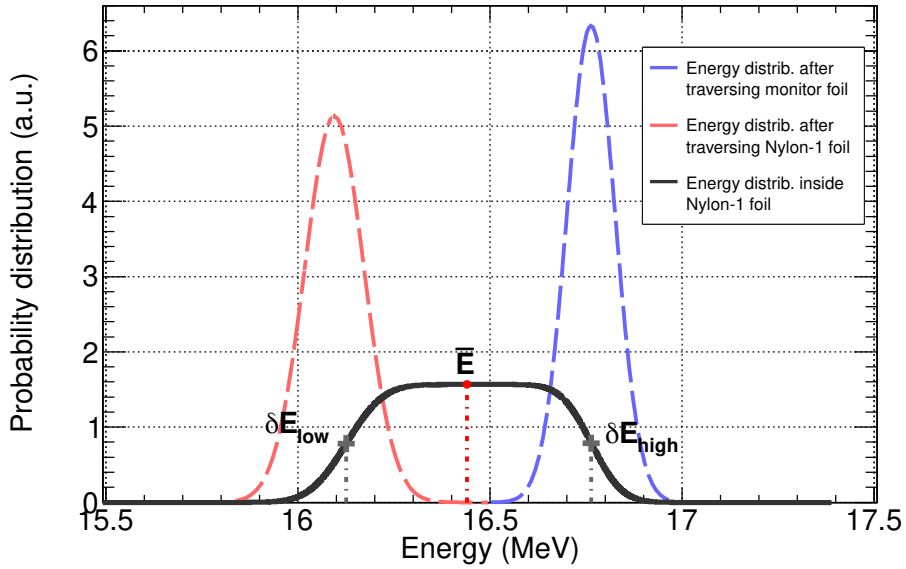

FIGURE 3.16: Calculation the energy distribution of the proton beam inside a Nylon foil (black line), calculated from the simulated energy distribution at the entrance (dotted blue line) and exit (dotted red line) of the target.

$$b_\sigma = \frac{\sigma z_i - \sigma z_f}{z_i - z_f}, \tag{3.27}$$

considering $z_i = 0$, z_f as the foil thickness, μ_{z_i}=$\bar{E}_{z_i}$ and μ_{z_f}=$\bar{E}_{z_f}$.

Then, the probability distribution within the foil is calculated as:

$$P_z(E) = \frac{1}{\sqrt{2\pi}\cdot\sigma_z(E)} \cdot e^{-\frac{1}{2}\left(\frac{E-\mu_z(E)}{\sigma_z(E)}\right)^2}. \tag{3.28}$$

The proton energy in each foil is then defined as the mean value of the corresponding $P(E)$ distribution:

$$\bar{E} = \int E \cdot P(E)\, dE, \tag{3.29}$$

with an asymmetric energy spread calculated as the point in which the probability function reaches its half maximum values. As an example, the energy distribution ($P(E)$), mean energy ($\bar{E}$) and energy spread (δE) of a Nylon-6 foil irradiated with a 16.76(6) MeV beam, together the initial and final energy distributions ($P_i(E)$ and $P_f(E)$), are displayed in Figure 3.16.

3.4.1 Experimental Setup I: multi-foil activation combined with PET

In the frame of this thesis, a new method has been developed with the goal of obtaining energy differential cross sections in the full energy range of interest without having to perform one irradiation and one activation measurement per energy value. The so-called multi-foil activation technique consists on the irradiation of a target made as an assembly of thin foils in such a way that the beam features a different energy as it traverses each foil. The novelty of the method employed in this work consists on the subsequent measurement of the induced activity in all the foils individually but simultaneously, by using a PET scanner as sketched in Figure 3.17. Inside the scanner, the foils are embedded in a matrix

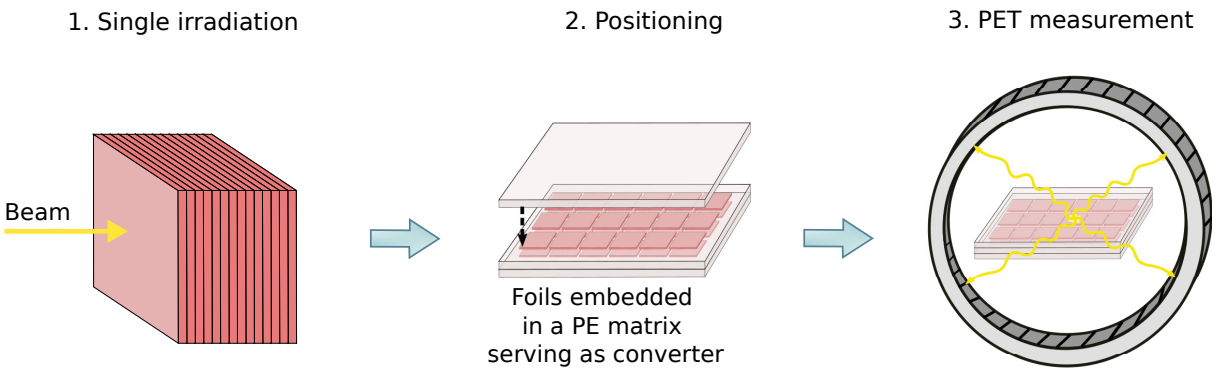

FIGURE 3.17: Steps involved in the multi-foil activation technique with PET measurement: (1) single irradiation of a target assembly of thin foils, (2) positioning of the thin films in a polyethylene matrix, (3) activity measurement with a PET scanner.

TABLE 3.2: Detailed information of the multi-foil target assemblies irradiated at the 18 MeV CNA cyclotron. *In bold, the dominant reactions for the production of ^{11}C and ^{13}N below 18 MeV and the monitor reaction.

Material	ρ (g/cm^3)	Composition	# foils	Thickness (mm)		Range (mm) E_p=16.7 MeV	Main reactions*
				foil	total		
PE	0.96	C_2H_4	15	0.198(2)	2.97(3)	3.03	^{12}C(p,pn)^{11}C ^{12}C(p,γ)^{13}N
PMMA	1.18	$C_5O_2H_5$	14	0.171(2)	2.39(3)	2.36	^{16}O(p,3p3n)^{11}C **^{16}O(p,α)^{13}N**
Nylon-6	1.13	$C_6H_{11}NO$	14	0.183(5)	2.56(7)	2.67	**^{14}N(p,α)^{11}C** ^{14}N(p,pn)^{13}N
Copper	8.92	Cu	8	0.068(1)	0.544(8)	0.586	**^{63}Cu(p,n)^{63}Zn**

of polyethylene (PE) that serves both to position them inside the scanner and to ensure the annihilation of the positrons into two 511 keV annihilation photons in the close vicinity of each foil. As all the foils are measured simultaneously, this requires just a single irradiation; hence minimizing the errors associated to reproducibility of the irradiation parameters as well as the irradiation and measuring times, which are scarce and expensive, especially when using clinical beams.

This multi-foil activation technique has been applied in the experiments at CNA and WPE. At CNA, the 18 MeV cyclotron allows to measure the energy differential reaction cross sections at the distal fall-off of the induced activity curve in the patient, i.e. in the Bragg peak region. At WPE, the clinical accelerator provides beam energies between 100 and 200 MeV, which has allowed measuring cross sections between 30 and 200 MeV. Both experiments were performed minimizing the number of irradiations (one at CNA and four at WPE per target assembly) and consecutive activity measurements, maximizing the efficiency in the outcome of the experiments, as all reactions of interest are measured "simultaneously".

As previously described, the energy distribution inside each foil within the multi-foil target were assessed using Geant4 simulations, and the proton energy and its asymmetric energy spread, i.e. errorbars, are defined as the mean value and values at half of the maximum of the corresponding distribution.

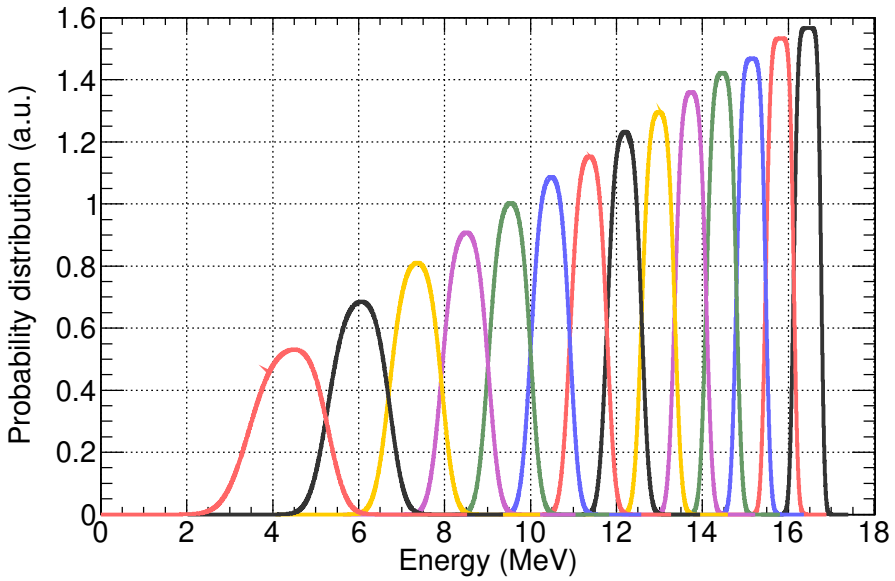

FIGURE 3.18: Proton energy distribution inside nylon-6 foils at CNA.

TABLE 3.3: Details of the performed irradiations at CNA. *The current integrator was calibrated from the results of the integral activity of ^{63}Zn induced in the copper target (see section 3.4.3.2)

Target	Current* (nA)	Duration (s)	Number of protons (x10^{13})	c_{decay} (%) (isotope of interest)
PE	33.8(16)	300(1)	6.3(3)	18.39(5) (^{13}N) 8.73(3) (^{11}C)
PMMA	15.9(8)	420(1)	4.17(20)	26.31(5) (^{13}N) 12.37(3) (^{11}C)
Nylon-6	33.4(16)	300(1)	6.3(3)	18.39(5) (^{13}N) 8.73(3) (^{11}C)

3.4.1.1 Experimental setup at CNA

The irradiation setup at CNA consists on three stacks (multi-foil) of thin foils rich in carbon (polyethylene), oxygen (Poly(methyl-methacrylate), abbreviated as PMMA) and nitrogen (polycaprolactam, abbreviated as Nylon-6) to study the reactions producing ^{11}C and ^{13}N. For each material, the stack was made of a certain number of thin foils with a total thickness slightly smaller than the corresponding beam range, so that the protons traverse the targets and exit with an energy just below the corresponding reaction threshold, hitting the 2 mm graphite beam dump where the current is measured as described in Section 3.2.1. The optimal thicknesses and the beam energy degradation along the target assembly have been calculated via Geant4 simulations. For instance, the proton energy distributions inside the foils of the nylon-6 assembly are shown in Figure 3.18. The characteristics of the targets are summarized in detail in Table 3.2.

The three target stacks are mounted on a target holder coupled to a motorized table that allows placing the targets of different materials in the beam without entering the experimental room (see Figure 3.19, right). This setup minimizes the time span between the irradiations of the different targets, and hence the decay of the activity between the irradiations and the PET measurement. The laser positioning system of the experimental room was employed for the alignment. A scintillator sheet was also placed in the holder in order to visually verify the position, size and shape of the beam with a

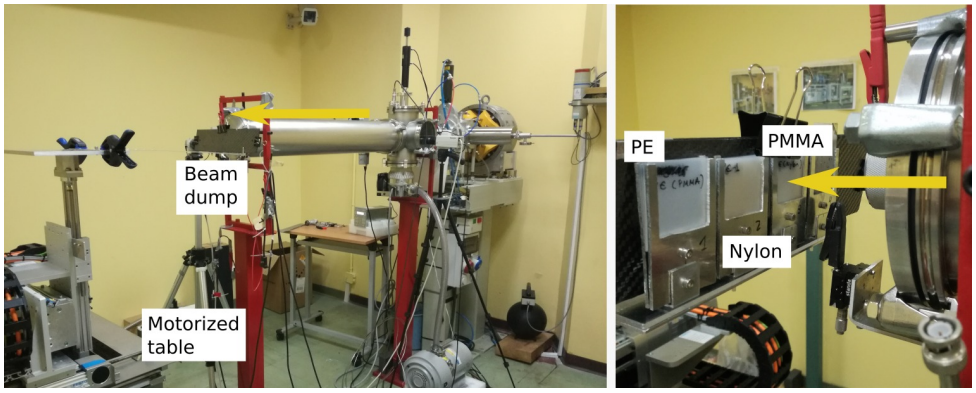

FIGURE 3.19: (Left) Experimental beam line at CNA. (Right) Irradiation setup at CNA.

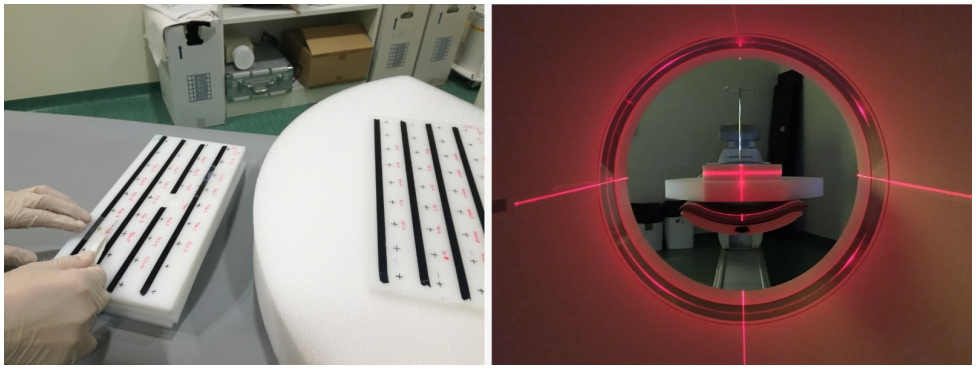

FIGURE 3.20: (Left) Positioning of the irradiated foils between the PE thick layers. (Right) PET measurement of the activity of the irradiated foils embedded in the PE matrix at CNA.

video camera from the control room. A 125 μm thick Mylar vacuum window closes the beam line and the irradiations are performed in air, at 55 mm from the window.

The details of each irradiation (duration, current, accumulated charge and fraction of isotopes that decays during the irradiation) are summarized in Table 3.3. In all cases the current was low enough to prevent damaging the targets and the duration of the irradiations was chosen to produce enough activity in each target, but within the radio-protection limits of the facility. Following the irradiation, and after the time span needed to access the experimental area, the targets were transported to the measuring station at the PET/CT.

After the three irradiations, the activity of all the foils is measured simultaneously with the PET scanner described in Section 3.3.1. A total of 46 foils were inserted into the PE matrix, forming two layers as illustrated in Figure 3.20. As mentioned already, the PET scanner was operated in dynamic mode recording 60 s interval acquisitions during five hours, although after the first three hours the signal was already very close to the background level, as the half-lives of ^{11}C and ^{13}N are 20.36 and 9.97 min, respectively.

3.4.1.2 Experimental setup at WPE

The experiment at WPE consists on the irradiation of three stacks of foils rich in carbon (polyethylene, C_2H_4, PE), oxygen (silicon dioxide), SiO_2) and nitrogen (aluminum nitride, AlN) at four different energies, allowing the measurement of the reaction cross sections of ^{11}C, ^{13}N and ^{15}O from ~30 MeV up to 200 MeV in narrow energy intervals. The optimal thickness of the foils during the experiment at WPE was chosen to optimise the covered energy range with the minimum number of irradiations. The target thicknesses were 1 mm for the PE and SiO_2 foils and 0.64 mm in the case of AlN (see Table

TABLE 3.4: Detailed information of the target assemblies at WPE. *In bold the main reactions for the production of ^{11}C, ^{13}N and ^{15}O. **Copper target placed always behind SiO_2 assembly.

Material	ρ (g/cm^3)	Composition	Thickness (mm)	Reactions channels*
PE	0.96	C_2H_4	1	^{12}**C(p,x)**^{11}**C**
Quartz	2.2	SiO_2	1	^{16}O(p,x)^{11}C, ^{16}O(p,x)^{13}N, ^{16}**O(p,x)**^{15}**O**
Aluminum nitride	3.3	AlN	0.64	^{14}N(p,x)^{11}C, ^{14}**N(p,x)**^{13}**N**, ^{14}N(p,γ)^{15}O
Copper	8.92	Cu	1	^{nat}**Cu(p,x)**^{63}**Zn** (monitor)

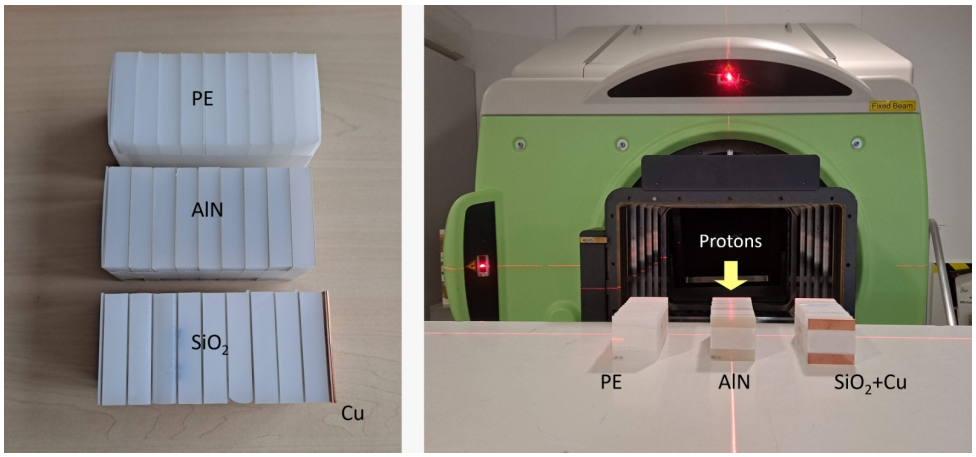

FIGURE 3.21: (Left) Experimental setup during the irradiations at WPE. (Right) The SiO_2 stack made of 10 thin foils of SiO_2 between thicker PE degraders. The first and last foils are the PE and copper monitor foils, respectively.

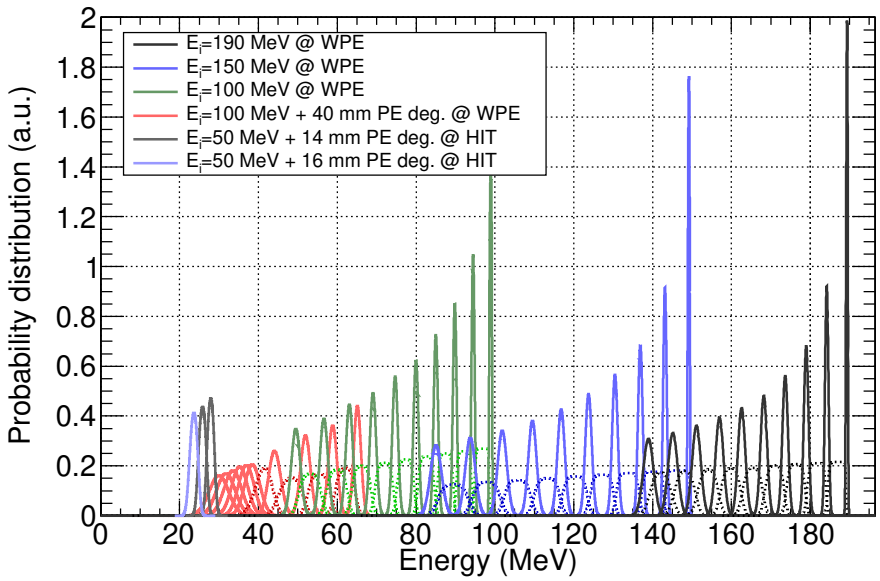

FIGURE 3.22: Proton energy distribution inside PE foils at different initial beam energies for the WPE and HIT irradiations. Dotted lines: Proton energy distributions inside PE degraders placed between target foils.

3.4 for details), significantly thicker than the foils of hundred of μm used for low energy experiments at CNA.

During the irradiations, the foils were embedded between 5 or 10 mm thick PE slabs (see Figure 3.21) to degrade the proton beam energy down to the desired value in each foil. As the minimum

TABLE 3.5: Details of the performed irradiations at WPE, including the initial irradiation energy (E_i), the polyethylene (PE) degrader thicknesses used in each case, the beam characteristics and the accumulated charge.

E_i (MeV)	Initial PE degrader	PE degrader between foils	Beam size		Accumulated charge (nC)
			σ_x (mm)	σ_x (mm)	
100	40 mm	5 mm after the first three foils and 3 mm after the fourth foil	8.08	7.81	64.9(7)
100	-	5 mm (2 mm after the last two foils of AlN & SiO_2 assemblies)	8.08	7.81	64.9(7)
150	-	10 mm	5.53	5.23	87.2(9)
190	-	10 mm	4.07	4.02	103.0(10)

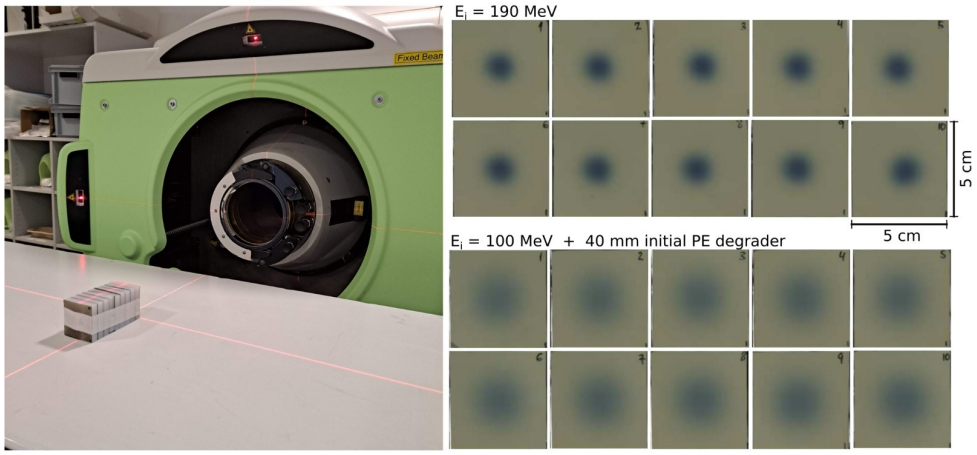

FIGURE 3.23: (Left) Irradiation of Gafchromic EBT3 foils placed between PE degraders. (Right) Irradiated Gafchromic EBT3 foils at E_i=190 MeV and 100 MeV, in the latter case using 40 mm of initial PE degrader in front of the assembly.

extracted energy at WPE is 100 MeV, in order to measure down to ~30 MeV, a PE slab of 40 mm was used in front of each stack to degrade it down to 60 MeV. The optimization of the foils and degraders configuration (summarized in Table 3.5) was assessed with Geant4 simulations. Figure 3.22 shows the energy distributions inside each PE foil for each initial beam energy as an illustrative example of the how the full energy range interest is covered at WPE.

The alignment and targets' positioning at the isocenter was carried out with the help of the laser positioning system. The lateral spreading of the beam as it traverses the degraders and target foils has been verified using Gafchromic EBT3 foils for each one of the incident energy and degraders configuration. Figure 3.23 displays the irradiation setup and the irradiated Gafchromic foils at the extreme cases of incident energies.

The experiments at WPE were performed using PBS, where the direction of the beam can be magnetically adjusted. This allows the irradiation of three stacks with the same initial beam energy without entering the treatment room and without having to move the targets (as it was done at CNA). This way, the time span between the irradiation of the different targets was practically negligible, and the radioactive decay between the irradiations and the PET measurement was minimized. The total number of monitor units for each irradiation was fixed to 5000 MU. Table 3.5 summarizes the nominal beam size and accumulated charge for each irradiation.

After each irradiation with a given beam energy, the activity from all the irradiated foils was measured simultaneously using the PET scanner in dynamic mode, recording 60 s images during four hours, time enough to reach the background level. The PET/CT scanner at WPE is located close to

FIGURE 3.24: (Left) Positioning of the irradiated foils between the polyethylene thick layers. (Right) PET measurement of the activity of the irradiated foils embedded in the PE matrix at WPE.

the treatment rooms, which allowed to transport and place the irradiated foils inside the PET scanner rapidly enough to measure the decay of ^{15}O, with a half-life of just 122 s. Figure 3.24 shows: (left) the disposition of the irradiated foils in two layers within the PE matrix, (right) the complete PE matrix inside the PET scanner at WPE. Equally to the determination of the spatial efficiency, the images were reconstructed using the mentioned two protocols (iterative and TrueX, both with ToF), which provided compatible results within less than 1%.

3.4.2 Experimental Setup II: single-foil activation at HIT

The experiments on long-lived (~minutes) isotopes at CNA and WPE left uncovered the energy region between ~17 MeV and ~30 MeV, a region that is interesting because it corresponds to several reactions' thresholds, and is hence a region with a rapid increase of the corresponding cross sections. Therefore, an experiment was designed at HIT, which features a minimum beam energy of just 50 MeV (compared to 100 MeV at WPE), to complement the mentioned experiments at CNA and WPE for long-lived β^+ emitters.

Additionally, a completely different set-up was designed in order to measure on-line the production of short-lived (ms to s) β^+ emitters in the full energy range from reactions' threshold up to 200 MeV.

The two experimental set-up developed at HIT are described in the following.

3.4.2.1 Measurement of long-lived β^+ emitters at HIT

The minimum initial beam energy available at WPE is 100 MeV, which means that the energy spread is too large when the beam is degraded down to ~30 MeV. On the other hand, the maximum beam energy available at CNA is 18 MeV. Therefore the production of long-lived β^+ emitters in the energy range between 18 and ~30 MeV was performed at the HIT facility, which can deliver proton beams with a minimum of 50 MeV. Unfortunately, HIT is not equipped with a PET/CT scanner and hence a different approach (from the previously described in Section 3.4.1) had to be implemented for measuring the induced β^+ activities.

As in WPE, the proton energy was degraded using PE layers with different thicknesses to achieve the desired proton energy distribution inside each foil (see Figure 3.25 (a)). The above-mentioned Figure

TABLE 3.6: Details of the performed irradiations at HIT to measure the long-lived isotopes, listing the initial irradiation energy (E_i), polyethylene (PE) degrader used in each case, the two target materials used in each irradiation, beam characteristics and accumulated charge.

E_i (MeV)	PE degrader (mm)	Target 1	Target 2	Beam size FWHM (mm)	Accumulated charge (nC)
50.6	14	PE	PE	31.3	8.9(3)
50.6	15	SiO_2	SiO_2	31.3	19.3(6)
50.6	13	AlN	AlN	31.3	19.3(6)
50.6	16	AlN	Cu	31.3	19.3(6)
50.6	16	PE	Cu	31.3	19.3(6)

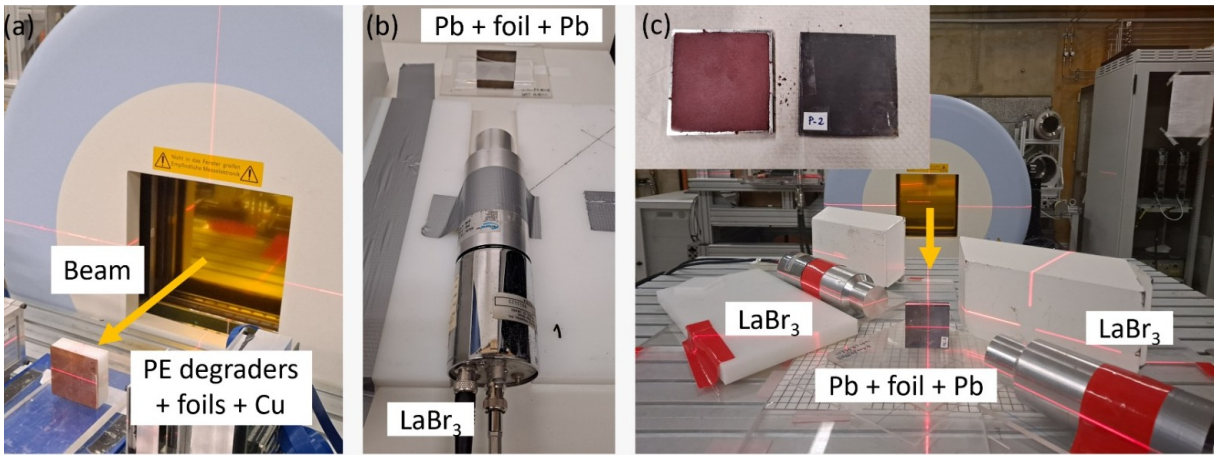

FIGURE 3.25: Setup for the measurement of the long-lived isotopes of interest at HIT, consisting on (a) irradiation of the target assembly and (b) measurement of the induced activity using a $LaBr_3$ detector, and the measurement of the short-lived isotopes (c), showing on the top of the figure an example of phosphorus powder target.

3.22 displays as well the energy probability distribution in the PE foils measured at HIT, illustrating the improved energy resolution achieved at HIT with respect to WPE in the low proton energy range.

At HIT, five assemblies of two foils (the same foils as used at WPE) were irradiated. The reaction cross sections in carbon and nitrogen were obtained at three energy values and two in the case of oxygen. Table 3.6 summarizes the details of each irradiation: initial energy, targets, degraders in front of each target, nominal beam size (FWHM) at the isocenter and accumulated charge. As in WPE, the experiments were performed using PBS, positioning the assembly with the laser system, and measuring with Gafchromic EBT3 foils the size of the beam at the foils positions.

After each irradiation, the activity in the corresponding foils were measured using the $LaBr_3$ γ-ray detectors discussed in Section 3.3.2.1 (see Figure 3.25 (b)). These were placed just outside the irradiation room, hence allowing to measure the decay of ^{15}O. During the measurements, each target was sandwiched between a pair of 1 mm thick lead foils, acting as positron converters, and placed at 150 mm from the front face of the detector. The detectors were connected to the mentioned CAEN DT5730 digitizer that provided the signals' integral with the corresponding timestamp, allowing to study the decay curve from the positron emitters of interest.

3.4.2.2 Measurement of short-lived β^+ emitters at HIT

The short-half life of the ^{12}N, ^{38m}K and ^{29}P produced in carbon, calcium and phosphorus, respectively, prevented from moving the irradiated foils to any other detection system, such as the previously-described PET. Therefore, the induced activity is measured simultaneously to the irradiation. Protons

TABLE 3.7: Detailed information of the irradiated foils.

Foil	ρ (g/cm^3)	Composition	Thickness (mm)	Reactions channels
PE	0.96	C_2H_4	5	^{12}C(p,x)^{12}N
Ca	1.55	Ca	4	^{40}Ca(p,x)^{38m}K
P-1	1.70	red phosphorus	4	^{31}P(p,x)^{29}P
P-2	1.76	red phosphorus	4	^{31}P(p,x)^{29}P
P-3	1.79	red phosphorus	4	^{31}P(p,x)^{29}P

TABLE 3.8: Details of the performed irradiations at HIT to measure ^{12}N, listing the initial irradiation energy (E_i), thickness of the Pb converter, nominal beam size, accumulated charge and beam on/off cycles.

E_i (MeV)	Pb thick. (mm)	Beam size FWHM (mm)	Accumulated charge (nC)	Beam on (ms)	Beam off (ms)	# cycles
50.60	2.5	31.3	9.3(3)	30	600	1000
50.60	2	31.3	9.3(3)	30	600	1000
60.90	2	26.3	9.3(3)	30	600	1000
70.03	2	22.8	9.3(3)	30	600	1000
80.04	2	19.6	9.3(3)	30	600	1000
90.70	2	17.4	9.3(3)	30	600	1000
110.24	2	14.4	9.3(3)	30	600	1000
130.52	2	12.5	9.3(3)	30	600	1000
160.09	2	10.6	9.3(3)	30	600	1000

are delivered as a succession of beam-on/beam-off periods, whose duration depends on the half-life under study. As the background level is reached in each beam-off period, several cycles are summed to improve the statistics.

Three different thin foils (see Table 3.7 for details) were irradiated at ~10 different energies in order to obtain the reaction cross sections of interest from threshold (~20 MeV) up to 200 MeV. The target thicknesses were 5 mm for the polyethylene (PE) and 4 mm in the case of pure calcium and pure phosphorus targets. In the case of the calcium foils, 8 foils of 30x30x2 mm^3 were assembled together to form a 60x60x4 mm^3 target. In the case of phosphorus targets, red phosphorus powder was compressed and packed in three capsules made of 50x50x2 mm^3 or 50x50x1 mm^3 lead foils, depending on the desired energy distribution inside each one. Figure 3.25 (c) shows the irradiation set up and an example of phosphorus powder target.

During the irradiations, the targets were sandwiched between a pair of several millimetres thick lead foils, acting as positron converters in order to maximize the conversion efficiency. The optimization of the Pb thickness configuration, PE degraders and final energy distribution inside each foil were assessed with Geant4.

As seen in Figure 3.25, the targets were placed perpendicularly to the beam. Then, a pair of $LaBr_3$ detectors were used to measure the activity produced in each proton beam cycle. These were placed one at each side of the target, at 10 cm from it and with an angle of 45 degrees to enhance the detection efficiency. The detectors were connected to the CAEN V1750 digitizer that measured continuously, that is during both beam-on and beam-off periods. The timestamp of the signals allowed to study the decay curves of the β^+ decays with and without applying coincidence conditions between the detectors.

Table 3.8, 3.9 and 3.10 summarize the details of each irradiation for the PE, Ca and P targets, respectively. The irradiations were also performed using the PBS mode. As mentioned in the previous section, the centering of the foil was verified using the laser and Gafchromic EBT3 foils.

TABLE 3.9: Details of the performed irradiations at HIT to measure ^{38m}K, listing the initial irradiation energy (E_i), thickness of the Pb converter, thickness of the PE degrader, nominal beam size, accumulated charge and beam on/off cycles.

E_i (MeV)	Pb thick. (mm)	PE thick. (mm)	Beam size FWHM (mm)	Accumulated charge (nC)	Beam on (s)	Beam off (s)	# cycles
50.60	2.5	-	31.3	16.0(5)	5	50	10
50.60	-	10	31.3	16.0(5)	5	50	10
50.60	-	5	31.3	16.0(5)	5	50	10
50.60	-	-	31.3	4.81(14)	5	50	10
60.90	2	-	26.3	16.0(5)	5	50	10
60.90	-	-	26.3	4.81(14)	5	50	10
70.03	2	-	22.8	16.0(5)	5	50	10
70.03	-	-	22.8	4.81(14)	5	50	10
80.04	-	-	19.6	4.81(14)	5	50	10
90.70	-	-	17.4	4.81(14)	5	50	10
110.24	-	-	14.4	4.81(14)	5	50	10
130.52	-	-	12.5	4.81(14)	5	50	10
160.09	-	-	10.6	4.81(14)	5	50	10
200.11	-	-	8.4	4.81(14)	5	50	10

TABLE 3.10: Details of the performed irradiations at HIT to measure ^{29}P, listing the initial irradiation energy (E_i), thickness of the Pb converter, nominal beam size, accumulated charge and beam on/off cycles.

E_i (MeV)	Pb thick. (mm)	Beam size FWHM (mm)	Accumulated charge (nC)	Beam on (s)	Beam off (s)	# cycles
50.60	2	31.3	16.0(5)	5	50	10
50.60	1	31.3	4.81(14)	5	50	10
60.90	2	26.3	16.0(5)	5	50	10
70.03	2	22.8	16.0(5)	5	50	10
80.04	2	19.6	4.81(14)	5	50	10
90.70	2	17.4	4.81(14)	5	50	10
110.24	2	14.4	4.81(14)	5	50	10
130.52	2	12.5	4.81(14)	5	50	10
160.09	2	10.6	4.81(14)	5	50	10
200.11	2	8.4	4.81(14)	5	50	10

3.4.3 Validation strategies

The experiments reported herein have been performed at different facilities and using different experimental set-ups. Furthermore, the preparation and analysis of the experiments are based on calculations and simulations that are not straightforward. Therefore, an effort has been made to design and implement a strategy that has allowed validating the measuring and analysis techniques.

3.4.3.1 Monitor foils (in setup I)

In front of each target assembly in the multi-foil experiments there was a PE foil used for monitoring purposes. The idea is that the activity induced in the monitor foils of the three stacks irradiated with the same energy must be proportional to the beam charge accumulated by each stack. Furthermore, the measurement of activity of the monitor foils with the PET scanner requires to apply the corresponding corrections associated to the decay during the irradiation and the transport of the foils. Therefore, the agreement between the activity of the different monitor foils allows validating both the relative beam current measurements and the decay corrections applied.

TABLE 3.11: Details of the thick-target irradiations at CNA. *The current integrator was calibrated from the results of the integral activity of ^{63}Zn induced in the copper target.

Target	Current* (nA)	Duration (s)	Number of protons (x10^{13})	c_{decay} (%) (isotope of interest)
PMMA	2.17(11)	48(1)	6.4(3)	2.75(6) (^{13}N) 1.37(3) (^{11}C)
Nylon-6	2.15(11)	176(1)	23.7(12)	9.60(5) (^{13}N) 4.91(3) (^{11}C)
^{nat}Cu	2.37(12)	31(1)	4.59(23)	0.464(15) (^{63}Zn)

3.4.3.2 The IAEA ^{nat}Cu(p,x)^{63}Zn monitor reaction (in setups I and II)

The cross section results from the experiments at CNA, WPE and HIT were all validated using a complementary measurement of a well established reaction cross section: the IAEA standard reaction ^{nat}Cu(p,x)^{63}Zn [145], with the β^+ emitter ^{63}Zn featuring a half-life of 38.47(5) min. A thick target of ^{nat}Cu was irradiated independently (CNA) or together with at least one of the target foils (WPE and HIT). This allows to measure the integrated (also referred to as "thick-target") production yield below ~20 MeV and compare it against the expected value from the IAEA evaluation. In the following, the setup in each facility is described.

1. At CNA, the irradiation of a 0.544 mm Cu target below 18 MeV was carried out independently from the target assemblies (see Table 3.2 for target details and Table 3.11 for irradiation details). The resulting activity was measured sandwiching the target within a pair of 1 mm thick lead foils (acting as positron converters) and placing it at 9.8 cm from the front face of the already mentioned 1.5"x1.5" $LaBr_3$ detector. In the case of CNA, this well-known reaction was used as reference to calibrate against it the current integrator module.

2. At WPE, two C targets of 1 mm (see Table 3.4 for details) were placed behind the SiO_2 stack for each specific initial beam energy, as shown in Figure 3.21. The induced activity was measured simultaneously with the rest of the foils in the PET scanner.

3. At HIT, two Cu targets of 1 mm were irradiated behind a PE and a AlN targets, respectively (see Table 3.6). The copper targets were the same as the used at WPE. The induced activity was measured with the $LaBr_3$ detectors.

3.4.3.3 Integral vs. differential yields of ^{11}C and ^{13}N at CNA

The experimental setup I previously described in Section 3.4.1 was applied for the first time at CNA, so a complementary measurement to obtain the thick target production yields of ^{13}N in oxygen and ^{11}C in nitrogen using conventional detectors was performed to validate the results from the differential measurements in the PET scanner, and the results are shown in Section 4.5.3. Regarding the production of ^{13}N in oxygen and ^{11}C in nitrogen, there are two IAEA evaluations below 30 MeV, since these are the typical radioisotopes used in PET diagnostic. In Section 5.1, the experimental production yields are compared against the value from the evaluation.

For this purpose, two targets of PMMA and Nylon-6 with the same thickness of the target assembly used for the PET measurement were irradiated under the same conditions (see Table 3.11). Then, the activity produced in the thick targets was measured with a NaI and $LaBr_3$ detectors, respectively, in the same configuration as the one discussed in the previous section of ^{nat}Cu target, where the targets were placed between Pb converters at 100 mm from the front face of the detector.

Chapter 4

Data analysis

This chapter is devoted to the analysis of the measurements carried out at the CNA, WPE and HIT facilities. It includes detailed discussions about the corrections (positron conversion efficiency, γ-ray detection efficiency and decay during irradiation and transport), decay curve fitting and validations (from monitor foils, the monitor ^{63}Cu(p,n)^{63}Zn reaction, and thick vs. multi-foil target tests). Last, the determination of the cross section values from the observables is explained and the summary of uncertainties assessed.

THE DATA ANALYSIS procedure starts with the decay curves obtained with the different detection systems. The corresponding curve fitting allows determining the amount of β^+ emitters produced per incident proton, but firstly the data have to be corrected by the positron annihilation and γ-rays detection efficiencies, and the decay during the irradiation and the transport of the targets. The data are then normalized to the incident beam current and the curve fitting takes place. Before transforming the results into cross section values, a series of tests and comparison are performed in order to validate all the mentioned corrections and validations. Then, the duly corrected results from the curve fitting are transformed into reaction cross section values with their corresponding uncertainties.

4.1 Escaping positrons and photon attenuation

The positrons emitted in the β+ decay feature an energy distribution with a maximum corresponding to the Q-value. The corresponding range is such that the annihilation of the positrons, which occurs only once they come to rest, can happen outside the irradiated foil. As the positron endpoint energy typically increases with decreasing half-life (see Table 2.1), the effect of escaping positrons is larger for shorter half-lives; for instance, the range of the most energetic positrons (up to 16.3 MeV, in the case of ^{12}N) is about ~6.5 m in air, while it is reduced to ~7 mm in lead. While in some of the configurations employed a complete annihilation of the positrons in the proximity of the target has been achieved, in some case this has not been possible and a correction related to the fraction of escaping positrons had to be estimated. In addition, once the positrons are annihilated and converted into a pair of 511 keV photons, these must traverse a not negligible amount of material (the foils themselves, the positron converters and a given distance in air) before reaching the corresponding detection system. The correction due to the attenuation of the photons had as well to be estimated for each specific set-up.

These two corrections, escaping positrons and photon attenuation, are strongly dependent on the experimental set-up and on the reaction under study.

In the experimental setups using the PET scanners at CNA and WPE, a 100% positron conversion efficiency was ensured by the PE matrix within which the foils are placed. In this matrix, the distance between foils was larger than the maximum positron range and hence the annihilation occurred in the vicinity of each foil without overlap with its neighbor. Then, the photons attenuation was calculated and corrected for automatically by the reconstruction software of the PET scanner based on the the CT information, as it is custom in PET/CT diagnostics.

In the experimental set-ups using $LaBr_3$ and NaI detectors, both corrections, escaping positrons and photon attenuation, were calculated with Geant4. The *PrimaryGeneratorAction.cc* class of the Geant4 toolkit was adapted to simulate the isotropic emission of positrons with the energy predicted by the Fermi theory of β-decay (see Equation 2.13). The spatial origin of the emitted positrons source was defined according to the size of the beam spot in each irradiation, i.e. the activated area, parameterized as a Gaussian distribution characterized by the FWHM of the beam for each beam energy. The β^+ emission depth was randomly distributed over the target thickness. The effect of escaping positrons and the subsequent attenuation of the 511 keV photons was assessed simultaneously by looking at the number of photons per emitted positron depositing precisely 511 keV in the actual detectors. This was done in the realistic geometry corresponding to each experimental set-up, as it is illustrated in Figure 4.1, which shows the $LaBr_3$ detector and Cu targets embedded between the lead plates. Both $LaBr_3$ and NaI crystals are encapsulated in 2 mm and 2.5 mm thick aluminium, respectively, and the actual size of the crystals is considered as described in Section 3.3.2.3.

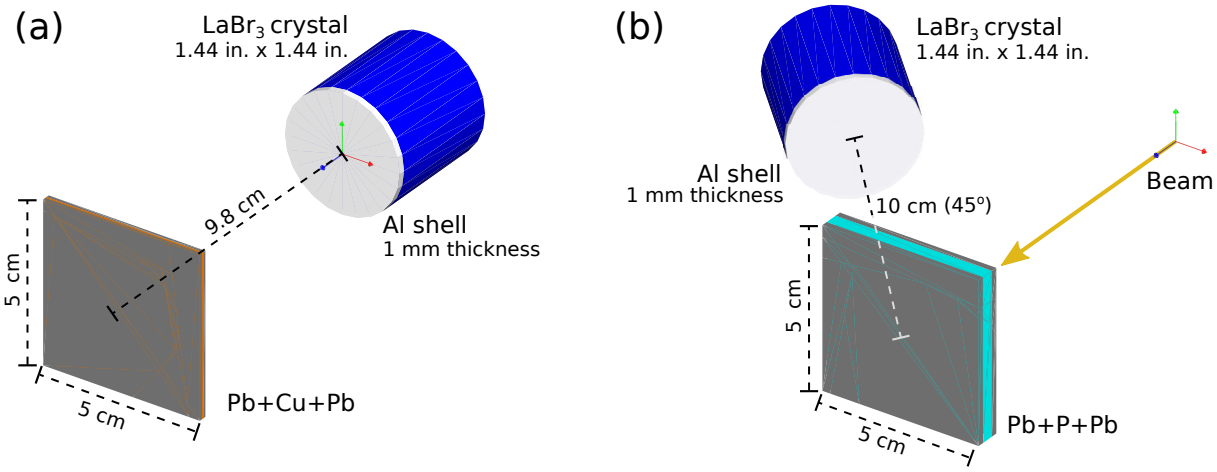

FIGURE 4.1: Geant4 geometry model of the setup to measure (a) the induced activity in a copper foil as described in Section 3.4.3.2, and (b) the induced activity of short-lived isotopes as described in Section 3.4.2.2.

TABLE 4.1: $^{63}Cu(p,pn)^{63}Zn$ reaction yield determined at CNA via the detection of the 511, 670 and 962 keV lines. In the case of the 511 keV line, the detection efficiency is calculated by simulating directly the pair of 511 keV photons (as a point source emission) or the actual positron (i.e. considering the realistic possibility of escaping positrons).

Source	I(%)	ε(%)	Yield* (kBq/nC)
(2x) 511 keV	92.8(5)	0.572(8)	1.80(9)
e^+	92.8(5)	0.459(6)	2.24(11)
670 keV	8.19(32)	0.1773(14)	2.31(11)
962 keV	6.50(16)	0.1284(18)	2.24(11)

**Values before the correction due to the emission of secondary electrons (see Section 4.3).*

The Geant4 application developed to estimate the detection efficiencies of each set-up (including the effect of escaping positrons and photon attenuation) was validated through the analysis of the activation of a copper target below 18 MeV at CNA using the experimental setup described in Section 3.4.3.2. A 544 μm thick ^{nat}Cu target was irradiated (see details in Table 3.2) and the formed ^{63}Zn ($t_{1/2}$ =38.5 min) activity was studied with the $LaBr_3$ detector after sandwiching the target in between 1 mm thick lead foils to increase the positron conversion efficiency. The analysis was made looking at both the 511 keV photons from the annihilation of positrons (emitted mostly outside the target, in the converters) and the γ-ray lines of 670 and 962 keV from the decay of ^{63}Zn (hence emitted from inside the target and without positron range effects). The efficiency for detecting the 670 and 962 keV photons was calculated with Geant4 as described in 3.3.2.3. For the case of the 511 keV, the efficiency was calculated assuming a direct emission from the target and also assuming the realistic case of positrons emitted in the target, then transported and then, not always, annihilated within the target+converter assembly. The results, summarized in Table 4.1 (see Section for discussion on the quoted uncertainties), illustrate the compatibility within just 1.7% of the results from the analysis of the direct γ-rays emission (670 and 962 keV photons) and of that with study of the 511 keV photons when the realistic simulation of positron emission is considered. However, if the positron annihilation is neglected and the efficiency is calculated as if the two 511 keV photons were always emitted from the target itself, the result is underestimated by 20% because the fact that some positrons escape the target assembly is not considered; hence demonstrating the importance of a detailed simulation of the positron transport and annihilation which, as mentioned above, is very dependent on the particular Q-value and

TABLE 4.2: Detection efficiency for β^+ decays obtained from Geant4 simulations using realistic geometries and positron emission. The experimental set-up corresponds to that illustrated in the left panel of Figure 4.1 for the off-line measurement of long-lived isotopes.

Foil (thickness)	Pb thickness	Isotope	Q_β (MeV)	I_β (%)	ε (%)
PE (1 mm)	-	^{11}C	0.960	99.750(13)	0.154(3)
SiO_2 (1 mm)	1 mm	^{11}C	0.960	99.750(13)	0.209(4)
		^{13}N	1.198	99.818(13)	0.223(4)
		^{15}O	1.735	99.885(6)	0.219(4)
AlN (0.64 mm)	1.5 mm	^{11}C	0.960	99.750(13)	0.207(4)
		^{13}N	1.198	99.818(13)	0.178(3)
		^{15}O	1.735	99.885(6)	0.228(4)
(2x) 511 keV (simplified)	-	-	-	92.8(5)	0.546(12)

TABLE 4.3: Detection efficiency for β^+ decays obtained from Geant4 simulations using realistic geometries and positron emission. The experimental set-up corresponds to that illustrated in the right panel of Figure 4.1 for the on-line measurement of short-lived isotopes.

Foil (thickness)	Pb thickness	Isotope	Q_β (MeV)	I_β	ε (%) (E_i=50 MeV)	ε (%) (E_i=200 MeV)
PE (5 mm)	2.5	^{12}N	16.316	96.17(5)	0.249(4)	-
	2				0.238(4)	0.246(4)
Ca (4 mm)	-	^{38m}K	5.022	99.883(6)	0.254(4)	0.238(4)
	2 mm				0.302(5)	-
	2.5 mm				0.270(5)	-
P-1 (679(18) mg/cm^2)	1 mm	^{29}P	3.921	98.22(3)	0.389(7)	-
P-2 (703(18) mg/cm^2)	2 mm				0.286(5)	-
P-3 (718(19) mg/cm^2)	2 mm				0.285(5)	0.308(5)
(2x) 511 keV (simplified)	-	-	-	92.8(5)	0.546(12)	

the experimental set-up.

The efficiency for detecting the β^+ decays from each of the target foils in each of the configurations used at HIT has been calculated and the results are given in Tables 4.2 and 4.3. The case of Table 4.2 correspond to the measurement of long-lived isotopes, which were brought to the measuring station displayed in the left panel of Figure 4.1. On the other hand, Table 4.3 is related to the short-lived isotopes that are measured in between irradiation cycles using the set-up displayed in the right panel Figure 4.1. The two efficiency values correspond to beam spots and hence activated areas with FWHM values of 31 and 8 mm corresponding to the beams with 50 and 200 MeV, respectively, and illustrate the non negligible effect of the spatial distribution of the β^+ emitters. In both tables there is a last line corresponding to the simplified case in which a pair of 511 keV photons would be emitted from the target position (as a point source) in the absence of target or converter. Once again, if the positron annihilation is neglected both in the target and the converters and the efficiency is calculated as if the two 511 keV photons were always emitted from the target itself, the results are underestimated by a factor more than 2; hence demonstrating again the importance of a detailed simulation of the positron transport and annihilation.

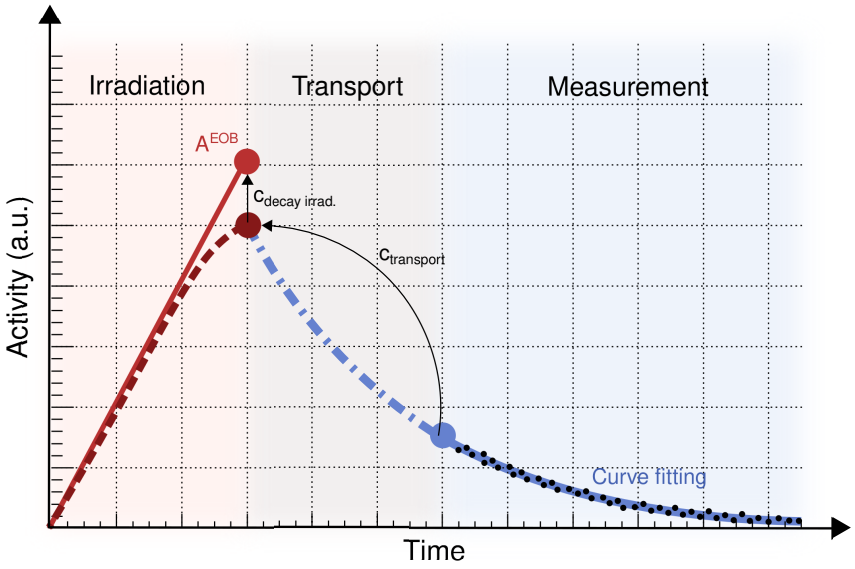

FIGURE 4.2: Scheme of the reconstruction of the overall isotope production from the activity measured some time after the irradiation, illustrating the effect of the decay during the irradiation and the transport.

4.2 Decay during the irradiation and transport

The differential equation describing the process of radioisotope formation by the activation technique and subsequent decay is defined by two terms: the mentioned reaction rate R_k, defined by Equation 3.10, and the rate of decay given by the law of the radioactive decay, defined by Equation 3.13. Therefore, the radioisotope formation process can be expressed as:

$$\frac{dN_k}{dt} = R_k - \lambda \cdot N_k = N_k \cdot \sigma_k \cdot I_p - \lambda \cdot N_k, \tag{4.1}$$

Solving this equation for $N_k(0) = 0$, the number of produced nuclei at the end of bombardment (EOB)

$$N_k^{EOB} = N_k \cdot \sigma_k \cdot I_p \cdot t_{irrad} \frac{1 - e^{-\lambda t_{irrad}}}{\lambda \cdot t_{irrad}}, \tag{4.2}$$

where the fraction in the right term accounts for the decay during the irradiation.

In order to keep this correction limited, the irradiation times were kept lower than three half-lives of the isotopes of interest. This correction was the largest for the case of the CNA experiments where the beam current had to be kept low in order not to damage the very thin (~100 μm) targets employed, hence requiring long irradiation times. For instance, in the particular case of the PMMA targets, ~26% and ~12% of the ^{13}N and ^{11}C isotopes decayed during the corresponding irradiation, respectively.

It must also be considered that the activity measurements are performed some time after the irradiation, with times ranging from ~5 minutes at HIT and WPE up to ~45 minutes at CNA. Therefore, besides the above-mentioned correction, the measured activity must be corrected by the fraction that decayed during the transport:

$$c_{transport} = 1 - e^{-\lambda t_{transport}}, \tag{4.3}$$

where $t_{transport}$ stands for time required to place the foils in the detection system since the irradiation. The largest $c_{transport}$ correction occurred also for the case of the PMMA foils at CNA, which required 45 minutes to transport and place the foils inside the PET scanner. During that time, 95.5% of the amount of ^{11}C decayed. This very long transport time was due to the fact that the radio-protection rules of this

facility did not allow entering the experimental room above a certain room dose limit.

The two corrections mentioned herein are illustrated in Figure 4.2.

4.3 Beam current monitoring: the effect of secondary electron emission

As described in Equation 3.15, the induced activity at EOB is normalized to the total number of incident protons during the irradiation to obtain the production yield y (activity per unit incident charge, in units of Bq/C) as:

$$y = \frac{A^{EOB}}{I_p \cdot t_{irr}}, \tag{4.4}$$

where I_p is the proton beam current and t_{irr} is the irradiation time, with the A^{EOB} previously corrected by the factors described in the Section 4.2. Section 3.2 describes the procedure to measure the beam current in each facility.

The experiments at the proton therapy centers (HIT and WPE) were performed at high energies that enable the use of devices in the beam line upstream of the targets to measure the beam current. However, in the experiments at CNA (with a maximum energy of 18 MeV), the beam current is measured using a beam dump placed behind the foils and connected to a current integrator, but neglecting the the effect of secondary electrons not being recovered by applying a positive voltage, because it was in air. Hence, the measured current was overestimated by a factor that had to be experimentally determined. In particular, we measured the production yield of the IAEA monitor reaction ^{63}Cu(p,pn)^{63}Zn [145] at 16.76(6) MeV, the energy of the 18 MeV beam of the cyclotron after traversing the vacuum window and the air gap. The expected ^{63}Zn production yield was calculated as the convolution of the IAEA production yield with the proton energy distribution incident in the Cu targets, given by a Geant4 calculation. The resulting value of 2.01(8) kBq/nC is 11% lower than those given in Table 4.1, indicating the size of the beam current overestimation due to the secondary electron emission. The beam current measurements along the different irradiation at CNA were hence scaled down by applying a factor of 0.90(4).

4.4 Analysis of the decay curves from activated foils

In all experiments, the measured quantity was the counting rate as a function of time. This is converted into an activity per incident charge decay curve $A(t)$ by dividing it by the efficiency of each detection system (PET scanner, $LaBr_3$ or NaI in each case), the intensity associated to the decay (see Table 4.2 and 4.3), and the integrated beam current. The time is set to zero at the exact moment when the irradiation is stopped. Then, the corresponding activity value at the end of the bombardment A^{EOB} is determined by fitting each decay curve to the linear combination of a constant background plus the expected exponential decays of the isotopes produced:

$$A(t) = C + \sum_i A_i^{EOB} e^{-\lambda_i t}, \tag{4.5}$$

where i represents each β^+ isotopes (^{11}C, ^{12}N, ^{13}N, ^{15}O, ^{29}P and/or ^{38m}K) produced in the foil.

To obtain the production yields of ^{11}C, ^{13}N and ^{15}O in the main elements of the human body in the full energy range of interest in proton therapy, the experiments were performed at three different facilities: CNA, HIT and WPE, each one covering a specific energy range. Then, the production yields

of ^{29}P, ^{38m}K and ^{12}N in phosphorus, calcium and carbon were measured at HIT in the full energy range of interest. The following section contains the details of the analysis and decay curves fitting for a selection of foils rich in carbon (PE), nitrogen (nylon-6, AlN), oxygen (PMMA, SiO_2), phosphorus and calcium irradiated in each facility.

4.4.1 Analysis of PE, PMMA and nylon-6 foils at CNA

At CNA, foils rich in carbon (PE), oxygen (PMMA) and nitrogen (nylon-6) were irradiated below 18 MeV to obtain the production yields of ^{11}C and ^{13}N. The induced activity on each foil were fitted to :

$$A(t) = C + A^{EOB}_{^{11}C} e^{-\lambda_{^{11}C} t} + A^{EOB}_{^{13}N} e^{-\lambda_{^{13}N} t} + A^{EOB}_{^{18}F} e^{-\lambda_{^{18}F} t}, \tag{4.6}$$

where the term corresponding to ^{18}F ($t_{1/2}$=109.77 min) has been included because it can be produced via the ^{18}O(p,n) despite the very low abundance of ^{18}O in oxygen, ranging between 0.001(87) and 0.002(22) [146, 147]. Although the production of ^{18}F can be studied, given the substantial variations in the isotopic abundances of ^{18}O in natural and terrestrial materials, the absolute values of the cross section of ^{18}O were not obtained in this work.

Figure 4.3 shows a few examples of the decay curves for PE, PMMA and nylon-6, two foils of each case. The fits reproduce very well the data and, in general, indicate a negligible constant term, as expected. As mentioned before, the parameters of the fit ($A^{EOB}_{^AZ}$) provide the activity per unit charge just after the irradiation for each of the produced β^+ emitters. Given the large count statistics acquired and the sufficient length of the measurements that allow reaching the background level, the uncertainty in the fit is in most cases negligible, i.e. less than 1%, as given by ROOT [143].

Regarding Figure 4.3:

- In the study of the production in carbon using the PE foils, ^{11}C is only produced in the first foil, whose energy is E_i=16.4(4) MeV, an energy close to the energy threshold of the reaction. In this case, both isotopes ^{11}C and ^{13}N contribute comparably to the total β^+ production, as shown in Figure 4.3 (a). In the rest of the PE foils, only ^{13}N is produced (Figure 4.3 (b)), reaching the negligible background level after approximately five ^{13}N half-lives.

- The production in oxygen was studied using PMMA foils, which contain both oxygen and carbon and therefore different reaction channels contribute to the production of the β^+ emitters ^{11}C and ^{13}N. Below 18 MeV, the main β^+ isotope produced on oxygen is ^{13}N via (p,α), which is shown to be clearly identified and quantified in Figure 4.3 (c,d). However, the production of ^{11}C is often comparable to that of ^{18}F, see (c), or even considerably lower, see (d). This results in quite large uncertainties in the determination of $A^{EOB}_{^{11}C}$, which changes significantly if both or neither the ^{18}F and background terms are considered, fixed or left free to vary. Therefore, the production cross section of ^{11}C in oxygen is not considered for this work.

- The production on nitrogen is studied using nylon-6 foils, which contains oxygen and carbon besides nitrogen. Below 18 MeV, the main β^+ isotope produced on nitrogen is ^{11}C (see Figure 4.3 (e,f)) via (p,α), which is observed very well above the ^{18}F and background level, which are negligible. Then ^{13}N is also clearly observed, but its origin is from oxygen via (p,α) rather than from ^{14}N(p,pn)^{13}N reactions.

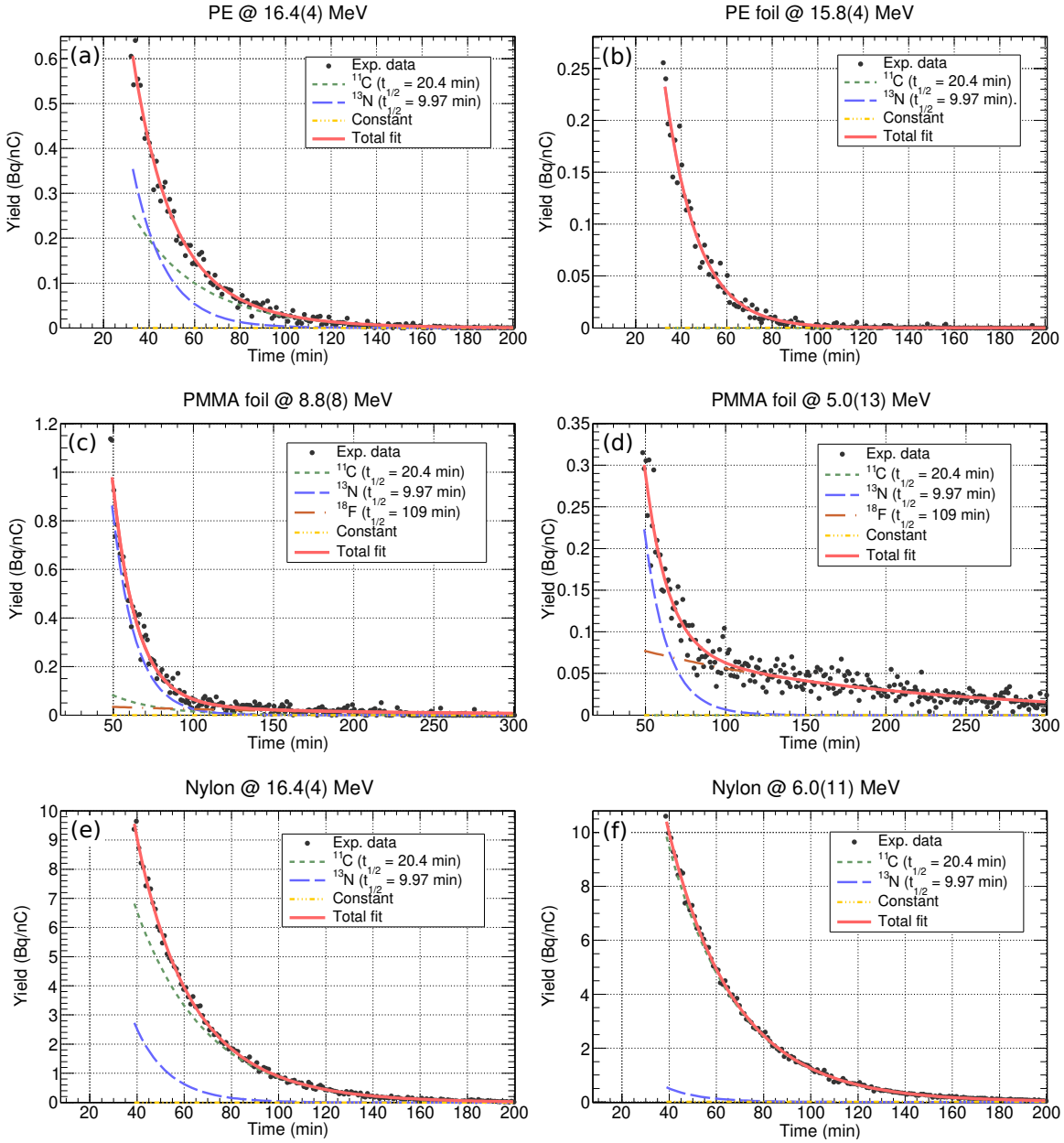

FIGURE 4.3: Decay curves for two PE (a,b), PMMA (c,d) and nylon-6 (e,f) foils measured with the PET scanner at CNA. The lines correspond to the total and partial contributions to the fit to Equation 4.6. For the sake of clarity, some decay curves are displayed only up to 200 min, although they are fitted up to 300 min.

4.4.2 Analysis of PE, SiO_2 and AlN foils at WPE and HIT

Above 18 MeV, the experiments to obtain the production cross section of the long-lives isotopes ^{11}C, ^{13}N and ^{15}O consisted on the irradiation of thin foils of PE, SiO_2 and AlN at HIT and WPE, as described in Sections 3.4.1.2 and 3.4.2.1.

Figure 4.4 and 4.5 show an example of the decay curves of the PE, SiO_2 and AlN foils irradiated at WPE (activity measured with a PET scanner) and HIT (activity measured with $LaBr_3$ detectors), respectively. The fits correspond to the production of ^{11}C, ^{13}N and ^{15}O, as:

$$A(t) = C + A_{^{11}C}^{EOB} e^{-\lambda_{^{11}C} t} + A_{^{13}N}^{EOB} e^{-\lambda_{^{13}N} t} + A_{^{15}O}^{EOB} e^{-\lambda_{^{15}O} t}. \quad (4.7)$$

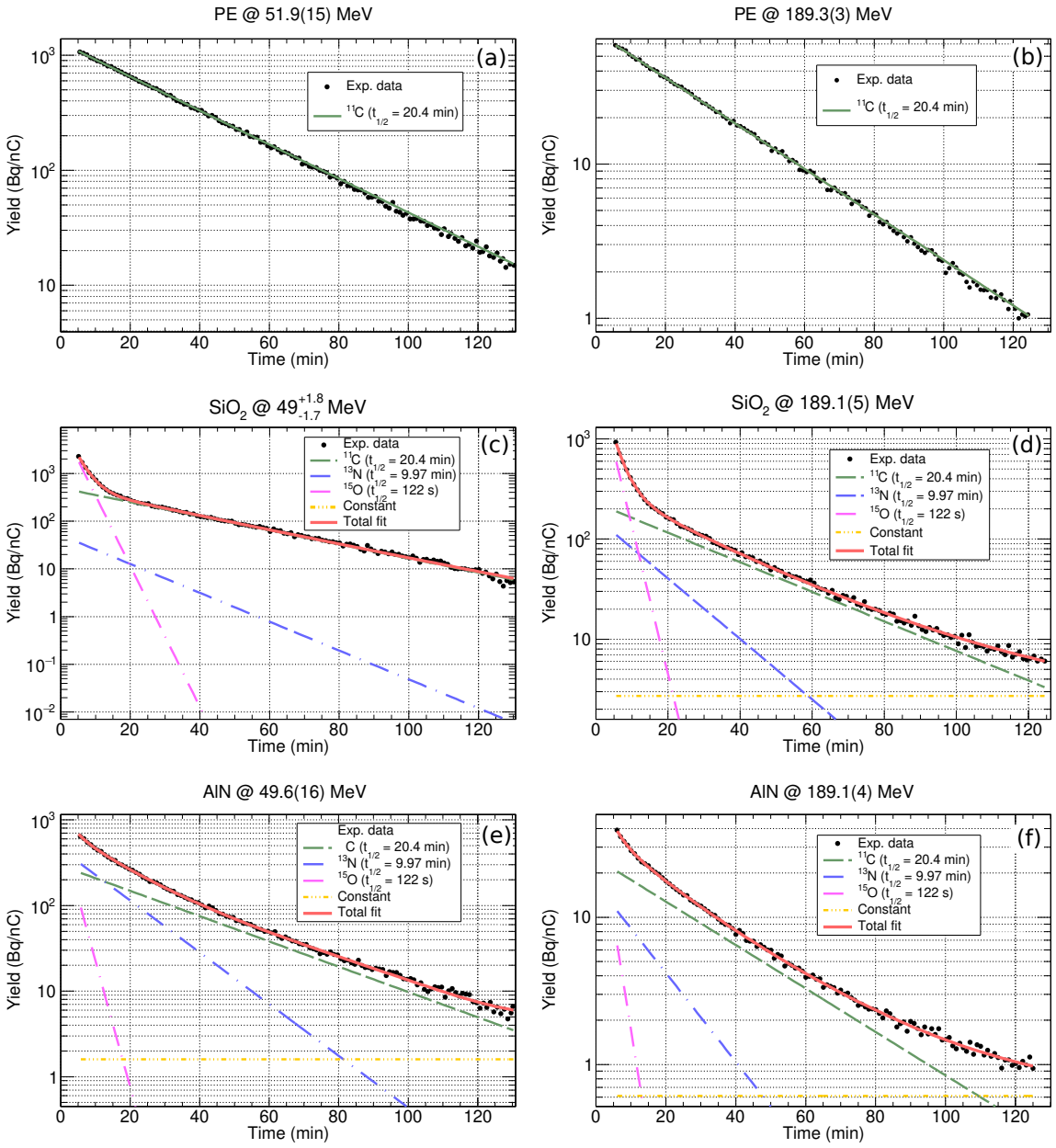

FIGURE 4.4: Decay curves for two PE (a,b), SiO_2 (c,d) and AlN (e,f) foils measured with the PET scanner at WPE. The lines correspond to the total and partial contributions to the fit to Equation 4.6. For the sake of clarity, some decay curves are displayed only up to 130 min, although they are fitted up to 250 min.

Compared to the case at CNA discussed above, the ^{15}O ($t_{1/2}$=122 s) has been included because the transport time was short enough for it to have a sizable contribution, and ^{18}F is not considered because its contribution was negligible above ~20 MeV.

Regarding the decay curves and fits for the data at WPE, corresponding to the energy from ~30 to 200 MeV, and shown in Figure 4.4, the data are nicely reproduced by the decay contributions of the three mentioned isotopes and the constant background term is negligible. The three isotopes under study are produced in SiO_2 and AlN foils, but with different probabilities depending on the beam energy: for instance, the production in AlN at 190 MeV (f) is about one order of magnitude lower than at 50 MeV (e). The figure illustrates how the decay curves are dominated by the decay of one or another isotope depending on the time interval, for instance in (c) the decay of ^{15}O dominates

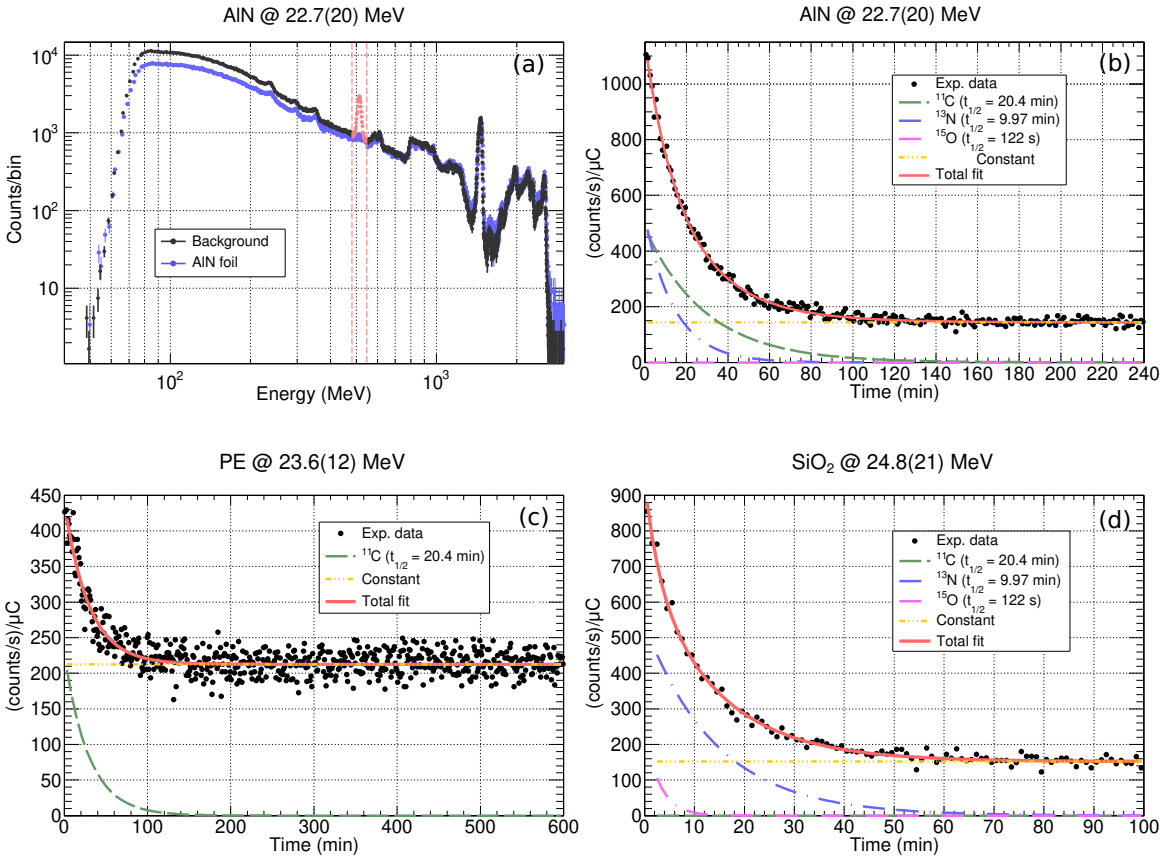

FIGURE 4.5: (a) Energy spectrum for an AlN foil measured at HIT. The read peak comes from the the 511 keV annihilation photons. The dotted red lines indicate the energy range. In black, the background energy spectrum. (b, c, d) Time spectrum of the 511 keV intensity peak for a AlN (b), PE (c) and SiO_2 (d) foils measured at HIT. The dash-dotted green, blue and pink lines show the fit of the decay of the ^{11}C, ^{13}N and ^{15}O, respectively. The dash-dotted yellow line represents the background level. The red line shows the total fit.

during the few first minutes, but eventually ^{11}C prevails.

The decay curves of the data at HIT, corresponding to the energy from ~20 to ~30 MeV, shown in Figure 4.5, are produced by integrating as function of the time the 511 keV peak observed in the deposited energy spectra of the $LaBr_3$ detectors, illustrated in the left panel of Figure 4.5 (a). The fits show nicely the contributions to the decay curves of the different β^+ emitters, but in comparison to the data from WPE a sizable background component is observed. This is related to the fact that the PET at WPE operates in coincidence mode, while the $LaBr_3$ observes only one of the 511 keV photons and hence is subject to all the background radiation whose Compton contributions fall within the 511 keV range. Nevertheless, the background is well assessed and has a negligible effect in the determination of the A^{EOB} values from the fits.

4.4.3 Analysis of PE, Ca and P foils at HIT

The half-lives of ^{12}N, ^{29}P and ^{38m}K is so short that there was not enough time to irradiate the targets and then bring them to a detection set-up. Hence the $LaBr_3$ detectors were installed looking at the targets in the beam line (see Figure 3.25) and the irradiation planning was adjusted to measure in beam-on/beam-off cycles with a length associated to the half-life of interest (see Section Section 3.4.2.2). In Figures 4.6 and 4.7 the top panel shows the energy deposited spectra in the detector during the beam on/off times, the middle panel shows the integral of the 511 keV peak as function of the time,

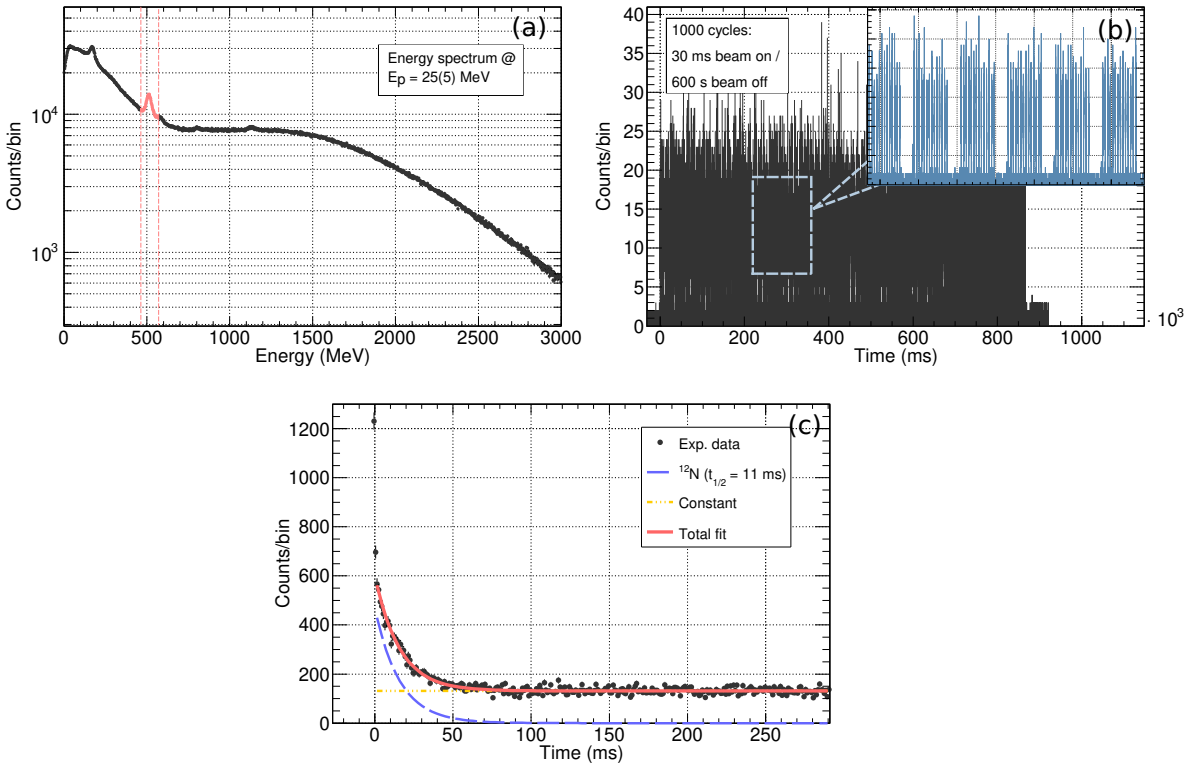

FIGURE 4.6: (a) Energy spectrum for a PE foil measured at HIT, with the red points and lines indicating the energy window to integrate the 511 keV peak of interest. (b) Time spectrum of the integrated peak. (c) Summed time spectrum. The dotted blue and yellow lines show the fit of the decay of the ^{12}N and the background level, respectively. The red line shows the total fit.

illustrating the beam-on/beam-off cycles employed for the study of each β^+ emitter, and the bottom panel shows the decay curve resulting from the sum of all the cycles. In all cases, the results reported later correspond to the average and standard deviation of all the cycles summed up and also, when the statistics allows, of the first and last cycles analyzed individually. In some random cycles, mostly in the very short ones, the DAQ could not stand the high counting rate registered during the beam-on periods and the subsequent beam-off cycles are corrupted, in which case they are neglected in the analysis.

Regarding the analysis of the decay curves in Figures 4.6 and 4.7:

- The production of ^{12}N ($t_{1/2}$=11 ms) in C was assessed with a PE target using 30 ms on/600 ms off duty cycle (see Figure 4.6). In this case, the production in each cycle is quite low and hence all cycles are summed and fitted to the production of ^{12}N plus a constant term, without any additional contribution.

- The production of ^{29}P ($t_{1/2}$=4.142 s) was assessed with a phosphorus target using a 5 s on/50 s off duty cycle (see Figure 4.7, c). The curve fits shows a clean ^{29}P contribution on top of a constant background. In addition, in the last cycle the beam-off period is longer, which served to validate the fitting with the longer-lived isotope ^{30}P ($t_{1/2}$=2.50 min).

- The production of ^{38m}K ($t_{1/2}$=924 ms) was assessed with a calcium target using as well a 5 s on/50 s off duty cycle (see Figure 4.7, d). In this case, it was necessary to include in the fit a

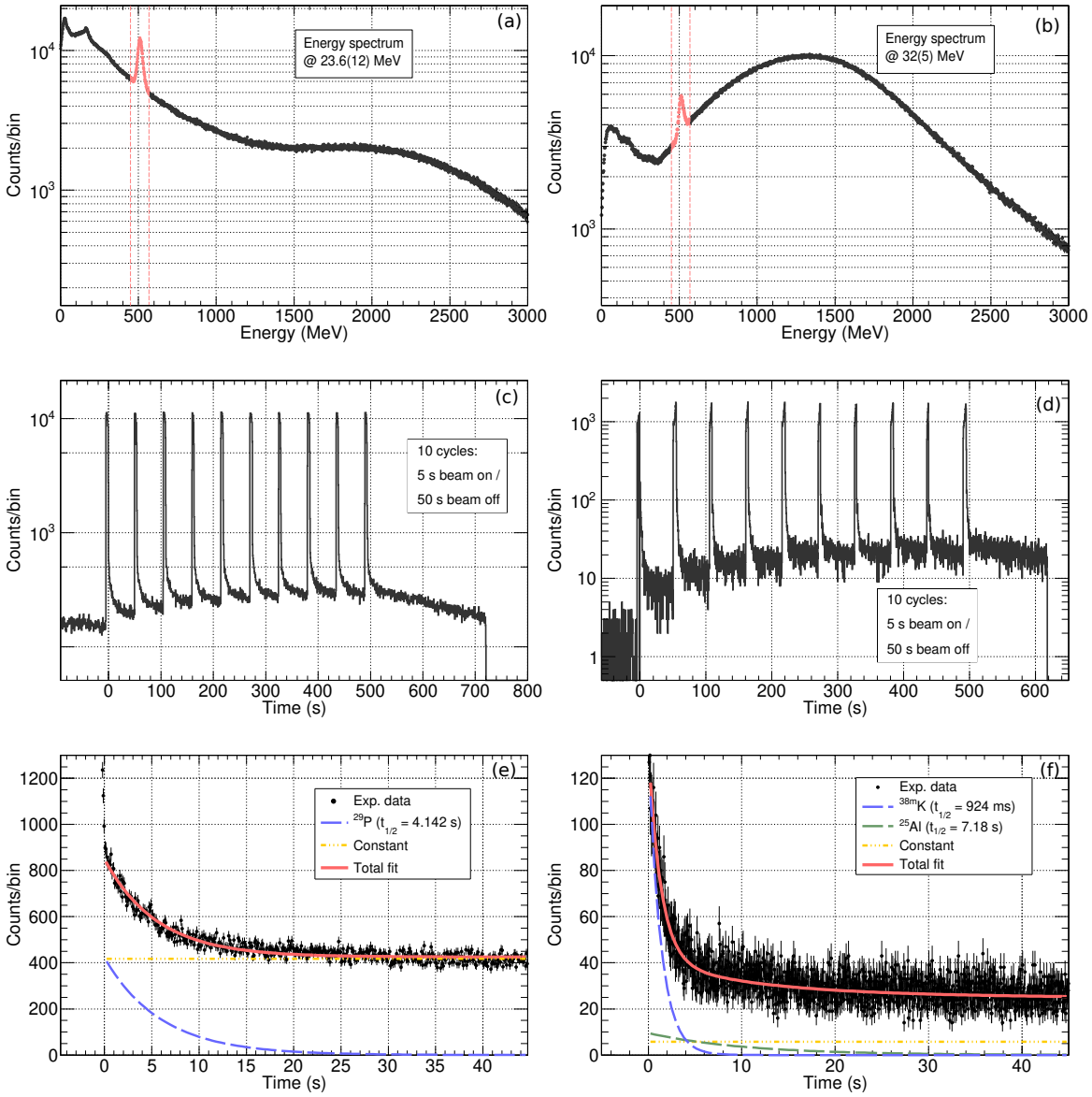

FIGURE 4.7: (a, b) Energy spectrum for phosphorus and calcium foils measured at HIT, with the red points and lines indicating the energy window to integrate the 511 keV peak of interest. (c, d) Time spectrum of the integrated peak, showing the corresponding cycles. (e, f) Summed time spectrum. The dotted lines show the fit of the decay of the ^{29}P, ^{38m}K or ^{37}K. The yellow line shows the background level. The red line shows the total fit.

slight contribution from ^{25}Al ($t_{1/2}$=7.183 s) produced in the Mg impurities of the Ca target: if not included the production of ^{38m}K is overestimated by up to 10%.

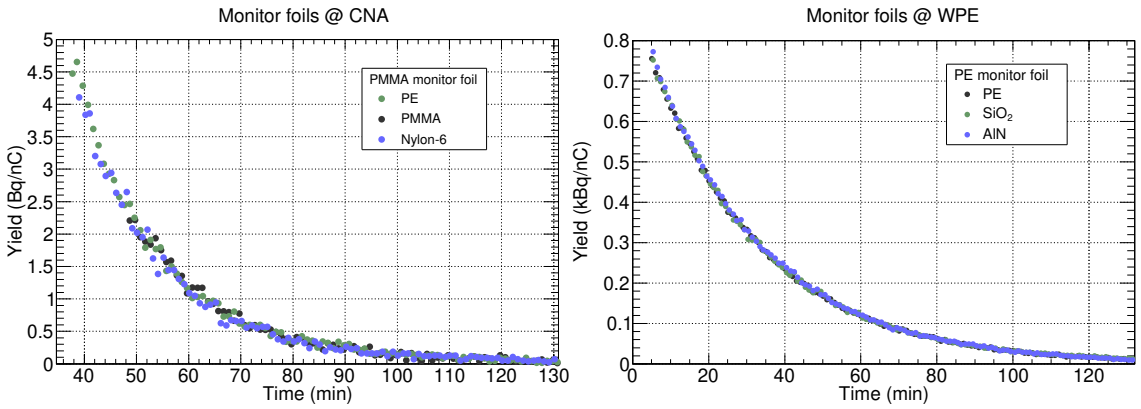

FIGURE 4.8: Decay curves of the monitor PMMA and PE monitor foils irradiated at CNA (18 MeV) and WPE (150 MeV), respectively. In addition to the normalization to the integrated beam current, the curves are corrected for the decay during the irradiation and the time offset related to the corresponding transport times.

TABLE 4.4: A^{EOB} values corresponding to the monitor foils employed at CNA and WPE.

Facility	E_i (MeV)	A^{EOB}			Standard deviation
		PE	$PMMA/SiO_2$	Nylon-6/AlN	
CNA	18	57(62) Bq/nC	61(3) Bq/nC	56(3) Bq/nC	4.5%
WPE	100*	1.16(4)	1.12(4) kBq/nC	1.16(5) kBq/nC	1.8%
WPE	100	0.92(4)	0.94(4) kBq/nC	0.96(4) kBq/nC	1.7%
WPE	150	0.92(4)	0.94(4) kBq/nC	0.92(4)kBq/nC	0.88%
WPE	190	0.69(3)	0.67(3) kBq/nC	0.68(3) kBq/nC	1.5%

* *A 40 mm PE degrader was placed in front of the first monitor to bring the initial energy of 100 MeV down to ~60 MeV.*

4.5 Validation measurements and results

4.5.1 Validation with monitor foils

As discussed in Section 3.4.3.1, the first foil in each stack of the multi-foil experiments at CNA and WPE was of PMMA and PE, respectively. These monitor foils were measured simultaneously with the rest of the foils with the PET scanner.

The activity curves corresponding to CNA (18 MeV beam energy) and one of the irradiation at WPE (150 MeV beam energy) are displayed in Figure 4.8. The data have been previously corrected by the decay during the irradiation and a time offset corresponding to the time needed to transport the irradiated foils from irradiation room to the PET scanner. The clear agreement between the activity of the different foils validates simultaneously the reproducibility of the beam current measurement and the corrections related to the decay during irradiation and transport. As summarized in Table 4.4, the level of agreement between the A^{EOB} values is 4.5% at CNA and better than 2% at WPE, uncertainties that are later considered in the overall accuracy assessment of Section 4.7.

4.5.2 Validation with the IAEA monitor reaction ^{nat}Cu(p,x)^{63}Zn

Among the available reference cross sections for charged-particle monitor reactions evaluated recently by the IAEA [145], the ^{nat}Cu(p,x)^{63}Zn reaction has been used in this work.

The experimental set-up for the copper irradiation in each facility was described in Section 3.4.3.2. The resulting decay curves are fitted to the sum of three exponentials, corresponding to the production

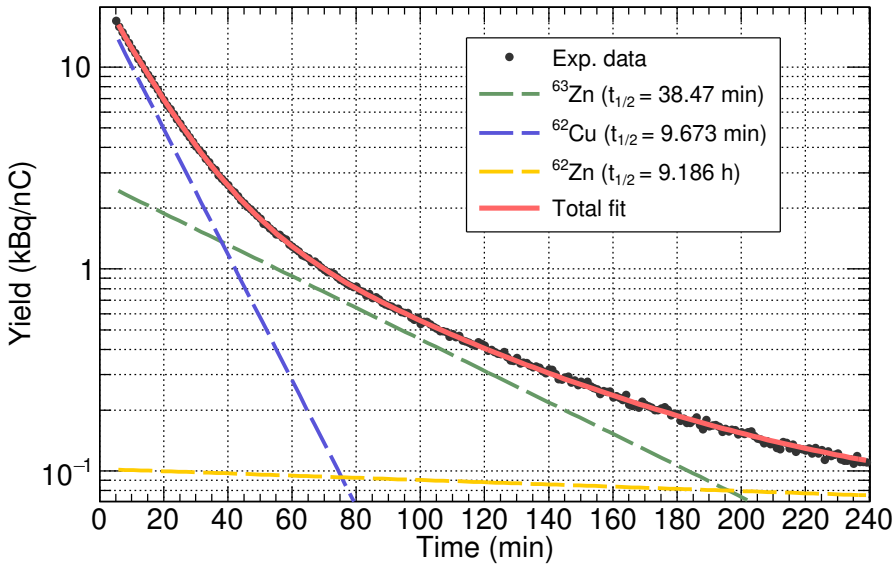

FIGURE 4.9: Production yields for the ^{nat}Cu target at WPE. The dotted green, blue and yellow lines show the fit of the decay of the ^{63}Zn, ^{62}Cu and ^{62}Zn, respectively. The red line represents the total fit.

of ^{63}Zn ($t_{1/2}$=38.47 min), ^{62}Cu ($t_{1/2}$=9.673 min) and ^{62}Zn ($t_{1/2}$=9.186 h):

$$A(t) = C + A^{EOB}_{^{63}Zn} e^{-\lambda_{^{63}Zn} t} + A^{EOB}_{^{62}Cu} e^{-\lambda_{^{62}Cu} t} + A^{EOB}_{^{62}Zn} e^{-\lambda_{^{62}Zn} t}, \tag{4.8}$$

As an illustrative example, the activity curve at WPE and the corresponding fit to Equation 4.8 are shown in Figure 4.9.

The experimental values are then compared to the expected ^{63}Zn production yields calculated as the convolution of the IAEA reference cross section with the proton energy distribution incident in the corresponding Cu target, which is calculated with Geant4 after the degradation occurred upstream for the Cu targets. The experimental and calculated values are summarized in Table 4.5:

- At CNA, the measured thick target physical yield is 2.24(10) kBq/nC, 11% larger than the IAEA evaluation for ^{63}Cu(p,n)^{63}Zn for 16.7 MeV protons. As mentioned in Section 4.3, the beam dump where the beam current was measured at CNA was not suppressed for secondary electrons, and hence the IAEA monitor reaction is used for normalization purposes: i.e. the measured integrated currents are scaled up by a 1.11 value.
- At WPE, the measured and expected thick target physical yields differ by only 4%, which is actually the quoted accuracy of the monitor reaction cross section.
- At HIT, two different copper targets were measured. In both cases, the measured and expected thick target physical yields are also in a very good agreement, 4 and 6%.

Considering that the ^{nat}Cu(p,x)^{63}Zn cross section is an IAEA monitor cross section featuring low uncertainties, these results serve as validation of the measuring technique, the analysis strategy and corrections applied for both experiments; it validates the beam current measurements, the detection efficiency calculation and the decay corrections.

TABLE 4.5: Comparison between the IAEA and experimental production yields of the ^{nat}Cu(p,x)^{63}Zn reaction

Experiment	Target with which it is irradiated	Y_{exp} (kBq/nC)	Y_{theo} (kBq/nC)	Ratio
CNA	-	2.24(10)	2.01(8)	1.11*
WPE	SiO_2	2.72(11)	2.62(11)	1.04
HIT	PE	2.28(8)	2.38(10)	1.04
HIT	AlN	2.16(7)	2.28(9)	1.06

* *This value is used as normalization for the CNA measurements (see text for details)*

4.5.3 Validation with thick vs. thin multi-foil targets

Since the multi-foil activation technique combined with the subsequent PET measurements were first applied in this work, a complementary measurement to obtain the thick target production yields using conventional detectors was performed to validate the results from the differential measurements in the PET scanner. The experimental procedure is described in Section 3.4.3.3.

In the case of the Nylon-6 target, the production of ^{11}C was determined as 502(17) Bq/nC. The corresponding value from the PET measurement, obtained as the sum of the activities of each one of the individual foils, amounts to 520(30) Bq/nC. In the case of PMMA, the integral production of ^{13}N was determined as 709(23) Bq/nC, and the corresponding value from the PET measurement as 760(40) Bq/nC.

Both PET measurements are in agreement with the value from the thick target within 4% and 7%, respectively. The average deviation of the integral and PET measurement (5%) is assumed by the uncertainty related to the reproducibility of the irradiations, hence validating the use of a PET scanner as a detector capable of making accurate absolute activity measurements. This is remarkable considering that the attenuation corrections are very different in both set-ups: 2 mm of lead in the stand-alone scintillator detector case (accounted for via Geant4 simulations) vs. several centimetres of polyethylene plus the bed in the PET scanner (accounted for the PET reconstruction software using the corresponding CT image).

4.6 From activity to cross sections

The reaction cross section at a specific beam energy of the beam traversing a thin foil is calculated using Equation 3.14, from the corresponding yield calculated in Equation 4.4, resulting in:

$$\sigma_{j\rightarrow i} = \frac{A_i^{EOB}}{I_p \cdot t_{irr} \cdot \lambda_i \cdot n_j}, \tag{4.9}$$

where A^{EOB} is the activity at the *end of bombardment*, j and i stand for the seed and produced isotope, n_j is the surface density (atoms/barn) of the isotope j, p_j is the isotopic relative abundance, $I_p \cdot t_{irr}$ is the integrated beam current, and λ_i is the decay constant of i.

However, the PMMA and Nylon-6 foils used at the CNA experiments are not "pure" foils of oxygen and nitrogen, as they contain also carbon, and oxygen and carbon, respectively, which also contribute to the production of ^{11}C and ^{13}N. Therefore the production yield in oxygen and nitrogen were obtained, respectively, by subtracting the carbon contribution (obtained previously from the PE films) from PMMA and the carbon and oxygen contributions (obtained previously with the PMMA foils) from Nylon-6. The production cross section of ^{11}C and ^{13}N in ^{12}C, ^{16}O and ^{14}N can be written as:

$$\sigma_{j\to i} = \frac{A_i^{EOB}}{I_p \cdot t_{irr} \cdot \lambda_i \cdot n_j} - \sum_{k(k\neq j)} \frac{n_k \cdot \sigma_{k\to i}}{n_j}, \tag{4.10}$$

where the terms with k refer to the other isotopes from which i can be produced.

The subtraction term in Equation 4.10 for the experiments at CNA is case dependent:

- ^{12}C(p,*): nothing needs to be subtracted.
- ^{16}O(p,3p3n)^{11}C: only extra ^{12}C(p,pn)^{11}C contribution to be considered. The subtraction term is lower than 1%, as the production in carbon is negligible.
- ^{16}O(p,α)^{13}N: only extra ^{12}C(p,γ)^{13}N contribution to be considered. The subtraction term ranges between 3% and 9%, except below 7.7(6) MeV, where it is increased up to 24%.
- ^{14}N(p,α)^{11}C: only extra ^{16}C(p,3p3n)^{11}N contribution to be considered, as the carbon contribution is negligible. The subtraction term is lower than 2%.
- ^{14}N(p,pn)^{13}N: only extra ^{16}O(p,α)^{13}N contribution to be considered, while the carbon contribution is negligible. The contribution from ^{16}O is so important, >70% and higher at all energies, that this reaction is not considered.

The experiments at WPE and HIT are not affected by this issue, since the foils used in both facilities were “pure” foils of carbon (PE), oxygen (SiO_2) and nitrogen (AlN), and pure foils of phosphorus and calcium. SiO_2 and AlN foils were chosen and are considered “pure” because silicon and aluminum do not contribute to the production of the long-lived isotopes under study in this work.

4.7 Estimation of systematic uncertainties

The systematic uncertainties of the reported cross sections resulting from this work have contributions from the detection efficiency (of the PET or the $LaBr_3$ detectors in each case), the uncertainty in the foil thickness, the accuracy of the measurement in the beam current, and the corrections due to the decay during the irradiation and transport (always less than 0.5%, so it is neglected in the discussion below).

The different contributions mentioned are summarized in Table 4.6 for each one of the experimental setups used to measure the reaction cross sections of the long- and short-lived isotopes. Following the rules of systematic error propagation via quadratic sum, the individual uncertainties add up to a combined total systematic cross section uncertainty ranging between 4.6% and 6%. In addition to these general considerations, each cross section value has an additional contribution of statistical nature from the fit (given by ROOT [143]), which depends on each specific fit.

Overall:

- At CNA, the best accuracy reached amounts to ~6.1%, with contribution from the uncertainties of the spatial dependence of the PET scanner efficiency (4.5%), the foil thickness (1%) and the normalization of the integrated beam current using the mentioned ^{nat}Cu(p,xn)^{63}Zn current integrator (4%). In this case, the total uncertainty has also contribution from the subtraction of the competing reactions mentioned in the previous section (see Equation 4.10).
- At the WPE experiment, the best accuracy reached amounts to ~4.6%, with contributions from the uncertainties of the spatial dependence of the PET scanner efficiency (3%), the activity of the ^{22}Na calibration source (1.5%), the foil thickness (1%) and the beam current measurement (1%).

TABLE 4.6: Systematic uncertainties contributing to the overall accuracy of the reaction cross section measured in this work.

Experiment	Detection efficiency	Foil thickness	Beam current	Total
CNA	4.5%	1%	4%	6.1%
WPE	4.4%	1%	1%	4.6%
HIT	2.2%	1%	5%	5.6%

- At HIT, the best accuracy is ~3%, with contribution from the uncertainties of the detection efficiency at a specific target-detector distance determined from the Geant4 simulation (1.7%, see Section 4.1), the ^{137}Cs and ^{60}Co used to characterize the detector size (1% in both cases), the foil thickness (1% when shipping by the manufacturer, and almost 3% for the "home-made" phosphorus targets) and the beam current measurement (5%).

Overall, the quoted systematic uncertainties allow reaching an accuracy of a few percent that is in the order of that of the IAEA reference cross sections. Furthermore, for the particular purpose PET range verification in proton therapy, the shape, i.e. the dependence with the proton energy, of the cross sections is more important than the actual absolute value. In this respect, the uncertainties reported herein do not feature a dependence with the beam energy and hence provide a very accurate "pure" cross section. This is demonstrated through the very good agreement between different experiments (irradiation energies and/or facilities) in the energy regions where they overlap, as it is discussed in detail in the next chapter.

Chapter 5

Resulting cross sections and their impact in PET range verification

This chapter presents the results of the reaction cross sections of the long-lived ^{11}C, ^{13}N and ^{15}O in carbon, oxygen and nitrogen, and the short-lived ^{12}N, ^{29}P and ^{38m}K in carbon, phosphorus and calcium, respectively. While the detailed cross section values are listed in Appendix A, figures of each reaction are presented individually and compared with the data available in the literature, both the experimental and evaluated values. Then, calculations of the activity induced in phantoms of different materials are shown to illustrate the effects and implications of the new data for the implementation of PET beam range verification in proton therapy.

THE CROSS SECTIONS for all the reactions of interest have been calculated from the production yields using Equation 3.14. The data presented herein have been obtained either by the multi-foil activation technique combined with the measurement with a PET scanner or by single activation and measurements using conventional detectors. Both experimental procedures are described in Chapter 3, while the data analyses and the corrections applied are discussed in Chapter 4.

In the following, the results of this work for the production of ^{11}C, ^{13}N and ^{15}O on C, N and O, and and the production of ^{12}N, ^{29}P and ^{38m}K in C, P and Ca, respectively are presented and discussed separately. The cross section obtained for each particular reaction is discussed individually and compared to the experimental and evaluated data available in the literature (ENDF and JENDL). Regarding the evaluations, it should be noted that the original evaluated data of the ENDF/B-VIII.0 library is considered but, in order to cover the full energy range of interest, the corresponding ICRU63 extrapolation beyond 150 MeV has been included.

Along the cross sections comparisons, the energy thresholds are also discussed in detail because they are of especial interest for PET range verification. This is discussed in the last section, which contains realistic calculations of activation of phantoms to illustrate the impact of the new cross section data in PET range verification.

5.1 Production cross sections of long-lived β^+ emitters

Although the approach to measure the β^+ emitters' production cross sections via the determination of the 511 keV photons followed in previous works is comparable to the standard one, also followed in this work, the methodology (multi-foil vs. single-foil irradiation, PET scanner vs. conventional scintillator detectors, and different experimental facilities) is quite different. Our complete data set includes data from different facilities using different approaches. Also, the multi-foil activation combined with PET acquisition is an innovative strategy that allows to measure multiple cross sections points as a function of the proton energy with a single irradiation and single activity measurement.

Therefore, several validation strategies have also been followed in order to validate the developed technique and our results: monitor foils (see Section 4.5.1), measurement of a standard IAEA reaction cross section (see Section 4.5.2), cross-check of differential yields with integral yields (see Section 3.4.3.3), then enhancing the confidence in the obtained cross section data.

The results of the production cross sections at low energy measured at CNA, i.e., in the Bragg peak region, have been published in [148]. The production cross sections obtained at HIT and WPE at higher energies have been published in [149]. These publications include the point-wise values of the reaction cross sections, which can be also found in Appendix A.

5.1.1 ^{12}C(p,x)^{11}C reaction

There are quite some data sets in the literature for the ^{12}C(p,x)^{11}C reaction, as it has been previously considered for instance as reference cross section [150] or as a proxy for beam monitoring in proton therapy [151]. However, all previous experiments cover only a restricted energy range.

From Figure 5.1 one can observe two main groups of data: one including the data of Hintz et al. (1952) [115], Aamodt et al. (1952) [108], Bäcker et al. (2019) [104], and another one with Gauvin et al. (1962) [109], Matsushita et a. (2016) [116] or Horst et al. (2019) [105]; the latter being about 15 to 25% lower than the first one, even though there are recent works in both groups. It is noticeable that the two most recent data sets, reported by Bäcker et al. [104] and Horst et al. [105], show differences beyond

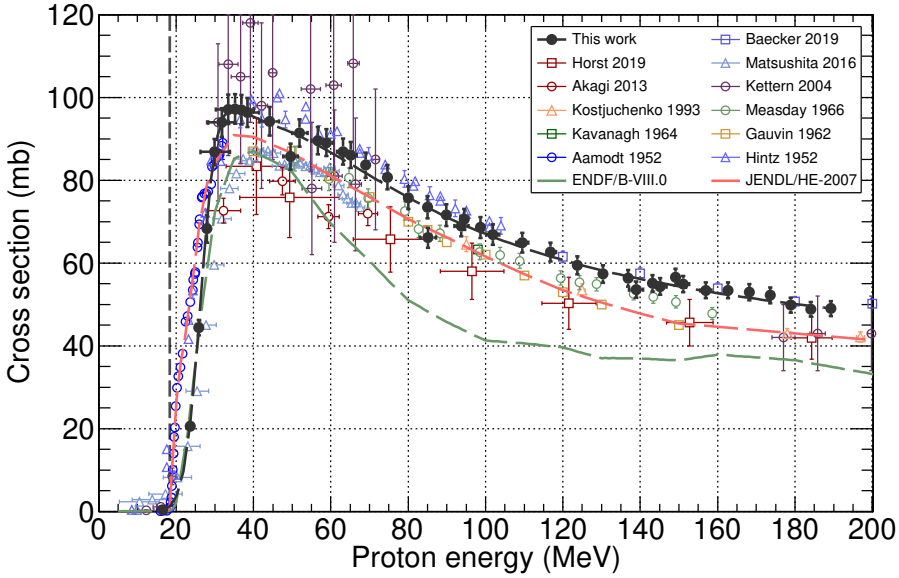

FIGURE 5.1: Cross sections for the production of ^{11}C on C.

15% around 100 MeV. Furthermore, all measurements indicate an underestimation by the ENDF/B-VIII.0 library. This situations illustrates the need of new data with enhanced accuracy covering the full range of interest, as done in this work.

Since the energy threshold of this reaction is 17.9 MeV, ^{11}C was only produced in the first foil of the multi-foil assembly in the experiment at CNA, whose energy is E_i=16.4(4) MeV, as illustrated in Figure 4.3 (a). At higher energy, the experiments at HIT and WPE provided three and forty cross section values, respectively. As shown in Figure 5.1, the cross section reported herein is in very good agreement with the higher cross section data group mentioned before i.e. with Hintz et al. (1952) [115], Aamodt et al. (1952) [108] and, the more recent, Bäcker et al. (2019) [104].

While deviations of the cross section values obtained in the present experiments from values published in the 1950s may not be particularly surprising, the deviation from the cross section at energies higher than 100 MeV reported very recently (2019) by Horst et al. [105] is noteworthy, since these are important energies for proton therapy dosimetry and the differences are in the range of 15%, which is significant considering the quoted uncertainties.

5.1.2 ^{16}O(p,x)^{11}C reaction

The ^{16}O(p,x)^{11}C production channel has been less investigated than others in previous studies, but it is also of interest in PET range verification, as about the 65% of the human body is composed by oxygen.

As illustrated in Figure 5.2, the previous data from Albouy et al. (1962) [110], Kettern et al. (2004) [152], Akagi et al. (2013) [153] and Masuda et al. (2018) [154] show significant discrepancies, with differences up to 40% in the low energy region (~50 MeV) and even larger discrepancies right above the reaction threshold.

Considering the sizable uncertainty (~20%) of the only data available up to around 200 MeV (Kettern et al. 2004), the new data presented herein are in a reasonable agreement with them; indicating a ~25% overestimation and ~20% overestimation of the ENDF/B-VIII.0 and JENDL evaluations, respectively. The latter are based in the data of Albouy et al. (1962), which seems to be clearly far form

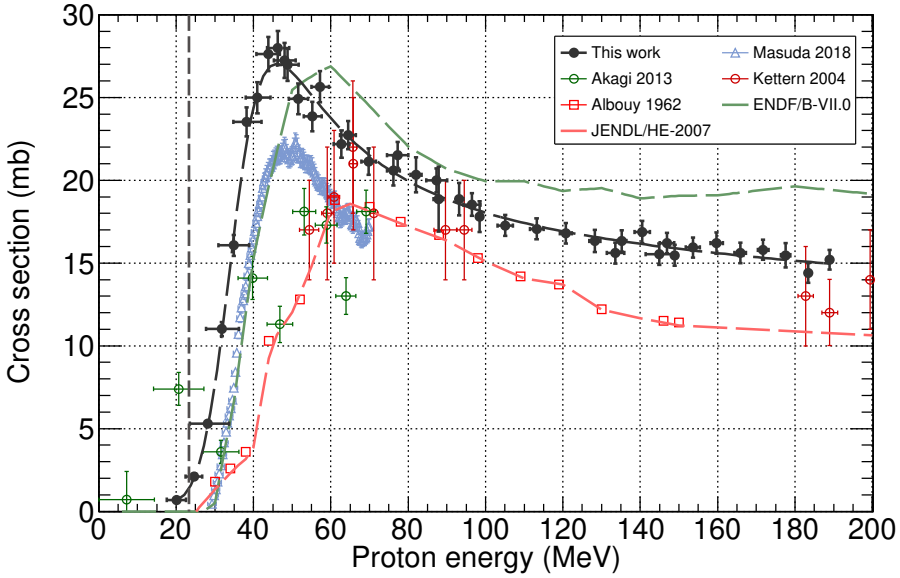

FIGURE 5.2: Cross sections for the production of ^{11}C on O.

the expected behaviour near and right above the 24 MeV threshold. Regarding more recent data, the data of Akagi et al., (2013) show inconsistencies between neighboring data points and a sizable cross section even below the threshold. Last, it seems that the previous most recent data (Masuda et al., 2018) underestimate the reaction cross sections, with a starting point considerably above the energy threshold. Overall, the cross section values measured in this work represent the most complete data set, covering the whole energy range of interest from threshold up to 200 MeV, showing sizable differences with previous data and evaluations in both shape and absolute value in the region right above the reaction threshold, which is the region closest to the Bragg peak and hence of most importance for PET range verification.

5.1.3 ^{14}N(p,x)^{11}C reaction

Nitrogen is the fourth most abundant element in the body after oxygen, carbon, and hydrogen. Regarding the production of ^{11}C in N, although it is not as significant as the one in C or O, the ^{14}N(p,x)^{11}C reaction features a threshold of only 3.1 MeV, which makes it the dominant reaction for ^{11}C production at low proton energies, i.e. below the reaction thresholds around 20 MeV of the other reactions, hence at the very end of the beam range.

In relation to its low threshold, this is the main reaction used to produce ^{11}C for PET diagnostics. Therefore there is an IAEA evaluation, which is based on nine of the thirteen data sets available in EXFOR in the region below 25 MeV: Blaser et al. (1952) (scaled up by 30% and shifted by -0.7 MeV) [155], Nozaki et al. (three data sets) (1966) [156], Jacobs et al. (1974) [157], Ingalls et al. (1976) [158], Casella et al. (1978) [159], Bida et al. (1980) (5 data points were removed)[160] and Köhl et al. (1990) (scaled down by 29%) [161]. This data sets with a total of 306 cross section values was used as input for a least-squares Padé fit with 75 parameters, which provided and analytical shape with accuracy between 60% around 5 MeV, which decreases to better than 8% between 13 and 28 MeV and rises again up to 10% at the highest energy [162].

The evaluation is displayed in Figure 5.3, together with the individual unmodified data sets and the results of this work from the experiments at low energy performed at CNA. After the mentioned

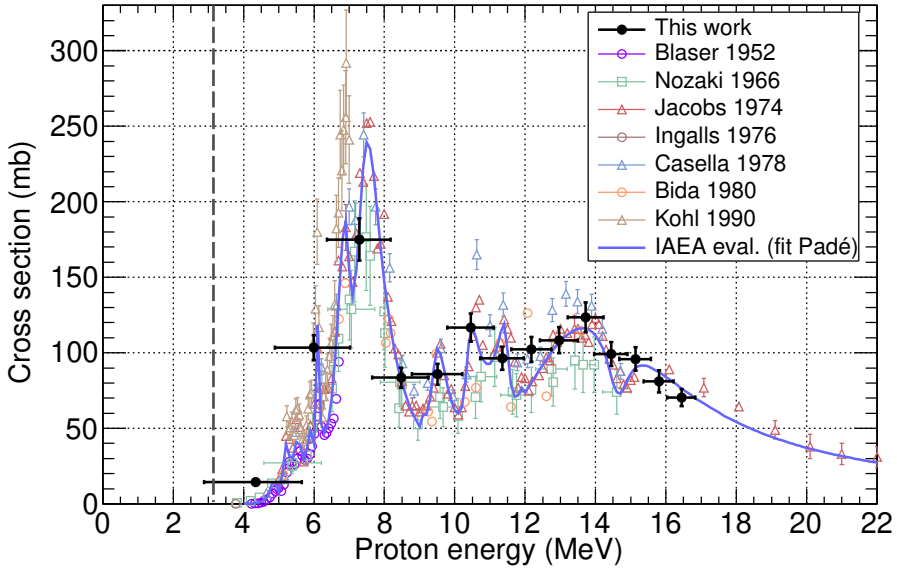

FIGURE 5.3: Cross sections for the production of ^{11}C on N, including selected data from EXFOR for the IAEA evaluation and the corresponding recommended curve.

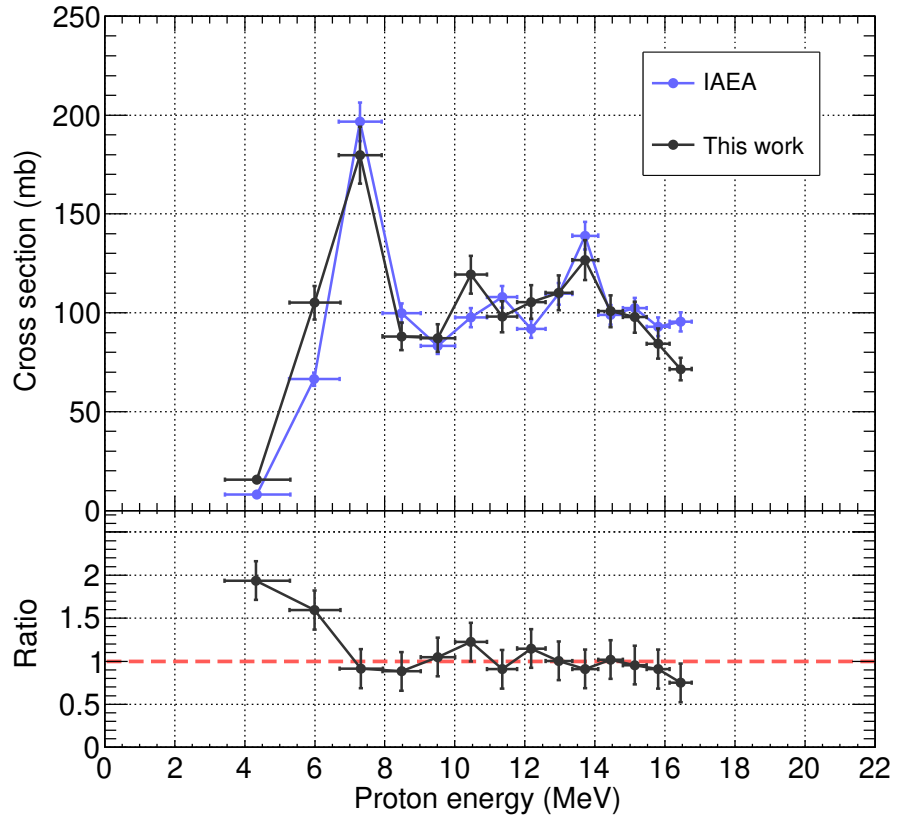

FIGURE 5.4: Experimental and evaluated data considering the energy intervals of our measurement and ratio with respect the evaluation for ^{14}N(p,x)^{11}C reaction.

modifications, the deviations of the selected data sets from the evaluation are on average 4%. The uncertainty of the point-wise cross section values of the evaluation is not given in [162], so we consider as the uncertainty bars for this IAEA evaluation in Figure 5.4 the deviations of the selected data sets

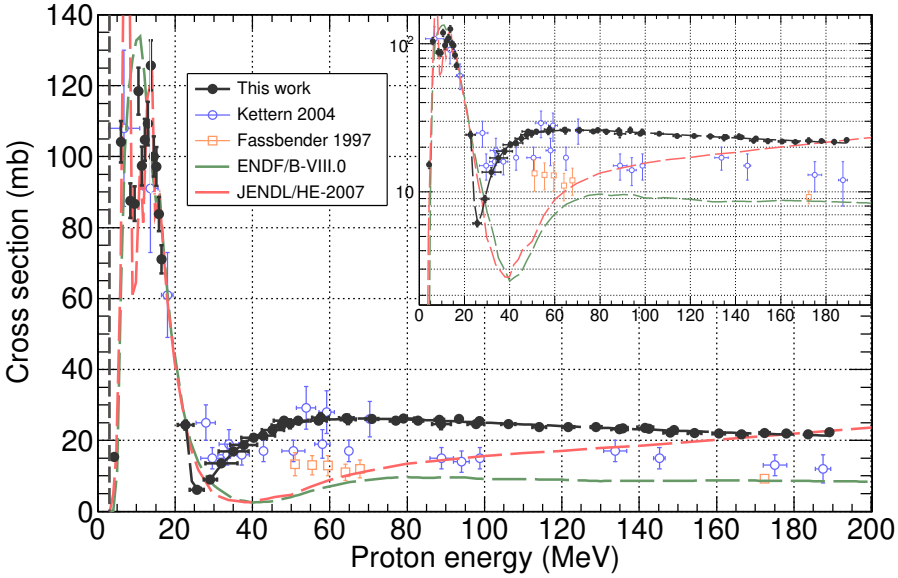

FIGURE 5.5: Cross sections for the production of ^{11}C on N.

from the evaluation curve.

Our measurement reproduces the resonance structure quite well, even with the limited resolution of our method at low energies, i.e. at the very end of the proton beam range. However, the graphical representation of Figure 5.3 can be misleading in the sense that the experimental data (in particular in this work) are integrated over an energy interval (shown as a error bar in the ex axis) corresponding to the proton energy distribution in each thin foil, and hence they cannot be directly compared with the analytical curve of the evaluation. Therefore, the evaluation has been convoluted with the energy distribution inside each foil, i.e., in the energy intervals defined by our data points, resulting in the values displayed in Figure 5.4. The cross section ratios displayed in the bottom panel of Figure 5.4 illustrate the good agreement of our data with the evaluation, with sizable discrepancies only in the two lowest energy points at the tail of the resonance, thus having a very limited overall impact. On average, considering the ratio weighted by the energy distribution in each foil, the agreement between our results and the evaluation is a remarkable 2%.

At higher energies, the state-of-the-art for the ^{14}N(p,x)^{11}C reaction is considerably different because there is almost no previous experimental data. As it can be seen in Figure 5.5, there are only two data sets between 20 and 200 MeV, being our data well above those of Fassbender et al. (1997) [163] and, compared to the recent data of Kettern et al. (2004) [152], not far below ~70 MeV but as much as a factor two larger beyond 80 MeV.

5.1.4 ^{12}C(p,x)^{13}N reaction

Figure 5.6 displays the production cross section of ^{12}C(p,x)^{13}N, which features no threshold, obtained from 2 to 16.4 MeV at CNA. The only other existing data are from Cohen et al. (1955) [164], with only two data points without quoted uncertainties which are significantly above our data. The cross section is indeed very small, in the 1 mb range, but the results form this work are considered accurate even for such a small cross sections because: (a) The data correspond to the activation of the polyethylene and hence there is no other progenitor for producing ^{13}N, and (b) the decay curve shows only the ^{13}N contribution (except for some ^{11}C in in the first), which allow for a very accurate fit.

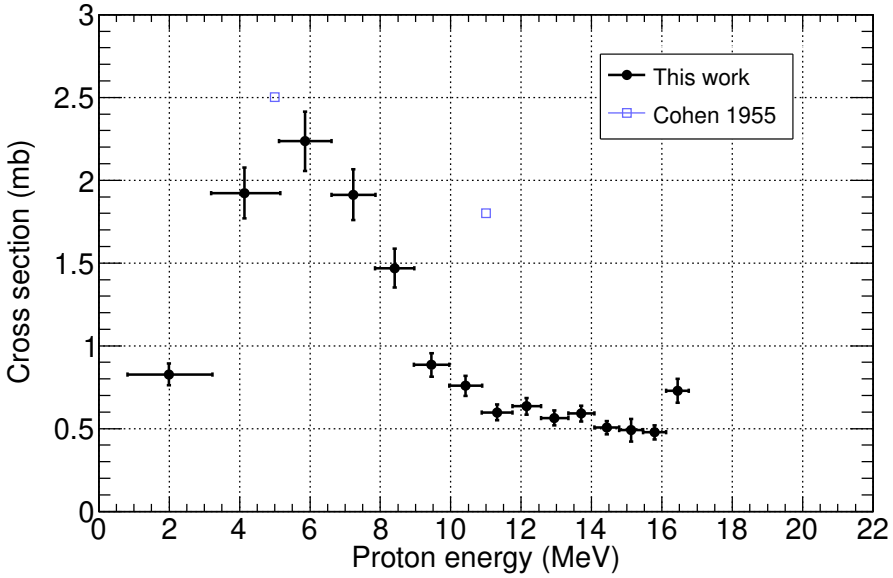

FIGURE 5.6: Cross sections for the production of ^{13}N on C.

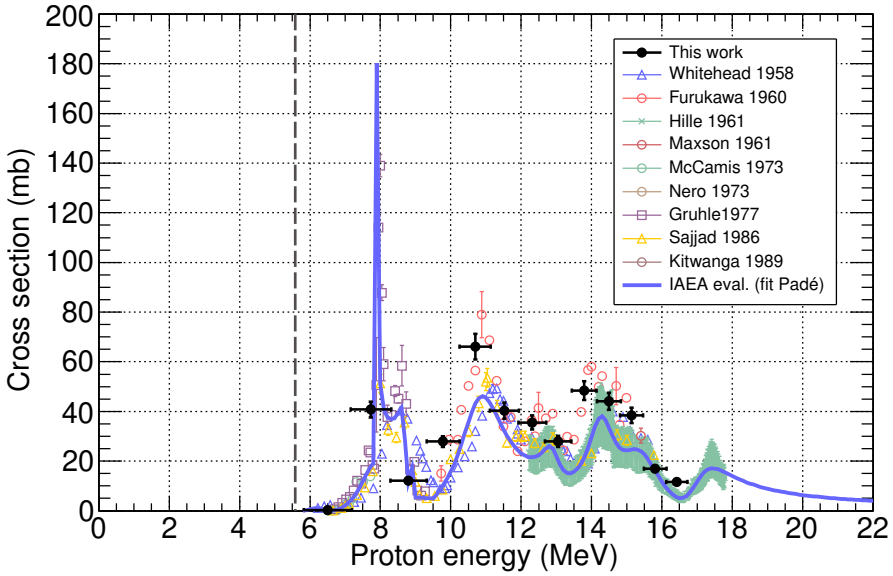

FIGURE 5.7: Cross sections for the production of ^{13}N on O, including selected data from EXFOR for the IAEA evaluation and the corresponding recommended curve.

At higher energies, no production of ^{13}N is observed when irradiating PE foils. This is illustrated in Figure 4.4 and 4.5 for a selection of foils irradiated at WPE and HIT, respectively, featuring only contributions from ^{11}C and not from ^{13}N.

5.1.5 ^{16}O(p,x)^{13}N reaction

As in the case of ^{14}N(p,x)^{11}C, there is an IAEA evaluation below 30 MeV for the ^{16}O(p,x)^{13}N reaction related to the production of ^{13}N for PET diagnostics. In this case, the evaluation is based in ten of the fourteen data sets available up to 35 MeV, including the data of Whitehead et al. (1958) [165] (shifted by -0.3 MeV), Furukawa et al. (1960) (scaled down by 30%) [166], Hille et al. (1961) [167], Maxson et

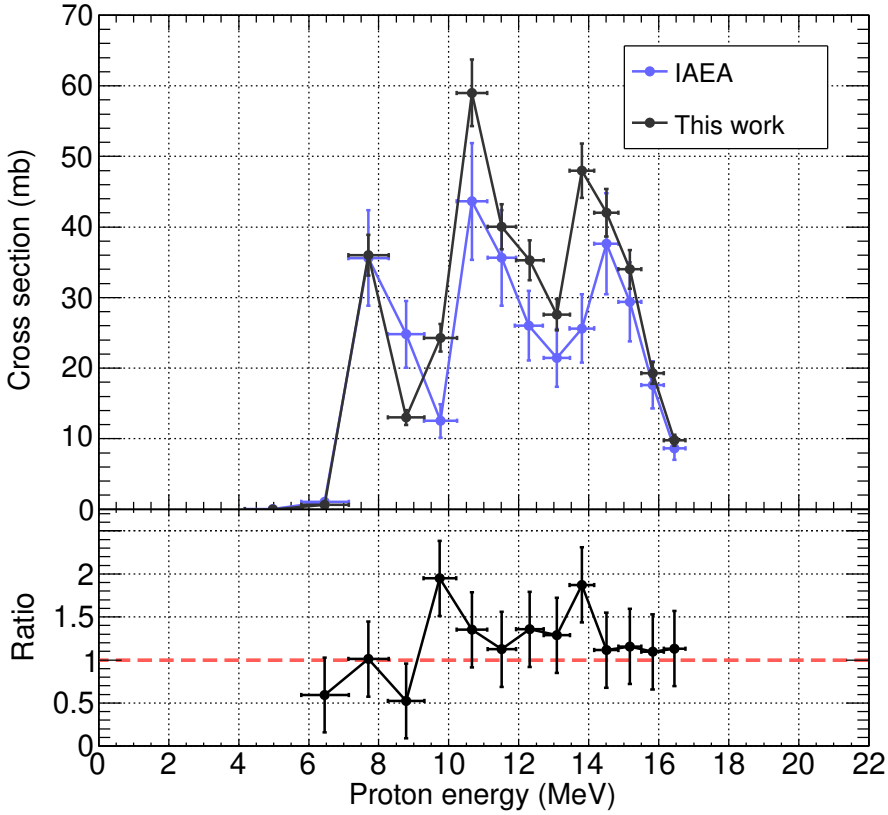

FIGURE 5.8: Production cross sections for the ^{16}O(p,x)^{13}N reaction.

al. (1961) [168], Dangle et al. (1964) [169], McCamis (1973) [170], Nero et al. (1973) [171], Gruhle et al. (1977) [172], Sajjad et al. (1986) [173] and Kitwanga et al. (1989) [174]. The deviations of the selected data from the evaluation are on average about 19%. This set of 607 data points was used as input for a least-squares Padé fit with 40 parameters, providing an analytical shape of the cross section with deviations of 65% near the reaction threshold, decreasing to better than 7% between 11 and 18 MeV and then monotonically increasing to 12% at the highest energy [162]. The evaluation and the data are illustrated in Figure 5.7, together with the results of this work. In this case, after the mentioned modifications, the deviations of the selected data sets from the evaluation are on average 14%, which we consider the uncertainty bars for this IAEA evaluation curve in Figure 5.8 as well.

As in the case of the ^{14}N(p,x)^{11}C reaction, the IAEA evaluated cross section considering the energy intervals from this work and the corresponding cross section ratios are displayed in Figure 5.8. Our data feature nicely the first very narrow resonance structure even with the limited energy resolution of the method, which may be the cause of the slight different cross section shapes between 9 and 10 MeV. Above 10 MeV, our data are systematically larger than the evaluation, 20% considering the ratio weighted by the energy distribution in each foil. This difference is significant but in the order of that observed in other data sets. Indeed, the original data of Furukawa, Whitehead and Gruhle are 53%, 37% and 43% larger than the evaluation, respectively; sizable differences pointing in the same direction than our results: an clear underestimation of the evaluated cross section.

Again, because most previous studies were motivated by the production of radioisotopes for PET diagnostics, data above 30 MeV are not so prolific. Figure 5.9 shows the new data together with the four data sets available: Foley et al. (1962) [175] (only one point), Albouy et al. (1962) [110], Valentin et al. (1963) [176] and Kettern et al. (2004) [152]. Between 20 and 40 MeV, the data presented herein

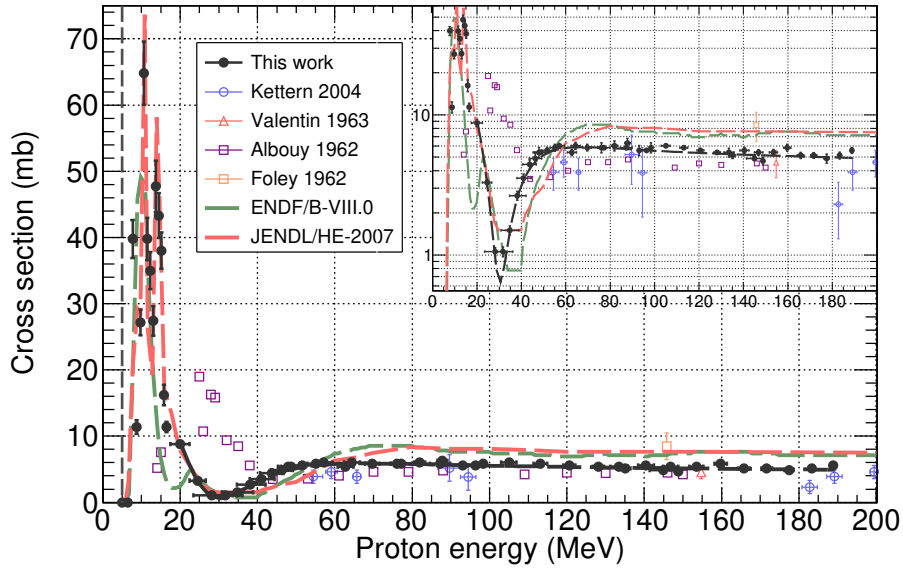

FIGURE 5.9: Cross sections for the production of ^{13}N on O.

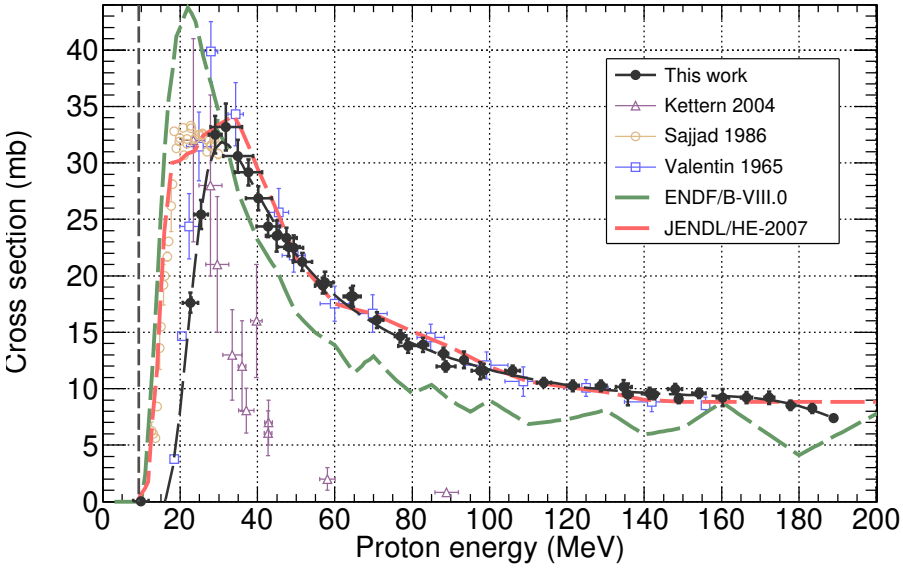

FIGURE 5.10: Cross sections for the production of ^{13}N on N.

are considerable lower than Albouy et al., which do not show the clear dip seen in our data and also in the evaluations. At higher energies, our data are about a ~25-30% higher than Albouy et al., Kettern et al. and Valentin et al, but about 20% lower than the evaluations, which were adjusted to pass by the single data point of Foley et al. at 145 MeV. The low cross sections, of just a few mb, might be the cause of the sizable disagreements observed.

5.1.6 ^{14}N(p,x)^{13}N reaction

Although the production cross section of ^{13}N in N is larger than in oxygen, the latter is the most abundant element in the human body and hence is the dominant seed for ^{13}N. Maybe that is why the ^{14}N(p,pn)^{13}N reaction channel has not been investigated much in the past, being there only three

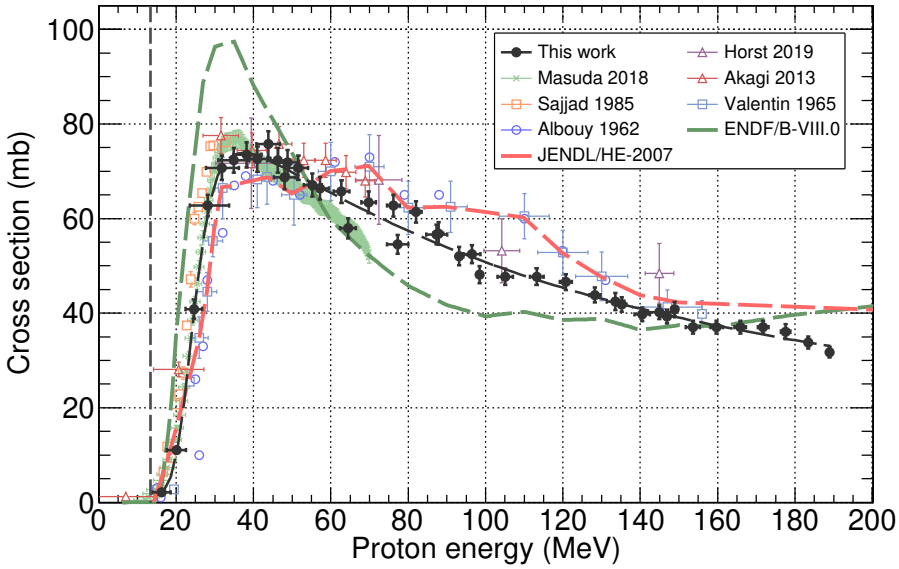

FIGURE 5.11: Cross sections for the production of ^{15}O on O.

data sets published so far: Valentin et al. (1965) [111], Sajjad et al. (1986) [173] and Kettern et al. (2004) [152]. Regarding the evaluations, JENDL is explicitly mentioned to be based on the data of Sajjad et al. and Valentin et al. below and above 30 MeV, respectively. However, both data sets disagree below 30 MeV, showing a significant energy shift of more than 5 MeV near the threshold that implies very different activation profiles for PET range verification precisely near the Bragg peak, where it is more important. This issue is solved with the new data reported herein, which confirm very clearly the validity of Valentin's data in the full energy region, with just a slight overestimation in the 30 MeV peak. Then, the recent data of Kettern et al. are far for any other measurements of evaluation, falls surprisingly fast down to negligible values just at a few tens of MeV. Last, ENDF is also far from all data sets, which indicates the need of a re-evaluation.

5.1.7 ^{16}O(p,x)^{15}O reaction

In delayed PET range verification, the biological washout of the generated isotopes plays an important role in the feasibility of the technique. Isotopes with shorter half-lives are recommended to avoid this effect, for instance ^{15}O, which is produced mainly by the ^{16}O(p,x)^{15}O reaction (see Figure 5.11).

The increasing interest in using this isotope brings about new measurements, such as in Akagi et al. (2013) [153], Masuda et al. (2018) [154] and Horst et at. (2019) [105], to complete the old ones from Albouy et al. (1962) [110], Valentin et al. (1965) [111] and Sajjad et al. (1985) [177]. It seems that in this case, our data and most previous measurements are in good agreement, especially below ~80 MeV, while above that energy our data are slightly lower than all others. Again, the JENDL evaluation is based on data, this time on Valentin et al., and hence is in good overall agreement with all available data, while ENDF is based on models and falls far from the available data, which, again, indicates the need of a re-evaluation.

5.1.8 ^{14}N(p,x)^{15}O reaction

Although its role in the context of range verification in proton therapy is very limited, for the sake of completeness, the production of ^{15}O in nitrogen has been obtained as well. In this particular case,

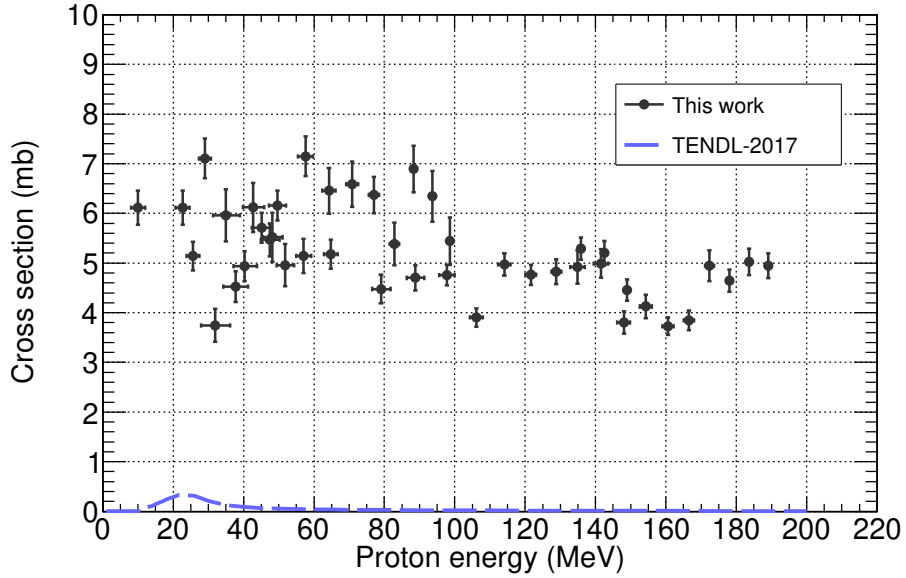

FIGURE 5.12: Cross sections for the production of ^{15}O on N.

the previous measurements of Kuan et al. (1970) [178], Harakeh et al. (1975) [179] and Schröder et al. (1987) [180] are not available in EXFOR database, so they have not been included in Figure 5.12.

The evaluated data are not available in ENDF/B-VIII.0 library (and therefore neither they are in ICRU63 and TENDL-2019). The only data available are in older TENDL libraries, calculated with TALYS code, which offer in general less confidence. This available TENDL data is also shown in Figure 5.12.

As displayed in Figure 5.12, the uncertainty in the cross sections value seems to be underestimated. In this case, due to the very low production of ^{15}O in N, the confidence in the low uncertainty values obtained in the fitting (given by ROOT) should be called into question.

5.2 Short-lived β^+ emitters

The ^{12}N ($t_{1/2}$=11 ms) β^+ emitter is produced on carbon, which is abundant throughout the human body. It is the most generally useful short-lived isotope for online PET range verification due to its very short half-life of only 11 ms, which would allow practically immediate feedback on the delivered dose and a quick response to reformulate the treatment plan.

The ^{38m}K ($t_{1/2}$=0.924 s) and ^{29}P ($t_{1/2}$=4.1 s) short-lived isotopes produced in calcium and phosphorus, respectively, are also of great interest in online PET range verification, as calcium and phosphorus are the main constituent elements of bone tissues. The high density of these tissues reduces the range of the positrons emitted by these radioisotopes and then the possible blurring of the images, making these short-lived isotopes of significant importance for online range verification.

The point-wise cross section values obtained in this work are listed in Appendix A. The corresponding publication is in preparation. There are no previous data regarding the cross sections of these isotopes, besides the integral production yield below 55 MeV studied by Dendooven et al. (2019) [98]. Therefore, in the following sections our results will be compared to this integral production by simulating the production of each isotope in a phantom similar to the one used in the experiments of Dendooven et al., but using these new cross section values. Furthermore, the ENDF and JENDL evaluations are displayed, when they are available. In this case, also TENDL-2017 is displayed, in order to illustrate the significant differences between evaluated databases, which makes sense because there

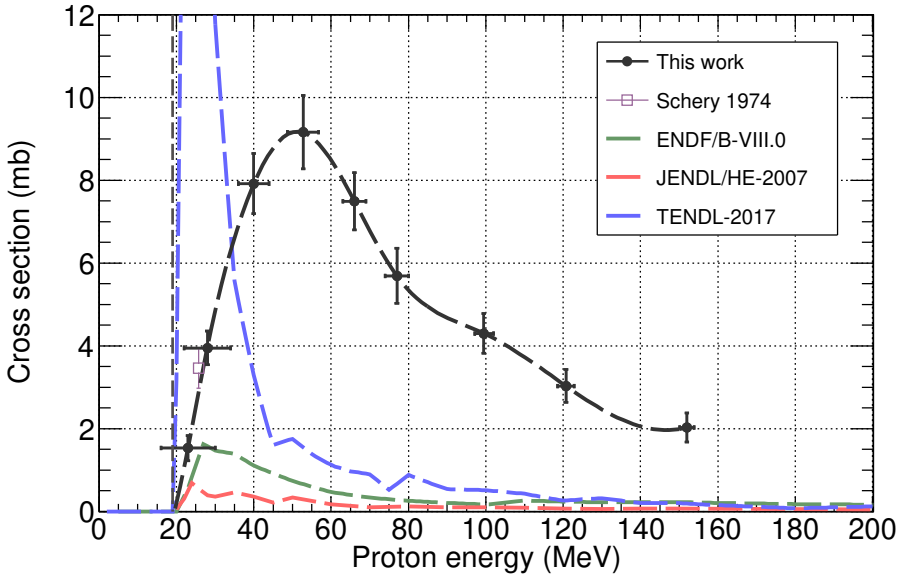

FIGURE 5.13: Cross sections for the production of ^{12}N on C.

are no previous experimental data and they depends only on theoretical calculations, hence evidencing the importance of experimental data.

5.2.1 ^{12}C(p,n)^{12}N reaction

The ^{12}C(p,n)^{12}N reaction cross section has not been studied previously, apart from the data of Rimmer and Fisher (1968) [181] (not available in EXFOR), a single point at 25.8 MeV by Schery et al. (1974) [182], and the mentioned integral production below 55 MeV ($4.46{\cdot}10^{-4}$ nuclei/proton). The data obtained in this work are in fairly good agreement with all previous measurements. The production of ^{12}N per incident proton below 55 MeV was calculated using the new data, obtaining $8.0(8){\cdot}10^{-4}$ nuclei/proton, a 57% higher value with respect to the integral measurement of Dendooven et al. [98], then agreeing in the order of magnitude but considerably higher than the most recent measurement.

Figure 5.13 displays the new values from this work and the previous measurement from Schery et al., the ENDF and JENDL evaluations. As previous mentioned, the TENDL-2017 data is also shown, with sizeable differences between them.

Therefore, the new data presented herein, covering the whole range of interest, constitutes the basis for a new evaluation, based on both experimental and theoretical models of the reaction cross section, in order to ensure a reliable implementation of online PET range verification.

5.2.2 ^{40}Ca(p,x)^{38m}K reaction

The ^{40}Ca(p,x)^{38m}K reaction cross section has not been studied previously. Figure 5.14 displays the cross section from this work and the TENDL-2017 evaluation (the only available evaluation found in the literature). As mentioned before, this is based exclusively on theoretical models, since there was no previous cross section data of this reaction, and the reliability of this curve should be put into question. The evaluation is, overall, smaller than the data by a factor that varies from ~2 at the 40 MeV peak to ~2 at 200 MeV.

Comparing with the mentioned integral measurement from Dendooven et al. [98] ($4.79{\cdot}10^{-3}$ nuclei/proton), the production obtained in this work is 40% lower ($3.1(3){\cdot}10^{-3}$ nuclei/proton), which

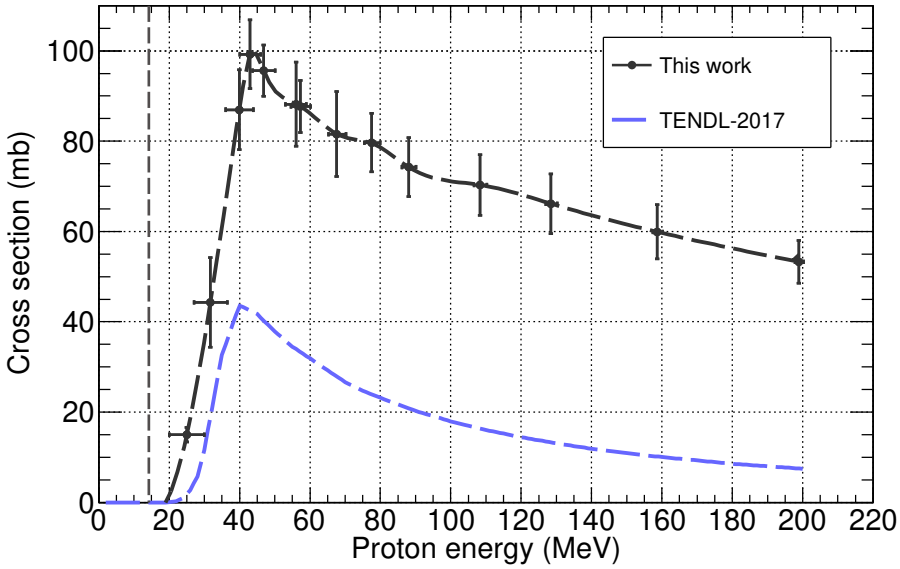

FIGURE 5.14: Cross sections for the production of ^{38m}K on Ca.

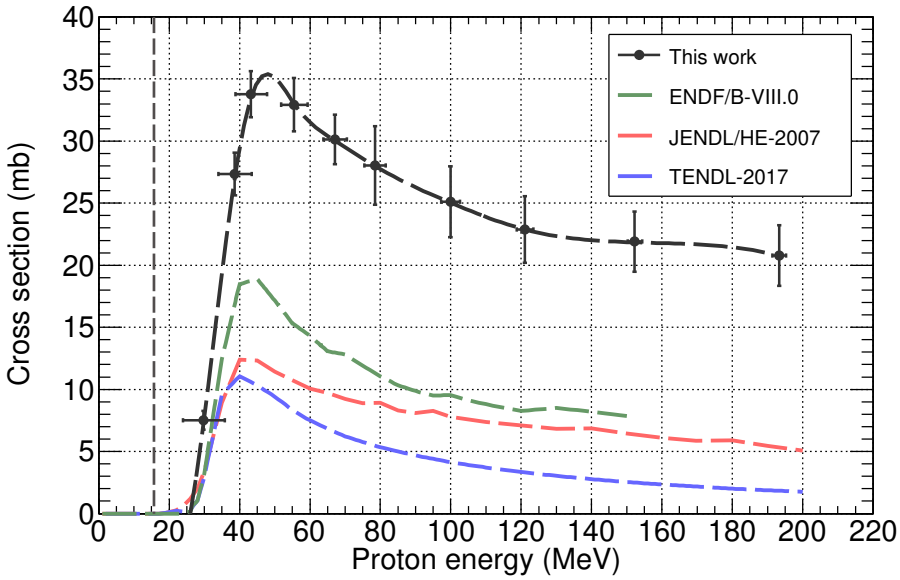

FIGURE 5.15: Cross sections for the production of ^{29}P on P.

seems, however, as if the trend is in completely the opposite direction than in the previous case of ^{12}N. Nevertheless, the fairly good agreement between the two measurements improves the confidence in our data in comparison to the evaluations.

Once again, this work provide the first production cross sections of the β^+ emitter ^{38m}K in the full energy range of interest for online PET range verification.

5.2.3 ^{31}P(p,x)^{29}P reaction

Last, the ^{31}P(p,x)^{29}P reaction cross section has also been obtained for the first time, covering the full energy range of interest for online PET verification. The experimental data are displayed in Figure 5.15, together with the currently available TENDL-2017, JENDL and ENDF evaluations. These are smaller

than the data, showing very significant differences, larger in TENDL than in the ENDF and JENDL. In this case, the production of ^{29}P in P (1.37(14)·10^{-3} nuclei/proton) is a 17% lower than that of Dendooven [98] (1.67·10^{-3} nuclei/proton).

5.3 Impact of the new data in PET range verification

The work presented in this manuscript is motivated by the increasing interest within the proton therapy community to improve the dose delivery in the patient by means of PET range verification. This, as discussed in Section 2.3.3, requires accurate production cross section data that should lead to more precise cross section evaluations. The use of such updated and more accurate evaluations should definitely improve the accuracy in the Monte Carlo simulations to calculate the β^+ activity distributions in the body needed for implementing PET range verification [93].

In this context, in the following, a study of the production and activity profiles of different β^+ emitters in heterogeneous phantoms using the cross sections from this work and from the current evaluations is presented. The phantoms considered in this work includes the main elements of the human body (hydrogen, carbon, oxygen, nitrogen, phosphorus or calcium), which are seeds for the production of the β^+ emitters studied. This shall illustrate the importance and impact of the new data and the subsequent need for new evaluations in the full energy range of interest in proton therapy.

5.3.1 Monte Carlo simulations of the β^+ emitters' production profiles

The production of β^+ emitters as function of the depth in different phantoms can been calculated by means of Monte Carlo simulations using for instance the Geant4 toolkit [35]. By default, Geant4 uses models for estimating the probability of nuclear reactions; section 3.1.2 includes a brief description of the reaction mechanisms which provide these probability distributions. However, a more accurate treatment of nuclear reactions requires considering instead detailed cross section evaluations. This can be done by including the *G4ParticleHP* package [183], which uses the ENDF/B-VII.1 evaluation for proton-induced reactions up to 150 MeV, and TENDL for higher energies (up to 200 MeV). The ENDF/B-VII.1 evaluation contains reactions for production of 46 isotopes of interest in medical applications, including those considered in this work, except ^{38m}K.

However, the reaction probabilities of interest for PET range verification are small, making this microscopic treatment quite computationally inefficient. Therefore, a different approach has been followed in this work. The new developed Geant4 application consists on two steps: i) the transport of the proton beam in a phantom of choice using Geant4, and ii) the calculation of the corresponding production of β^+ emitters using an external cross section data of choice.

In more detail, the developed application simulates the transport of the individual protons through the phantom, following the energy lost by each proton and calculating their energy and flux at each of the depth distances previously defined, which in this case are 1 mm apart. In a second step, the corresponding production rate P_z of the radioisotope of interest along the phantom is calculated by the convolution of the cross sections of choice (new data from this work or any evaluations) with the previously calculated proton flux (energy and number of particles) at each depth, i.e.:

$$P_z = n_s \int_z^{z+\Delta z} \left(\frac{dN}{dE}\right) \sigma(E) dE, \tag{5.1}$$

where P_z is the production rate (per mm and primary proton) of the given isotope, n_s is the surface density of target nuclei (atoms/barn), (dN/dE) is the proton spectrum at the given depth and

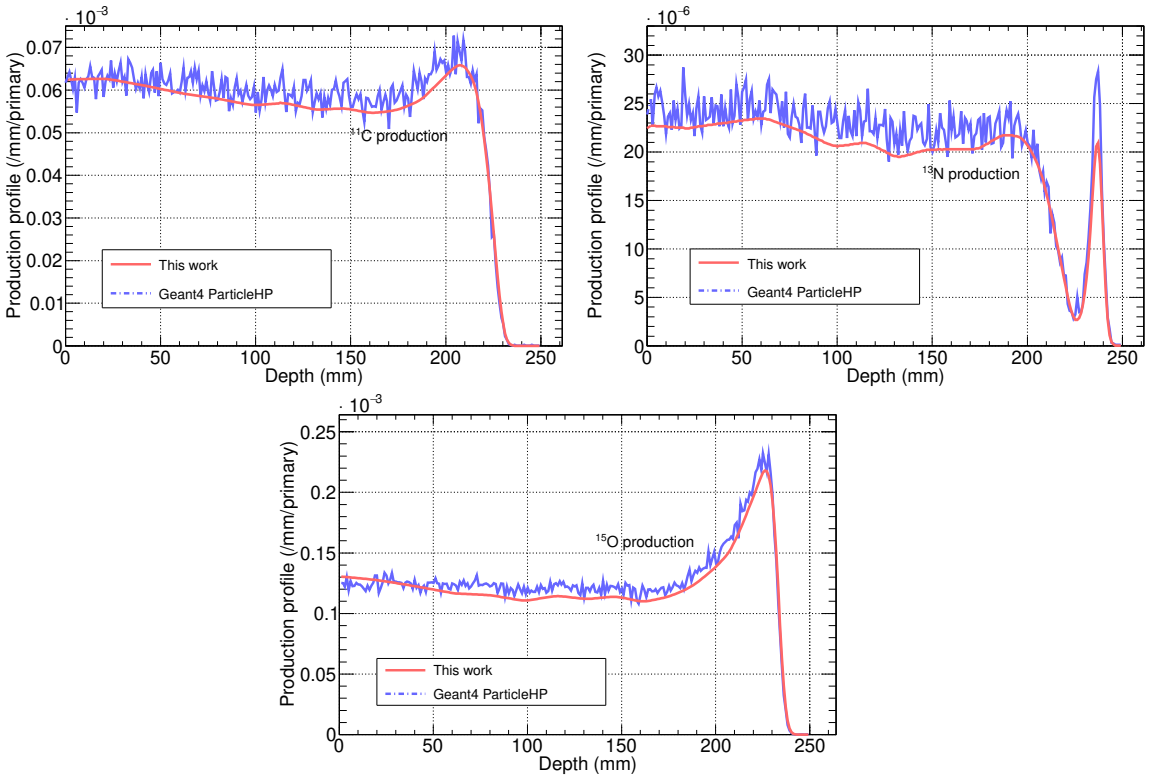

FIGURE 5.16: Production profiles of ^{11}C (top), ^{13}N (middle) and ^{15}O (bottom) produced by a 190 MeV proton beam in water.

$\sigma(E)$ (barn) is the interpolated cross section of choice (new data or evaluations) at that specific energy E. For the particular aim of this work, this two step method is equally accurate than using the $G4ParticleHP$ method.

Before proceeding to the calculations of interest for this work, a study was performed to validate the macroscopic two step calculation method proposed herein against the microscopic Monte Carlo simulation using *G4ParticleHP*. The simulation with *G4ParticleHP* were performed using the Geant4-10-07 (patch-03) version and 10^7 primary protons to have enough statistics, thus lasting for days. The simulation with the two step method developed in this work choosing the ENDF/B-VIII.0 evaluation (equal to the previous ENDF/B-VII.1 version used in *G4ParticleHP*) considered only 10^5 primary protons, lasting only 10 minutes. The comparison, displayed in Figure 5.16, shows the production rates of ^{11}C, ^{13}N and ^{15}O in a simple water phantom, demonstrating the consistency between the more efficient two-step calculation and the microscopic Monte Carlo simulation. Some slight discrepancies are observed and, although its study is out of scope of this work, several tests seem to indicate that they could be associated to the implementation of *G4ParticleHP*. Aside the relatively small noted discrepancies, this comparison shows a reasonable consistency between the two calculation methodologies. It can be appreciated the much better statistics of the two step method calculation reached in a 10.000 shorter CPU time, because all the transported protons contribute to the calculation of the probability of producing β^+ emitters and because the reaction probability is not calculated as each microscopic step. It is hence closer to what an adaptative treatment planning system would do for PET range verification.

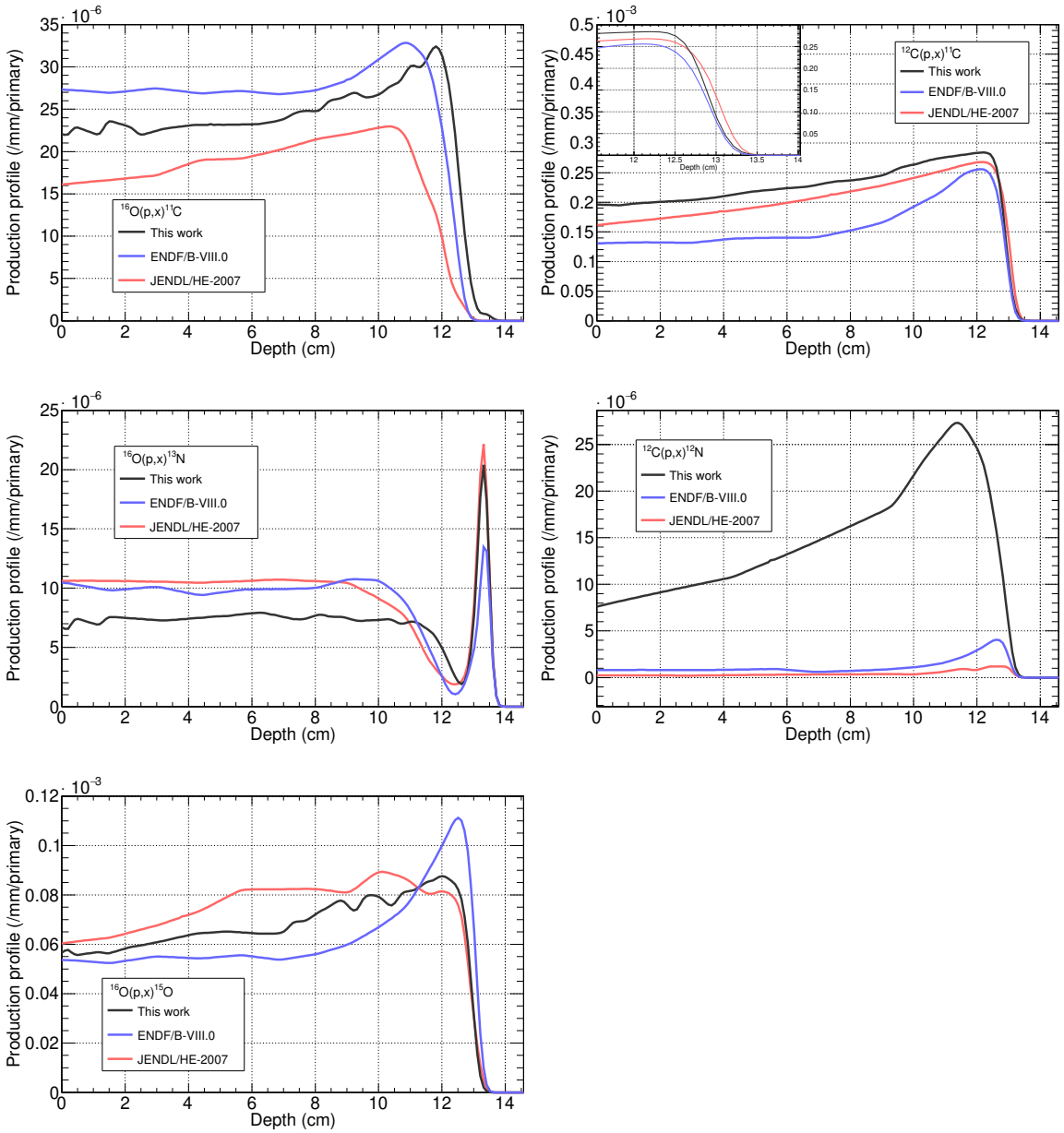

FIGURE 5.17: Comparison of the profile distributions produced by a 150 MeV proton beam in PMMA, calculated with different cross sections data sets. (Left) ^{11}C, ^{13}N and ^{15}O production in oxygen nuclei. (Right) ^{11}C and ^{12}N production in carbon nuclei.

5.3.2 β^+ emitters' production profiles: data vs. evaluations

Once the consistency of the two step macroscopic calculation was demonstrated, a set of simulations were performed in order to assess the impact in PET range verification of the new data obtained in this work. This has been achieved by determining and comparing the production of β^+ emitters with different external cross section data sets: the ones from this work and the currently available evaluations.

An homogeneous phantom made of PMMA has been irradiated with a proton beam of 150 MeV and the production profiles of ^{11}C, ^{13}N and ^{15}O has been calculated using the new data presented herein as well as the ENDF/B-VIII.0 and JENDL/HE-2007 evaluations. PMMA was chosen due to its resemblance to human tissues in terms of composition ($(C_5O_2H_8)_n$) and density (1.18 g/cm^3). The

result of the simulations is displayed in Figures 5.17 for production of β+ emitters in carbon (right) and oxygen (left).

- In carbon (see Figure 5.17 (right panel)), the calculations for the production of ^{11}C are different but not so much when considering the new data and the evaluations, indeed the distal fall-off of the profiles agree within ~2 mm. This nice agreement is related to the large amount of previous data on the ^{12}C(p,x)^{11}C, but this by far is not the case of the production of the short-lived ^{12}N. In this case, due to the absence of previous data, the evaluations are based only on models and are thus really far from the reality.
- In oxygen (see Figure 5.17 (left panel)), because of its high abundance in the human body (65% of the total mass vs. 18% of the total mass in the case of carbon), the accuracy of the production cross section are of great importance for PET range verification. However, in this case the discrepancies of the production profiles both in absolute value and shape, in particular the position of the drop at the distal fall-off, are quite significant. The most extreme case corresponds to ^{11}C, with a difference of about 1 cm in the position of the distal fall-off. Regarding ^{15}O, the new data indicate the absence of the nice peak near the end of the range predicted by the ENDF/B-VIII.0 evaluations, which, if existing, could have been very useful for off-line in-room PET range verification.

Overall, it can be concluded that the implementation of PET range verification with a precision in the millimetre range requires updated evaluations of all the reaction cross sections of interest up to 200 MeV. This requires a new complete and accurate data base, which was the aim and is the result of this thesis.

5.3.3 Activity depth profiles as function of time

The production of all the β^+ emitters produced in a tissue-equivalent phantom by a 150 MeV proton beam is illustrated in the top panel of Figure 5.18. For the sake of simplicity, this phantom considers the average density and composition of the soft tissues in the human body (see Table 5.1).

Here, it is observed that the dominant production corresponds to ^{15}O in oxygen, followed by ^{11}C in carbon and oxygen. As expected, the production of ^{15}O is almost one order of magnitude higher than the production of ^{13}N. The production in nitrogen nuclei are a almost two orders of magnitude lower than ^{15}O. However, it is worth noting the distinctive distal fall-off of the ^{13}N in oxygen depth profile, due to the considerably lower energy threshold of this reaction, which could serve for an accurate determination of the position of the Bragg peak.

However, in PET range verification what will be measured is not the number of produced isotopes but the corresponding activities (decays per unit time), and hence the half-lives of the different β+ emitters come into play to change very significantly the situation. This is illustrated in the bottom panel of Figure 5.18, where the dominant contribution in terms of activity now corresponds clearly to ^{12}N followed by ^{15}O. And this is not the end of the story, as the activities of the different isotopes decrease with time and hence the situation show in Figure 5.18 is not static but dynamic. Accordingly, the activity profile will be very different if the PET acquisition is made online (within ms or s), in-room (within a few minutes) or off-line (after tens of minutes). Therefore, in the following, the simulated production profiles have been converted into activity profiles at different times by multiplying the production profiles P_z by the appropriate decay constants λ and applying the corresponding exponential decay:

$$A_z(t) = \lambda P_z e^{-\lambda t} \tag{5.2}$$

TABLE 5.1: Composition (fraction by total number of nuclei) and density of the heterogeneous phantom used in this work.

Material	^{1}H (%)	^{12}C (%)	^{14}N (%)	^{16}O (%)	^{31}P (%)	^{40}Ca (%)	Density (g/cm^{3})
Soft tissue	62.0	12.0	1.0	25.0	-	-	1.0
Cortical bone	5.1	14.4	4.2	44.6	10.5	21.2	1.85

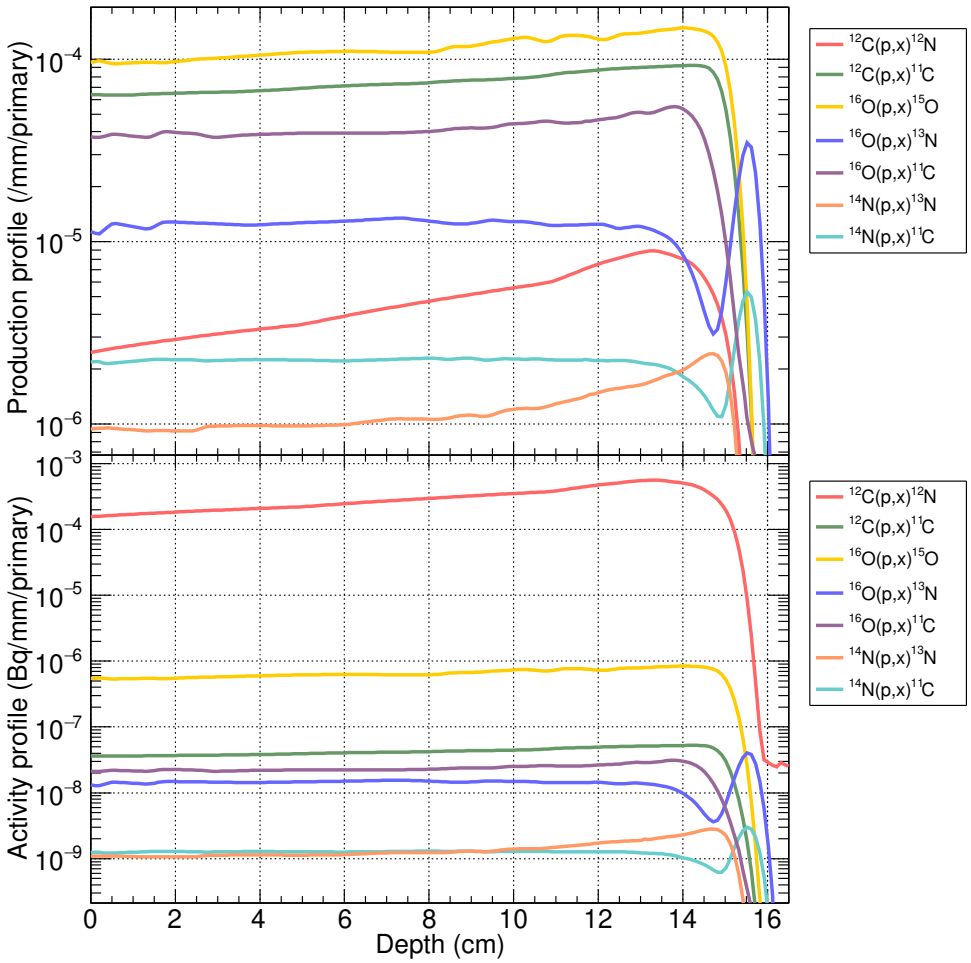

FIGURE 5.18: Production and activity profiles of ^{11}C, ^{13}N, ^{15}O and ^{12}N produced by a 150 MeV proton beam in soft tissue.

In order to both illustrate the evolution of the activity profiles with time, and at the same time demonstrate the viability of online PET range verification using short-lived isotopes; an heterogeneous phantom has been used. Its geometry resembles a human body, in a very simplified manner, as a 18.5 cm soft-tissue block with a 2.5 cm cortical bone inserted in the center. The composition and density of each material is detailed in Table 5.1.

A sketch of the simulated phantom is shown at the top of Figure 5.19, where an exemplary 5 mm thick "tumour" inside the soft tissue block is depicted at 13 cm. In order to treat such tumour, the phantom is irradiated with a 150 MeV proton beam featuring a Bragg peak within the tumour volume, precisely with a R80 of 13.7 cm.

The corresponding activity profiles as a function of time in Figures 5.19 and 5.20. Figure 5.19 displays the subsequent activity profiles for online PET range verification, i.e. at 0, 100 and 1000 ms after

the irradiation. Then Figure 5.20 corresponds to times suited for offline PET range verification, i.e. up to more than 10 minutes after the irradiation (10, 100 and 1000 s).

As illustrated in Figure 5.19, in t=0 the decay of the abundantly produced ^{12}N isotope dominates the PET images in the early stages of the verification acquisitions, followed closely by ^{15}O. For tens of ms after the irradiation, both ^{12}N and ^{15}O contribute equally to the total activity profile. As they are produced in C and O, respectively, they appear all along the beam trajectory, i.e. both in soft tissue and bone. This makes online PET range verification relying on the short-lived isotopes, especially ^{12}N during the very few ms after the treatment (~seconds for carbon-rich tissues), a very attractive option because it provides practically immediate feedback of the dose profile delivered, which would allow for adaptive proton therapy to correct deviations from the treatment plan. Moreover, the rapid acquisition makes that these short-lived isotopes are the least influenced by biological wash-out effects, hence reducing the blurring of the PET images.

Considering that in current PET diagnostics ~8 MBq/kg of ^{18}F is introduced into the patient, i.e. ~$1.2{\cdot}10^{5}$ ^{18}F nuclei/mm^3 in t=0, and that usually PET images takes ~30 min to have a good resolution, then it is expected to have PET images with ~$3.5{\cdot}10^{6}$ counts/mm^3, for a PET coincidence detection efficiency and attenuation of 511 keV photons of 15% and 17%, respectively [184, 185]. Estimating the production of ^{12}N as ~$4{\cdot}10^{-6}$ per mm and per incident proton, then it results in ~$2.5{\cdot}10^{-4}$ Bq per mm and per incident proton, considering the same efficiency than before, in ~$6{\cdot}10^{-6}$ counts per mm and per incident proton. The intensity of conventional proton therapy treatments ranges from 10^8 to 10^{10} protons per seconds. Considering an irradiation of 30 ms and PET measurement long enough to measure all produced isotopes (about 5 half-lifes of ^{12}N), it results in ~20-2000 counts/mm, which after the repetition and sum of several beam on/off cycles, then it could potentially provide enough number of counts to reduce statistical fluctuations and reach the aimed millimetric precision.

Furthermore, the short-lived isotopes ^{29}P and ^{38m}K stand out in bone, which is rich in phosphorus and calcium. Looking at the decay of these isotopes in this time scale would allow for a clear determination of the bone structures inside the body: i.e. the superposition of the PET with the treatment planning reference images would serve to verify the position of the patient, enhancing the confidence of the correctness of the dose delivered.

One second after the treatment all the ^{12}N has decayed and the activity profile is dominated by ^{15}O, followed closely by ^{11}C. Also, the induced activity of ^{29}P and ^{38m}K in bone still dominates the activity profile, then allowing again the identification of the bone structures inside the body.

In the time scale of tens of seconds, the total activity measured with a PET scanner is dominated by the decay of ^{15}O, which would be still about an order of magnitude larger than that of ^{11}C. As discussed before, the ^{15}O half-life of only 122 s would allow the use of in-room PET range verification, which makes use of conventional PET scanners placed inside the treatment room. Indeed, the reduction of the complexity of the scanner compared to the online case, and the benefits from a faster response and higher counting rate in comparison to offline acquisitions, make in-room PET range verification looking at ^{15}O very appealing. Furthermore, the increase activity in the bone structure should serve, as discussed just above, to identify the position of the bones and hence ensure at the same time the beam range and the correct positioning of the patient during the irradiation.

A few minutes after the irradiation, for t=1000 s, the major activity contribution stems from the decay of the longest-lived isotope: ^{11}C. It is worthy to mention again that, just at the end of the beam range (below ~18 MeV), the low energy threshold reaction ^{16}O(p,x)^{13}N provokes an increment in the PET activity and a peak in the total activity curve. This peak has aroused considerable interest to verify the actual position of the Bragg peak and its feasibility has been addressed also by recent works [186, 187], although using more oxygen-rich phantoms than in this work. For the sake of simplicity, this

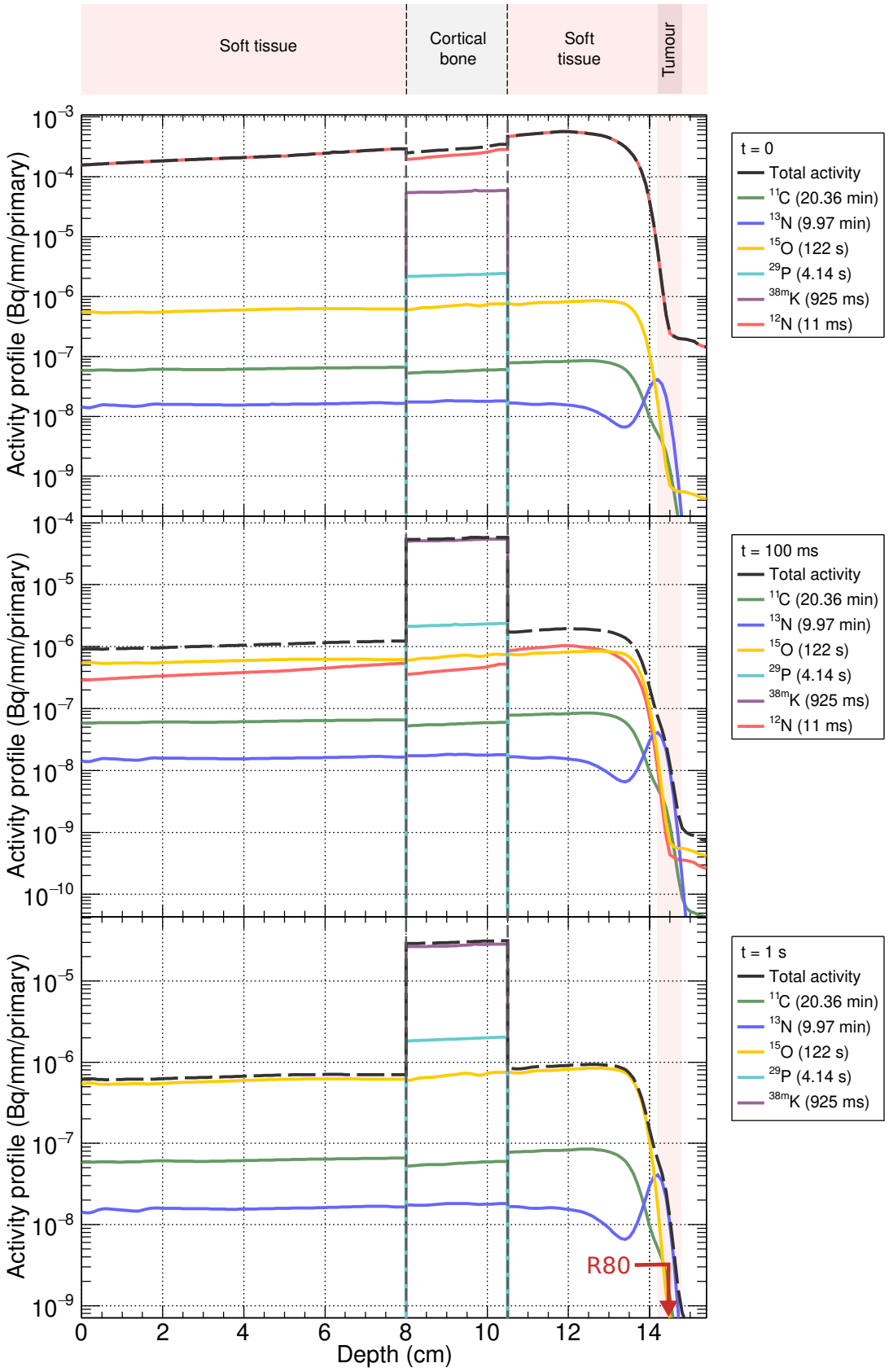

FIGURE 5.19: Activity depth profiles of ^{11}C, ^{13}N, ^{15}O, ^{29}P, ^{38m}K and ^{12}N produced by a 150 MeV proton beam, calculated with the cross sections data sets obtained in this work, for t=0 (top), t=100 ms (middle) and t=1 s (bottom).

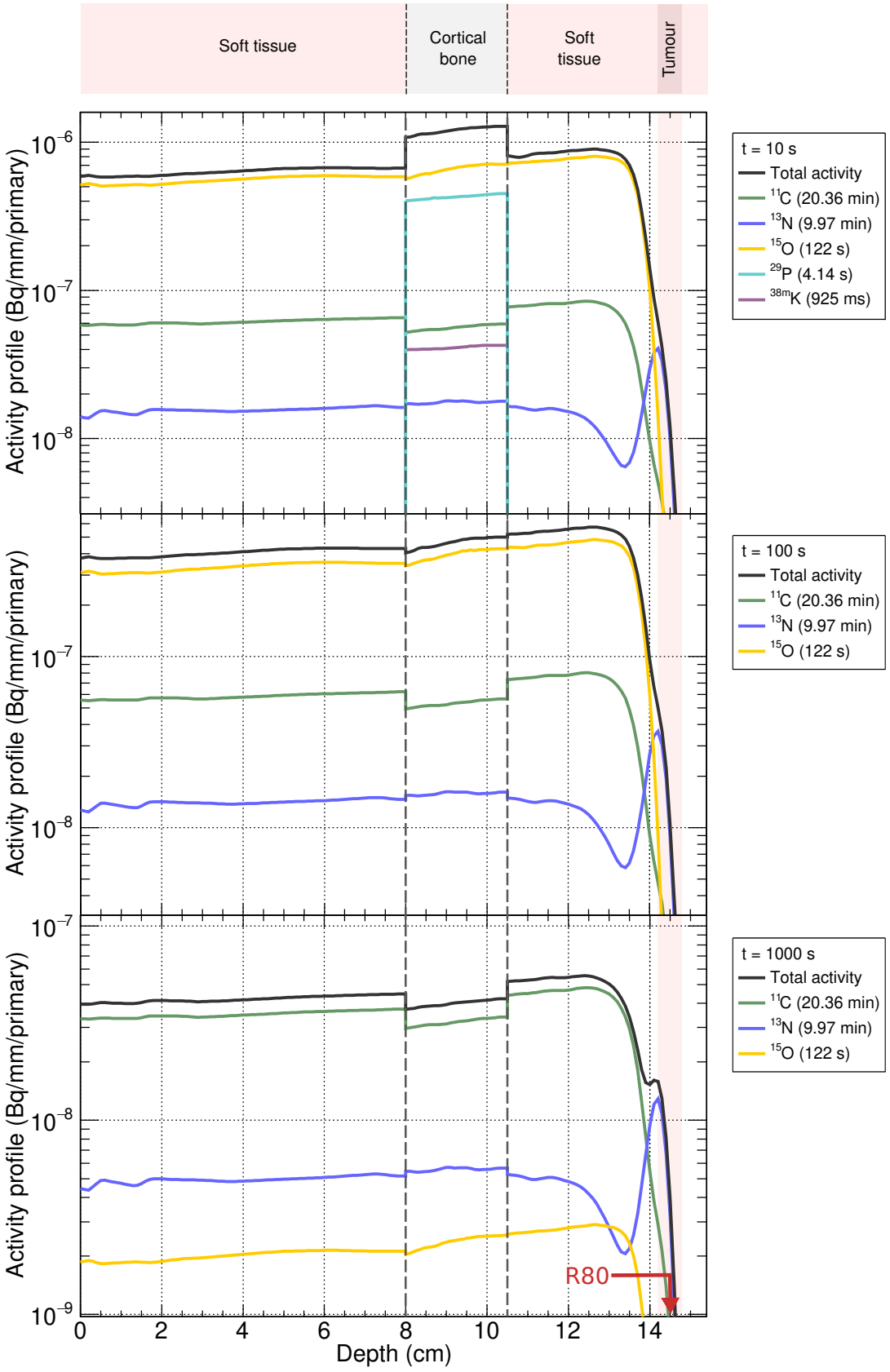

FIGURE 5.20: Activity depth profiles of ^{11}C, ^{13}N, ^{15}O, ^{29}P, ^{38m}K and ^{12}N produced by a 150 MeV proton beam, calculated with the cross sections data sets obtained in this work, for t=10 s (top), t=100 s (middle) and t=1000 s (bottom).

study considers an average abundance of oxygen in soft tissues and tumours, but this peak may be arising more prominently for those tumours or tissue types with higher concentration of oxygen, all of them contributing to make it a very promising technique to identify the Bragg peak position.

Although more studies are necessary to test the feasibility of PET verification in real clinical cases, which deals with the challenges of acquisition system technologies, biological wash-out effect, expected activity distributions, etc., PET range verification has demonstrated to offer different possibilities and advantages depending on the time scale in which its acquisition is performed. Hopefully, the new cross section data sets resulting from this work will be implemented in the evaluations and then in simulations codes for PET range verification and, together with further investigations, may possibly constitute a baseline in overcoming some of the current constraints of proton therapy.

Chapter 6

Summary, conclusions and future work

This chapter summarizes the work and main conclusions of the research presented in this thesis aiming to improve the accuracy of PET range verification in proton therapy treatments. It also includes some prospective work towards the implementation of PET range verification regarding the Monte Carlo simulations that would use the data resulting for this work for calculating realistic activity profiles.

PROTON THERAPY allows to maximize deposited dose inside the tumour while reducing the dose in the healthy tissues, thanks to its superior depth-dose distribution when compared against conventional photon therapy. However, uncertainties in the proton beam range could limit the benefits by the irradiation of surrounding healthy tissues while the tumour does not receive the actual dose prescribed. To account for this and in view of the absence of clinical routines for range verification, a safety margin around the targeted tumour is applied to ensure that the prescribed dose is delivered to it. In general, a safety margin of about 2.5-3.5% of the total range is added in current treatments, a fact that has remained relatively unchanged since the beginning of proton therapy and still limits the full exploitation of the benefits of this technique. Furthermore, for specific treatment sites, additional margins may be added, because of uncertainties due to the difficulty of the patient immobilization and setup, or due to motion of the patient during treatment.

In this context, this thesis is focused on PET range verification. In this technique, the β^+ activity that remains in the patient (produced by nuclear reaction induced by the proton beam) is measured with a PET scanner and compared with the expected curve from a Monte Carlo simulation of the treatment plan. This should allow to identify any possible deviation of the beam range delivered with respect to the plan. Related to its implementation, previous studies highlighted the need of more accurate cross-section data of the reaction channels contributing to the production of PET isotopes by proton beams up to 200 MeV [20, 93, 114]. These data are essential for improving the evaluated databases, which shall improve the accuracy of the Monte Carlo simulations with which the measured activity distributions need to be compared to look for deviations within a 1 mm precision.

6.1 Summary and final remarks

This work has addressed the need of new and more accurate production cross section values of the nuclear reactions of interest in PET range verification by:

1. a new experimental methodology for the measurement of cross sections has been developed,
2. cross section measurements has been carried out making use of the accelerator facilities, two of them featuring clinical beams,
3. a series of validation strategies have been implemented in the experiments and analysis,
4. the impact of the new cross section data base in PET range verification calculations has been assessed by Monte Carlo simulations.

The experimental method developed in this work for measuring long-lived β^+ emitters (^{11}C, ^{13}N and ^{15}O, with half-lives in the range of minutes) combines the commonly employed multi-foil activation technique with the use of PET scanner as γ-ray detector. This allows measuring the activity of all the foils at the same time in a single PET acquisition, hence minimizing the number of irradiations needed and reducing possible systematic errors in the irradiation and thus in the subsequent activity determination. For the case of short-lived β^+ emitters with half-lives in the order of milliseconds to seconds (^{12}N, ^{29}P and ^{38m}K), the methodology developed is more standard, consisting in the irradiation of single foils and the detection of the 511 keV with conventional $LaBr_3$ detectors, but including the design of adequate positron annihilation converters.

These two methods have been applied to the measurements of reactions displayed in Figure 6.1, occurring on:

- Carbon: ^{12}C(p,x)^{11}C, ^{12}C(p,x)^{12}N and ^{12}C(p,x)^{13}N.

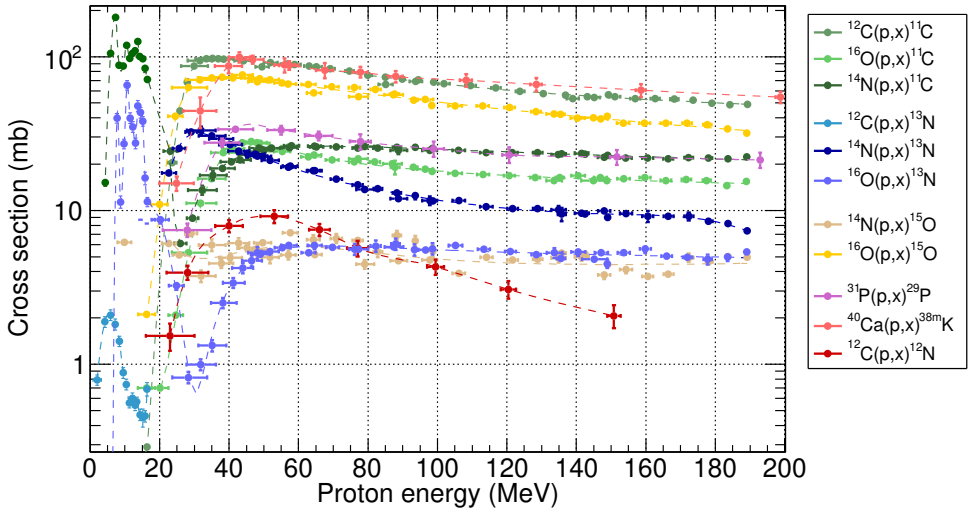

FIGURE 6.1: The complete production cross section data sets obtained in this work. In green shades, the production of ^{11}C; in blue shades, the production of ^{13}N; in yellow shades, the production of ^{15}O, and in red shades, the production of the short-lived isotopes.

- Nitrogen: ^{14}N(p,x)^{11}C, ^{14}N(p,x)^{13}N and^{14}N(p,γ)^{15}O.
- Oxygen: ^{16}O(p,x)^{11}C, ^{16}O(p,x)^{13}N and ^{16}O(p,x)^{15}O.
- Phosphorus: ^{31}P(p,x)^{29}P
- Calcium: ^{40}Ca(p,x)^{38m}K

The reactions yielding the long-lived isotopes ^{11}C, ^{13}N and ^{15}O, featuring low reaction thresholds of just a few MeV, required experiments at three different facilities. The low energy (<18 MeV) and high energy (>50 MeV) were studied at the CNA (Spain) and WPE (Germany) facilities, respectively. Both feature a PET scanner in the proximity of the irradiation rooms and hence the multi-foil plus PET technique could be applied. Then, the intermediate energy region had to be studied at HIT (Germany), which did not have a PET scanner available but which allowed for lower proton beams than WPE, 55 vs. 100 MeV. The reactions yielding the short-lived isotopes ^{12}N, ^{29}P and ^{38m}K required a very flexible irradiation system in which beam-on/beam-off cycles could be adapted to the half-lives of those isotopes, which vary between milliseconds and a few seconds. This was achieved again at HIT (Germany), using the mentioned $LaBr_3$ detectors on-line.

In order to ensure the accuracy of the results from this work, a significant effort has been made to implement several quality assurance and validation techniques:

- The multi-foil activation combined with PET measurements have been validated by means of two integral production yield measurements using a Nylon-6 and PMMA thick targets and conventional scintillator detectors. The agreement between integral measurements and the sum of the activities of each one of the individual foils (4% and 7% for Nylon-6 and PMMA, respectively) validates the use of the PET scanner for this purpose.
- A monitor foil has been placed in front of each multi-foil stack and used to validate both the relative beam current measurements and the corrections applied during the analysis. The results indicates an agreement within 4.5% and less than a 1.8% at CNA and WPE, respectively. Therefore, an uncertainty of these values related to the reproducibility of the irradiations in these experiments were considered during the cross section uncertainty estimations.

- The cross section results were validated using a complementary measurement of a well established reaction cross section: the IAEA standard reaction ^{nat}Cu(p,x)^{63}Zn [145]. Considering that this IAEA monitor reaction features low uncertainties, the results (a 4% agreement at WPE and an average 5% agreement at HIT) validates the measuring technique, the analysis strategy and corrections applied for both experiments; it validates the beam current measurements as well as the detection efficiency calculation.
- At WPE and HIT, the beam energies were chosen such that some data points are measured twice, resulting in a agreement between them within uncertainties.

The outcome of the measurements and analyses is a complete new data set of cross sections of interest for, but not only, PET range verification calculations, featuring:

- 11 different proton induced reactions on C, N, O, P and Ca, four of them studied in this work for the first time.
- Coverage of the complete energy range of interest, i.e. between the corresponding thresholds and 200 MeV.
- An energy grid of ~60 and ~10 data points for long-lived and short-lived isotopes, respectively.
- Analytical descriptions by means of least-squares Padé fits of all reactions.

In order to illustrate and assess the impact of the new data resulting from this work in the particular case of PET range verification calculations, the following has been done. The β^+ emitters' production and activity depth profiles in tissue-equivalent phantoms have been calculated with Geant4 Monte Carlo simulations using as input the reaction cross sections from this work and then those from different evaluations. The comparison shows sizable differences in both shape and absolute value, and, most importantly, in the position of distal fall-off of the activity curve. For some relevant reactions in offline range verification, such as the ^{16}O(p,x)^{11}C reaction, a variation of more than 10 mm is observed.

The overall role in PET range verification of the different isotopes studied has been discussed upon the results of the mentioned activity depth profiles but for an heterogeneous phantom geometry and, more importantly, its evolution in time. This is important for deciding whether online, in-room or offline PET range verification are more of less well suited for clinical practice. The simulations indicate that ^{12}N dominates overall in the time scale of tens of milliseconds. From the estimated activity curves for ^{12}N, it is plausible that, for any tissue except carbon-poor one, online PET verification provides enough number of counts to be a reliable verification method. Regarding bone tissue, ^{38m}K dominates the activity profile until ~1 s, then ^{29}P and then ^{15}O dominate the activity curves; hence bone structures will be clearly visible in online PET verification, serving as a patient positioning and anatomical cross-check when comparing with the corresponding CT images. Looking at longer times, ^{15}O dominates the activity profile in the time scale of tens of seconds, while after 10 minutes only ^{11}C and ^{13}N stand still. It is of particular interest the ^{13}N peak produced by the low energy threshold reaction ^{16}O(p,x)^{13}N, which has made it increasingly interesting to verify the position of the Bragg peak.

The results illustrate the importance of new data and the subsequent evaluations in the full energy range of interest in proton therapy for a reliable implementation of PET range verification. This is more evident of the case of short-lived isotopes, for which this work has provided the first cross section data ever. In order to contribute to an accurate implementation of PET range verification, the nuclear data evaluations for the production of the long- and short-lived isotopes considered in this work should be revised including this new data set. In this way, the corresponding PET measurements and Monte Carlo calculations should allow for an accurate implementation of online and offline PET range verification contributing to even real-time adaptive proton therapy treatments.

6.2 Future work

This thesis has assessed the need of new and more accurate data of the production cross sections of β^+ emitters of interest in PET range verification. From this new cross section data base, now Monte Carlo simulations allow calculating more accurate than ever activity profiles in realistic geometries, which can then be studied as function of time.

As a continuation of this work and in relation to the simulation using the new data base, and always with the aim of contributing to the eventual implementation of PET range verification, the following research topics have been identified:

- The Geant4 toolkit makes use of the *G4ParticleHP* package to simulate nuclear reactions. Currently, the underlying cross section database is ENDF/B-VII.1, and therefore, until a new evaluation is released and Geant4 starts using it as reference, the new cross section database should be translated into the required format to make it available for Geant4 calculations using *G4ParticleHP* option.

- In this work, pencil beams were simulated to obtain and discuss the production and activity profiles. As a next step, SOBP treatments will be simulated, with beams impinging from the same or different directions to conform the tumour.

- β+ activity profiles should be simulated not just for heterogeneous phantoms but for realistic patient's geometry and clinical cases. This can be done by implementing CT geometries and clinical treatments plans, which is possible for instance with the TOPAS toolkit (based on Geant4 but specially adapted to radiotherapy making it easier to use for medical physicists).

- Upon the availability of an online PET scanner, experiments of actual PET range verification should be done, first with phantoms and then with patients, and compared to the activity profiles calculated with the new data. Indeed, in the frame of a collaboration with the group of C. Domingo, from the Instituto de Física Corpuscular (IFIC), experiments were performed at CNA at low energy [188], i.e. at the Bragg peak region, and HIT at clinical energies (analysis ongoing), using the novel iTED detectors as a PET scanner. Future research lines will continue the established collaboration.

- Due to the increasing interest of using carbon and helium beams for particle therapy, the corresponding β^+ production cross sections for PET range verification will be also determined. Indeed, experiments has been already performed at HIT, using an experimental approach and setups similar to those described in this thesis. The analysis is ongoing.

Bibliography

[1] J. Ferlay et al., "Global cancer observatory: cancer today.", International Agency for Research on Cancer **68** (2020) (cited on page 4).

[2] *National Institute of Health (NCI) website: Radiation therapy for cancer*, Visited on October 2022, https://www.cancer.gov/ (cited on pages 4–5).

[3] J. M. Galvin et al., "Implementing IMRT in clinical practice: a joint document of the American Society for Therapeutic Radiology and Oncology and the American Association of Physicists in Medicine", International Journal of Radiation Oncology, Biology and Physics **58**, DOI: 10.1016/j.ijrobp.2003.12.008 (2004) (cited on page 5).

[4] J. ur Rehman et al., "Intensity modulated radiation therapy: a review of current practice and future outlooks", Journal of Radiation Research and Applied Sciences **11**, DOI: 10.1016/j.jrras.2018.07.006 (2018) (cited on page 5).

[5] J. M. Borras et al., "How many new cancer patients in Europe will require radiotherapy by 2025? an ESTRO-HERO analysis", Radiotherapy and Oncology **119**, DOI: 10.1016/j.radonc.2016.02.016 (2016) (cited on page 5).

[6] H. Cambazard, E. O'Mahony, and B. O'Sullivan, "A shortest path-based approach to the multileaf collimator sequencing problem", Discrete Applied Mathematics **160**, DOI: 10.1016/j.dam.2011.09.008 (2012) (cited on page 5).

[7] L. S. Rowe, A. V. Krauze, H. Ning, K. A. Camphausen, and A. Kaushal, "Optimizing the benefit of CNS radiation therapy in the pediatric population-Part 2: novel methods of radiation delivery", Oncology **31** (2017) (cited on page 5).

[8] R. Orecchia et al., "Particle beam therapy (hadrontherapy): basis for interest and clinical experience", European Journal of Cancer **34**, DOI: 10.1016/S0959-8049(97)10044-2 (1998) (cited on pages 5–6).

[9] R. R. Wilson, "Radiological use of fast protons.", Radiology **47**, DOI: 10.1148/47.5.487 (1946) (cited on pages 6–7).

[10] G. Neary, R. Preston, and J. Savage, "Chromosome aberrations and the theory of RBE", International Journal of Radiation Biology and Related Studies in Physics, Chemistry and Medicine **12**, DOI: 10.1080/09553006714550881 (1967) (cited on pages 6, 18).

[11] M. Durante and H. Paganetti, "Nuclear physics in particle therapy: a review", Reports on Progress in Physics **79**, DOI: 10.1088/0034-4885/79/9/096702 (2016) (cited on pages 7, 15).

[12] C. A. Tobias et al., "Pituitary irradiation with high-energy proton beams: a preliminary report", Cancer Research **18** (1958) (cited on page 7).

[13] R. N. Kjellberg, A. M. Koehler, W. M. Preston, and W. H. Sweet, "Stereotaxic instrument for use with the Bragg peak of a proton beam", Stereotactic and Functional Neurosurgery **22**, DOI: 10.1159/000104360 (1962) (cited on page 7).

[14] R. N. Kjellberg, W. H. Sweet, W. M. Preston, and A. M. Koehler, "The Bragg peak of a proton beam in intracranial therapy of tumors.", Transactions of the American Neurological Association **87** (1962) (cited on page 7).

[15] E. S. Gragoudas et al., "Proton beam irradiation of uveal melanomas: results of 5.5-year study", Archives of Ophthalmology **100**, DOI: 10.1001/archopht.1982.01030030936007 (1982) (cited on page 7).

[16] A. M. Koehler, R. J. Schneider, and J. M. Sisterson, "Flattening of proton dose distributions for large field radiotherapy", Medical Physics **4**, DOI: 10.1118/1.594317 (1977) (cited on page 7).

[17] *Particle Therapy Co-operative Group (PTCOG) website*, Visited in October, 2022, https://www.ptcog.ch/ (cited on pages 7–8).

[18] M. Durante, R. Orecchia, and J. S. Loeffler, "Charged-particle therapy in cancer: clinical uses and future perspectives", Nature Reviews Clinical Oncology **14**, DOI: 10.1038/nrclinonc.2017.30 (2017) (cited on page 7).

[19] A. C. Knopf and A. Lomax, "In vivo proton range verification: a review", Physics in Medicine and Biology **58**, DOI: 10.1088/0031-9155/58/15/R131 (2013) (cited on page 8).

[20] H. Paganetti et al., "Range uncertainties in proton therapy and the role of Monte Carlo simulations", Physics in Medicine and Biology **57**, DOI: 10.1088/0031-9155/57/11/R99 (2012) (cited on pages 8, 26, 32, 37, 114).

[21] G. F. Knoll, *Radiation Detection and Measurement*, Third Edition (1981) (cited on pages 12, 59).

[22] H. Bethe, "Zur theorie des durchgangs schneller korpuskularstrahlen durch materie", Annalen der Physik **397**, DOI: 10.1002/andp.19303970303 (1930) (cited on page 12).

[23] F. Bloch, "Zur bremsung rasch bewegter teilchen beim durchgang durch materie", Annalen der Physik **408**, DOI: 10.1002/andp.19334080303 (1933) (cited on page 12).

[24] U. Fano, "Penetration of protons, alpha particles, and mesons", Annual Review of Nuclear Science **13**, DOI: 10.1146/annurev.ns.13.120163.000245 (1963) (cited on page 12).

[25] C. Leroy and P. G. Rancoita, *Principles of radiation interaction in matter and detection*, Third Edition (2011) (cited on page 12).

[26] Y. S. Kim, "Density effect in de/dx of fast charged particles traversing various biological materials", Radiation Research **56**, DOI: 10.2307/3573787 (1973) (cited on page 13).

[27] M. Berger, J. Coursey, M. Zucker, and J. Chang, "ESTAR, PSTAR, and ASTAR: computer programs for calculating stopping-power and range tables for electrons, protons, and helium ions (version 1.2.3)", National Institute of Standards and Technology (2005) (cited on pages 13–15).

[28] ICRU, "ICRU Report 90: Key data for ionizing-radiation dosimetry: measurements standards and applications", Journal of the International Commission on Radiation Units and Measurements **14** (2016) (cited on page 13).

[29] G. Moliere, "Theorie der Streuung schneller geladener Teilchen II Mehrfach-und Vielfachstreuung", Zeitschrift fur Naturforschung - Section A Journal of Physical Sciences **3**, DOI: 10.1515/zna-1948-0203 (1948) (cited on page 14).

[30] H. A. Bethe, "Molière's theory of multiple scattering", Physical Review **89**, DOI: 10.1103/PhysRev.89.1256 (1953) (cited on page 14).

[31] D. Schardt, T. Elsässer, and D. Schulz-Ertner, "Heavy-ion tumor therapy: physical and radiobiological benefits", Reviews of Modern Physics **82**, DOI: 10.1103/RevModPhys.82.383 (2010) (cited on page 15).

[32] C. Zeitlin and C. L. Tessa, "The role of nuclear fragmentation in particle therapy and space radiation protection", Frontiers in Oncology **6**, DOI: 10.3389/fonc.2016.00065 (2016) (cited on page 15).

[33] W. D. Newhauser and R. Zhang, "The physics of proton therapy", Physics in Medicine and Biology **60**, DOI: 10.1088/0031-9155/60/8/R155 (2015) (cited on page 16).

[34] P. V. Vavilov, "Ionization losses of high-energy heavy particles", Soviet Physics JETP **5** (1957) (cited on page 16).

[35] J. Allison et al., "Recent developments in Geant4", Nuclear Instruments and Methods in Physics Research, Section A: Accelerators, Spectrometers, Detectors and Associated Equipment **835**, DOI: 10.1016/j.nima.2016.06.125 (2016) (cited on pages 16, 34, 104).

[36] M. C. Joiner and A. van der Kogel, *Basic Clinical Radiobiology*, Fifth Edition (2009) (cited on page 17).

[37] J. F. Ward, "The complexity of DNA damage: relevance to biological consequences", International Journal of Radiation Biology **66**, DOI: 10.1080/09553009414551401 (1994) (cited on page 18).

[38] K. M. Prise, M. Pinto, H. C. Newman, and B. D. Michael, "A review of studies of ionizing radiation-induced double-strand break clustering", Radiation Research **156**, DOI: 10.1667/0033-7587(2001)156[0572:arosoi]2.0.co;2 (2001) (cited on page 18).

[39] F. Kamlah et al., "Comparison of the effects of carbon ion and photon irradiation on the angiogenic response in human lung adenocarcinoma cells", International Journal of Radiation Oncology Biology Physics **80**, DOI: 10.1016/j.ijrobp.2011.03.033 (2011) (cited on page 19).

[40] F. E. Horst, "Measurement of nuclear reaction cross sections for applications in radiotherapy with protons, helium and carbon ions", PhD thesis (Justus-Liebig-Universität Giessen, 2019) (cited on page 19).

[41] H. Paganetti, "Report of the AAPM TG-256 on the relative biological effectiveness of proton beams in radiation therapy", Medical Physics **46**, DOI: 10.1002/mp.13390 (2019) (cited on page 18).

[42] Y. Y. Zhang et al., "Brain-specific relative biological effectiveness of protons based on long-term outcome of patients with nasopharyngeal carcinoma", International Journal of Radiation Oncology Biology Physics **110**, DOI: 10.1016/j.ijrobp.2021.02.018 (2021) (cited on page 18).

[43] ICRU, "Prescribing, recording, and reporting proton-beam therapy", Journal of the International Commission on Radiation Units and Measurements **7**, DOI: 10.1093/jicru_ndm021 (2007) (cited on page 18).

[44] H. Paganetti, *Proton Therapy Physics*, Second Edition (2016) (cited on pages 19–22, 24, 26).

[45] J. Fourrier, J. Pasternak, and F. Méot, "Acceleration in spiral FFAG using field map data", 11th European Particle Accelerator Conference (EPAC) - Contribution to the Proceedings (2008) (cited on page 22).

[46] S. Antoine et al., "Principle design of a proton therapy, rapid-cycling, variable energy spiral FFAG", Nuclear Instruments and Methods in Physics Research, Section A: Accelerators, Spectrometers, Detectors and Associated Equipment **602**, DOI: 10.1016/j.nima.2009.01.025 (2009) (cited on page 22).

[47] D. Trbojevic and V. Morozov, "Non-scaling fixed field alternating gradient permanent magnet cancer therapy accelerator", 2nd International Particle Accelerator Conference (IPAC) - Contribution to the Proceedings (2011) (cited on page 22).

[48] K. R. Symon, D. W. Kerst, L. W. Jones, L. J. Laslett, and K. M. Terwilliger, "Fixed-field alternating-gradient particle accelerators", Physical Review **103**, DOI: 10.1103/PhysRev.103.1837 (1956) (cited on page 22).

[49] *Advanced Oncotherapy: LIGHT website*, https://www.avoplc.com/en-gb/ (cited on page 22).

[50] B. Baricevic, A. Bardorfer, R. Cerne, G. de Michele, and Y. Ivanisenko, "Light proton therapy LiNaC LLRF system development", 29th Linear Accelerator Conference (LINAC) - Contribution to the Proceedings, DOI: 10.18429/JACoW-LINAC2018-MOPO081 (2018) (cited on page 22).

[51] S. V. Andres et al., "The TERA high gradient test program for hadron therapy linacs", Radiotherapy and Oncology **102**, DOI: 10.1016/s0167-8140(12)70173-1 (2012) (cited on page 22).

[52] C. D. Martinis et al., "Acceleration tests of a 3 GHz proton linear accelerator (LIBO) for hadrontherapy", Nuclear Instruments and Methods in Physics Research, Section A: Accelerators, Spectrometers, Detectors and Associated Equipment **681**, DOI: 10.1016/j.nima.2012.04.017 (2012) (cited on page 22).

[53] D. Margarone et al., "Elimaia: a laser-driven ion accelerator for multidisciplinary applications", Quantum Beam Science **2**, DOI: 10.3390/qubs2020008 (2018) (cited on page 22).

[54] S. C. Wilks et al., "Energetic proton generation in ultra-intense laser-solid interactions", Physics of Plasmas **8**, DOI: 10.1063/1.1333697 (2001) (cited on page 22).

[55] V. Malka et al., "Practicability of proton therapy using compact laser systems", Medical Physics **31**, DOI: 10.1118/1.1747751 (2004) (cited on page 22).

[56] C. M. Ma et al., "Development of a laser-driven proton accelerator for cancer therapy", Laser Physics **16**, DOI: 10.1134/s1054660x06040165 (2006) (cited on page 22).

[57] A. M. Koehler, R. J. Schneider, and J. M. Sisterson, "Range modulators for protons and heavy ions", Nuclear Instruments and Methods **131**, DOI: 10.1016/0029-554X(75)90430-9 (1975) (cited on page 23).

[58] H. Jiang, B. Wang, X. G. Xu, H. D. Suit, and H. Paganetti, "Simulation of organ-specific patient effective dose due to secondary neutrons in proton radiation treatment", Physics in Medicine and Biology **50**, DOI: 10.1088/0031-9155/50/18/007 (2005) (cited on page 23).

[59] Y. Han, "Current status of proton therapy techniques for lung cancer", Radiation Oncology Journal **37**, DOI: 10.3857/roj.2019.00633 (2019) (cited on page 23).

[60] T. Kanai et al., "Spot scanning system for proton radiotherapy", Medical Physics **7**, DOI: 10.1118/1.594693 (1980) (cited on page 24).

[61] P. Lansonneur et al., "First proton minibeam radiation therapy treatment plan evaluation", Scientific Reports **10**, DOI: 10.1038/s41598-020-63975-9 (2020) (cited on page 24).

[62] L. D. Marzi et al., "Implementation of planar proton minibeam radiation therapy using a pencil beam scanning system: a proof of concept study", Medical Physics **45**, DOI: 10.1002/mp.13209 (2018) (cited on page 24).

[63] T. Schneider, L. D. Marzi, A. Patriarca, and Y. Prezado, "Advancing proton minibeam radiation therapy: magnetically focussed proton minibeams at a clinical centre", Scientific Reports **10**, DOI: 10.1038/s41598-020-58052-0 (2020) (cited on page 24).

[64] X. Ding et al., "Improving dosimetric outcome for hippocampus and cochlea sparing whole brain radiotherapy using spot-scanning proton arc therapy", Acta Oncologica **58**, DOI: 10.1080/0284186X.2018.1555374 (2019) (cited on page 24).

[65] G. Liu et al., "Improve the dosimetric outcome in bilateral head and neck cancer (HNC) treatment using spot-scanning proton arc (SPArc) therapy: a feasibility study", Radiation Oncology **15**, DOI: 10.1186/s13014-020-1476-9 (2020) (cited on page 24).

[66] S. Mein et al., "Spot-scanning Hadron Arc (SHArc) therapy: a study with light and heavy ions", Advances in Radiation Oncology **6**, DOI: 10.1016/j.adro.2021.100661 (2021) (cited on page 24).

[67] J. R. Hughes and J. L. Parsons, "Flash radiotherapy: current knowledge and future insights using proton-beam therapy", International Journal of Molecular Sciences **21**, DOI: 10.3390/ijms21186492 (2020) (cited on page 24).

[68] U. Schneider, E. Pedroni, and A. Lomax, "The calibration of CT Hounsfield units for radiotherapy treatment planning", Physics in Medicine and Biology **41**, DOI: 10.1088/0031-9155/41/1/009 (1996) (cited on page 26).

[69] B. Schaffner and E. Pedroni, "The precision of proton range calculations in proton radiotherapy treatment planning: experimental verification of the relation between CT-HU and proton stopping power", Physics in Medicine and Biology **43**, DOI: 10.1088/0031-9155/43/6/016 (1998) (cited on page 26).

[70] A. V. Chvetsov and S. L. Paige, "The influence of CT image noise on proton range calculation in radiotherapy planning", Physics in Medicine and Biology **55**, DOI: 10.1088/0031-9155/55/6/N01 (2010) (cited on page 26).

[71] S. España and H. Paganetti, "Uncertainties in planned dose due to the limited voxel size of the planning CT when treating lung tumors with proton therapy", Physics in Medicine and Biology **56**, DOI: 10.1088/0031-9155/56/13/007 (2011) (cited on pages 26, 32).

[72] F. Albertini et al., "Sensitivity of intensity modulated proton therapy plans to changes in patient weight", Radiotherapy and Oncology **86**, DOI: 10.1016/j.radonc.2007.11.032 (2008) (cited on page 26).

[73] J. Krimmer, D. Dauvergne, J. M. Létang, and Testa, "Prompt-gamma monitoring in hadrontherapy: a review", Nuclear Instruments and Methods in Physics Research, Section A: Accelerators, Spectrometers, Detectors and Associated Equipment **878**, DOI: 10.1016/j.nima.2017.07.063 (2018) (cited on page 27).

[74] A. Wrońska, "Prompt gamma imaging in proton therapy - status, challenges and developments", Journal of Physics: Conference Series **1561**, DOI: 10.1088/1742-6596/1561/1/012021 (2020) (cited on page 27).

[75] J. Lerendegui-Marco, J. Balibrea-Correa, V. Babiano-Suárez, I. Ladarescu, and C. Domingo-Pardo, "Towards machine learning aided real-time range imaging in proton therapy", Scientific Reports **12**, DOI: 10.1038/s41598-022-06126-6 (2022) (cited on page 27).

[76] K. S. Ytre-Hauge, K. Skjerdal, J. Mattingly, and I. Meric, "A Monte Carlo feasibility study for neutron based real-time range verification in proton therapy", Scientific Reports **9**, DOI: 10.1038/s41598-019-38611-w (2019) (cited on page 27).

[77] L. Sulak et al., "Experimental studies of the acoustic signature of proton beams traversing fluid media", Nuclear Instruments and Methods **161**, DOI: 10.1016/0029-554X(79)90386-0 (1979) (cited on page 27).

[78] K. C. Jones, A. Witztum, C. M. Sehgal, and S. Avery, "Proton beam characterization by proton-induced acoustic emission: simulation studies", Physics in Medicine and Biology **59**, DOI: 10.1088/0031-9155/59/21/6549 (2014) (cited on page 27).

[79] H. M. Lu, "A potential method for in vivo range verification in proton therapy treatment", Physics in Medicine and Biology **53**, DOI: 10.1088/0031-9155/53/5/016 (2008) (cited on page 28).

[80] T. T. Pham et al., "Magnetic resonance imaging (MRI) guided proton therapy: a review of the clinical challenges, potential benefits and pathway to implementation", Radiotherapy and Oncology **170**, DOI: 10.1016/j.radonc.2022.02.031 (2022) (cited on page 28).

[81] K. S. Krane, *Introductory Nuclear Physics*, First Edition (1989) (cited on pages 29–31).

[82] E. Fermi, *Nuclear Physics: a course given by Enrico Fermi at the University of Chicago. Course notes compiled by J. Orear, A.H. Rosenfeld and R.A. Schluter*, Revised Edition (1950) (cited on page 29).

[83] C. J. Malmer, "ICRU Report 63: Nuclear data for neutron and proton radiotherapy and for radiation protection", Medical Physics **28**, DOI: 10.1118/1.1369116 (2001) (cited on pages 31, 34, 37).

[84] A. M. Paans and J. M. Schippers, "Proton therapy in combination with PET as monitor: a feasibility study", IEEE Transactions on Nuclear Science **40**, DOI: 10.1109/23.256709 (1993) (cited on page 32).

[85] S. Vynckier et al., "Is it possible to verify directly a proton-treatment plan using positron emission tomography?", Radiotherapy and Oncology **26**, DOI: 10.1016/0167-8140(93)90271-9 (1993) (cited on page 32).

[86] U. Oelfke, G. K. Lam, and M. S. Atkins, "Proton dose monitoring with PET: quantitative studies in Lucite", Physics in Medicine and Biology **41**, DOI: 10.1088/0031-9155/41/1/013 (1996) (cited on page 32).

[87] D. W. Litzenberg, "On-line monitoring and PET imaging of the positron-emitting activity created in tissue by proton radiotherapy beams", Medical Physics **25**, DOI: 10.1118/1.598193 (1998) (cited on page 32).

[88] K. Parodi, W. Enghardt, and T. Haberer, "In-beam PET measurements of β^+ radioactivity induced by proton beams", Physics in Medicine and Biology **47**, DOI: 10.1088/0031-9155/47/1/302 (2002) (cited on page 32).

[89] K. Parodi et al., "Patient study of in vivo verification of beam delivery and range, using positron emission tomography and computed tomography imaging after proton therapy", International Journal of Radiation Oncology Biology Physics **68**, DOI: 10.1016/j.ijrobp.2007.01.063 (2007) (cited on pages 32–33).

[90] J. Bauer, D. Unholtz, C. Kurz, and K. Parodi, "An experimental approach to improve the Monte Carlo modelling of offline PET/CT-imaging of positron emitters induced by scanned proton beams", Physics in Medicine and Biology **58**, DOI: 10.1088/0031-9155/58/15/5193 (2013) (cited on page 32).

[91] A. Lühr, M. Priegnitz, F. Fiedler, N. Sobolevsky, and N. Bassler, "Dependence of simulated positron emitter yields in ion beam cancer therapy on modeling nuclear fragmentation", Applied Radiation and Isotopes **83**, DOI: 10.1016/j.apradiso.2012.12.018 (2014) (cited on page 32).

[92] F. T. Tárkányi et al., "Recommended nuclear data for medical radioisotope production: diagnostic positron emitters", Journal of Radioanalytical and Nuclear Chemistry **319**, DOI: 10.1007/s10967-018-6380-5 (2019) (cited on pages 32, 37).

[93] A. L. Nichols and R. Capote, "Nuclear data for medical applications - recent developments and future requirements", Nuclear Data Sheets **120**, DOI: 10.1016/j.nds.2014.07.056 (2014) (cited on pages 32, 37, 104, 114).

[94] X. Zhu et al., "Monitoring proton radiation therapy with in-room PET imaging", Physics in Medicine and Biology **56**, DOI: 10.1088/0031-9155/56/13/019 (2011) (cited on pages 32, 34).

[95] Y. Hishikawa et al., "Usefulness of positron-emission tomographic images after proton therapy", International Journal of Radiation Oncology Biology Physics **53**, DOI: 10.1016/S0360-3016(02)02887-0 (2002) (cited on page 33).

[96] A. C. Knopf et al., "Accuracy of proton beam range verification using post-treatment positron emission tomography/computed tomography as function of treatment site", International Journal of Radiation Oncology Biology Physics **79**, DOI: 10.1016/j.ijrobp.2010.02.017 (2011) (cited on page 33).

[97] W. C. Hsi et al., "In vivo verification of proton beam path by using post-treatment PET/CT imaging", Medical Physics **36**, DOI: 10.1118/1.3193677 (2009) (cited on page 33).

[98] P. Dendooven et al., "Corrigendum: Short-lived positron emitters in beam-on PET imaging during proton therapy", Physics in Medicine and Biology **64**, DOI: 10.1088/1361-6560/ab23d7 (2019) (cited on pages 33, 35, 101–102, 104).

[99] M. G. Bisogni et al., "INSIDE: In-beam positron emission tomography system for particle range monitoring in hadrontherapy", Journal of Medical Imaging **4**, DOI: 10.1117/1.jmi.4.1.011005 (2016) (cited on page 34).

[100] W. Enghardt et al., "Charged hadron tumour therapy monitoring by means of PET", Nuclear Instruments and Methods in Physics Research, Section A: Accelerators, Spectrometers, Detectors and Associated Equipment **525**, DOI: 10.1016/j.nima.2004.03.128 (2004) (cited on page 34).

[101] T. Yamaya and H. Tashima, "OpenPET enabling PET imaging during radiotherapy", Personalized Pathway-Activated Systems Imaging in Oncology: Principal and Instrumentation, DOI: 10.1007/978-981-10-3349-0_4 (2017) (cited on page 34).

[102] T. Nishio et al., "The development and clinical use of a beam on-line PET system mounted on a rotating gantry port in proton therapy", International Journal of Radiation Oncology Biology Physics **76**, DOI: 10.1016/j.ijrobp.2009.05.065 (2010) (cited on page 34).

[103] *EXFOR database website*, Visited in 2021-2022, https://www-nds.iaea.org/exfor/ (cited on page 34).

[104] C. M. Bäcker et al., "Measurement of nuclear activation cross sections of protons on natural carbon for proton beam energies between 100 and 220 MeV", Nuclear Instruments and Methods in Physics Research, Section B: Beam Interactions with Materials and Atoms **454**, DOI: 10.1016/j.nimb.2019.06.011 (2019) (cited on pages 35, 37, 92–93).

[105] F. Horst et al., "Measurement of PET isotope production cross sections for protons and carbon ions on carbon and oxygen targets for applications in particle therapy range verification", Physics in Medicine and Biology **64**, DOI: 10.1088/1361-6560/ab4511 (2019) (cited on pages 35, 37, 92–93, 100).

[106] M. B. Chadwick, "ENDF nuclear data in the physical, biological, and medical sciences", International Journal of Radiation Biology **88**, DOI: 10.3109/09553002.2011.595879 (2012) (cited on page 37).

[107] M. Chadwick et al., "LA150 documentation of cross sections, heating, and damage: part A (incident neutrons) and part B (incident protons)", Technical Report LA-UR-99-1222, Los Alamos National Laboratory, Los Alamos, NM (1999) (cited on page 37).

[108] R. L. Aamodt, V. Peterson, and R. Phillips, "^{12}C(p,pn)^{11}C cross section from threshold to 340 MeV", Physical Review **88**, DOI: 10.1103/PhysRev.88.739 (1952) (cited on pages 37, 92–93).

[109] H. Gauvin, M. Lefort, and X. Tarrago, "Émission d'hélions dans les réactions de spallation", Nuclear Physics **39**, DOI: 10.1016/0029-5582(62)90403-0 (1962) (cited on pages 37–38, 92).

[110] G Albouy et al., "Spallation of oxygen by protons with 20 to 150 MeV", Phys. Letters **2**, DOI: 10.1016/0031-9163(62)90119-1 (1962) (cited on pages 37, 93, 98, 100).

[111] L. Valentin, "Réactions (p,n) et (p,pn) induites à moyenne énergie sur des noyaux légers", Nuclear Physics **62**, DOI: 10.1016/0029-5582(65)90072-6 (1965) (cited on pages 37, 100).

[112] "IAEA-Tecdoc-1211: Charged particle cross-section database for medical radioisotope production: diagnostic radioisotopes and monitor reactions", (2001) (cited on page 37).

[113] J. W. Engle, A. L. Nichols, and R. Capote, "Summary report of the Technical Meeting on Long Term Data Needs in Medical Applications. INDC(NDS)-0776", IAEA technical report (2018) (cited on page 37).

[114] S. España et al., "The reliability of proton-nuclear interaction cross-section data to predict proton-induced PET images in proton therapy", Physics in Medicine and Biology **56**, DOI: 10.1088/0031-9155/56/9/003 (2011) (cited on pages 37, 114).

[115] N. M. Hintz and N. F. Ramsey, "Excitation functions to 100 MeV", Physical Review **88**, DOI: 10.1103/PhysRev.88.19 (1952) (cited on pages 37, 92–93).

[116] K. Matsushita et al., "Measurement of proton-induced target fragmentation cross sections in carbon", Nuclear Physics A **946**, DOI: 10.1016/j.nuclphysa.2015.11.007 (2016) (cited on pages 38, 92).

[117] *Encyclopedia Britannica website*, https://www.britannica.com/ (cited on page 42).

[118] M. Herman et al., "EMPIRE: Nuclear Reaction Model Code System for Data Evaluation", Nuclear Data Sheets **108**, DOI: 10.1016/j.nds.2007.11.003 (2007) (cited on page 44).

[119] A. J. Koning and D. Rochman, "Modern nuclear data evaluation with the TALYS code system", Nuclear Data Sheets **113**, DOI: 10.1016/j.nds.2012.11.002 (2012) (cited on page 44).

[120] G. Folger, V. N. Ivanchenko, and J. P. Wellisch, "The binary cascade: nucleon nuclear reactions", European Physical Journal A **21**, DOI: 10.1140/epja/i2003-10219-7 (2004) (cited on page 44).

[121] *Centro Nacional de Aceleradores website*, Visited in October, 2022, http://cna.us.es/index.php/es/ (cited on pages 48, 54).

[122] J. Gómez-Camacho et al., "Research facilities and highlights at the Centro Nacional de Aceleradores (CNA)", European Physical Journal Plus **136**, DOI: 10.1140/epjp/s13360-021-01253-x (2021) (cited on page 48).

[123] *Model Brookhaven 1000c Current Integrator website*, Visited in October, 2022, http://www.bicorp.com/products/1000C/1000c.htm (cited on page 49).

[124] *West German Proton Therapy Centre website*, Visited in October, 2022, https://www.wpe-uk.de/ (cited on page 49).

[125] C. Bäumer et al., "Dosimetry intercomparison of four proton therapy institutions in Germany employing spot scanning", Zeitschrift für Medizinische Physik **27**, DOI: 10.1016/j.zemedi.2016.06.007 (2017) (cited on page 50).

[126] C. Bäumer et al., "Measurement of absolute activation cross sections from carbon and aluminum for proton therapy", Nuclear Instruments and Methods in Physics Research, Section B: Beam Interactions with Materials and Atoms **440**, DOI: 10.1016/j.nimb.2018.11.020 (2019) (cited on page 50).

[127] E. Grusell, U. Isacsson, A. Montelius, and J. Medin, "Faraday cup dosimetry in a proton therapy beam without collimation", Physics in Medicine and Biology **40**, DOI: 10.1088/0031-9155/40/11/005 (1995) (cited on page 50).

[128] *Heidelberg Ion-Beam Therapy Centre website*, Visited in October, 2022, https://www.klinikum.uni-heidelberg.de/interdisziplinaere-zentren/heidelberger-ionenstrahl-therapiezentrum-hit/ (cited on page 50).

[129] T. Haberer et al., "The Heidelberg Ion Therapy Center", Radiotherapy and Oncology **73**, S186–S190 (2004) (cited on page 50).

[130] D. Ondreka and U. Weinrich, "The Heidelberg Ion Therapy (HIT) accelerator coming into operation", 11th European Particle Accelerator Conference (EPAC) - Contribution to the Proceedings (2008) (cited on pages 50–51).

[131] C. Schoemers et al., "The intensity feedback system at Heidelberg Ion-Beam Therapy Centre", Nuclear Instruments and Methods in Physics Research, Section A: Accelerators, Spectrometers, Detectors and Associated Equipment **795**, DOI: 10.1016/j.nima.2015.05.054 (2015) (cited on page 51).

[132] T. Tessonnier et al., "Dosimetric verification in water of a Monte Carlo treatment planning tool for proton, helium, carbon and oxygen ion beams at the Heidelberg Ion Beam Therapy Center", Physics in Medicine and Biology **62**, DOI: 10.1088/1361-6560/aa7be4 (2017) (cited on page 51).

[133] P. Forck, "Lecture Notes on Beam Instrumentation and Diagnostics", Joint University Accelerator School (2011) (cited on page 51).

[134] Y. S. Lee et al., "Performance measurement of PSF modeling reconstruction (True X) on Siemens Biograph TruePoint TrueV PET/CT", Annals of Nuclear Medicine **28**, DOI: 10.1007/s12149-014-0815-z (2014) (cited on page 53).

[135] M. S. Tohme and J. Qi, "Iterative image reconstruction for positron emission tomography based on a detector response function estimated from point source measurements", Physics in Medicine and Biology **54**, DOI: 10.1088/0031-9155/54/12/007 (2009) (cited on page 53).

[136] *Image Processing Software (PMOD) website*, https://www.pmod.com/web/ (cited on page 53).

[137] *DICOM website*, https://www.dicomstandard.org/about-home (cited on page 53).

[138] *Siemens Healthineers Biograph Vision website*, https://www.siemens-healthineers.com (cited on page 54).

[139] B. Kunnen, C. Beijst, M. G. Lam, M. A. Viergever, and H. W. de Jong, "Comparison of the Biograph Vision and Biograph mCT for quantitative ^{90}Y PET/CT imaging for radioembolisation", EJNMMI Physics **7**, DOI: 10.1186/s40658-020-0283-6 (2020) (cited on page 54).

[140] B. Arjomandy et al., "AAPM task group 224: comprehensive proton therapy machine quality assurance", Medical Physics **46**, DOI: 10.1002/mp.13622 (2019) (cited on page 56).

[141] *Saint Gobain Scintillation Materials website*, https://www.crystals.saint-gobain.com/ (cited on page 58).

[142] *CAEN website*, https://www.caen.it/ (cited on page 58).

[143] *Root data analysis framework website*, https://root.cern.ch/ (cited on pages 58, 79, 88).

[144] *CoMPASS, CAEN website*, https://www.caen.it/products/compass/ (cited on page 58).

[145] A. Hermanne et al., "Reference cross sections for charged-particle monitor reactions", Nuclear Data Sheets **148**, DOI: 10.1016/j.nds.2018.02.009 (2018) (cited on pages 72, 78, 85, 116).

[146] J. R. D. Laeter et al., "Atomic weights of the elements: Review 2000 (IUPAC Technical Report)", Pure and Applied Chemistry **75**, DOI: 10.1351/pac200375060683 (2000) (cited on page 79).

[147] M. E. Wieser and T. B. Coplen, "Atomic weights of the elements 2009 (IUPAC Technical Report)", Pure and Applied Chemistry **83**, DOI: 10.1351/PAC-REP-10-09-14 (2009) (cited on page 79).

[148] T. Rodríguez-González et al., "Production yields at the distal fall-off of the β^+ emitters ^{11}C and ^{13}N for in-vivo range verification in proton therapy", Radiation Physics and Chemistry **190**, DOI: 10.1016/j.radphyschem.2021.109759 (2022) (cited on page 92).

[149] T. Rodríguez-González et al., "Production of 11C, 13N and 15O in proton-induced nuclear reactions up to 200 MeV", Nuclear Data Sheets **187**, 579–596 (2023) (cited on page 92).

[150] D. F. Measday, "The ^{12}C(p,pn)^{11}C reaction from 50 to 160 MeV", Nuclear Physics **78**, DOI: 10.1016/0029-5582(66)90621-3 (1966) (cited on page 92).

[151] V. Kostjuchenko and D. Nichiporov, "Measurement of the ^{12}C(p,pn)^{11}C reaction from 95 to 200 MeV", Applied Radiation and Isotopes **44**, 1173–1175 (1993), https://www.sciencedirect.com/science/article/pii/096980439390060N (cited on page 92).

[152] K. Kettern et al., "Formation of short-lived positron emitters in reactions of protons of energies up to 200 MeV with the target elements carbon, nitrogen and oxygen", Applied Radiation and Isotopes **60**, DOI: 10.1016/j.apradiso.2004.02.007 (2004) (cited on pages 93, 96, 98, 100).

[153] T. Akagi et al., "Experimental study for the production cross sections of positron emitters induced from ^{12}C and ^{16}O nuclei by low-energy proton beams", Radiation Measurements **59**, DOI: 10.1016/j.radmeas.2013.07.005 (2013) (cited on pages 93, 100).

[154] T. Masuda et al., "Measurement of nuclear reaction cross sections by using Cherenkov radiation toward high-precision proton therapy", Scientific Reports **8**, DOI: 10.1038/s41598-018-20906-z (2018) (cited on pages 93, 100).

[155] Blaser et al., "Anregungsfunktion der Kernreaktion ^{14}N(p,α)^{11}C", Helvetia Physica Acta (1952) (cited on page 94).

[156] T. Nozaki et al., "The radioactivation analysis of semiconductor graphite for nitrogen by the ^{14}N(p,α)^{11}C reaction", Bulletin of the Chemical Society of Japan **39**, DOI: 10.1246/bcsj.39.2685 (1966) (cited on page 94).

[157] W. W. Jacobs et al., "Production of Li and B in proton and alpha particle reactions on ^{14}N at low energies", Physical Review C **9**, DOI: 10.1103/PhysRevC.9.2134 (1974) (cited on page 94).

[158] P. D. Ingalls, J. S. Schweitzer, B. D. Anderson, and M. Rios, "^{14}N(p,α)^{11}C cross-sections from 3.8 to 6.4 MeV", Physical Review C **13**, DOI: 10.1103/PhysRevC.13.524 (1976) (cited on page 94).

[159] V. R. Casella et al., "Excitation functions for the ^{14}N(p,α)^{11}C reaction up to 15 MeV", Radiochimica Acta **25**, DOI: 10.1524/ract.1978.25.1.17 (1978) (cited on page 94).

[160] G. T. Bida, T. J. Ruth, and A. P. Wolf, "Experimentally determined thick target yields for the ^{14}N (p,α)^{11}C reaction", Radiochimica Acta **27**, DOI: 10.1524/ract.1980.27.4.181 (1980) (cited on page 94).

[161] F. Koehl et al., "Determination of nitrogen in semiconductor materials using the ^{14}N(p,α)^{11}C and ^{14}N(d,n)^{15}O nuclear reactions", Nuclear Inst. and Methods in Physics Research, B **50**, DOI: 10.1016/0168-583X(90)90321-K (1990) (cited on page 94).

[162] A. Hermanne, F. T. Tárkányi, A. V. Ignatyuk, S. Takács, and R. Capote, "Upgrade of IAEA recommended data of selected nuclear reactions for production of PET and SPECT isotopes", Nuclear Data Sheets **173**, DOI: 10.1016/j.nds.2021.04.008 (2021) (cited on pages 94–95, 98).

[163] M.Fassbender, B.Scholten, Yu.N.Shubin, and S.M.Qaim, "Activation cross section data for (p,x) processes of therapeutic relevance", International Conference on Nuclear Data for Science and Technology - Contribution in the Proceedings (1997) (cited on page 96).

[164] B. L. Cohen, "(p,γ) cross sections", Physical Review **100**, DOI: 10.1103/PhysRev.100.206 (1955) (cited on page 96).

[165] A. B. Whitehead and J. S. Foster, "Activation cross-sections for ^{12}C(p,pn)^{11}C,^{16}O(p,α)^{13}N and ^{19}F(p,pn)^{18}F", Canadian Journal of Physics **36**, DOI: 10.1139/p58-132 (1958) (cited on page 97).

[166] M. Furukawa et al., "Excitation function for the reaction ^{11}B(p,n)^{11}C up to E_p=15 MeV and energy levels of ^{12}C", Journal of the Physical Society of Japan **15**, DOI: 10.1143/JPSJ.15.2167 (1960) (cited on page 97).

[167] Hille et al., "High-resolution measurements of the ^{16}O(p,α)^{13}N excitation function", Physical Review **123** (1961) (cited on page 97).

[168] D. R. Maxson, "^{16}O(p,α)^{13}N angular distributions at 13.5–18.1 MeV", Physical Review **123**, DOI: 10.1103/PhysRev.123.1304 (1961) (cited on page 98).

[169] R. L. Dangle, L. D. Oppliger, and G. Hardie, "^{16}O(p,α)^{13}N and ^{16}O(p,p')^{16}O differential cross-sections", Physical Review **133**, DOI: 10.1103/PhysRev.133.B647 (1964) (cited on page 98).

[170] R. H. McCamis, G. A. Moss, and J. M. Cameron, "Total cross-section of ^{16}O(p,α)^{13}N from threshold to 7.7 MeV", Canadian Journal of Physics **51**, DOI: 10.1139/p73-223 (1973) (cited on page 98).

[171] A. V. Nero and A. J. Howard, "^{16}O(p,α)^{13}N cross-section measurements", Nuclear Physics, Section A **210**, DOI: 10.1016/0375-9474(73)90503-4 (1973) (cited on page 98).

[172] W. Gruhle and B. Kober, "The reactions ^{16}O(p,α), ^{20}Ne(p,α) and ^{24}Mg(p,α)", Nuclear Physics, Section A **286**, DOI: 10.1016/0375-9474(77)90601-7 (1977) (cited on page 98).

[173] M. Sajjad, R. M. Lambrecht, and A. P. Wolf, "Cyclotron isotopes and radiopharmaceuticals XXXVII. Excitation functions for the ^{16}O(p,α)^{13}N and ^{14}N(p,pn)^{13}N reactions", Radiochimica Acta **39**, DOI: 10.1524/ract.1986.39.3.165 (1986) (cited on pages 98, 100).

[174] S. W. Kitwanga et al., "Production of ^{13}N radioactive nuclei from ^{13}C(p,n) or ^{16}O(p,α) reactions", Physical Review C **40**, DOI: 10.1103/PhysRevC.40.35 (1989) (cited on page 98).

[175] K. J. Foley, G. L. Salmon, and A. B. Clegg, "Gamma radiation from the bombardment of ^{16}O and ^{19}F nuclei with 150 MeV protons", Nuclear Physics **31**, DOI: 10.1016/0029-5582(62)90727-7 (1962) (cited on page 98).

[176] L. Valentin, G. Albouy, J. P. Cohen, and M. Gusakow, "Reactions induites par des protons de 155 MeV sur des noyaux legers", Physics Letters **7**, DOI: 10.1016/0031-9163(63)90651-6 (1963) (cited on page 98).

[177] M. Sajjad, R. M. Lambrecht, and A. P. Wolf, "Cyclotron Isotopes and Radiopharmaceuticals: XXXVI. Investigation of Some Excitation Functions for the Preparation of ^{15}O, ^{13}N and ^{11}C", Radiochimica Acta **38**, DOI: doi:10.1524/ract.1985.38.2.57 (1985) (cited on page 100).

[178] H. M. Kuan, M. Hasinoff, W. J. O'Connell, and S. S. Hanna, "The giant dipole resonances in 11c and 15o observed with the reactions 10b(p,)11c and 14n(p,)15o", Nuclear Physics, Section A **151**, DOI: 10.1016/0375-9474(70)90973-5 (1970) (cited on page 101).

[179] M. H. Harakeh, P. Paul, H. M. Kuan, and E. K. Warburton, "E1 excitations in a=15 nuclei", Physical Review C **12**, DOI: 10.1103/PhysRevC.12.1410 (1975) (cited on page 101).

[180] U. Schröder et al., "Stellar reaction rate of 14n(p,)15o and hydrogen burning in massive stars", Nuclear Physics, Section A **467**, DOI: 10.1016/0375-9474(87)90528-8 (1987) (cited on page 101).

[181] E. M. Rimmer and P. S. Fisher, "Resonances in the (p, n) reaction on 12c", Nuclear Physics, Section A **108**, DOI: 10.1016/0375-9474(68)90324-2 (1968) (cited on page 102).

[182] S. D. Schery, D. A. Lind, H. W. Fielding, and C. D. Zafiratos, "The (p,n) reaction to the isobaric analogue state of high-Z elements at 25.8 MeV", Nuclear Physics, Section A **234**, DOI: 10.1016/0375-9474(74)90382-0 (1974) (cited on page 102).

[183] P. Arce et al., "Report on G4-Med, a Geant4 benchmarking system for medical physics applications developed by the Geant4 Medical Simulation Benchmarking Group", Medical Physics **48**, DOI: 10.1002/mp.14226 (2021) (cited on page 104).

[184] P. Crespo, G. Shakirin, and W. Enghardt, "On the detector arrangement for in-beam pet for hadron therapy monitoring", Physics in Medicine and Biology **51**, DOI: 10.1088/0031-9155/51/9/002 (2006) (cited on page 109).

[185] I. Perali et al., "Prompt gamma imaging of proton pencil beams at clinical dose rate", Physics in Medicine and Biology **59**, DOI: 10.1088/0031-9155/59/19/5849 (2014) (cited on page 109).

[186] M. R. Islam et al., "Proton range monitoring using 13 n peak for proton therapy applications", PLoS ONE **17**, DOI: 10.1371/journal.pone.0263521 (2022) (cited on page 109).

[187] J. Cho et al., "Feasibility study of using fall-off gradients of early and late pet scans for proton range verification", Medical Physics **44**, DOI: 10.1002/mp.12191 (2017) (cited on page 109).

[188] J. Balibrea-Correa et al., "Hybrid in-beam PET- and Compton prompt-gamma imaging aimed at enhanced proton-range verification. ", European Physical Journal Plus **137**, DOI: https://doi.org/10.1140/epjp/s13360-022-03414-y (2022) (cited on page 117).

Appendix A

Tabulated reaction cross sections

TABLE A.1: ^{12}C(p,x)^{11}C and ^{12}C(p,γ)^{13}N reaction cross sections.

Facility	E (MeV)	σ (mb)	
		^{12}C(p,x)^{11}C	^{12}C(p,γ)^{13}N
CNA	2.0(12)	0	0.79(6)
	4.2(10)	0	1.89(15)
	$5.9^{+0.7}_{-0.8}$	0	2.09(17)
	7.2(6)	0	1.82(15)
	8.4(6)	0	1.41(11)
	9.5(5)	0	0.88(7)
	10.4(5)	0	0.74(6)
	11.3(4)	0	0.56(4)
	12.2(4)	0	0.60(5)
	12.9(4)	0	0.54(4)
	13.7(4)	0	0.56(4)
	14.4(4)	0	0.47(4)
	15.1(3)	0	0.45(6)
	15.8(3)	0	0.46(4)
	16.4(3)	0.29(3)	0.69(7)
HIT	23.6(12)	20.5(8)	-
	25.8(11)	44.4(18)	-
	27.9(10)	68(3)	-
WPE	30(3)	87(3)	-
	32(3)	94(3)	-
	33(3)	97(4)	-
	35.2(24)	97(4)	-
	36.9(23)	97(4)	-
	38.4(23)	96(3)	-
	44.1(18)	94(3)	-
	51.9(15)	91(3)	-
	58.2(13)	89(3)	-
	68.1(11)	86(3)	-
	$49.5^{+1.4}_{-1.3}$	86(3)	-
	56.6(12)	90(3)	-
	63.1(11)	87(3)	-
	69.1(10)	83(3)	-
	74.7(8)	81(3)	-
	80.0(8)	76(3)	-
	85.0(7)	73(3)	-
	89.8(6)	72(3)	-
	94.4(4)	71(3)	-
	98.9(4)	68.3(25)	-
	85.1(17)	66.1(24)	-
	93.7(15)	68.9(25)	-

Continued on next page

Continued from previous page

101.9(14)	66.9(24)	-
109.5(12)	64.8(23)	-
116.8(11)	62.6(23)	-
123.8(10)	59.5(21)	-
130.5(8)	57.3(21)	-
136.9(7)	56.3(20)	-
143.1(5)	55.1(20)	-
149.2(3)	56.6(20)	-
138.9(15)	53.5(19)	-
145.1(14)	54.3(20)	-
151.1(13)	54.9(20)	-
157.0(12)	53.3(19)	-
$162.6^{+1.1}_{-1.2}$	53.4(19)	-
168.2(10)	52.9(19)	-
173.6(9)	52.1(19)	-
179.0(7)	49.8(18)	-
184.2(5)	48.8(18)	-
189.3(3)	48.9(18)	-

TABLE A.2: ^{16}O(p,x)^{11}C, ^{16}O(p,x)^{13}N and ^{16}O(p,x)^{15}O reaction cross sections.

Facility	E (MeV)	σ (mb)		
		^{16}O(p,x)^{11}C	^{16}O(p,x)^{13}N	^{16}O(p,x)^{15}O
CNA	5.0(8)	-	0	-
	6.5(7)	-	0.63(7)	-
	7.7(6)	-	36(3)	-
	8.8(5)	-	13.0(10)	-
	9.8(5)	-	24.3(19)	-
	10.7(4)	-	59(5)	-
	11.5(4)	-	40(3)	-
	12.3(4)	-	35(3)	-
	13.1(4)	-	27.9(22)	-
	13.8(4)	-	48(4)	-
	14.5(3)	-	42(3)	-
	15.2(3)	-	34(3)	-
	15.8(3)	-	19.3(15)	-
	16.4(3)	-	9.8(8)	-
HIT	$20.2^{+2.5}_{-2.4}$	0.69(3)	8.7(5)	10.9(5)
	24.8(21)	2.08(11)	3.24(19)	40.8(21)
WPE	28^{+4}_{-3}	5.3(2)	0.82(7)	62.6(23)
	32(3)	11.0(4)	0.98(8)	70(3)
	35(3)	16.1(6)	1.32(11)	72(3)
	$38.2^{+2.5}_{-2.4}$	23.5(9)	2.51(19)	73(3)
	$41.2^{+2.1}_{-2.0}$	24.9(9)	3.39(25)	72(3)
	43.9(19)	27.3(10)	4.2(3)	75(3)
	$46.5^{+1.9}_{-1.8}$	28.0(10)	4.7(4)	72(3)
	$49.0^{+1.8}_{-1.7}$	27.0(10)	5.20(21)	72(3)
	57.2(14)	25.6(9)	5.94(25)	66.2(24)
	64.6(13)	22.7(8)	5.9(3)	57.8(21)
	$48.2^{+1.8}_{-1.7}$	27.2(11)	5.3(5)	68.7(25)
	$51.8^{+1.6}_{-1.5}$	24.9(9)	5.4(3)	70(3)
	55.3(15)	23.8(9)	5.7(3)	67.0(24)
	62.9(13)	22.1(8)	5.3(3)	65.5(24)
	69.7(12)	21.1(8)	5.8(3)	63.4(23)
	$76.2^{+1.1}_{-1.0}$	20.6(9)	5.6(5)	62.6(23)
	82.2(9)	20.3(11)	5.9(5)	61.4(23)
	87.9(8)	18.8(20)	6.0(5)	56.8(24)
	93.3(8)	18.8(10)	5.6(5)	52.0(19)
	98.6(7)	17.8(9)	5.6(5)	48.1(18)
	77.3(21)	21.5(8)	5.60(21)	54.4(20)
	87.4(19)	20.0(7)	5.78(21)	56.6(20)
	96.6(16)	18.5(7)	5.54(20)	55.5(19)
	105.2(14)	17.2(6)	5.91(22)	47.5(17)

Continued on next page

Continued from previous page

113.3(12)	17.0(6)	5.59(20)	47.6(17)
121.0(11)	16.8(6)	5.40(20)	46.5(17)
128.4(9)	16.3(7)	5.17(20)	43.8(16)
135.5(8)	16.3(6)	4.88(25)	41.8(15)
142.3(6)	15.5(6)	4.82(19)	40.1(15)
148.9(5)	15.4(6)	4.5(3)	40.8(15)
133.7(17)	15.6(6)	5.3(4)	42.3(18)
140.5(15)	16.8(7)	5.4(3)	39.7(14)
147.2(15)	16.2(6)	5.3(3)	39.3(14)
153.6(13)	15.9(6)	5.3(3)	37.0(13)
159.9(12)	16.2(6)	5.6(3)	37.0(13)
166.0(11)	15.6(6)	5.0(3)	37.0(13)
$172.0^{+1.0}_{-0.9}$	15.8(6)	4.97(23)	37.0(13)
177.8(8)	15.5(7)	4.8(4)	36.0(15)
183.5(6)	14.4(6)	5.0(3)	33.7(12)
189.1(5)	15.2(6)	5.4(3)	31.7(11)

TABLE A.3: ^{14}N(p,x)^{11}C, ^{14}N(p,x)^{13}N and ^{14}N(p,x)^{15}O reaction cross sections.

Facility	E (MeV)	σ (mb)		
		^{14}N(p,x)^{11}C	^{14}N(p,x)^{13}N	^{14}N(p,γ)^{15}O
CNA	$4.3^{+0.9}_{-1.0}$	14.4(13)	-	-
	6.0(7)	103(8)	-	-
	7.3(6)	175(14)	-	-
	8.5(5)	84(7)	-	-
	9.5(5)	86(7)	-	-
	10.5(5)	117(9)	-	-
	11.3(4)	96(7)	-	-
	12.2(4)	102(8)	-	-
	13.0(4)	108(8)	-	-
	13.7(4)	123(9)	-	-
	14.4(3)	99(9)	-	-
	15.1(3)	96(8)	-	-
	15.8(3)	81(7)	-	-
	16.4(3)	70(5)	-	-
HIT	22.7(20)	24.3(12)	17.5(9)	6.1(3)
	25.6(18)	6.1(3)	25.4(13)	5.1(3)
	29.1(17)	9.0(5)	32.5(17)	7.1(4)
WPE	32(3)	13.6(9)	33.0(21)	3.7(3)
	35(3)	17.0(12)	30.5(14)	6.0(5)
	37.8(24)	18.8(8)	29.2(11)	4.5(3)
	$40.3^{+2.3}_{-2.2}$	20.8(9)	26.8(11)	4.9(3)
	$42.7^{+2.1}_{-2.0}$	21.3(9)	24.3(10)	6.1(5)
	45.1(19)	22.9(9)	23.5(14)	5.7(3)
	47.5(17)	24.3(10)	23.3(9)	5.5(3)
	49.6(16)	24.7(12)	22.4(11)	6.2(3)
	57.6(14)	26.4(13)	19.4(10)	7.2(3)
	64.7(12)	25.9(13)	18.1(9)	5.2(3)
	$48.2^{+1.8}_{-1.7}$	25.5(10)	22.5(8)	5.5(5)
	51.8(16)	25.5(10)	21.2(8)	5.0(4)
	57.0(14)	25.5(12)	19.0(7)	5.1(3)
	64.2(12)	26.3(11)	18.1(8)	6.4(5)
	70.9(11)	26.0(11)	16.0(7)	6.5(5)
	77.0(9)	25.5(10)	14.6(5)	6.4(4)
	82.8(8)	25.5(10)	13.8(6)	5.4(4)
	88.3(8)	25.8(11)	13.0(5)	6.8(5)
	93.6(7)	25.8(12)	12.5(7)	6.3(5)
	$98.6^{+0.7}_{-0.6}$	25.4(10)	11.6(6)	5.4(5)
	$79.0^{+2.0}_{-1.9}$	26.1(10)	13.7(6)	4.5(3)
	88.8(19)	24.6(14)	11.9(4)	4.7(3)
	97.8(16)	24.6(9)	11.6(8)	4.76(20)

Continued on next page

Continued from previous page

106.1(14)	24.6(9)	11.6(5)	3.90(18)
114.1(13)	23.8(9)	10.5(4)	4.97(22)
121.6(11)	23.8(9)	10.3(5)	4.76(20)
$128.8^{+1.0}_{-0.9}$	23.7(9)	10.3(5)	4.8(3)
135.8(8)	23.5(9)	9.5(10)	5.29(22)
142.5(6)	23.3(9)	9.5(4)	5.20(24)
149.0(5)	22.9(9)	9.0(4)	4.45(21)
134.8(17)	23.2(11)	10.0(6)	4.9(3)
141.5(16)	23.6(9)	9.5(5)	4.9(3)
148.1(14)	22.2(8)	9.8(4)	3.81(22)
154.3(13)	22.0(8)	9.6(4)	4.07(23)
160.6(12)	21.9(8)	9.2(7)	3.73(18)
166.5(10)	21.7(8)	9.2(5)	3.79(20)
172.3(9)	22.1(10)	9.2(5)	4.9(3)
178.1(7)	22.0(8)	8.5(4)	4.58(22)
183.7(6)	21.8(8)	8.2(4)	5.0(3)
189.1(4)	22.4(8)	7.4(4)	4.9(3)

TABLE A.4: ^{12}C(p,x)^{12}N reaction cross sections.

E (MeV)	σ (mb)
23(7)	1.5(3)
28(6)	4.0(4)
40(4)	7.9(7)
53(4)	9.2(9)
66(3)	7.5(7)
77(3)	5.7(7)
$99.5^{+2.5}_{-2.4}$	4.3(5)
120.7(22)	3.0(4)
152.0(19)	2.0(4)

TABLE A.5: ^{40}Ca(p,x)^{38m}K reaction cross sections.

E (MeV)	σ (mb)
25(5)	15.0(16)
32(4)	44(10)
40(4)	87(9)
43(3)	99(8)
47(3)	96(6)
56(3)	88(9)
57(3)	87(6)
67.6(24)	82(9)
$77.8^{+2.2}_{-2.1}$	79(6)
$88.0^{+2.1}_{-1.9}$	74(6)
108.3(18)	70(7)
128.5(16)	66(7)
158.7(14)	60(6)
198.9(12)	53(5)

TABLE A.6: ^{31}P(p,x)^{29}P reaction cross sections.

E (MeV)	σ (mb)
30(6)	7.4(8)
39(5)	27.3(17)
43(4)	33.7(18)
56(4)	32.9(22)
67(3)	30.0(20)
78(3)	28.0(31)
100(3)	25.0(28)
$121.3^{+2.4}_{-2.3}$	22.9(26)
$152.4^{+2.1}_{-1.9}$	21.8(24)
193.5(19)	20.7(24)

Appendix B

Publication Record

PEER-REVIEWED PUBLICATIONS AS FIRST-AUTHOR:

1. T. Rodriguez-Gonzalez, et al. Feasibility of online PET range verification in proton therapy using short-lived isotopes. (In preparation).

2. T. Rodriguez-Gonzalez, et al. Proton-induced nuclear cross sections of ^{12}N, ^{38m}K and ^{29}P up to 200 MeV/u for PET range verification. (In preparation).

3. T. Rodriguez-Gonzalez, et al. Proton-induced nuclear cross sections of ^{11}C, ^{13}N and ^{15}O up to 200 MeV/u for PET range verification. Nuclear Data Sheets **187**, 579 (2023). https://doi.org/10.1016/j.nds.2023.01.004

4. T. Rodriguez-Gonzalez, et al. Production yields at the distal fall-off of the β^+ emitters ^{11}C and ^{13}N for in-vivo range verification in proton therapy. Radiation Physics and Chemistry **190**, 109759 (2022). https://doi.org/10.1016/j.radphyschem.2021.109759

PEER-REVIEWED CONFERENCE PROCEEDINGS AS FIRST-AUTHOR:

1. T. Rodriguez-Gonzalez, et al. Preliminary results of the experimental cross sections of the long-lived β^+ emitters of interest in PET range verification in proton therapy at clinical energies. European Physical Journal - Web of Conferences **261**, 05007 (2022). https://doi.org/10.1051/epjconf/202226105007

2. T. Rodriguez-Gonzalez, et al. Production yields of β^+ emitters for range verification in proton therapy. European Physical Journal - Web of Conferences **239**, 24003 (2020). https://doi.org/10.1051/epjconf/202023924003

3. T. Rodriguez-Gonzalez, et al. Measurement of the production cross section of β^+ emitters for range verification in proton therapy. In: García-Ramos JE., Andrés M., Valera J., Moro A., Pérez-Bernal F. (eds) Basic Concepts in Nuclear Physics: Theory, Experiments and Applications. Rábida 2018. Springer Proceedings in Physics **225** Springer, Cham. https://doi.org/10.1007/978-3-030-22204-8_16

PEER-REVIEWED PUBLICATIONS AS CO-AUTHOR:

1. J. Balibrea-Correa, et al. Hybrid in-beam PET- and Compton prompt-gamma imaging aimed at enhanced proton-range verification. The European Physical Journal Plus **137**, 1258 (2022). https://doi.org/10.1140/epjp/s13360-022-03414-y

2. J. Balibrea-Correa, et al. First in-beam tests on simultaneous PET and Compton imaging aimed at quasi-real-time range verification in hadron therapy. European Physical Journal - Web of Conferences **261** 05002 (2022). https://doi.org/10.1051/epjconf/202226105002

3. V. Babiano-Suárez, et al. Imaging neutron capture cross sections: i-TED proof-of-concept and future prospects based on Machine-Learning techniques. European Physical Journal A **57** 197 (2021). https://doi.org/10.1140/epja/s10050-021-00507-7

4. C. Guerrero, et al. Neutron Capture on the s-Process Branching Point $^{171}\mathrm{Tm}$ via Time-of-Flight and Activation. Physical Review Letters **125** 142701 (2020). https://doi.org/10.1103/PhysRevLett.125.142701

5. B. Fernández, et al. HiSPANoS facility and the new neutron beam line for TOF measurements at the Spanish National Accelerator Lab (CNA). Journal of Physics: Conf. Ser. **1643** 012033 (2020). https://doi.org/10.1088/1742-6596/1643/1/012033

6. C. Domingo-Pardo, et al. Review and new concepts for neutron-capture measurements of astrophysical interest. Journal of Physics: Conf. Ser. **1668** 012013 (2020). https://doi.org/10.1088/1742-6596/1668/1/012013

7. M.A. Millán-Callado, et al. Laser-driven neutrons for time-of-flight experiments? European Physical Journal - Web of Conferences **239** 17012 (2020). https://doi.org/10.1051/epjconf/202023917012

8. M. A. Millán-Callado, et al. Neutron Radiography at CNA. In: García-Ramos JE., Andrés M., Valera J., Moro A., Pérez-Bernal F. (eds) Basic Concepts in Nuclear Physics: Theory, Experiments and Applications. Rábida 2018. Springer Proceedings in Physics **225** Springer, Cham. https://doi.org/10.1007/978-3-030-22204-8_13